The Effectiveness of Hooks for Plain Steel Reinforcement

A Thesis

Submitted to the College of Graduate and Postdoctoral Studies

In Partial Fulfillment of the Requirements

For the Degree of Master of Science

In the Department of Civil, Geological, and Environmental Engineering

University of Saskatchewan

Saskatoon, SK

By:

Bjørn Erik Vørs

Permission to Use

In presenting this thesis in partial fulfilment of the requirements for a postgraduate degree from the University of Saskatchewan, I agree that the Libraries of the University may make it freely available for inspection. I further agree that permission for copying of this thesis in any manner, in whole or in part, for scholarly purposes may be granted by the professor or professors who supervised my thesis work or, in their absence, by the Head of the Department or the Dean of the College in which my thesis work was done. It is understood that any copying or publication or use of this thesis or parts thereof for financial gain shall not be allowed without any written permission. It is also understood that due recognition shall be given to me and to the University of Saskatchewan in any scholarly use which may be made of any material in my thesis.

Requests for permission to copy or make other use of material in this thesis in whole or part should be addressed to:

Head of the Department of Civil, Geological, and Environmental Engineering
University of Saskatchewan
Engineering Building
57 Campus Drive
Saskatoon, Saskatchewan S7N 5A9

Or

Dean of College of Graduate and Postdoctoral Studies
University of Saskatchewan
116 Thorvaldson Building, 110 Science Place
Saskatoon, Saskatchewan S7N 5C9

Abstract

As buildings age, their structural integrity must be assessed and reassessed at regular intervals to ensure the safety of their continued use and to advise on retrofits and repairs necessary for preventative maintenance and responsive repair. Historic buildings often contain plain reinforcement whereas modern buildings exclusively contain modern deformed reinforcement. Younger engineers in particular have not been trained with or worked with plain bar. Modern American Concrete Institute (ACI) and Canadian Standards Association (CSA) Group codes largely do not contain adequate provisions to assess the structural integrity of many historic buildings.

Twenty-four beam-column joint specimens with four different hook configurations were tested under tension to compare the anchorage capacities of embedded plain and modern deformed 90° and 180° hooked bars. Six replicates of each configuration were tested to determine whether statistically significant differences at the 95% confidence level existed between the anchorage capacities of plain versus modern deformed hooked bars. Visual observations were documented manually to assess differences between crack patterns and observed failure modes.

Typical cracking patterns were observed for groups of both specimens containing 90° and 180° hooks. The degree of cracking observed aligned with results of similar studies. All specimens with 90° hooks failed by side blowout whereas those with 180° hooks failed by front blowout. No evidence of group effects (i.e. decreased anchorage capacity) was observed. Statistically significant differences in maximum normalized tensile load at the 95% confidence level were observed between 90° plain and modern deformed bars, wherein the plain bars had a 3.8 kN/MPa lower maximum; 180° plain and modern deformed bars, wherein the plain bars had a 5.6 kN/MPa lower maximum; and 90° and 180° modern deformed hooked bars, wherein the 90° bars had a 4.0 kN/MPa lower maximum. No statistically significant differences in displacement at maximum normalized load were observed.

An extensive replicate-based study of plain hooked bar incorporating additional parameters (e.g. lead length, bend angle, etc.) is recommended. The value of the recommended work is in determining the sensitivity of hooked bar performance to variations in these parameters.

Co-Authorship

All experimental work presented in this thesis was conducted by Bjørn Vørs and reviewed by Dr. L.R. Feldman. The results of a select number of specimens from this study were published in the proceedings of the 2019 CSCE Annual General Conference in Laval, Canada. A manuscript summarizing the findings of thesis related to plain and modern deformed hooked bars was submitted to the ACI Structural Journal on March 17, 2020. A revised version of the manuscript was pending submission at the time of thesis submission.

Acknowledgements

The author would like to thank Dr. Lisa R. Feldman. The author would also like to thank the following people from the University of Saskatchewan: Dr. Leon Wegner, Dr. Bruce Sparling, Serge Nazarenko, Bryce Marcotte, Ryan Stallmann, Owen Beach, Amy Miller and, Brennan Pokoyoway. Special thanks are extended to the American Concrete Institute. Financial support was also provided by Dr. Feldman's NSERC Discovery Grant and the Saskatchewan Centre for Excellence in Transportation and Infrastructure (SCETI). The author would also like to thank Lafarge Canada Inc. and SSAB for providing in-kind support. The author would like to thank their family and friends for all the support throughout this endeavor. The countless phone calls and visits were amazing. The author would also like to thank Megan Fulmes for her help and support in answering all my random questions about writing; her explanations truly helped me to become a better writer.

“To strive, to seek, to find, and not to yield”

Alfred Tennyson

Table of Contents

List of Tables

List of Figures

List of Symbols

A_b	Cross-section reinforcement area per bar
C	Compressive reaction
d_b	Diameter of reinforcing bar
E_c	Modulus of elasticity of concrete
E_s	Modulus of elasticity of reinforcement
f_b	Bearing stress
f'_c	Concrete compressive strength
$f'_{c,7\text{-}day}$	Seven day concrete compressive strength
f_r	Modulus of rupture of concrete
f_{yd}	Dynamic yield strength of reinforcement
f_{ys}	Static yield strength of reinforcement
f_y	Nominal yield strength of the reinforcement
l_d	Development length of hooked reinforcing bar
N_i	Number of samples for statistical analysis
P_c	Applied axial compressive force
P_{max}	Maximum normalized tensile load applied to the hooked bars
P_n	Normalized tensile load applied to the hooked bars
r_i	Inside radius of a hook
R_y	Surface roughtness of reinforcement
R_1	Upper reaction force
R_2	Lower reaction force
S_i	Standard deviation for statistical analysis
T	Applied tensile force
T_{stat}	T statistic for statistical analysis
u	Bond stress
v	Degrees of freedom for statistical analysis
w	Distributed load

x_i	Individual value for statistical analysis
Y_i	Average for statistical analysis
$\dot{\varepsilon}$	Strain rate of reinforcement
λ	Adjustment factor for lightweight concrete
ψ_e	Adjustment factor for epoxy-coated or zinc and epoxy dual-coated reinforcement
ψ_c	Adjustment factor for concrete cover
ψ_o	Adjustment factor for hook placement
ψ_r	Confining reinforcement adjustment factor

Chapter 1
Introduction

1.1 Background

Historic and contemporary structures often incorporate steel-reinforced concrete beams to provide flexural strength. Structures with reinforced concrete leverage the tensile and compressive strengths of steel reinforcement and of concrete for structural integrity. The investigation detailed in this thesis concerns the capacity of two types of steel reinforcement significantly represented in historical and contemporary structures, respectively – plain and modern deformed reinforcement.

Historic buildings often contain plain reinforcement and modern buildings exclusively contain modern deformed reinforcement. In the past, a wide range of steel reinforcement types were used but plain reinforcement was very common (Abrams 1913, Meinheit and Felder 2014). The popularity of plain reinforcement decreased significantly as modern deformed reinforcement proved to be a superior structural component (ACI Committee 408 2003). This transition from plain to modern deformed reinforcement is evidenced by changes to both the American and Canadian concrete codes. In 1963 and 1970, the American Concrete Institute (ACI) 318, *Building Code Requirements for Structural Concrete and Commentary*, and the CSA Group (CSA) A23.3, *Design of Concrete Structures,* respectively, contained provisions for embedded plain reinforcement for the last time (ACI Committee 318 1963, CSA 1970).

Engineers must assess and reassess the structural integrity of buildings when a change of use occurs to ensure the building can withstand the new loads. While the ACI 318 and CSA A23.3 contain provisions which guide engineers in designing structurally sound buildings for new construction, neither contains provisions for the assessment of historic or contemporary existing structures. Engineers tasked with the assessment of existing buildings, therefore, lack provisions to guide their work, particularly with respect to historic structures. Two primary factors explain this situation: (1) historic structures often contain plain reinforcement and

provisions for this reinforcement type have not been included in the ACI 318 or CSA A23.3 for decades and (2) the ACI 318 and CSA A23.3 do not contain provisions for the assessment of existing buildings.

The full structural capacity of reinforced concrete is realized when an adequate reaction exists between the reinforcement and its surrounding concrete that effectively transfers stresses between the two (Nadim Hassoun and Al-Manaseer 2008). A significant factor affecting bond strength is the length of embedded reinforcement. Inadequate bond to effectively transfer stresses is observed where the length of embedded reinforcement is insufficient. The capacity of reinforced concrete may be enhanced by the presence of hooks. Hooks are used where beams meet exterior columns and the incorporation of a sufficient horizontal length of embedded reinforcement is not possible due to constrained space within the column (MacGregor and Wight 2012). Hooked reinforcement is common throughout historic and modern buildings and two hook geometries, 90° and 180°, predominate. Figure 1.1 illustrates these two hook geometries for a 25M bar per CSA A23.1 code (CSA 2014A).

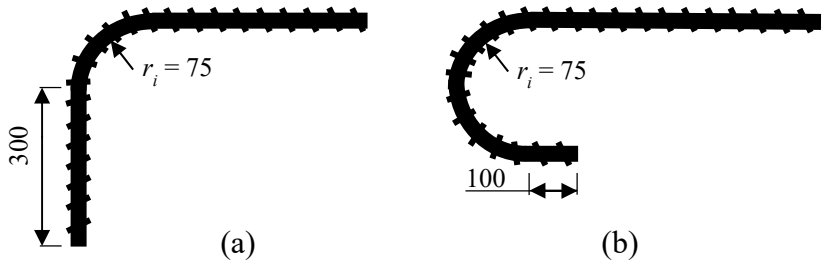

Note: Dimensions shown for 25M modern deformed reinforcement

Figure 1.1: Hooks (a) 90º, and (b) 180º

Relatively few research programs have investigated the capacity of plain hooked bars since they were replaced by modern deformed bars due to the superior bond capabilities of the latter. Abrams (1913), Mylrea (1928), and Cleland et al. (2001) incorporated but failed to explicitly evaluate the performance of plain hooked bars. Considerably more research has

focused on the evaluation of modern deformed hooked bars; however, direct and replicate-focused comparisons between the capacities of plain and modern deformed hooks have not been made. Much of the previous research concerning the anchorage capacity of hooked reinforcement has been parametric and focused on assessing or developing concrete code provisions (i.e. Minor and Jirsa (1975), Marques and Jirsa (1975), Pinc et al. (1977), Johnson and Jirsa (1981), Soroushian et al. (1988), and Sperry et al. (2017)). These research programs did not incorporate replicates and, thus, contributed little to the direct comparison of the anchorage capacities of different hooked bar configurations. These programs exclusively assessed modern deformed bar and, therefore, did not compare differences in anchorage capacity between plain and modern deformed bar types. The investigation detailed in this thesis concerns the differences, if any, between the anchorage capacities of plain and modern deformed bars with 90º and 180º hook geometries. It was hypothesized that the modern deformed hooked bars would exhibit greater anchorage capacity due to their raised deformations. The anchorage capacities of plain and modern deformed hooked bars are directly compared through the use of replicates.

1.2 Objectives

This investigation contributes to the body of information required to assess the structural integrity of existing historical buildings incorporating concrete reinforced with plain bar. This information includes a direct comparison of the anchorage capacities of plain and modern deformed hooked bars. This investigation had the following specific objectives:

- To ascertain whether the structural performance under tensile load of plain versus modern deformed hooked bars differs as related to anchorage capacity, bar displacement at maximum load, visually-determined failure mode, and suddenness of failure;
- To establish whether the structural performance under tensile load of 90º versus 180º plain hooked bars differs as related to anchorage capacity, bar displacement at maximum load, visually-determined failure mode, and suddenness of failure; and
- To contribute to the existing body of knowledge regarding whether the structural performance under tensile load of 90º versus 180º modern deformed hooked bars differs

as related to anchorage capacity, bar displacement at maximum load, visually-determined failure mode, and suddenness of failure.

1.3 Scope of Research

Four beam-column joint specimen configuration groups with six replicates per group were constructed and tested to evaluate the differences, if any, between plain and modern deformed bars with 90° and 180° hook geometries. The four configurations tested were: 90º plain, 180º plain, 90º modern deformed, and 180º modern deformed hooked bars. All other specimen parameters were controlled, including the overall dimensions of the specimens, concrete cover, bar diameter, embedded length of the straight portion of the hooked bars, spacing and type of longitudinal and transverse reinforcement, and applied axial load. Six replicate specimens of each configuration were tested in order to increase the statistical precision and reproducibility of the experimental findings and to facilitate use of the Student's t-test for statistical comparison of different groups. Anchorage capacity, bar displacement at maximum load, visual observations (i.e. cracking and failure modes), and suddenness of failure were used to assess performance across specimen groups. The specimen parameters held constant in this investigation are relevant as potential variables in future work.

This research partially addresses the noted gap in the provisions of the ACI and CSA regarding assessments of historical structures. Young engineers in particular have not been trained with or worked with plain bar. The potential impact of research within this scope provides structural engineers, particularly the younger cohort, with additional knowledge allowing them to make more accurate, safe, and cost-effective recommendations based on their assessments of structures containing plain and modern deformed hooked bar.

1.4 Thesis Outline

The outline of this thesis is as follows:

Chapter 1 presents the background, objectives, and scope of this research study on the effectiveness of plain hooked bars.

Chapter 2 presents the literature reviewed for this study and the relevant changes over time in the ACI 318 and CSA A23.3 codes.

Chapter 3 presents the experimental program including the test parameters, specimen geometry, material selection, construction phases, specimen construction, and testing of specimens.

Chapter 4 presents analyses of experimental results including the material properties, identification of outliers, visual observations, failure modes, suddenness of failures, maximum normalized tensile loads, and displacements of the hooked bars.

Chapter 5 presents conclusions drawn from this study and provides recommendations for future work to improve the body of knowledge surrounding plain hooked bars.

Chapter 2
Literature Review

2.1 Introduction

This literature review presents the foundational published research relevant to this study which pertains to hooked plain and modern deformed bars. Plain reinforcement is a hot-rolled steel bar with a round or square cross-section and an unpolished surface. Modern deformed reinforcement has a round cross-section and is characterized by regular deformations along its length (MacGregor and Wight 2012). This chapter reviews the mechanics of bond in reinforced concrete and the bond behaviour of embedded hooked bars. Changes to the CSA and the ACI codes over time are then contextualized by contemporary research. This chapter concludes with a brief discussion of the knowledge gaps left unaddressed by the existing body of research and how the objectives of this study address those gaps.

2.2 Mechanics of Bond in Reinforced Concrete

This section defines bond as it applies to straight bar lengths as well as hooked bars and reviews literature on the mechanics of bond in reinforced concrete. Bond is the transfer of flexural tensile forces between concrete and embedded reinforcement (MacGregor and Wight 2012). Bond is essential to structural integrity because the noted transfer of forces enables a structure to act compositely to carry its design load. Bond stresses in reinforced concrete under tension act along the length of the embedded reinforcement.

2.2.1 Bond Behaviour of Straight Plain and Modern Deformed Bars in Concrete

Plain bars bond with surrounding concrete exclusively due to adhesion and then wedging action. This wedging action, which contributes to frictional sliding resistance, occurs when bar displacement has begun and small concrete particles break free from the adjacent concrete surface as the bar moves. These free particles wedge between the bar and intact concrete and

increase frictional sliding resistance. The presence of the deformations that characterize modern deformed reinforcement affects its bond behaviour in concrete. The bond mechanisms of chemical adhesion and frictional sliding resistance contribute to the bond behaviours of both plain and modern deformed reinforcement types; mechanical interlock is a third bond behaviour mechanism that applies only to modern deformed reinforcement (Abrams 1913, MacGregor and Bartlett 2000, Feldman and Bartlett 2005). These three bond mechanisms are discussed in this sub-section and described by free body diagrams for each embedded reinforcement type, subject to tension. The bond resistance of a straight length of plain bar is, therefore, inferior to deformed bar due to its lack of deformations (ACI Committee 408 2003, MacGregor and Wight 2012).

Figure 2.1 is a free body diagram for a straight length of embedded plain reinforcement under externally applied tension, T. Bond stress, u, at the interface between the reinforcement and concrete shown in Figure 2.1 is comprised of chemical adhesion and frictional sliding resistance and opposes tension, T. The bond mechanism of chemical adhesion occurs between embedded reinforcement and concrete and is caused by the grip or stickiness caused by molecular-level interactions between the two components (Nawy 2003). Frictional sliding resistance initiates when chemical adhesion has been overcome and the loaded reinforcement begins to slip from the surrounding concrete (Abrams 1913). Frictional sliding resistance is caused by both the roughness of the contact surfaces and by small particles of concrete breaking off and becoming wedged between the intact concrete and the loaded reinforcement. This wedging action, in turn, creates bursting pressure.

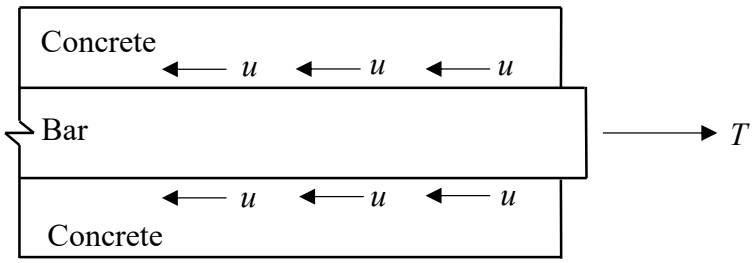

Figure 2.1: Free body diagram for embedded plain reinforcement under tension

Figure 2.2 illustrates a point-loaded beam member and the couple produced which maintains force equilibrium. For the loading shown, the top of the beam is in compression while the bottom is in tension (i.e. the couple) as a point load is applied and the beam deflects downward (Beer et al. 2005). This couple facilitates the transfer of tension, T, in the reinforcement into the concrete via bond stress, u.

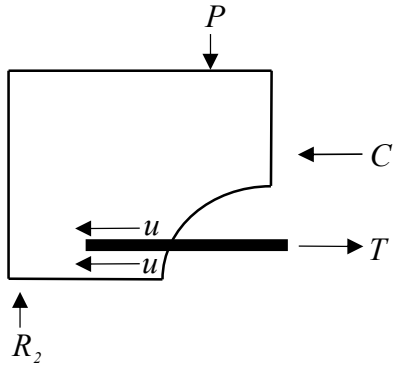

Figure 2.2: Free body diagram of cross-section at the mid-span of a supported beam

The deformations characteristic of modern deformed reinforcement introduce the bond mechanism of mechanical interlock via their raised deformations. Mechanical interlock is caused by the deformations bearing on adjacent concrete (MacGregor and Bartlett 2000). Mechanical interlock is the primary bond mechanism observed in actively slipping embedded modern deformed reinforcement because displacement occurs only after chemical adhesion and static frictional sliding resistance have both been overcome (MacGregor and Wight 2012).

Figure 2.3 is a free body diagram for a straight length of embedded modern deformed reinforcement under tension, T. The regular, raised deformations characterizing modern deformed reinforcement are primarily introduced to facilitate bearing resistance on each rib (ACI Committee 408 2003). Additionally, the shape of the deformations allows for frictional sliding resistance to occur on the slope of each rib. Bearing resistance and friction between the concrete and ribs is important for force transfer in bond. Chemical adhesion and frictional sliding

resistance are omitted from Figure 2.3 to highlight mechanical interlock. Figure 2.3 shows mechanical interlock causing bearing stress, f_b, to resist displacement from the applied tension, T. Bearing stress, f_b, acts at a right angle to the face of the deformations and is created when they contact the surrounding concrete due to the applied tension, T. Bearing stress can be separated into horizontal and vertical components. The horizontal component of the bearing stress counteracts applied tension, T, to prevent reinforcement displacement. The vertical component of the bearing stress causes a bursting pressure that leads to radial cracks forming in the concrete. These radial cracks are considerably more extensive than any observed in concrete surrounding plain reinforcement (MacGregor and Wight 2012).

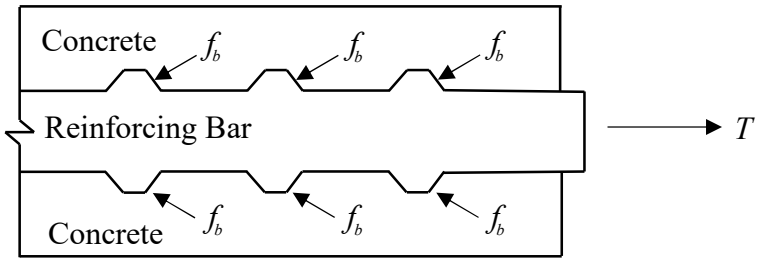

Figure 2.3: Free body diagram for embedded modern deformed reinforcement under tension

2.2.2 Anchorage Behaviour of Hooked Reinforcing Bars and the Surrounding Concrete

Mechanical anchorage is a mechanism used to prevent displacement of the embedded reinforcement. Successful use of mechanical anchorage improves the anchorage capacity of the embedded reinforcement. Mechanical anchorage can be introduced by a variety of reinforcement end pieces, including hooks. Such end pieces are used to shorten reinforcement length in cases of restrictive dimensions of the member without sacrificing structural integrity (MacGregor and Wight 2012). Hooks are used where beams meet exterior columns and the absence of space on the other side of the column prevents the use of a sufficiently long horizontal straight bar to prove adequate for bond. Anchorage capacity, therefore, depends on the engagement of the portion of the concrete that is in compression in advance of the hook.

Figures 2.4 (a) and 2.5 (a) illustrate the stresses and forces of mechanical anchorage acting on 90° and 180° hooks, respectively, due to externally applied tension (or tensile force), *T*. Lead length is defined as the straight length of reinforcement immediately preceding the curved portion of the hook. Tension, *T*, applied to the hooked bar must overcome both the chemical adhesion and static frictional sliding resistance of the lead length before the hook can begin to slip. As shown in Figures 2.4 (a) and 2.5 (a), the hooked bar will slip in the same direction as the external tension, *T*, it is subjected to. When the hook begins to slip, bond dissipates on its outer radius as the reinforcement bears against the concrete at the inner radius of the hook and causes this concrete to crush. Stresses are observed along the bend region of the hook and increase progressively toward the end of its tail due to the confining action of the concrete around the reinforcement.

Ninety-degree and 180° embedded hooked bars tend to straighten out when subjected to tail kickout stress. The tail of a 180° hook is confined more deeply in the concrete and has a longer path of resistance through the concrete to the outer surface of the rear face than does a 90° hook. For this reason, relatively minimal tail kickout stress results from tension, *T*, applied to 180° hooks and they are less susceptible to tail kickout stresses (MacGregor and Wight 2012). Specimens containing 90° hooks also tend to cause spalling of the concrete on the rear face more often than do specimens containing 180° hooks because of their relatively shallower concrete cover.

Figures 2.4 (b) and 2.5 (b) illustrate bond stress distributions between concrete and 90° and 180° hooked bars, respectively, subject to the external tensile force, *T*, of 200 kN, as reported by MacGregor and Wight (2012). Peak stress occurs at the face of the member where the hooked bar enters the concrete and then decreases in a non-linear fashion along the length of the reinforcement. The largest amount of reinforcement displacement occurs at the front face where the hook exits the member due to a gradient of deformation along the bar wherein the deepest portion of the reinforcement experiences the least displacement. The largest change in

bond stress occurs along the tail of the hook as it bears on the concrete against the inner radius of the hook.

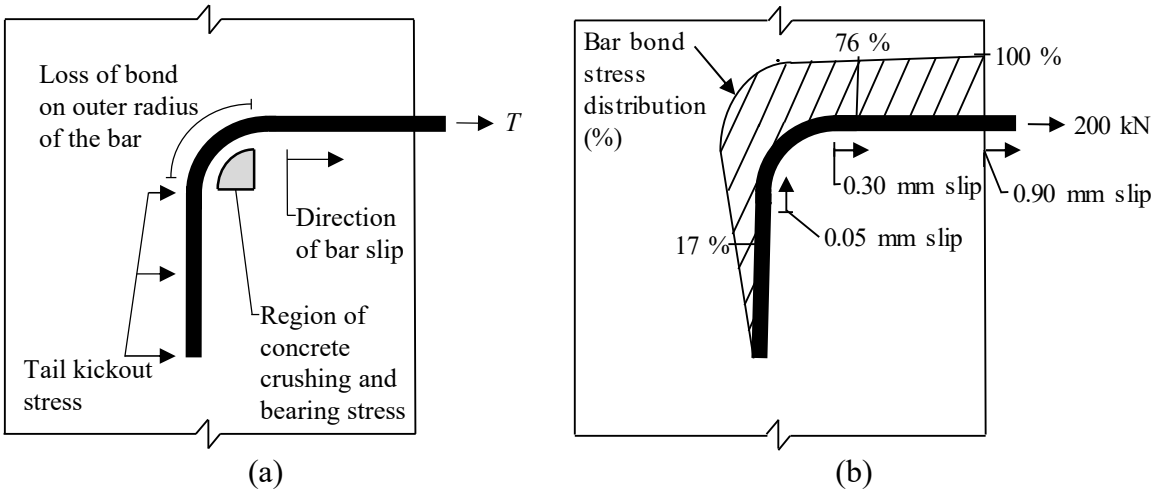

Figure 2.4: 90º hooked bar: (a) Stresses and forces acting on the bar (b) bond stress distribution (modified from MacGregor and Wight 2012)

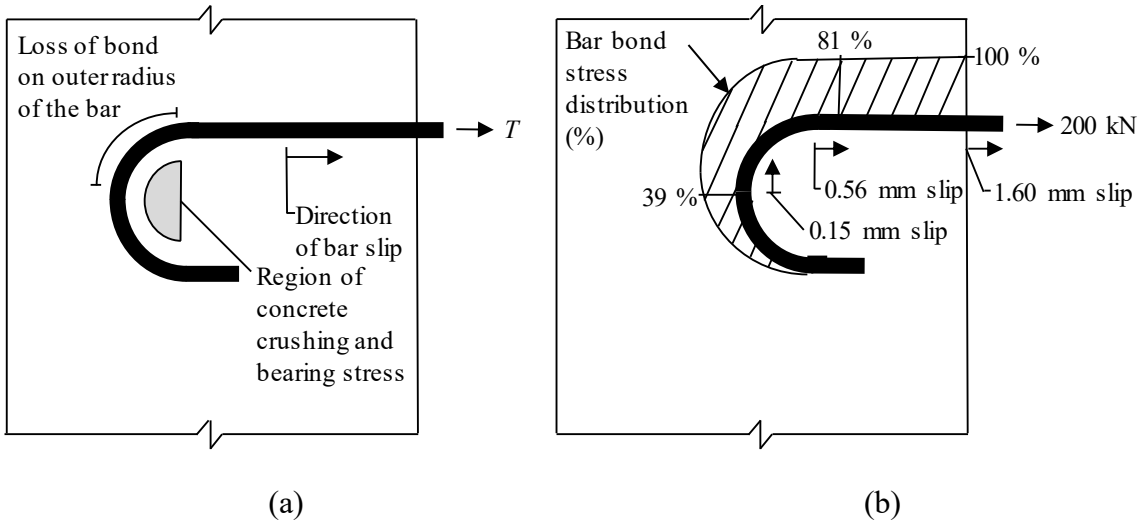

Figure 2.5: 180º hooked bar: (a) Stresses and forces acting on the bar (b) bond stress distribution (modified from MacGregor and Wight 2012)

2.2.3 Factors Affecting Bond

Factors affecting bond include: cross-sectional shape of the reinforcing bar, cross-sectional diameter, surface roughness, entire length of reinforcement embedded in the concrete, whether transverse reinforcement is present or not, concrete compressive strength, and concrete cover. These factors influence the magnitude of the bond mechanisms of chemical adhesion, frictional sliding resistance, and mechanical interlock (Nawy 2003, MacGregor and Wight 2012).

A variety of reinforcement types with different cross-sectional shapes were used in the past (i.e. round, square, irregular, etc.); however, modern deformed reinforcement fabricated to current ASTM-A615 and CSA G30.18 codes is the only currently allowable reinforcement in new structures (ACI Committee 408 2003, ACI Committee 318 2014, CSA 2014B). The cross-sectional shape of reinforcement affects adhesion, frictional sliding resistance, and the presence of mechanical interlock in bond, as discussed in Section 2.2.1. The plain and modern deformed bars relevant to this study have round cross-sectional shapes. The cross-sectional diameter of modern deformed reinforcement regularly oscillates along its length to create its characteristic deformations. The cross-sectional diameter of plain reinforcement is constant and results in a prismatic member.

The overall cross-sectional diameter of reinforcement also affects bond resistance. The length of embedded reinforcement required by code to develop the design strength of the reinforcement increases with bar diameter (ACI Committee 408 2003). An increase in bar diameter increases the cross-sectional area. As stress is equal to force divided by area, an increase in cross-sectional area translates into less stress in the bar. Larger reinforcement diameters, therefore, safely carry higher total bond forces than smaller reinforcement diameters when all other factors are held equal.

The surface roughness of embedded reinforcement affects bond between the bar and concrete (ACI Committee 408 2003). Reinforcement with a smoother finish exhibits lower bond

strength due to correspondingly lower frictional sliding resistance (Abrams 1913, Feldman and Bartlett 2005).

The length of reinforcement embedded in concrete is a factor affecting bond. Embedded length refers to the length of reinforcement subject to bond forces within the concrete (ACI Committee 408 2003). Development length is defined by the ACI 318 code as the length of embedded reinforcement necessary to develop yielding of the reinforcement (ACI Committee 318 2019). In this thesis, 'development length' refers exclusively to the development length of the hooked bar.

Researchers evaluating the impact of development length on bond for plain and modern deformed reinforcement types arrived at several conclusions. Marques and Jirsa (1975), Pinc et al. (1977), and Johnson and Jirsa (1981) evaluated specimens with hooked bars and concluded a minimum development length of modern deformed reinforcement is necessary to develop its designed yield strength. Hassan and Feldman (2012) and MacLean and Feldman (2014) evaluated specimens with straight bars and determined a linear and proportional relationship exists between applied load and the development length of plain reinforcement. ACI reported a linear but not proportional relationship between applied load and the development length and diameter of straight lengths of modern deformed bar (ACI Committee 318 2014). This difference in proportionality of the applied load and development length relationship between plain and modern deformed bars is hypothesized to be caused by mechanical interlock once slip initiates.

The presence of transverse reinforcement is a factor affecting bond. Transverse reinforcement improves anchorage capacity by confining the concrete and preventing crack propagation (ACI Committee 408 2003). The effects of transverse reinforcement are greater for modern deformed than plain reinforcement because the former exhibits more extensive radial cracking when the reinforcing bars are subject to tensile forces, as discussed in Section 2.2.1.

Concrete compressive strength also affects bond. Bond strength and concrete compressive strength exhibit a positive and proportional relationship. Orangun et al. (1977) and Feldman and Barlett (2005) found the square root of the concrete compressive strength is reasonably proportional to bond strength for straight lengths of modern deformed and plain reinforcement, respectively. Considering this research, current Canadian and American codes recognize that the square root of the concrete compressive strength is adequate for use in development length equations (CSA 2014B, ACI Committee 318 2014). The relationship between concrete compressive strength and bond suggests a tensile failure in concrete, as the tensile strength (or modulus of rupture) of concrete is proportional to the square root of its compressive strength.

Concrete cover refers to the shortest distance between the surface of the nearest embedded reinforcement and the face of the concrete member (CSA 2014B). The depth of concrete cover affects the bond of the embedded reinforcement and a specific depth of concrete cover is required by code. The minimum specified depth is known to mitigate the cracking effects of radial stresses and ensures that cracks do not propagate from the surface of the loaded bar all the way to the face of the concrete member. This minimum depth provides adequate confinement to prevent the embedded reinforcement from fracturing the concrete, spalling the concrete, and ultimately emerging from the member. A reduction in concrete cover below the minimum depth reduces bond strength (ACI Committee 408 2003).

Cairns et al. (2006) demonstrated that increased concrete cover increases the bond strength of plain reinforcement. In contrast, Feldman and Barlett (2005) found maximum average bond stress is independent of concrete cover depth for plain reinforcement. Feldman and Bartlett (2005) found specimens containing plain reinforcement showed only minor radial cracks and concluded the extent of radial cracking in these specimens was insensitive to concrete cover depth. Modern deformed reinforcement specimens are known to display extensive radial cracking and are consequently sensitive to concrete cover depth (MacGregor 1992).

2.3 Testing Methods for Hooked Bar Specimens

Historical research on the anchorage of hooked bars has relied on several different test specimen types which have evolved over time. This section presents the methodologies used to evaluate the three types of test specimens used to assess the bond and anchorage of hooked bars. These test specimens are called pullout, modified cantilever, and beam-column joint.

2.3.1 Pullout Test Specimen

The most basic of the three testing methods discussed in this thesis is the pullout test specimen. The pullout test specimen is comprised of a cylindrical block of concrete with a single bar located along the centroidal axis of the specimen protruding from one face. The pullout test specimen is positioned to be loaded monotonically on the testing apparatus which supports it and has a small opening for the reinforcement to pass through. The pullout test, shown in Figure 2.6, is performed by externally loading the reinforcement protruding from the specimen to induce tension, T, until the maximum load is observed and the structural capacity of the member is overcome. Pullout specimen tests are popular because the specimens are simple, cost effective, and easy to construct and evaluate.

The pullout test provides a poor representation of the behaviour between the concrete and embedded reinforcement because the testing apparatus support bears on and induces compression in the concrete (ACI Committee 408 2003). These compression struts produce unconservative bond values because they allow the specimen to bear a higher tensile force. The pullout specimen does not adequately approximate a flexural member.

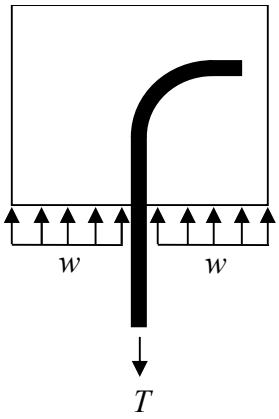

Figure 2.6: Free body diagram for pullout test specimen

2.3.2 Modified Cantilever Beam Test Specimen

The modified cantilever beam test specimen is comprised of a rectangular block of concrete with one or more bars protruding from one face. The supports provided by its testing apparatus create the couple discussed in Section 2.2.1. Figure 2.7 shows the free body diagram for the modified cantilever beam specimen. The specimen is tested by externally loading the protruding reinforcement with hydraulic jacks to induce tension, T, in the bar or bars until the maximum load is observed and the structural capacity of the member is overcome. This testing method more accurately represents a column with an actual adjoining beam in flexure than does pullout testing because it creates the appropriate couple between the externally applied tensile force, T, and bearing force, C. The bearing force, C, simulates that which would otherwise be introduced by a beam framing into a structural column. The bearing force is applied to the front face of the specimen a distance below the longitudinal axis of the embedded reinforcement protruding from the specimen (i.e. C is directly below T). R_1 and R_2 provide stabilising reactions in the test setup which prevent the specimen from overturning during testing.

The modified cantilever beam test specimen can include transverse reinforcement but does not generally include longitudinal reinforcement aside from the protruding loaded bar. Transverse reinforcement may be omitted from specimen design to mitigate its known positive

effects on anchorage capacity. A limitation of the modified cantilever beam testing mechanism is that it has not been built to incorporate vertical axial load existing in a column. This limitation prevents the test from better approximating a structural column in a building.

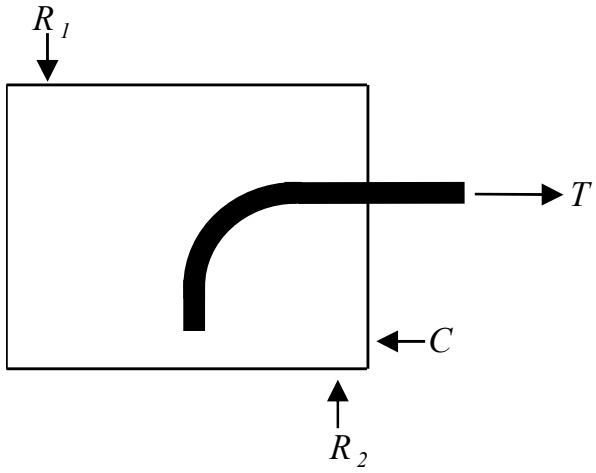

Figure 2.7: Free body diagram for modified cantilever beam specimen (modified from Minor and Jirsa 1975)

2.3.3 Beam-Column Joint Test Specimen

The beam-column joint test specimen is thought to represent best practice of the three methods discussed in this thesis. Figures 2.8 (a) and (b) show the beam-column joint test apparatus and specimen free body diagram, respectively. The beam-column joint specimen is tall, slender, and has a rectangular (or square) cross-section. This specimen has been designed to provide the best possible approximation of a column with an adjoining beam in flexure. The appropriate couple is created between the externally applied tensile force, T, and bearing force, C, where bearing force simulates a beam framing into a structural column. The bearing force is applied to the front face of the specimen a distance below the longitudinal axis of the loaded bar (i.e. C is directly below T). The apparatus also uses two stabilising forces, R_1 and R_2, to prevent the specimen from overturning during testing. The beam-column joint specimen can incorporate both longitudinal and transverse reinforcement which would be present in a column. These specimens replicate an

exterior beam-column joint with the beam intentionally left uncast to allow the protruding bar or bars to extend past the column face for loading. The beam-column joint test is performed by externally loading the embedded reinforcement protruding from the specimen by applying tension, T, until the maximum load is observed and the structural capacity of the member is overcome.

The beam-column joint test is the best of the three discussed in this section for several reasons. The testing apparatus creates a couple between applied tensile force, T, in the embedded reinforcement and lower resisting bearing force, C, as discussed in Section 2.2.1. The beam-column joint test apparatus is unique among those previously discussed in providing a mechanism by which axial load, P_c, may be variable.

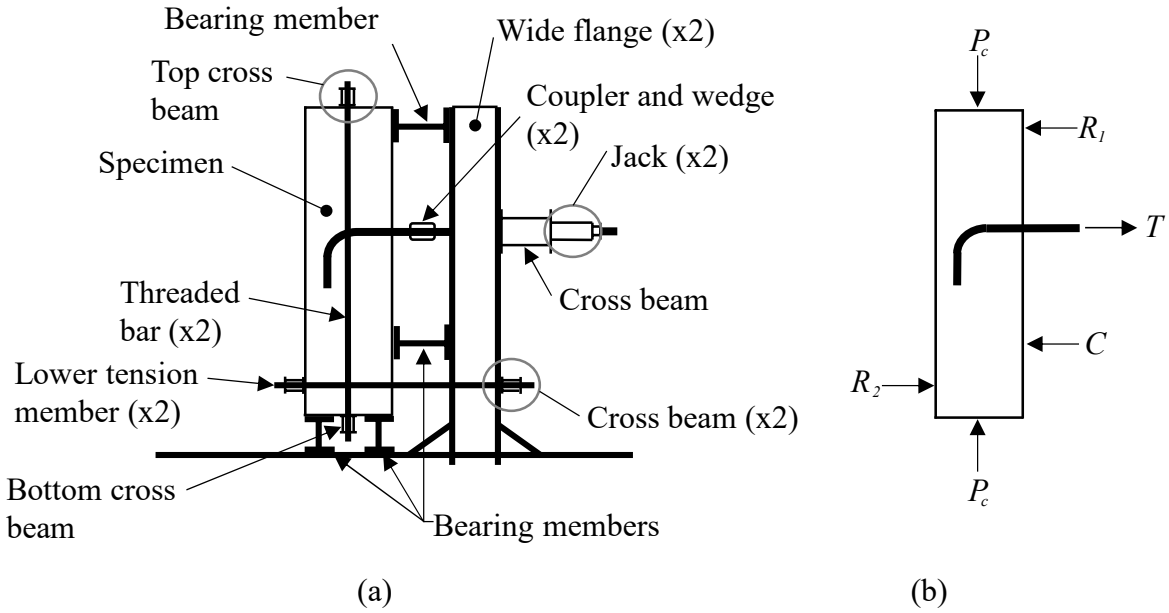

Figure 2.8: Beam-column joint test specimen: (a) apparatus, and (b) free body diagram

2.4 Failure Modes of Beam-Column Joint Specimens

Multiple failure modes for beam-column joint specimens have been observed in testing: front face pullout, front face blowout, side splitting, side blowout, and tail kickout (Marques and Jirsa

1975, Sperry et al. 2017a). The categorization of failure modes facilitates comparisons between specimen groups.

Two failure modes can be observed on the front face of a beam-column joint specimen. Front face pullout is observed in testing when a large piece of concrete is pulled forward from the front face of the column by the loaded hooked bar (Sperry et al. 2017a). As cracks propagate outward from the embedded hooked bar, the capacity of the concrete to bear the tensile load is overcome and the concrete shears, causing a trapezoidal chunk of concrete to separate from the specimen. Failure by front face blowout is defined as a more sudden version of front face pullout. Front blowout is characterized by a large and abrupt release of energy in conjunction with sudden displacement of the embedded hooked reinforcement. Figure 2.9 shows the cross-section of a specimen with the 'failure trapezoid' depicted by the grey shaded area. The grey shaded area does not resemble a traditional cone shape because the individual hooks each have failure cones (depicted in Figure 2.9 by white dashed lines) which have overlapped to form the so-called failure trapezoid.

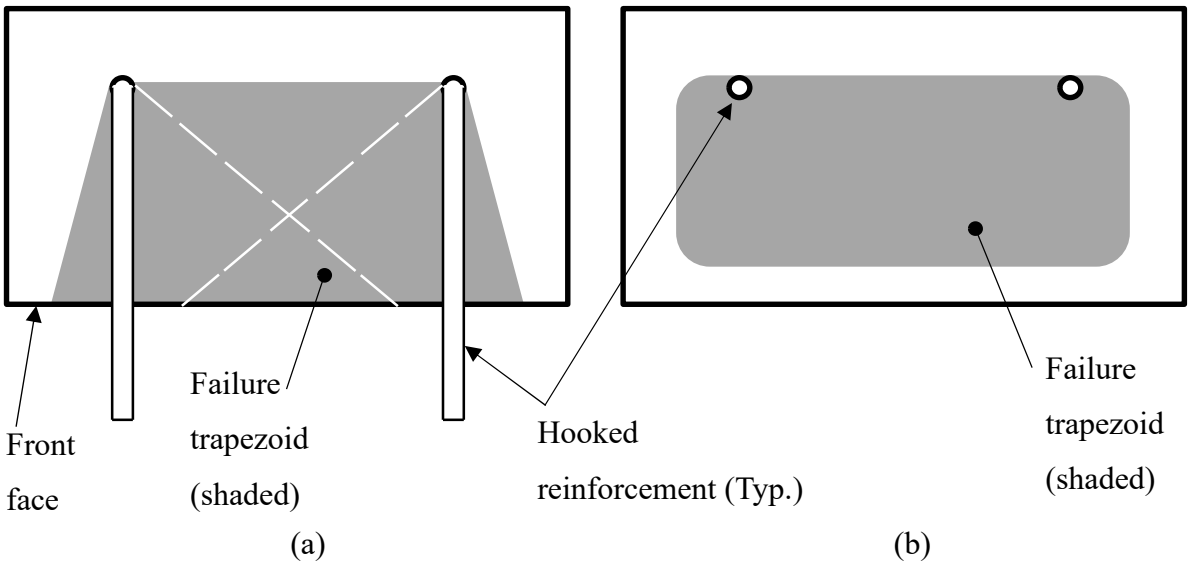

(Note: Longitudinal and transverse reinforcement not shown for clarity)

Figure 2.9: Specimen failure trapezoid associated with front face pullout and front blowout: (a) plan view, and (b) front view

Two failure modes can be observed on either side face of a beam-column joint specimen. Side splitting is observed when concrete cover on a side face of the specimen cracks and spalls away to expose the embedded hooked bar or bars (Sperry et al. 2017a). Side splitting is caused by cracks originating from where the loaded hooked bar exits the specimen, extending parallel to the front face to reach the edge, and then wrapping around to the side face. As cracks radiate out from the loaded hooked bar, bursting pressure causes the concrete cover to crack and spall. Side blowout is defined as a more sudden and extreme version of side splitting. The differences between side splitting and side blowout are more extensive cracking and significantly more concrete spalling in the case of the latter. Side blowout is characterized by a large and abrupt release of energy in conjunction with sudden displacement of the loaded hooked bar.

Tail kickout is considered a common secondary failure mode and often occurs in part due to bursting pressure after one of the above failure modes has been observed (Sperry et al. 2017a). Tail kickout failure is caused by the tail section of the embedded reinforcement attempting to straighten and push through the concrete cover on the rear face of the beam-column joint specimen due to tail kickout stresses, which were discussed in Section 2.2.2. Tail kickout is characterized by a vertical crack that is a projection of the tail section of the hooked reinforcement onto the rear face of the specimen (Marques and Jirsa 1975, Sperry et al. 2017a).

Group effects occur when hooks are spaced too closely (i.e. spacing of less than $6d_b$) within the member and act in unison instead of independently (Ajaam et al. 2018). The observation of a failure trapezoid can indicate group effects, as hooks acting independently create independent failure cones. The incidence of group effects cannot be determined in the absence of an observed coinciding loss of anchorage capacity.

2.5 Previous Research Related to the Anchorage of Hooked Bars

Abrams conducted a comprehensive investigation of bond in 1913. Abrams conducted pullout tests on seven commercially available types of reinforcement. Five replicates of each plain,

round bar pullout specimen configuration were tested. These specimens contained bars with 19 mm (0.75 inch) and 25 mm (1 inch) diameters which were confined by 6 mm spiral wire and were bent (at 0.25 and 0.5 of the circumference of a 76 mm diameter circle and at angles of 45°, 90°, 135°, and 180°) to provide anchorage. Spiral reinforcement is a type of transverse reinforcement with a continuous tie that spirals around longitudinal reinforcement. Hooks were produced with a sharp bend (i.e. a radius of zero, as if folded over upon itself). Abrams found plain hooked bar pullout specimens exhibited a maximum anchorage resistance that increased with the bend angle of the hook (Abrams 1913). Abrams attributed this finding to the tail sections of hooks with greater bend angles effectively being confined more deeply and bearing against greater depths of concrete, as measured from the rear specimen face, as the bar attempts to straighten at the hook bend (Abrams 1913).

Mylrea conducted an investigation of pullout specimens with plain hooked bars in 1928. The objective of this study was to determine the effects of spiral transverse reinforcement on anchorage capacity. This study varied whether the loaded hooked reinforcement was confined by spiral reinforcement or not. Twenty-two specimens with 13 mm (0.5 inch) diameter bar and variable inner hook bend diameters from $1d_b$ to $12d_b$ were evaluated. Mylrea, like Abrams (1913), determined that anchorage capacity increases with increased hook bend diameter. The diameter of the reinforcing bars used in this study was too small to be representative of actual structural beams and so findings do not form a reliable base for future beam-column joint research to build upon.

Abrams and Mylrea's use of the pullout testing method, which produces inflated anchorage capacity results, makes direct comparisons between their studies and later studies tenuous. Abrams' testing of sharply bent bars, i.e. having a radius of zero, is a further impediment to comparisons with later studies, as no later studies evaluated such unique configurations. Mylrea's testing of very small diameter bars poses a similar issue, as subsequent studies have not evaluated such minute bar diameters.

In 1975, Minor and Jirsa conducted a study on modern deformed hooked bars that built upon Abrams' investigation of bond. The primary objective of this study was to determine the effects of bond length on anchorage capacity. Bond length is the length of hooked reinforcement after the lead length which extends to the end of the tail section of the hook. Other objectives were to determine the effects of bend angle, bend radius, and reinforcement diameter on anchorage capacity. Minor and Jirsa conducted modified cantilever tests on 80 specimens with 37 different reinforcement configurations varying bond length (410 mm to 215 mm), bend angle (0°, 45°, 90°, 135°, and 180°), bend radius (25 mm, 38 mm, 51 mm, 64 mm, 76 mm, 102 mm, 114 mm, and 127 mm), and reinforcement diameter (nominal diameters of 16 mm (No. 5), 22 mm (No. 7), and 29 mm (No. 9)). Minor and Jirsa (1975) found a larger bend angle caused greater slip of the hooked bars. The researchers concluded that decreases in bend radius or reinforcement diameter resulted in greater overall bar displacement. Minor and Jirsa found 90° hooked bars performed better than 180° hooked bars with respect to overall reinforcement displacement. Minor and Jirsa's use of the modified cantilever test setup precludes meaningful comparisons between their study and others which used either the pullout or beam-column joint setup.

Marques and Jirsa conducted a study of beam-column joint specimens containing modern deformed hooked bars in 1975. The objectives of this study were to determine the effects of axial load, lead length, concrete cover, and transverse reinforcement on anchorage capacity. Marques and Jirsa conducted 22 beam-column joint tests on specimens that varied by hook bend angle (90° and 180°), axial load (623 kN to 2,469 kN), lead length (165 mm to 240 mm), concrete cover (38 mm to 73 mm), transverse reinforcement (whether present in the hook region or not), and reinforcement diameter (nominal diameters of 22 mm (No. 7) and 36 mm (No. 11)). Marques and Jirsa found no discernible difference in anchorage capacity with variations in axial loading, provided changes to the imparted stress remained less than 21 MPa. The researchers also found no difference in anchorage capacity between specimens with 90° or 180° hooked bars. The researchers determined that increased embedded length and increased concrete cover (i.e. from 38 mm to 64 mm) each translated into increased anchorage capacity. Increased anchorage

capacity corresponded with an increased resistance to side splitting. The researchers found the provisions of the ACI 318-71 were too conservative and suggested a new design equation that resulted in higher anchorage capacities for use in the ACI 318-77.

Pinc et al. (1977) built on the work of co-author Jirsa's 1975 studies with both Marques and Minor. The objective of this study was to determine the influence of different lead lengths on the anchorage capacities of members with hooked modern deformed bars. Pinc et al. conducted tests of 16 beam-column joint specimens varying hook bend angle (90° and 180°), lead length (111 mm to 381 mm), transverse reinforcement (whether present in the hook region or not), and reinforcement diameter (nominal diameters of 29 mm (No. 9) and 36 mm (No. 11)). Pinc et al. suggested a new design equation that resulted in higher anchorage capacities for use in the ACI 318-81, as the ACI 318-71 code provisions were found to be conservative. Pinc et al. recommended structures with modern deformed hooked bars with nominal diameters between 29 mm (No. 9) and 36 mm (No. 11) be designed based on anchorage capacities 20% greater than computed by the provisions of the ACI 318-71.

Johnson and Jirsa (1981) built on Jirsa's previous work with Minor, Marques, and Pinc. The researchers tested 36 beam-column joint specimens with 90° modern deformed hooked bars. Specimens tested varied by reinforcement diameter (nominal diameters of 13 mm (No. 4), 22 mm (No. 7), 29 mm (No. 9), and 36 mm (No. 11)), lead length (0 mm to 76 mm), concrete compressive strength (17 MPa, 31 MPa, and 40 MPa), and the length of the lever arm (i.e. distance between the applied tensile force and compressive reaction, as discussed in Section 2.3.3) (20 mm, 28 mm, 36 mm, 46 mm). Johnson and Jirsa validated the findings of Marques and Jirsa (1975) and Pinc et al. (1977) that a longer development length increases anchorage capacity. The anchorage capacity of hooked reinforcement was found to increase with bar diameter and be directly proportional to the square root of concrete compressive strength. The researchers also found that shortening the lever arm results in increased stress in the hook due to greater confinement of the hook.

Soroushian et al. (1988) tested seven beam-column joint specimens with 90° modern deformed hooked bars. Reinforcement diameters (nominal diameters of 19 mm (No. 6) and 32 mm (No. 10)) and concrete compressive strengths (26 MPa and 42 MPa) were varied. The researchers found the anchorage capacity of embedded modern deformed reinforcement containing hooks was unaffected by concrete compressive strength. This finding contradicted findings reported by Johnson and Jirsa (1981). This result may have occurred because Soroushian et al. tested only seven specimens whereas Johnson and Jirsa tested 36, therefore, the former was comparatively statistically underpowered. The study validated the finding of Johnson and Jirsa (1981) that hooked reinforcement capacity increases with reinforcement diameter.

In 2001, Cleland et al. assessed the shear capacity of bridge decks with plain round hooked bars. Twenty-four flexural beam specimens were tested and the researchers concluded the presence of hooks enhances anchorage capacity in beams. The usefulness of this study is limited because it focused on shear and not beam-column joints.

In 2017, Sperry et al. tested 337 beam-column joint specimens and varied the number of hooks (two, three, and four) in each specimen, concrete compressive strength (30 MPa to 114 MPa), reinforcement diameter (nominal diameters of 16 mm (No. 5), 25 mm (No. 8), and 36 mm (No. 11)), hook placement within the joint (inside or outside of the column core), hook geometry (90° and 180°), transverse reinforcement (whether present in the hook region), and concrete cover (38 mm to 102 mm). A constant axial load of 133 kN was used for most specimens because Marques and Jirsa (1975) had previously concluded anchorage capacity is independent of axial load. For early tests, however, the researchers varied the axial load from 133 kN to 365 kN. The researchers confirmed Marques and Jirsa' (1975) finding of no significant difference in anchorage capacity between 90° and 180° hooked bars (Sperry et al. 2017a). Sperry et al. assessed ACI 318-14 code anchorage capacity provisions and found anchorage capacities for larger hooked bars (i.e. nominal diameters 29 mm and greater) were overestimated by the code. The anchorage capacities calculated with ACI 318-14 code provisions also overestimated the effects of high compressive strength concrete and of transverse confining reinforcement. Sperry

et al. found anchorage capacity was directly proportional to concrete compressive strength raised to the power 0.29 instead of 0.5 (Sperry et al. 2017b). This finding contradicts Johnson and Jirsa (1981) and was at odds with the ACI 318-14 and CSA A23.3 codes, as discussed in Section 2.2.3 (CSA 2014B, ACI Committee 318 2014). Sperry et al. recommended structures containing hooked modern deformed bars be designed based on anchorage capacities greater than derived from the ACI 318-14 code provisions, which were deemed unconservative, and recommended an updated development length equation.

Ajaam et al. (2018) built on the work of Sperry et al. (2017a, 2017b) and analyzed 67 beam-column joint specimens with modern deformed hooked bars. The beam-column joint specimens varied by the number of hooks in each (three, four, and six), reinforcement diameter (nominal diameters of 16 mm (No. 5), 25 mm (No. 8), and 36 mm (No. 11)), concrete compressive strength (31 MPa to 84 MPa), and spacing between the hooked bars (6 d_b to 12 d_b). An objective of their research was to evaluate group effects and compare results to the ACI 318-14 (ACI Committee 318 2014). The provisions of the ACI 318-14 had been based on research conducted on specimens with two hooked bars and did not account for closely spaced bars or group effects. Ajaam et al. found hooked reinforcement with centre-to-centre spacing below 6 d_b had lower anchorage capacity due to group effects when all other factors were held constant. Anchorage capacity was determined to be insensitive to concrete side cover over the range of parameters investigated, which disagreed with the findings of Marques and Jirsa (1975). Ajaam et al. found ACI 318-14 code provisions were progressively more unconservative as concrete compressive strength and reinforcement diameter increased. The researchers recommended structures containing modern deformed hooked bars should be designed based on anchorage capacities less than derived by ACI 318-14 code provisions, which were deemed unconservative as concrete compressive strength and bar size increased.

Chun et al. (2017) tested 26 beam-column joint specimens with high-strength (550 MPa) hooked bars. The main parameter variables were reinforcement diameter (nominal diameters of 43 mm (No. 14) and 57 mm (No. 18)), concrete cover thickness (1 d_b and 2 d_b), concrete

compressive strength (42 MPa and 70 MPa), confining transverse reinforcement (none present and spacing varying between 120 mm to 140 mm), and embedded length of the hooked bars (10 d_b to 20 d_b). Chun et al. (2017) did not include an axial load in their tests because it was assumed to increase anchorage capacity; however, no citations were provided by the authors to support their rationale. Chun et al. confirmed Marques and Jirsa's (1975) conclusion that increased concrete cover or embedded length increase the anchorage capacity of hooked bars. The researchers also validated the finding of Johnson and Jirsa (1981) that the anchorage capacity of hooked bars is proportional to the square root of the compressive strength of the concrete.

In 2017, Hwang et al. conducted a meta-analysis of 493 existing modified cantilever and beam-column joint test specimens from studies published from 1975 onward to evaluate modern deformed hooked bars. One of the objectives of this analysis was to determine a design equation to predict the development length of hooked bars and compare results with the ACI 318-14 code. The researchers found their in-depth computational analysis of prior work provided an accurate prediction of the test results analyzed (with an average ratio of test results to predictions of 1.17). The model was able to predict the development length of hooked reinforcement. The models developed by the researchers were able to predict unit bond strength, bond stress distribution (as shown in Figures 2.4 (b) and 2.5 (b)), and bearing resistance of both 90° and 180° hooked bars. The models were proposed as useful tools for future research.

Table 2.1 provides a summary of the investigations discussed in this chapter.

Table 2.1: Summary of research related to the anchorage capacity of hooked bars

Authors	Year	Specimen type	Bar type	Number of specimens
Abrams	1913	Pullout	Plain	60
Mylrea	1928	Pullout	Plain	22
Minor and Jirsa	1975	Modified cantilever	Modern deformed	80
Marques and Jirsa	1975	Beam-column joint	Modern deformed	22
Pinc et al.	1977	Beam-column joint	Modern deformed	16
Johnson and Jirsa	1981	Beam-column joint	Modern deformed	36
Soroushian et al.	1988	Beam-column joint	Modern deformed	7
Cleland et al.	2001	Flexural beam	Plain	24
Sperry et al.	2017	Beam-column joint	Modern deformed	337
Chun et al.	2017	Beam-column joint	Modern deformed	26
Hwang et al.	2017	Meta-analysis	Modern deformed	493
Ajaam et al.	2018	Beam-column joint	Modern deformed	67

Table 2.1 continued: Summary of research related to the anchorage capacity of hooked bars

Authors	Parameter evaluated							
	Concrete strength	Concrete cover	Bend radius	Bar diameter	Lead length	Axial load	Transverse reinforcement	Bend angles
Abrams			●	●				●
Mylrea			●				●	
Minor and Jirsa			●	●	●			●
Marques and Jirsa		●		●	●	●	●	●
Pinc et al.				●	●		●	●
Johnson and Jirsa	●			●	●			
Soroushian et al.	●			●				
Cleland et al.								
Sperry et al.	●	●	●	●		●	●	●
Chun et al.	●	●	●	●	●		●	●
Hwang et al.								
Ajaam et al.	●			●	●	●		

Table 2.1 continued: Summary of research related to the anchorage capacity of hooked bars

Authors	Results			
	Anchorage capacity ↑ hook bend diameter ↑	90° hook has same capacity as 180° hook	Anchorage capacity ↑ development length ↑	Disagrees with ACI code parameters
Abrams	●			
Mylrea	●			
Minor and Jirsa				
Marques and Jirsa		●	●	●
Pinc et al.			●	●
Johnson and Jirsa	●		●	
Soroushian et al.	●			
Cleland et al.				
Sperry et al.		●		●
Chun et al.				
Hwang et al.				
Ajaam et al.				●

The results of investigations using different test setups cannot be meaningfully directly compared. The pullout testing method used by Abrams (1913) and Mylrea (1928) produces inflated anchorage capacities in comparison with the modified cantilever and beam-column joint testing methods. The modified cantilever method used by Minor and Jirsa (1975) precludes the results of their investigation being directly comparable to any of the other investigations noted, as all used either the pullout or beam-column joint test setups. Despite various noted

investigations using the beam-column joint specimen, wide variations in other aspects of their experimental designs often confound meaningful comparisons among them. The previously discussed investigations using beam-column joint specimens are often difficult to draw direct comparisons between due to differences in specimen footprint dimensions. Wide variations in the parameters incorporated into their experimental designs further complicate comparative analyses. Several of these investigations applied loads to specimens containing modern deformed hooked bar which could not be replicated in investigations of plain bar due to these loads exceeding the yield strength of plain bar.

Disagreements in the findings of previous investigations of hooked bars have resulted in several gaps that might be addressed by future research. For example, Minor and Jirsa (1975) found 90° hooked bars provided superior anchorage capacity than 180° hooked bars; however, Marques and Jirsa (1975) and Sperry et al. (2017) found no difference in anchorage capacity between these two hook geometries. This difference is hypothesized to result from Minor and Jirsa (1975) having used the modified cantilever test, which does not accurately represent a beam-column joint, as discussed in Section 2.3.2, whereas other researchers used the beam-column joint test. Current CSA A23.3 and ACI 318 codes align with the findings of the latter two research programs and contain provisions indicating 90° and 180° hook geometries are interchangeable (ACI Committee 318 2014, CSA 2014B).

Disagreement exists regarding the proportionality of the anchorage capacity of hooked bars to concrete compressive strength. Johnson and Jirsa (1981) found the anchorage capacity of hooked reinforcement was directly proportional to the square root of concrete compressive strength but this finding was contradicted by Soroushian et al. (1988) and Sperry et al. (2017a, 2017b). Soroushian et al. (1988) found anchorage capacity was unaffected by concrete compressive strength. Sperry et al. (2017) found anchorage capacity was directly proportional to concrete compressive strength raised to the power 0.29, contradicting Johnson and Jirsa (1981) and Soroushian et al. (1988) and at odds with both the ACI 318-14 and CSA A23.3-14 codes. In the future, researchers might address this lack of consensus.

Much of the research discussed in this literature review was parametric in nature and focused primarily on assessing or developing code provisions (i.e. Minor and Jirsa (1975), Marques and Jirsa (1975), Pinc et al. (1977), Johnson and Jirsa (1981), Soroushian et al. (1988), and Sperry et al. (2017)). These investigations evaluated wide ranges of independent variables to search for trends among specimens that could be applied to improve existing codes. These research programs were conducted to meet objectives related to creating or amending existing development length equations comprised of multiple parameters, each with high variability. Research programs incorporating replicates address the statistical certainty of experimental outcomes. The lack of research programs incorporating replicates represents a gap in the body of research that should be addressed by future experimental programs. The research programs noted, however, provided valuable information for code developments pertaining to hooked bars.

2.6 Historical Code Requirements for Hooked Bars

This section provides information on code developments over time pertaining to hook development length, discussed in Section 2.2.3, and minimum hook bend diameter. In 1963, the ACI 318 code, *Building Code Requirements for Structural Concrete and Commentary*, contained provisions for embedded plain hooked bars for the last time (ACI Committee 318 1963). Provisions for plain hooked bars were not included in successive code publications because modern deformed bars had become the norm in construction due to having superior bond when compared to plain bars. Publications of the ACI 318 code prior to 1971 centred on hook geometry and bar stress, shifting thereafter to focus on the development length of hooks.

The ACI 318 code was used widely in Canada prior to the more recent development of the CSA A23.3 code first published in 1959. The CSA A23.3 code, *Design of Concrete Structures*, contained provisions for plain reinforcement for the last time in 1970 (CSA 1970). The CSA did not include provisions for plain reinforcement after 1970 because modern deformed bars had effectively replaced plain bars in construction.

2.6.1 Development Length for Hooks

Table 2.1 presents the evolution of the development length, l_d, formulae for hooked modern deformed bars as provided in publications of the ACI 318 code, *Building Code Requirements for Structural Concrete and Commentary*, and CSA A23.3 code, *Design of Concrete Structures*. Figure 2.10 shows how the development lengths required by ACI 318 and the CSA A23.3 have evolved with respect to the recommendations on hooked bar development lengths made by researchers, as discussed in the previous section. Data is displayed as it pertains to hooked reinforcement with a diameter, d_b, of 25 mm and yield strength of 300 MPa. This diameter was chosen because it is represented in this study and is commonly used in flexural members. This yield strength was chosen because it was the more conservative of the two yield strengths represented in this study.

Table 2.1 shows the evolution of the post-1977 development length formulae provided in ACI 318 and CSA A23.3. The ACI 318 and CSA A23.3 included provisions for allowable stresses in hooked bars prior to incorporating development length. In 1977, the ACI 318 contained the first provisions for development length based on the recommendations of Marques and Jirsa (1975). The 1977 equation shown in Table 2.1 was a function of concrete compressive strength, f'_c; the cross-sectional area of the hooked bars, A_b; and the yield strength of the reinforcement, f_y (ACI Committee 318 1971). From 1983 to 1999, the development length equation was a function of reinforcement diameter and concrete compressive strength (ACI Committee 318 1983, 1999). In 2002, an adjustment factor for epoxy-coated or zinc and epoxy dual-coated reinforcement, ψ_e, was added to the equation. The same year, λ, an adjustment factor accounting for lightweight concrete was also incorporated. The CSA standard for development length was unchanged as of 2014 (CSA 2014B). A concrete cover factor, ψ_c, was incorporated in 2014 as an adjustment to account for varying depths of concrete cover. In 2014, the ACI 318 development length equation incorporated a confining reinforcement factor, ψ_r, because hooked bars are most effectively confined by closely spaced ties (Marques and Jirsa 1975). The

confining factor, ψ_r, was adjusted in 2019 to account for group effects (Ajaam et al. 2018). In 2019, the ACI 318 introduced a location factor, ψ_o, to account for whether the hook is located inside or outside of the column core (Johnson and Jirsa 1981, Sperry et al. 2017a, 2017b).

Table 2.2: ACI and CSA historical development length equations for hooked bars

Year	Code	Development Length Equation
1977	ACI	$l_d = 1.016A_b f_y / \sqrt{f'_c} > 0.01016 d_b f_y$
1983, 1986, 1989, 1992, 1995, and 1999	ACI	$l_d = 30480 d_b / \sqrt{f'_c}$
2002 and 2005	ACI	$l_d = (0.508 \psi_e f_y / \lambda \sqrt{f'_c}) d_b > 8 d_b > 150mm$
2008 and 2011	ACI	$l_d = (0.508 \psi_e f_y / \lambda \sqrt{f'_c}) d_b > 8 d_b > 150mm$
2014	ACI	$l_d = (0.2 H_y \psi_e \psi_c \psi_r / \lambda \sqrt{f'_c}) d_b > 8 d_b > 150mm$
2019	ACI	$l_d = (0.4618 f_y \psi_e \psi_r \psi_o \psi_c / \lambda \sqrt{f'_c}) d_b^{1.5} > 8 d_b > 150mm$
1984, 1994 2004, and 2014 CSA Building Code	CSA	$l_d = 100 d_b / \sqrt{f'_c}$

Figure 2.10 shows the evolution of development lengths for hooked bars required by the ACI 318 and CSA A23.3 codes and the development lengths recommended by researchers noted in this literature review. The figure shows a decreasing trend in the amount of development length required by the ACI 318 with succeeding code editions. This decreasing trend in the development length provisions in the ACI 318 code followed the recommendations of researchers (Marques and Jirsa 1975, Sperry et al. 2017b). The ACI 318 increased the minimum development length for the 2019 code edition due to the research reported by Ajaam et. al (2018) to account for a drop in anchorage capacity due to group effects. Figure 2.10 also shows that the CSA A23.3 code regarding required development length has not been amended over time and has always required a relatively short development length (i.e. 263 mm). The CSA committee

responsible for this section of the code has not responded to recent research or changes made to ACI code, as evidenced by the unchanging development length requirement over time.

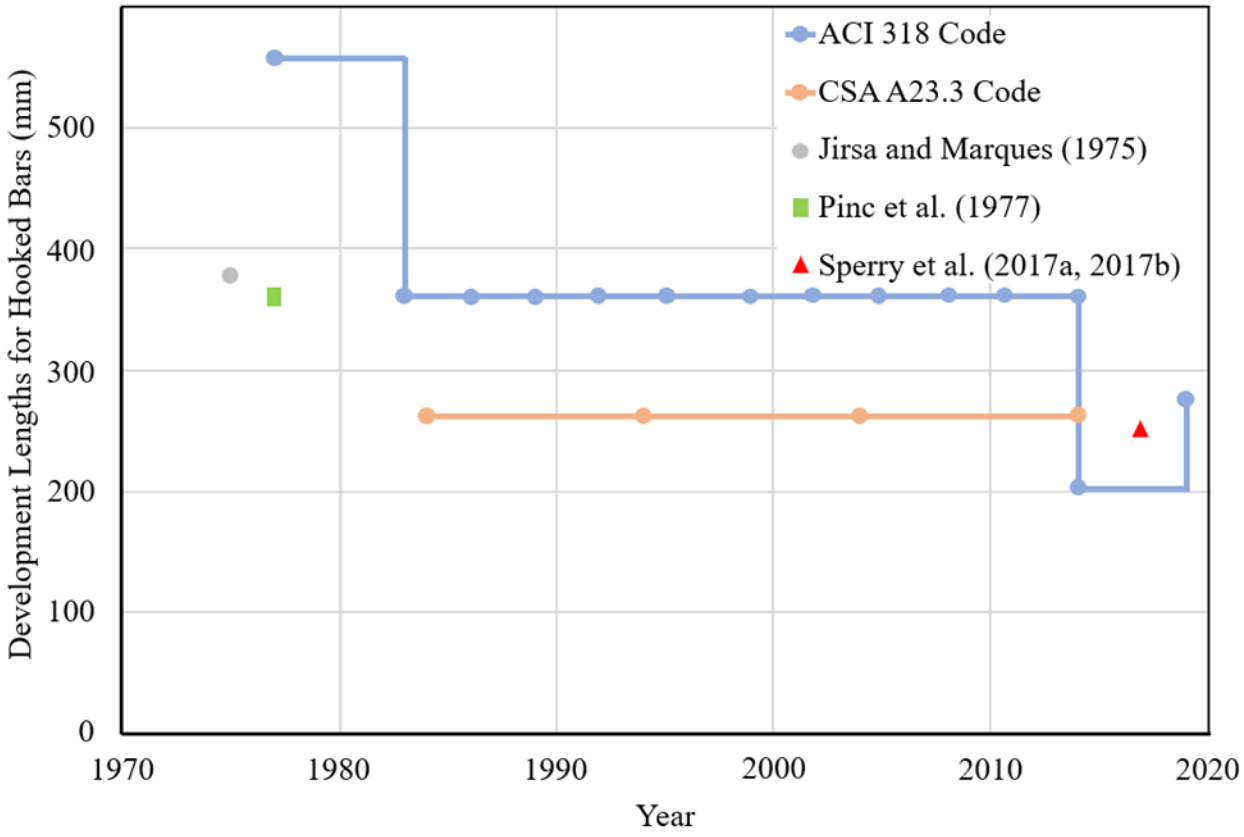

Figure 2.10: Development lengths for 300 MPa hooked bars with a 25 mm diameter

2.6.2 Minimum Yield Strengths of Reinforcing Steel and Minimum Bend Diameters for Hooks

Numerous changes have been made over time to the minimum hook bend diameters in ACI 318 and CSA A23.1 code provisions. The same is true of minimum required reinforcement yield strengths. Tables 2.2 and 2.3 show the timelines of ACI 318 and CSA A23.3 changes to the minimum bend diameter for hooks and minimum required reinforcement yield strength, respectively. Data is displayed as it pertains to hooked reinforcement with a diameter of 25 mm and yield strength of 300 MPa. This diameter was chosen because it is represented in this study and is commonly represented in flexural members. This yield strength was chosen because it was

the more conservative of the two strengths represented in this study. There are no direct correlations between the recommendations made by the researchers noted in Section 2.5 and the overall increases in both required minimum hook bend diameter and reinforcement yield strength. The change in minimum required reinforcement yield strength, however, corresponds with the lowering of required development length. The minimum 90° and 180° hook bend diameters required by the ACI and CSA increased from F_b to $6d_b$ and from $3d_b$ to $6d_b$, respectively. The minimum reinforcement yield strengths required by the ACI and CSA were initially 230 MPa and have since been increased to 275 MPa and 300 MPa, respectively.

Table 2.3: ACI and CSA minimum bend diameters for 25 mm hooked bars

Year	Code	Minimum 90° hook bend diameter	Minimum 180° hook bend diameter
1941 - 1956	ACI	F_b	$3d_b$
1963		$3d_b$	$3d_b$
1971 - 2019		$6d_b$	$6d_b$
1959	CSA	F_b	$3d_b$
1984 - 2014		$6d_b$	$6d_b$

Table 2.4: ACI and CSA minimum required reinforcement yield strength

Year	Code	Minimum reinforcement yield strength (MPa)
1911 - 1966	ACI	230
1967 - 2019		275
1914 - 1972	CSA	230
1973 - 1977		275
1978 - 2014		300

2.7 Summary

This chapter provided background knowledge and a chronological overview of research conducted on embedded hooked bars. Previous studies have not directly compared the anchorage capacities of hooked plain and modern deformed bars and have left a knowledge gap that impacts the assessment of anchorage capacity in historical buildings containing plain reinforcement. The anchorage capacities of plain and modern deformed bars are directly compared in this research program to address this knowledge gap. The significance of bar type on overall hooked bar performance will be determined by directly comparing the anchorage capacities of hooked plain and modern deformed bars. This will aid engineers tasked with the assessment of buildings reinforced with plain hooked bars that have been assigned a change of use, resulting in new loads. Further, the potential impact of research within this scope may provide structural engineers with additional knowledge allowing them to make more accurate, safe, and cost-effective recommendations based on their assessments of structures containing plain and modern deformed hooked bar. The next chapter provides the details of the experimental program for this study.

Chapter 3
Experimental Program

3.1 General

The experimental program facilitated comparison of the anchorage capacities of plain and modern deformed bars with 90° and 180° hooks. This chapter includes a discussion of the test parameters, specimen geometry, and material selection for both the concrete and reinforcing steel. Construction phasing and details of specimen preparation including form preparation, reinforcing cage assembly preparation, and concrete placement are also included. The testing procedures for the beam-column joint specimens and corresponding concrete companion cylinders and reinforcement tensile coupons are provided. Assessments of the compressive and splitting tensile strengths of concrete companion cylinder specimens and of the tensile strengths of longitudinal reinforcement specimens are also described.

3.2 Test Parameters

The experimental program consisted of four specimen configurations with six replicates per set to evaluate the differences, if any, between 90° and 180° hook geometries of both plain and modern deformed reinforcement. The parameters in this experimental design were: hook geometry (90° or 180°) and reinforcement type (plain or modern deformed). All other parameters were held constant including the overall dimensions of the specimens, concrete cover, bar diameter, embedded length of the straight portion of the hooked bars, spacing and type of longitudinal and transverse reinforcement, and applied axial load.

3.3 Specimen Geometry

Figure 2.8 in Section 2.3.3 showed the beam-column joint specimen design used in this study and based on that used by Marques and Jirsa (1975). The locations of all reactions for this testing setup replicated those from Marques and Jirsa's 1975 testing apparatus. As discussed in Section 2.3.3, this design does not incorporate a cast beam but instead adequately represents the

appropriate couple between an actual structural column and beam. The beam-column joint specimen design is, thus, best for replicating forces within actual structural members.

Figure 3.1 shows the beam-column joint specimen design including the cross-section (Figure 3.1 (a)), the bend details for 90º hooked bars (Figure 3.1 (b)), and the bend details for 180º hooked bars (Figure 3.1 (c)). The hooked bars were 25 mm in diameter. The specimens were 1,220 mm tall, 300 mm wide, and 250 mm deep. A 50 mm reduction in cross-section depth from the design of Marques and Jirsa (1975) was included in this study to ensure internal reinforcement stress remained below 300 MPa, which is the yield strength of the plain reinforcement. This reduction in cross-sectional depth did not affect the validity of the test or results, as it was held constant across all specimens. Concrete cover of 25 mm was used on all sides in accordance with the minimum requirements of CSA A23.3. Ajaam et al. (2018) showed center-to-center hook spacing of 6 d_b was an appropriate threshold to reduce the likelihood of group effects and was used in this study, as discussed in Section 2.5.

Transverse 10M ties spaced at 85 mm on centre above and below the hook region were included to prevent shear failure within the specimen during testing. Marques and Jirsa (1975) reported maximum load stress achieved by the hooked bars increased from 171 kN to 241 kN due to the presence of transverse reinforcement in the hook region. The transverse reinforcement confined the hook, reduced cracking and spalling of adjacent concrete, and increased overall anchorage capacity as a result. Transverse reinforcement was intentionally absent from the hook region to prevent increased hook capacity and ensure bond failure preceded the yielding of the reinforcement.

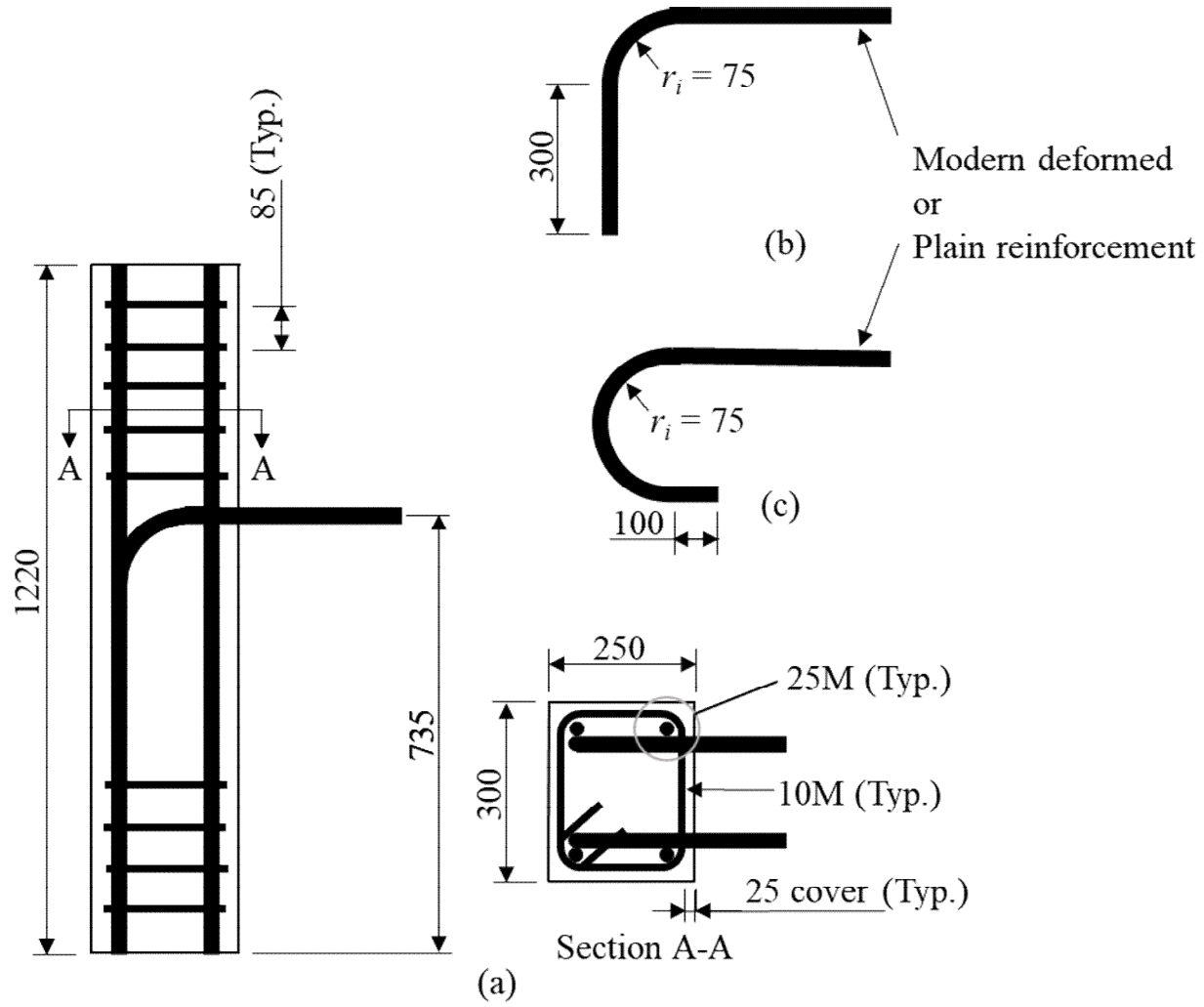

Figure 3.1: Beam-column joint specimen design: (a) specimen including cross-section, (b) bend details for 90º hooked bars, and (c) bend details for 180º hooked bars

Figure 3.2 shows the geometries of the four distinct hooks used in the different specimen groups. These four hooks represent the independent variables under investigation. Two different reinforcement types were used in this study: 25.4 mm diameter plain and 25M modern deformed. Figure 3.1 shows the bend radius of the hooks was the same for each bar type and conformed to CSA A23.1-14 (CSA 2014A). The 25.4 mm diameter plain and 25M modern deformed bar specimens with 90º hooks were produced per the design detailed in Figure 3.1.

Figure 3.3 shows the as-measured bend dimensions for the 180° hooked bars. The 25.4 mm diameter plain and 25M modern deformed bar specimens with 180º hooks did not conform to CSA A23.1 due to manufacturing constraints. The 180° hooked bars were manufactured 5 mm longer in the tail section than originally specified due to the grip length required by the bending machine used in the manufacturing process. This 5 mm addition was present on all specimens with 180° hooked bars and, therefore, hypothesized to have had no impact on the tests or results.

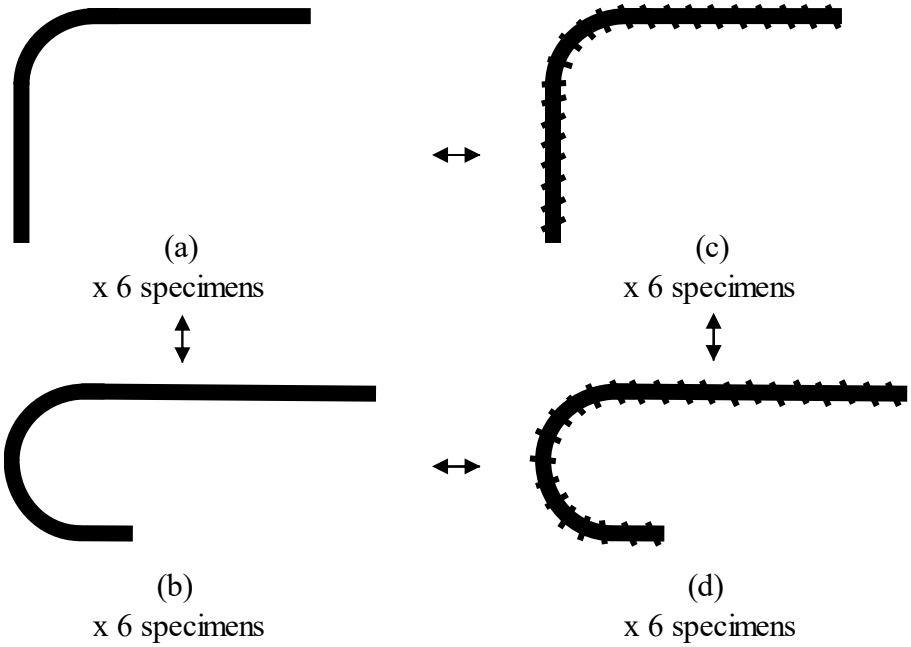

Note: Dimensions shown in Figure 3.1

Figure 3.2: Experimental design: (a) 90º hooked plain bar, (b) 180º hooked bar, (c) 90º hooked modern deformed bar, and (d) 180º hooked modern deformed bar

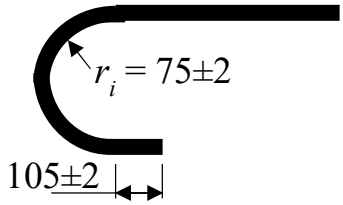

Figure 3.3: Manufactured 180° hooked reinforcement

3.4 Material Selection

The materials selected for use in the experimental program best replicate Abrams' (1913) study and reasonably approximate conditions found in turn-of-the-century concrete structures. This section presents information on the concrete and reinforcement used in this study.

3.4.1 Concrete

This study exclusively used a concrete mix with a target compressive strength, f'_c, of 20 MPa. The concrete mix design included Type GU Portland Cement without any admixtures or air entrainment. The specified compressive strength as selected was intended to reproduce concrete produced in the early 20th century as well as the concrete used in Abrams' 1913 study (Feldman and Bartlett 2005).

A ready-mix supplier produced and delivered the concrete for all three phases of this study due to the volume required. The mix design was adjusted by the concrete supplier to achieve a specified compressive strength, f'_c, of 20 MPa; these adjustments resulted in variations in mix design between phases. The mix design for phase one (per m^3 of concrete) was: 140 kg cement; 937 kg silica sand; 1,242 kg crushed granite, carbonate, and gneiss coarse aggregate; and 78 kg water. This mix design resulted in a water-cement ratio of 0.56. The mix design for phase two (per m^3 of concrete) was: 200 kg cement; 884 kg silica sand; 1,171 kg crushed granite, carbonate, and gneiss coarse aggregate; and 110 kg water. This second mix design resulted in a water-cement ratio of 0.55. The mix design for phase three (per m^3 of concrete) was: 160 kg

cement; 964 kg silica sand; 1,277 kg crushed granite, carbonate, and gneiss coarse aggregate; and 84 kg water, resulting in a water-cement ratio of 0.53. The fine aggregate for all phases was FA1 silica sand conforming to CSA A23.1-14 from the Lafarge Wakaw pit in Saskatchewan (CSA 2014A). The maximum coarse aggregate size was 20 mm conforming to CSA A23.1-14 from the Lafarge Watrous pit in Saskatchewan.

3.4.2 Reinforcing Steel

All plain reinforcement used in this study conformed to CSA G40.21-13 grade 300W and was procured from a single heat (CSA 2018). All modern deformed longitudinal and hooked bars were Grade 400W 25M conforming to CSA G30.18-09 and were exposed to the same heat during casting and rolling to ensure consistency (CSA 2014C). All transverse reinforcement was Grade 400W 10M modern deformed bar conforming to CSA G30.18-109 and procured from a single heat. Ties were bent by Harris Reinforcement in Saskatoon, SK to ensure proper size and tolerance.

Feldman and Bartlett (2005) found an average surface roughness of 11.3 μm accurately represented the surface conditions of historical reinforcement. Previous research at the University of Saskatchewan used aluminum oxide with a blast pressure of 698 kPa and a nozzle distance of 125 mm to attain the value of 9.58 μm (Hassan and Feldman 2012, MacLean and Feldman 2014, Poudyal and Feldman 2018). All plain reinforcement used in this study was sandblasted using silica sand at a blast pressure of 690 kPa and a nozzle distance of 250 mm to appropriately simulate the surface of historical reinforcement. Silica sand was selected preferentially over aluminum oxide due to its cost effectiveness. Surface roughness of the reinforcement, R_y, was measured using a Mitutoyo SJ-201 surface roughness tester with 0.25 mm/s stroke (Mitutoyo 2006). The maximum height of profile as calculated by the distance between the highest peak and the deepest valley on the reinforcement surface, R_y, was used to quantify reinforcement surface roughness. Ten roughness measurements were taken for each length of reinforcement. An average surface roughness, R_y, of 10.4 μm with a standard deviation

of 1.74 μm resulted. This value was deemed acceptable because it was conservative with respect to the target value of 11.3 μm. An increase in surface roughness would generate more frictional sliding resistance and result in unconservative maximum load data.

3.5 Construction Phases

Specimen construction was completed in three phases due to the space constraints of the laboratory and to deliver cost savings by reducing the total number of forms required. Table 3.1 outlines the three construction phases.

Table 3.1: Construction phases

Construction phase	Specimen type				
	90° plain hooked bars	180° plain hooked bars	90° hooked modern deformed bars	180° hooked modern deformed bars	Total number of specimens
1	1	1	1	1	4
2	0	5	0	5	10
3	5	0	5	0	10
Total number of each specimen type	6	6	6	6	24

The first construction phase served as a proof of concept. This phase comprised one of each specimen type: 25.4 mm diameter plain bars with 90º or 180º hooks and 25M modern deformed bars with 90º or 180º hooks. The second phase included the remaining ten specimens of both bar types with 180º hooks. The remaining specimens with 180° hooks were evaluated before those with 90° hooks, as their anchorage capacities were expected to exceed the latter. The first and third phases would be repeated with reduced specimen depth if the specimens evaluated in the second phase failed by yielding of the hooked bars. The third and final phase consisted of the remaining ten specimens with 90° hooks of both bar types.

3.6 Specimen Construction

This section outlines the steps taken to construct the beam-column joint specimens including the associated wooden forms and reinforcing cages. The testing of the plastic properties of the concrete prior to casting is discussed. The casting of concrete companion cylinders is also described.

3.6.1 Form Preparation

Wooden forms were designed and constructed in preparation for the casting of the beam-column joint specimens. Figure 3.4 shows a form without (Figure 3.4 (a)) and with (Figure 3.4 (b)) the final side attached. Ten wooden forms corresponding with the preparation of a single phase of ten specimens were fabricated in house. The wooden forms were designed to be easily assembled and disassembled for specimen stripping and reuse. The tolerance of the forms was measured to be ±10 mm for all internal dimensions in accordance with CSA A23.1-14 specifications (CSA 2014B).

(a) (b)

Figure 3.4: Wooden forms: (a) without final side, and (b) with final side

3.6.2 Reinforcing Cage Assembly

Figure 3.5 shows two assembled reinforcing cages. The average fabricated dimension measurements for each tie were 250 ±5 mm by 200 ±5 mm and conformed to the tolerance requirements provided in CSA A23.3-14 (CSA 2014B). The reinforcing cages were assembled by first resting two longitudinal 25M lengths between two tables to allow the placed ties to hang freely from the longitudinal length within their clear span. The ties were evenly distributed at specified intervals along only the ends of the two longitudinal bar lengths because ties in the hook region have been found to increase anchorage capacity, as discussed in Section 3.3 (Marques and Jirsa 1975). Transverse reinforcement was placed in such a way that the longitudinal bars rested in the top inside corners of the ties. The transverse reinforcement was then secured to the longitudinal bars using tie wire. The two remaining longitudinal bars were then inserted into the bottom inside corners of the transverse reinforcement and secured with tie wire at the appropriate intervals. The hooked bars were placed adjacent to their respective longitudinal bars and tied in place at their planned locations. The completed cages were placed by hand into the wooden forms before the final front faces of the forms were installed. The hooked bars protruding from the wooden forms were checked for proper alignment prior to concrete pouring.

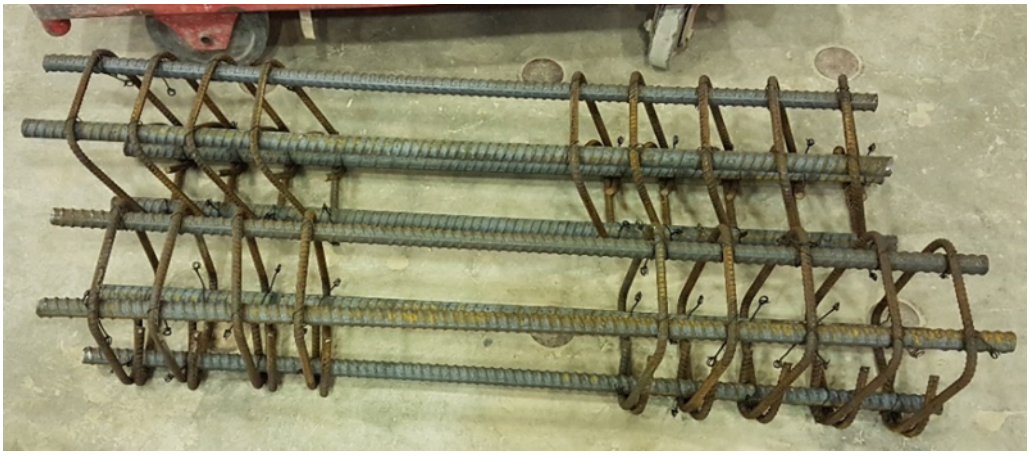

Figure 3.5: Reinforcing cages

3.6.3 Concrete Placement

The wooden forms containing the reinforcing cages were arranged in an arc on the laboratory floor to facilitate concrete placement from a concrete truck with a swinging boom. Specimens were internally vibrated during the casting process to ensure proper consolidation of the concrete. Care was taken to ensure that the electronic vibrator did not make contact with the reinforcing cage or the formwork. The top surface of the concrete of each specimen was screed off with a straight edge and the surface was finished with a trowel.

Companion cylinders were cast on the same days that beam-column joint specimens were cast. Seven 200 mm long concrete cylinders with diameters of 100 mm were cast for each of the 24 beam-column joint specimens in accordance with CSA A23.2-14 specifications (CSA 2014A). One cylinder from each set of seven was used to check the strength at seven days. Three of the remaining six cylinders from each set were used for compression testing and three were used for split cylinder testing, both on the same day as testing of the associated beam-column joint specimen testing.

The plastic properties of the concrete were tested at the time of casting to control quality. Figure 3.6 shows a slump test (Figure 3.6 (a)) and an air content test (Figure 3.6 (b)) performed in accordance with CSA A23.2-14 (CSA 2014A).

(a) (b)

Figure 3.6: Concrete testing: (a) slump, and (b) air content by pressure method

The curing process was carefully monitored after the casting of the specimens. Figure 3.7 shows moist burlap as placed on each cast specimen. Plastic was not placed over the moist burlap for the first or second phases; however, constant moisture was achieved through diligent monitoring. Plastic was placed over the moist burlap for the third phase to aid in moisture retention and the burlap was wetted daily to maintain moisture. Figure 3.8 shows the specimens following form removal. The specimens were removed from the forms after seven days of curing and were subsequently cured in the laboratory for an additional 21 days.

Figure 3.7: Specimens curing with moist burlap

Figure 3.8: Concrete specimens following form removal

3.7 Testing of Beam-Column Joint Specimens

A lift was used to place the beam-column joint specimens in the testing apparatus. The testing apparatus was designed by the author and built in-house in the Structures Laboratory at the University of Saskatchewan. The testing setup used in this study was modified from that implemented by Marques and Jirsa (1975) and Sperry et al. (2017a, 2017b). Those studies used hydraulic jacks to apply variable axial load; however, this study used a manual slugging wrench to tighten nuts on the 50 mm threaded bar to maintain a constant axial load of 200 kN.

Figures 3.9 and 3.10 show the testing setup and a photograph of the setup in the Structures Laboratory, respectively. The figure includes a beam-column joint specimen loaded for testing. Figure 3.11 shows a free body diagram of the forces applied by the testing mechanism to the specimen during testing. The upper front built-up double-webbed girder with attached hydraulic cylinders in combination with the lower W310x74 created the necessary couple resulting from the applied tensile force, T, and compressive reaction, C, respectively. The distance between T and C in the testing setup replicated that of Marques and Jirsa's (1975) setup.

The tensile force, T, was applied to the reinforcement protruding from the front face of the specimen by two Enerpac Rch-606 hollow plunger hydraulic cylinders at a computer-controlled rate of 5 kN/min. Figure 3.12 shows (a) the couplers and (b) a wedge that together ensured transfer of tensile force to the reinforcement. Appendix A includes a detailed drawing of a coupler. Couplers were each connected to the reinforcement by a wedge. The upper front built-up double-webbed girder held the hydraulic cylinders in place. Horizontal threaded bars connected the hydraulic cylinders to the couplers to transfer applied tensile force to the hooked bars. These horizontal bars were 25.4 mm (one inch) diameter threaded Rockwell C33 steel rod conforming to ASTM A35DD and having a nominal yield strength of 1,034 MPa (Tillman n.d., ASTM International 2017a). The couplers were comprised of Strenx® steel with a yield strength of 689 MPa. The steel wedges located inside of the couplers had a yield strength of 552 MPa.

Figure 3.9 shows the vertical 50 mm diameter threaded bar lengths confining the top and bottom double-webbed plate girders that applied axial load to the beam-column joint specimens. These bar lengths were made of high strength steel and were cut to a length of 2,400 mm and threaded by the University of Saskatchewan Engineering Shops. Figure 3.11 shows the axial load, P_c, applied to the beam-column joint specimens. This axial load of 200 kN, as measured by two load cells, represents the maximum possible by tightening via a slugging wrench. This axial load corresponds with a compressive stress of 2.67 MPa. Variable axial load was not necessary because it has been shown not to affect the anchorage capacity of hooked bars, as discussed in Section 2.5 (Marques and Jirsa 1975).

The upper W310 x 74 support beam provided the necessary stabilising support reaction, R_1, shown in Figure 3.11. The bottom double-webbed plate girder provided a stabilising force labeled, R_2, for the specimen. The lower front built-up double-webbed girder was used as a mounting point to tighten the connecting rods to the lower double-webbed plate girder shown in Figure 3.9. Detail A of Figure 3.9 shows the design of the custom-built top, lower, and bottom double-webbed plate girders. Detail B shows the built-up double-webbed girder comprised of two C250x30 channels and two 12x200 plates. Detail C shows the custom-built double-webbed plate girder used as a riser for the beam-column joint specimen to ensure (1) axial load could be applied to the bottom face and (2) the necessary clearance for proper tightening of the 50 mm nuts on the bottom of the 50 mm diameter threaded bar lengths.

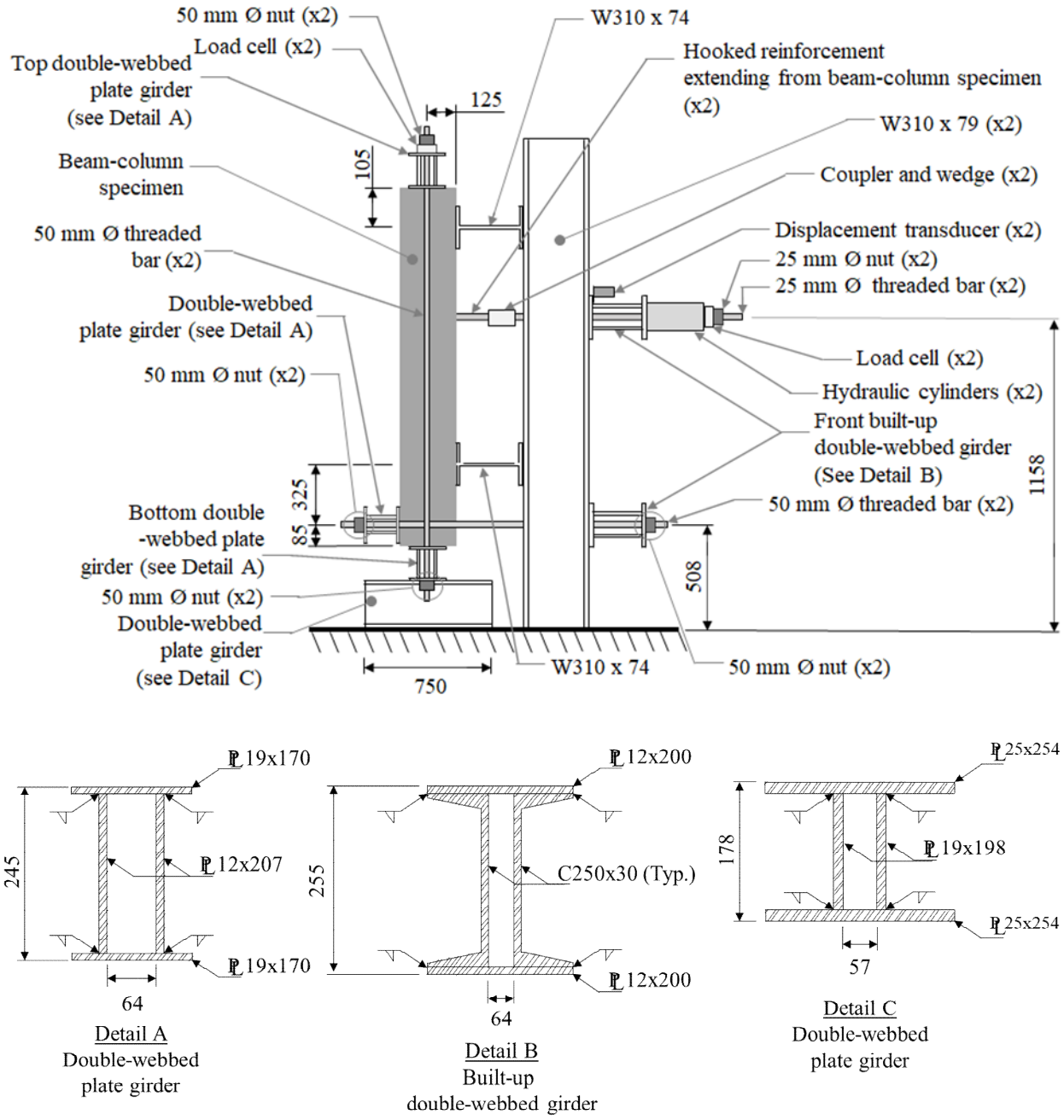

Figure 3.9: Specimen in testing apparatus

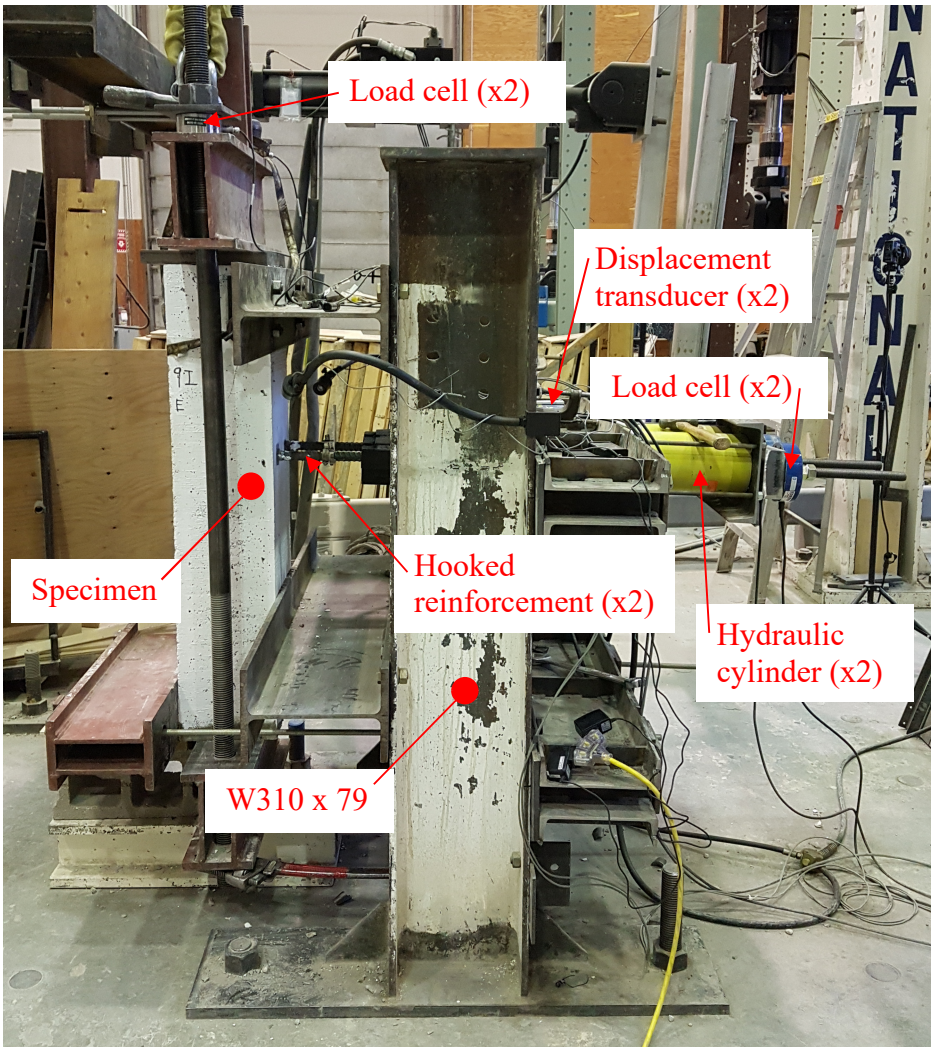

Figure 3.10: Specimen in testing apparatus in the Structures Laboratory

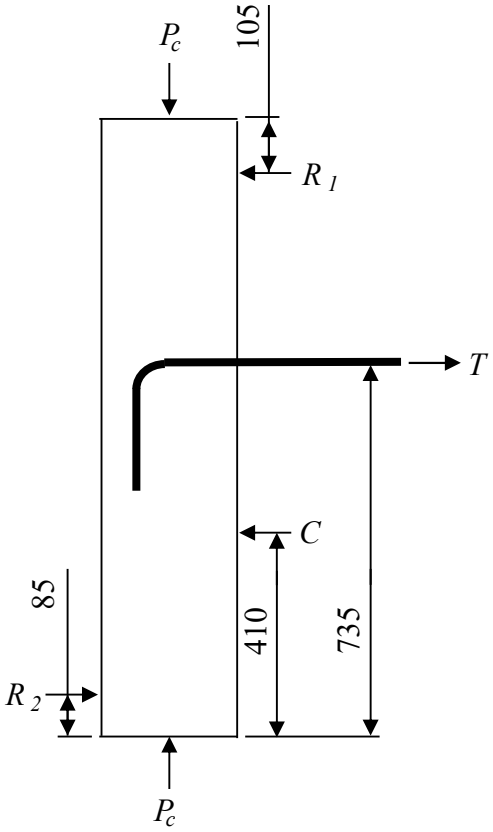

Figure 3.11: Forces applied by the testing apparatus

(a) (b)

Figure 3.12: Testing apparatus components: (a) couplers, and (b) wedge

Instrumentation was used during testing to gather required data. The tensile force applied by the two hydraulic cylinders was acquired via two Interface 1220AJ-50K load cells (Figure 3.13(a)), reinforcement displacement data was collected by two OptoNCDT Micro-Epsilon laser displacement transducers (Figure 3.13(b)), and axial load data was collected by two Omega LC8400-200-200K load cells (Figure 3.13(c)).

The Interface 1200AJ-50K load cells (Figure 3.13(a)) acquired data at a constant rate of 100 Hz. These load cells are accurate to ±0.05% and have a maximum capacity of 250 kN (Interface, Inc. 2018). This particular make and model of load cell was deemed appropriate for this experimental program because its capacity exceeded the yield force of a single hooked bar. The beam-column joint specimens were designed so the hooked bars would not yield during testing. There would, therefore, be no risk of overloading these load cells.

Displacement refers to the movement of the reinforcement relative to the upper front built-up double-webbed girder of the apparatus frame at the surface of the front face of the specimen in the direction of applied tension. Two OptoNCDT Micro-Epsilon laser displacement transducers (Figure 3.13(b)) were mounted on the top front built-up double-webbed girders, aimed at metal reflecting pads attached to the hooked bars directly adjacent to the front face of the specimen, and monitored the displacement of the bars throughout testing. These transducers acquired displacement data at a constant rate of 100 Hz, were accurate to ±670 μm, and had the capacity to measure a maximum displacement of 750 mm (Micro-Epsilon 2010). The maximum distance that the hydraulic jacks could travel before damaging the testing apparatus was 530 mm. This particular make and model of laser displacement transducer was deemed appropriate for the purposes of this experimental program because the maximum distance required for measurement was within specified limits.

Two Omega LC8400-200-200K load cells (Figure 3.13(c)) were used to measure the total axial load applied to each specimen. The load cells acquired data at a constant rate of 100 Hz. This particular make and model of load cell was chosen because it has a capacity of 890 kN and

an accuracy of ±0.05% (Omega Engineering Canada n.d.). This capacity exceeds the 100 kN load that each cell was subjected to per the experimental design.

(a) (b) (c)

Figure 3.13: Measurement devices: (a) Interface 1220AJ-50K load cell, (b) OptoNCDT Micro-Epsilon laser displacement transducer, and (c) Omega LC8400-200-200K load cell

The specimens were painted white prior to testing to aid in the visual identification of cracks. Cracks were marked with a black permanent marker at approximately 5 kN increments until immediately prior to the achievement of maximum load. Crack diagrams were traced from photos taken during testing.

It was necessary to manually halt testing as soon as possible after maximum load was achieved to prevent damage to the testing apparatus and instrumentation. The coupler and wedge system would be pulled through the top front double-webbed built-up girder if the hydraulic jacks had been allowed to continue operating past this point.

3.8 Testing of Companion Specimens

This section covers the compressive and tensile strength testing of concrete companion cylinders. This section also discusses the tensile testing of steel reinforcement coupons.

3.8.1 Compressive Strength Testing of Companion Concrete Cylinders

Each concrete cylinder that would be subjected to compression was sulphur-capped immediately prior to testing to ensure the top and bottom surfaces were level. Figure 3.14 shows a 100 mm diameter by 200 mm long companion cylinder loaded in the Universal Testing Machine ready for compressive strength testing. The Universal Testing Machine was operated in load control at a rate of 0.25 MPa/sec in compliance with CSA A23.2-14 (CSA 2014A). One companion cylinder for each beam-column joint specimen was tested at seven days after casting and three more were tested on the day that each corresponding beam-column joint specimen was tested.

Figure 3.14: Compression concrete cylinder testing using the Universal Testing Machine

3.8.2 Splitting Tensile Strength Testing of Companion Concrete Cylinders

Figure 3.15 shows a 100 mm diameter by 200 mm long companion cylinder loaded in the Universal Testing Machine for splitting tensile strength testing. The Universal Testing Machine was operated at a load rate of 0.25 MPa/sec in compliance with CSA A23.2-14 specifications

(CSA 2014A). Three companion cylinders for each specimen were tested on the day that each corresponding beam-column joint specimen was tested.

Figure 3.15: Split concrete cylinder testing using the Universal Testing Machine

3.8.3 Tensile Testing of Reinforcement

Figure 3.16 shows a tensile testing coupon machined from plain reinforcement (Figure 3.16 (a)) and an intact length of modern deformed reinforcement (Figure 3.16 (b)). Figures 3.17 (a) and (b) show plain and modern deformed reinforcement test specimens in the Universal Testing Machine. The rate of testing was controlled by strain at 1 mm/mm/sec. Strain was measured using an extensometer with a gauge length of 50 mm and precision of ±0.01 mm which was clamped to the coupon. The plain reinforcement was assumed to have uniform material properties throughout (ASTM International 2017a). Three coupons were machined from the plain reinforcement in accordance with ASTM Standard A370 (ASTM International 2017b). Appendix B provides a detailed drawing with measurements of a machined plain reinforcement test coupon. The modern deformed reinforcement lengths measured 40 cm. All tensile test coupons were taken from excess lengths of reinforcement that were cast and rolled in the same

heat as the reinforcement used in the corresponding beam-column joint specimen. Modern deformed reinforcement is comprised of recycled material and is manufactured via rolling and so does not have a uniform composition (ASTM International 2018). A machined coupon of modern deformed reinforcement, therefore, might not accurately represent the reinforcement due to cross-sectional variation in the recycled material.

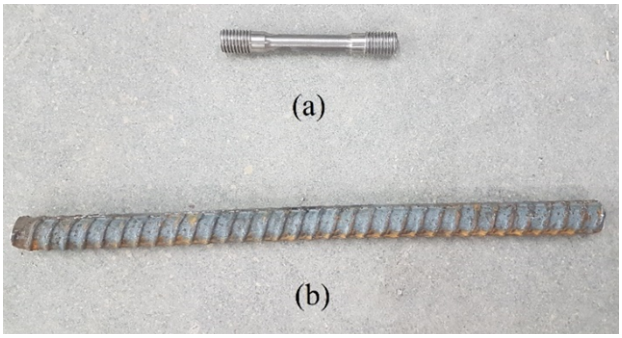

Figure 3.16: Reinforcement tensile test coupon and length: (a) plain reinforcement, and (b) modern deformed reinforcement

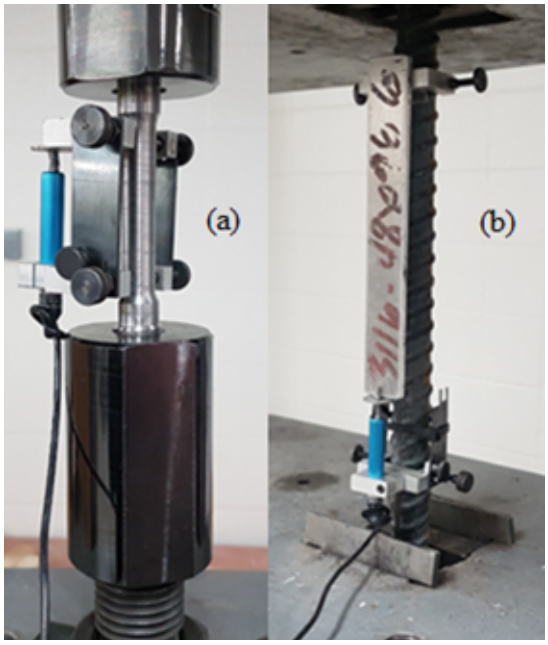

Figure 3.17: Tensile test coupon and length in the same Universal Testing Machine: (a) plain reinforcement, and (b) modern deformed reinforcement

3.9 Summary

This chapter presented the experimental design, construction, and testing as performed for this experimental program. The testing procedures for: the performance of the beam-column joint specimens, the compressive and splitting tensile strengths of concrete companion specimens, and the tensile strength of reinforcement coupons and lengths were presented. The results from testing of the beam-column joint specimens are presented in Chapter 4.

Chapter 4
Analysis of Results for Plain and Modern Deformed Hooked Bars

4.1 Introduction

This chapter provides details of the results from the experimental program outlined in Chapter 3. It outlines the material properties determined by testing the concrete companion cylinders and the reinforcement coupons and lengths. A data discussion and analysis related to the axial load as applied to all specimens is included. The identification of physical and statistical outliers is discussed. Observations made regarding crack patterns, group effects, and the effects of reinforcement deformations on concrete cover depth are detailed. These observations inform failure mode determination for each tested specimen. The maximum load and displacement results are provided. Details are also provided for the Student's t-test used to determine the statistical significance of the experimental data related to maximum load and displacement of the hooked bars.

As discussed in Chapter 3, each hooked bar was loaded by its own hydraulic jack and monitored by its own set of instrumentation equipment. Statistics for the pairs of hooked bars in each specimen are presented as averages because data was collected simultaneously per bar for the east and west hooked bars in each specimen and because taking the averages is considered a conservative methodology. As each bar was independently instrumented and could fail independently of its counterpart, taking averaged data from each specimen avoided potentially overstating individual bar performance, which could occur if statistics were reported in terms of specimen totals divided by the number of hooked bars per specimen, as in Sperry et al. (2017a). Reporting in terms of total load applied to the specimen divided by the number of hooked bars causes the sum of the maximum tensile resistances of the hooked bars in a specimen to exceed the total force applied to it at a point in time (Sperry et al. 2017a).

The naming convention used to identify experimental specimens throughout this thesis is as follows. A 'P' denotes plain reinforcement while 'MD' denotes modern deformed

reinforcement. The number that follows denotes the specimen number within the replicate group. The number following the dash denotes the hook bend angle. Each hook in the specimen pair is referred to as east ‘E’ or west ‘W’.

4.2 Material Properties

This section details the material properties of the concrete used in this investigation. These include: slump; air content; tensile strength, f_r; and compressive strength, f'_c. The material properties of the reinforcement are also presented and include the surface roughness of the plain bar and the dynamic yield strength, f_{yd}, static yield strength, f_{ys}, ultimate strength, f_u, and modulus of elasticity, E_s, of both plain and modern deformed bars.

4.2.1 Concrete

The concrete used in each of the three construction phases was tested at the time of delivery for slump and air content, as discussed in Section 3.6.3. The preparation of the concrete companion cylinders was discussed in Section 3.6.3 and the testing methods used to evaluate them were discussed in Section 3.8. Companion cylinders were tested at seven days and on the same day as the tests of corresponding beam-column joint specimens. The material properties reported in this section include the slump and air content at the time of concrete delivery; tensile strength, f_r, at the time of beam-column joint specimen testing; and compressive strengths, f'_c, at seven days and at the time of beam-column joint specimen testing. Normalization of the tensile load and displacement data and the relationship between anchorage capacity and concrete compressive strength are also discussed.

Three construction phases were required for this investigation, as discussed in Section 3.5, and companion cylinders were cast and tested in correspondence with each specimen in each phase. The mix designs for the concrete used in each construction phase were detailed in Section 3.4.1. Table 4.1 provides the measurements for slump; air content; tensile strength, f_r; and compressive strength, f'_c. Appendices C and D show the compressive stress versus strain

diagrams from the testing of the concrete companion cylinders at seven days and at the time of beam-column joint testing, respectively. Appendix E shows the tensile stress versus strain diagram from the testing of the concrete companion cylinders at the time of beam-column joint testing.

The individual compressive strengths of the concrete companion cylinders from the first phase of construction were found to be as low as 6.35 MPa at 49 days and, therefore, well below the target value of 20 MPa. This low concrete strength is attributed to an error that was not repeated in subsequent phases. Prior research performed at the University of Saskatchewan used concrete with a compressive strength that exceeded the target value of 20 MPa by a factor of 1.8 (Poudyal and Feldman 2018). The concrete supplier was directed to avoid this error made in previous deliveries to the University of Saskatchewan and adjusted the mix design accordingly. This amendment to the mix design was then compounded by the drum on the concrete truck having been inappropriately large for the amount of concrete it contained (2 m^3), causing the cement powder to stick to the inside wall of the drum. Powder sticking to the inside of the drum is not incorporated into the mixture and results in an inappropriate proportion of cement powder in the mix, deviating from the mix design specifications and resulting in decreased strength of the concrete. The too-large concrete drum issue and amended mix design resulted in over-compensation for the error made in previous deliveries to the University of Saskatchewan and, thus, a lower-than-targeted concrete compressive strength was observed in the first phase. Notably, Abrams (1913) reported compressive strength values as low as 4 MPa. The compressive strength of the phase one concrete (i.e. 6.35 MPa) was higher than 4 MPa and, thus, replicated the conditions in Abrams' study.

The concrete mixing error did not recur because the concrete manufacturer sent larger loads of concrete (3m^3) for the second and third phases, since larger loads are less likely to exhibit powder sticking to the inside of the drum. The concrete mix designs for the remaining two phases were also slightly modified at the discretion of the ready-mix supplier to ensure compressive strengths closer to the target of 20 MPa. These modifications included increasing all

components in the concrete mix, as discussed in Section 3.4.1. These modifications did not impact the experimental findings due to the normalization method used.

Concrete compressive strength is known to be positively correlated with anchorage capacity, as discussed in Section 2.2.3 (Orangun et al. 1977, Feldman and Bartlett 2005). A normalization method was required to mitigate the effects on anchorage capacity analysis of the inevitable variation in concrete compressive strength among specimens. The bond resistance of both plain straight bars and of modern deformed hooked bars is proportional to the square root of the compressive strength of the concrete (Marques and Jirsa 1975, Orangun et al. 1977, Darwin et al. 1992, Feldman and Bartlett 2005). The relationship between tensile stress and the square root of the compressive strength of the concrete implies that there is a tensile failure during testing as the compressive stresses become splitting stresses, as explained by the Poisson effect (Ellis 1988). This normalization method was appropriate for this study because the concrete immediately in front of the hooked bars was in compression while the majority of the other concrete surrounding the hook was in tension, as discussed in Section 2.4 with respect to the failure trapezoid. Further, while Orangun et al. (1977), Feldman and Barlett (2005), and Darwin et al. (1992) investigated straight lengths of reinforcement, their conclusion that bond resistance is proportional to the square root of the compressive strength of the concrete remains relevant to this investigation. This is true because reinforcement preceding the hook (i.e. the lead length) performs as a straight length of reinforcement, as discussed in Section 2.2.3, and because the hook design for all beam-column joint specimens produced for this investigation was constant. As the transverse reinforcement was not instrumented, additional relationships between the concrete compressive strength and other stresses (e.g. stress in confining reinforcement) could not be assessed. Normalization using the square root of the compressive strength of the concrete facilitated direct comparisons between samples in all phases regardless of variance in concrete compressive strength among the set. Normalization using the square root has been proven reasonable for the limited range of concrete compressive strengths reported in this investigation, assuming validity for both straight and hooked bars (Feldman and Bartlett 2005). This normalization method adequately incorporated the changing stresses in the failure trapezoid and

accounted for the bond resistance of the lead length of the hooked bars. There is not currently a normalization method able to compensate for changing forces in the hook area, as discussed in Section 2.2.2. Normalization using the square root of the compressive strength was the most appropriate and most widely accepted normalization method available for this investigation.

The modulus of rupture (or tensile strength) of the concrete provides information on the behaviour of the concrete under tension, particularly in the hook area as discussed in Section 2.2.2. Equation 4.1 is used to calculate modulus of rupture (or tensile strength) of concrete and is included in ACI 318-14[1] and CSA A23.3-14 (ACI Committee 318 2014, CSA 201D). This equation was adopted by ACI 318 in 1963 and by CSA A23.3 in 1984 (ACI Committee 318 1963, CSA 1984).

$$f_r = 0.6 \lambda \sqrt{f'_c} \qquad \text{[Eqn. 4.1]}$$

where f_r is modulus of rupture, λ is a constant term to adjust for the presence of lightweight concrete having an approximate density of 1700 kg/m^3 according to CSA A23.1-14 (normal weight concrete, which was used in this investigation, has a density of 2400 kg/m^3), and f'_c is compressive strength of the concrete.

Figure 4.1 shows the relationship between the compressive and tensile strength values for all concrete companion cylinders across all phases of this investigation, as discussed in Section 3.8. Figure 4.1 shows that observed tensile strength was lower than predicted by Equation 4.1.

[1] The equation found in the ACI 318-14 uses a value of 0.62 rather than the 0.6 used by CSA A23.3-14 and Equation 4.1.

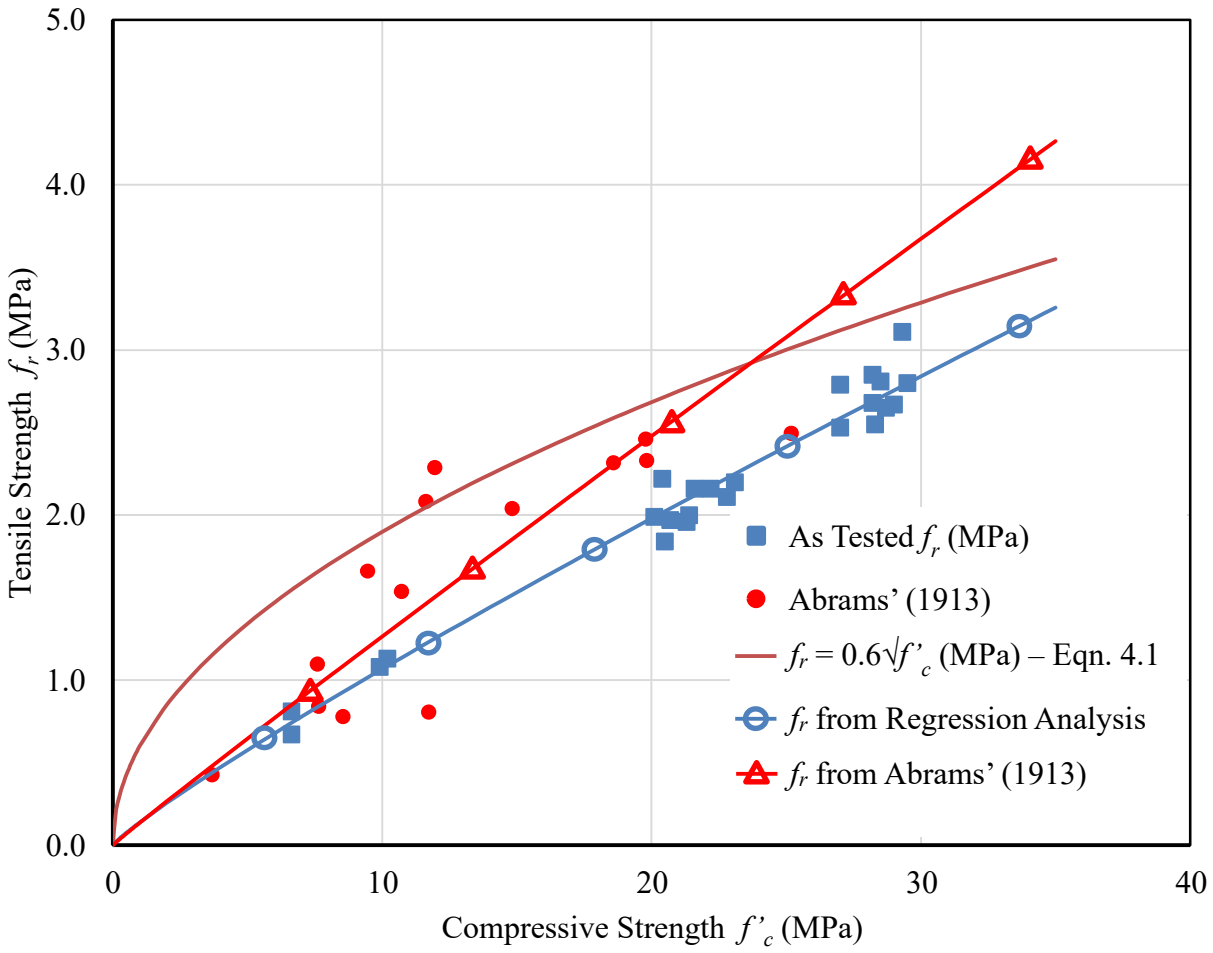

Figure 4.1: Actual and predicted tensile strength

A regression analysis was performed to approximate the observed trend between compressive and tensile strength values. A sample calculation for the regression is provided in Appendix F. The analysis showed the tensile strength of the concrete companion cylinders could be represented by the following equation with a root mean squared error of 0.65 MPa:

$$f_r = 0.1371\,\lambda\, f'^{\,0.891}_c \qquad \text{[Eqn. 4.2]}$$

Figure 4.1 and Equation 4.2 suggest the observed relationship between concrete compressive strength and tensile strength is close to the linear relationship suggested by Abrams (1913).

The near-linearity of the as-tested curve versus Equation 4.1 curve is primarily hypothesized to be caused by the near proportionality of f'_c to $\sqrt{f'_c}$ for concrete compressive strengths between 8 and 25 MPa (Feldman and Bartlett, 2005). The difference between the predicted (Equation 4.1) and as-tested results is also explained in part by split cylinder tests producing scattered data points and smaller values (Nilson et al. 2004, MacGregor and Wight 2012). The design of the split cylinder test setup produces stress concentrations during loading which can develop at a right angle to the tension stresses. This test setup, therefore, did not produce an exact representation of tensile strength in concrete but is an acceptable approximation that represents current best practice and has been used successfully by other researchers (Mindess and Young 1981, Nilson et al. 2004, McCormac and Brown 2015).

Table 4.1 shows the concrete properties from tests completed at the time of concrete casting, at seven days after casting, and at the time of beam-column joint specimen testing. Slump and air content readings were taken at the time of concrete casting, as outlined in Section 3.6.3. The measured values aligned with expectations per the mix design specifications. Concrete compressive strength measurements were taken at seven days after casting and at the time of beam-column joint specimen testing. Three concrete companion cylinders per beam-column joint specimen were tested at the time of beam-column joint specimen testing to determine their average compressive strengths, as outlined in Section 3.8.1. Three concrete companion cylinders per specimen were also tested at the time of beam-column joint specimen testing to determine their average tensile strengths, as outlined in Section 3.8.2. Compressive strength at seven days is known to approximate 65-70% of strength at 28 days (MacGregor 1992). Seven-day compressive strength results showed the concrete was curing, hardening, and gaining strength as expected. The results aligned with the nominally specified compressive strength. The compressive and tensile strength results from companion cylinder tests completed at the time of beam-column joint specimen testing indicated the concrete was cured as expected.

Table 4.1: Concrete properties

Specimen ID	Const. phase	Age of concrete at test date (days)	Slump (mm)	Air content (%)	Seven day compressive strength $f'_{c,\ 7\text{-}day}$ (MPa)	Average compressive strength f'_c (MPa)	Average tensile strength f_r (MPa)
P1-90	1	49	160	1.78	3.30	6.35	0.667
P2-90	3	46	68	3.27	11.6	22.2	2.16
P3-90	3	47			13.4	21.4	2.00
P4-90	3	48			12.8	21.6	2.16
P5-90	3	49			12.5	20.7	1.97
P6-90	3	50			11.4	20.1	1.99
P1-180	1	54	160	1.78	3.59	6.63	0.806
P2-180[a]	3	41	75	3.93	N/A[b]	27.0	2.53
P3-180	3	42			18.9	27.0	2.79
P4-180[a]	3	45			18.3	29.3	3.11
P5-180	3	46			19.0	28.5	2.81
P6-180	3	48			18.3	29.5	2.80
MD1-90	1	48	40	1.81	5.75	10.2	1.13
MD2-90[a]	2	53	68	3.27	14.1	22.8	2.11
MD3-90	2	54			12.7	23.1	2.20
MD4-90	2	55			11.8	20.5	1.84
MD5-90	2	56			9.92	20.4	2.22
MD6-90	2	57			11.1	21.3	1.96
MD1-180	1	44	40	1.81	5.74	9.91	1.08
MD2-180	2	49	75	3.93	18.8	28.2	2.68
MD3-180	2	52			17.8	28.7	2.65
MD4-180	2	54			18.4	28.3	2.55
MD5-180	2	55			17.9	28.2	2.85
MD6-180	2	56			18.1	29.0	2.67

[a] Denotes that this specimen was excluded as an outlier, as discussed in Section 4.4.
[b] Data is unavailable because strength data did not save after testing.

4.2.2 Reinforcement

This section provides the properties of the machined test coupons and intact reinforcement lengths for the plain and modern deformed bars, respectively, as used in the experimental program. The tensile testing of reinforcement was described in Section 3.8.3. The surface roughness, R_y, of the plain reinforcement and the dynamic yield strength, f_{yd}; static yield strength, f_{ys} (as defined below); ultimate strength, f_u; and modulus of elasticity, E_s, results for both plain and modern deformed bars are presented. As discussed in Section 3.7, the beam-column joint specimens were designed so the hooked bars would not yield during testing.

Appendices G and H show the stress versus strain diagrams from the testing of the plain reinforcement coupons and modern deformed reinforcement lengths used in this investigation. The dynamic, f_{yd}, and static, f_{ys}, yield strengths for plain and modern deformed bars, respectively, were 355 MPa, 328MPa, 419 MPa, and 395 MPa. The dynamic yield was taken from the stress-strain diagrams at the point at which slope changed from linear and positive to non-linear. The ultimate strength, f_u, values were 534 MPa and 649 MPa for plain and modern deformed bars, respectively. The modulus of elasticity, E_s, values were 198 GPa and 204 GPa for plain and modern deformed bars, respectively, and acceptably approximated the nominal specified value of 200 GPa. The modulus of elasticity was calculated using the average slope in the elastic range after the slope had stabilized.

A method taken from Rao et al. (1966) was used to calculate static yield. The static yield strength, f_{ys}, of plain and modern deformed bars was calculated as:

$$f_{yd} = 22.1 \text{ MPa} + 0.007\ \dot{\varepsilon} + f_{ys} \qquad \text{[Eqn. 4.3]}$$

where f_{yd} is the measured dynamic yield strength and $\dot{\varepsilon}$ is the strain rate in μmm/mm/s. Strain rates ranging from 200 to 1,600 μmm/mm/s are appropriate for use in this equation. All strain rates fell within the required range except for a single modern deformed reinforcement coupon, which had a strain rate of 41 μmm/mm/s, and a single plain reinforcement coupon, which had a strain rate of 2,063 μmm/mm/s. The low strain rate observed for the noted modern deformed reinforcement coupon is hypothesized to result from stress concentrations, random inclusions, or

preexisting damage such as a microcrack (McEvily and Kasivitamnuay 2013). The high strain rate observed for the noted plain reinforcement coupon is attributable to a non-programming-related, instrumentation-related computer error of the test machine. Equation 4.3 was deemed acceptable for use because the majority of the strain rates for the specimens fell within the allowable limits.

Table 4.2 provides the surface roughness values for plain reinforcement used in this investigation. The numbers provided in Table 4.2 were calculated as outlined in Section 3.4.2. As discussed in Section 3.4.2, the surface roughness, R_y, of each length of plain reinforcement was evaluated using a Mitutoyo SJ-201 roughness tester. The R_y values presented in Table 4.2 were deemed acceptable because they do not overestimate the average historical bar roughness value, reported as 11.6 μm (Feldman and Bartlett 2005). As noted in Section 3.4.2, an increase in surface roughness would generate more frictional sliding resistance and could produce an inflated maximum load value.

Table 4.2: Reinforcement properties

Specimen ID	Phase	Position	Surface roughness R_y (μm)	Average surface roughness R_y (μm)	Standard deviation of the surface roughness R_y (μm)
P1-90	1	East	10.9	10.5	2.25
		West	10.1		
P2-90	3	East	9.24	9.27	1.31
		West	9.30		
P3-90	3	East	9.84	9.56	1.45
		West	9.27		
P4-90	3	East	9.53	9.57	1.45
		West	9.60		
P5-90	3	East	9.46	9.48	1.36
		West	9.50		
P6-90	3	East	9.30	9.46	1.41
		West	9.61		
P1-180	1	East	10.1	10.0	2.04
		West	9.91		
P2-180	3	East	11.4	11.4	1.49
		West	11.4		
P3-180	3	East	11.3	11.1	1.48
		West	10.9		
P4-180[a]	3	East	9.22	9.29	1.31
		West	9.35		
P5-180	3	East	9.54	9.60	1.50
		West	9.66		
P6-180	3	East	9.49	9.63	1.49
		West	9.77		

[a] Denotes that this specimen was excluded as an outlier, as discussed in Section 4.4.

4.3 Applied Axial Load

Appendix I provides axial load data for each beam-column joint specimen. The axial load data is provided as the average of the axial load measurements obtained throughout the duration of each beam-column joint specimen test via load cells, as discussed in Section 3.7. The average axial load value from all beam-column joint specimen testing was 203 kN with a standard deviation of 6.65 kN and varied from 189 kN to 213 kN. Marques and Jirsa (1975) determined that variations of up to 1,846 kN in axial load do not affect anchorage capacity. The observed variation in average axial load is, therefore, inconsequential to this testing program.

4.4 Identification of Outliers

Physical outliers were identified by observation. ASTM E 178-16a standards were used to analyze potential statistical outliers using the recommended Student's t-test and all were found to be within the acceptable range (ASTM International 2016).

Two plain bar specimens with 180° hooks (P2-180 and P4-180) and one modern deformed bar specimen with a 90° hook (MD2-90) were tested at a very high rate (i.e. 25 times greater than for other specimens) because the computer hardware failed to control the load rate. The test was accidentally accelerated to completion in seconds rather than the usual 15 to 30 minutes. As a result, specimens P2-180, P4-180, and MD2-90 were excluded for two reasons: (1) the high load rate and (2) an uncommonly sudden loss of anchorage capacity. The displacements of specimens P1-180 and P5-180 were also omitted from the statistical analysis because the laser displacement transducers ceased measurement at maximum load and provided incomplete data. This malfunction occurred because a piece of spalled concrete from the specimen fell onto and disconnected the cables connecting the laser displacement transducers to the computer.

4.5 Visual Observations

Observations of concrete cracking were monitored and recorded throughout the duration of beam-column joint specimen testing, as described in Section 3.7. This section provides information on the documentation of crack patterns and evaluation of specimen failure modes.

4.5.1 Crack Patterns

Cracking is hypothesized, in part, to begin when the tensile force applied to the hooked bars surpasses the tensile capacity of the concrete. Bursting pressure also contributes to the initiation of cracking in both plain and modern deformed bar specimens, as discussed in Section 2.2.1. The cracking observed during beam-column joint specimen testing was documented.

The documentation of crack patterns during beam-column joint specimen testing provides information that aids in the analysis of the failure mode of the specimen. The determination of failure modes within and between specimen groups provides useful information regarding performance differences between plain and modern deformed and 90° and 180° hooked specimens. The bond behaviour of hooked bars was discussed in Section 2.2.2 and provides insight into how the type of hook affects how tensile stress is transferred into the concrete.

Figures 4.2 to 4.5 illustrate the crack patterns observed for specimens P6-90, P5-180, MD4-90, and MD3-180 at the maximum load level. These crack patterns were selected as representative of each of the four specimen groups tested. The crack patterns for all other beam-column joint specimen are provided in Appendix J. Appendix K provides the maximum normalized load at which cracking began on the different faces of the beam-column joint specimens.

A typical cracking pattern emerged from the observations made during the beam-column joint specimen testing in this investigation. Cracks were observed to originate on the front face of the specimen and radiate outward from the point at which the hooked bars exited the specimen.

Primary horizontal transverse cracks were observed to project from the lead length component of the reinforcement onto the east and west sides of the specimen. Once these cracks reached the edge of the front face, they began to extend horizontally on the adjoining east and west sides and extend vertically above and below the primary horizontal transverse cracks. The vertical cracks on the east and west sides of all specimens curved back toward the front face as they extended vertically upward and downward from the location of the primary horizontal transverse cracks. A vertical crack extending along the tail section of the hook was common for all specimen types. This progression was typical for all beam-column joint specimens. The degree of cracking observed for all specimens was similar to other studies (Marques and Jirsa 1975, Sperry et al. 2017a, 2017b, 2018, Ajaam et al. 2018).

Radial cracks originate perpendicular to the surface of the bar along its embedded length, as discussed in Section 2.2.1. Radial cracks are hypothesized to be caused by a loss of the adhesion between the lead length of the plain reinforcement and the surrounding concrete (MacGregor and Wight 2012). Radial cracking of beam-column joint specimens containing modern deformed bars occurred after adhesion between the lead length and surrounding concrete was overcome and the deformations bore against the adjacent concrete, as discussed in Section 2.2.1. Displacement occurs following the loss of adhesion and causes non-uniform stresses to form in the concrete along the length of the bar within the beam-column joint specimen. These non-uniform stresses result in cracking (Abrams 1913, Feldman and Bartlett 2005). Radial cracks on the surface of the front face of the specimen developed and progressed at approximately the same loads of for all specimen groups in this investigation. This shows that these beam-column joint specimens containing plain or modern deformed hooked bars develop cracks at the same approximate load regardless of hook geometry.

Figures 4.2 and 4.4 show surface cracks for 90° beam-column joint specimens containing plain and modern deformed hooked bars, respectively, as tested in this investigation. These specimens displayed the tendency for cracks to radiate vertically on the east and west sides in parallel with the tail section of the hook. The difference in the extent of cracking between

specimens containing 90° and 180° hooks is due to the differing geometries of their tail sections. As discussed in Section 2.2.2, the different internal stress distributions caused by these two hook geometries produce different cracking effects. The angles of near-vertical cracks on the east and west faces of the specimens varied between specimens containing plain and modern deformed bars. Near-vertical cracks with steeper angles were observed on the east and west faces of specimens containing modern deformed versus plain bars. A manual approximation as shown in Appendix L was calculated based on the average angle of the near-vertical cracks observed on each specimen, as angles varied amongst all specimens. The average angles of these cracks were 68° versus 55° and 72° versus 66° for specimens containing modern deformed and plain bars with 90° and 180° hooks, respectively. This steeper angle is hypothesized to be caused by bursting pressure due to the vertical component of bearing force around bar deformations. Further, the presence of deformations is hypothesized to cause the Mohr rupture envelopes of plain and modern deformed bar to differ; these differences present as differences between the angles of observed cracks (MacGregor and Wight 2012).

As previously noted, the near-vertical cracks on the east and west sides of all specimens curved back toward the front face. The specimens containing 180 hooks, which failed via front face blowout, were noted to display cracking bearing particular similarity to arching action. Arching action generally occurs in short, deep beams which are horizontally restrained on both ends; compressive forces travel diagonally within the beam from the upper middle down to the end supports (Park and Paulay 1975). Figures 4.3 and 4.5 show this type of cracking and suggest that in this study shear within the beam-column joint was resisted by diagonal strut action, similar to arching action in beams (Fenwick and Irvine 1977). Struct action occurs where a diagonal compressive strut runs from the middle of the column down to the point where compressive reaction is caused by the beam (Park and Paulay 1975).

Cracks were projected onto the rear face at the lower tail section of specimens with 90° hooked bars, indicating the incidence of tail kickout. The cracking patterns on the rear specimen

face described in this investigation align with those reported in previous studies (Marques and Jirsa 1975, Sperry et al. 2017a, 2017b, 2018, Ajaam et al. 2018).

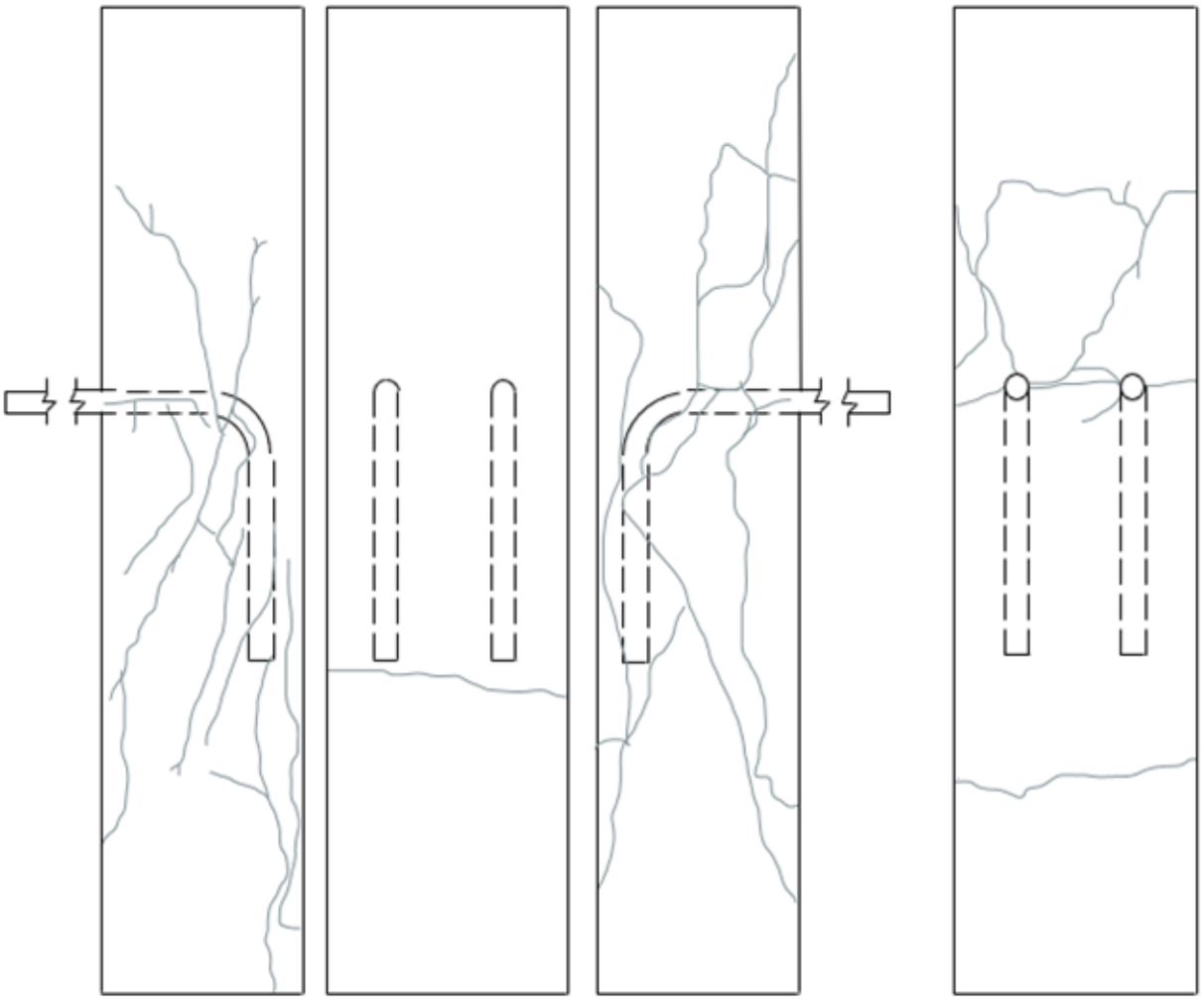

(a) (b) (c) (d)

Figure 4.2: Crack pattern at maximum normalized tensile load for beam-column joint specimen P6-90: (a) west side face, (b) back face, (c) east side face, and (d) front face

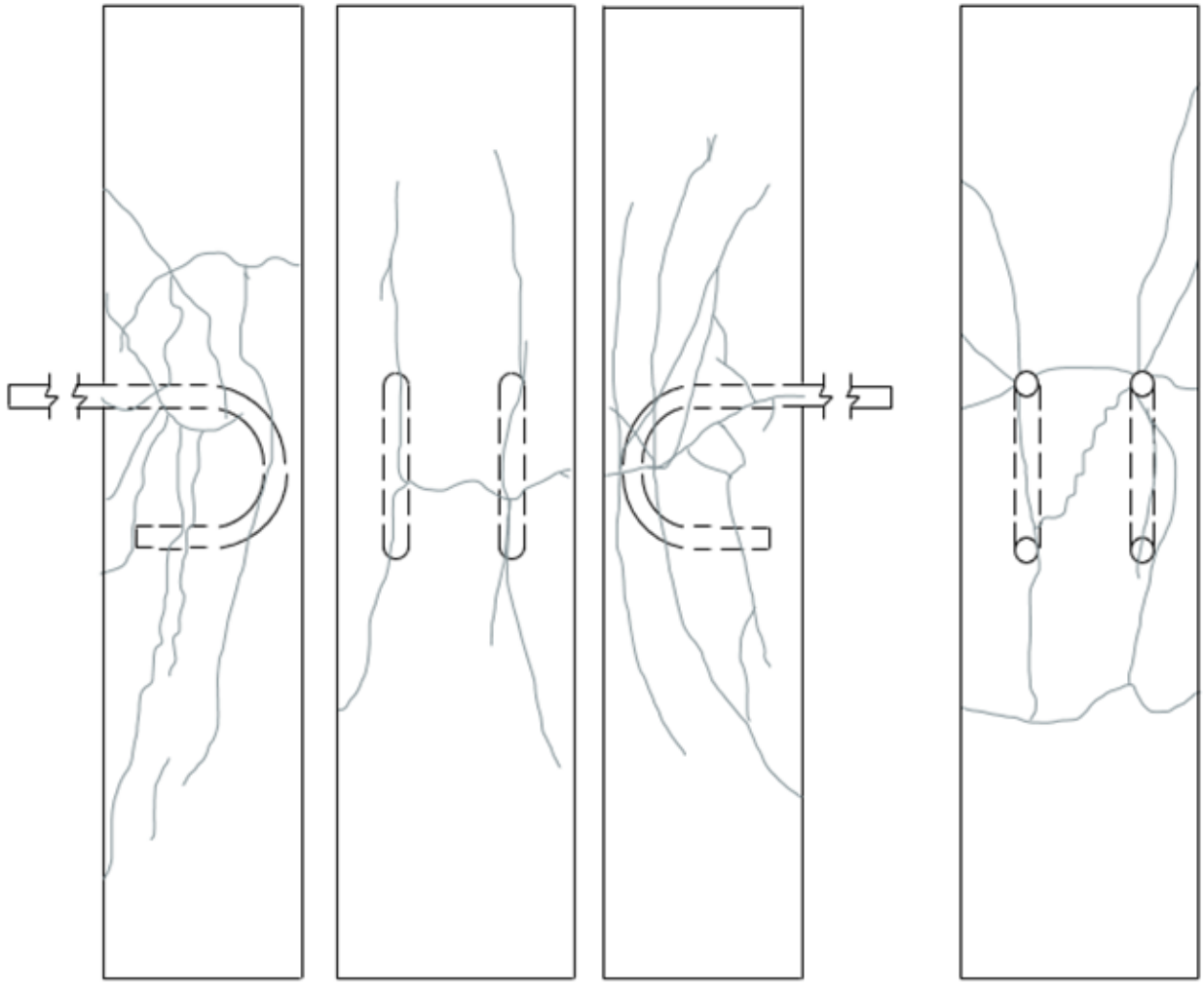

(a) (b) (c) (d)

Figure 4.3: Crack pattern at maximum normalized tensile load for beam-column joint specimen P5-180: (a) west side face, (b) back face, (c) east side face, and (d) front face

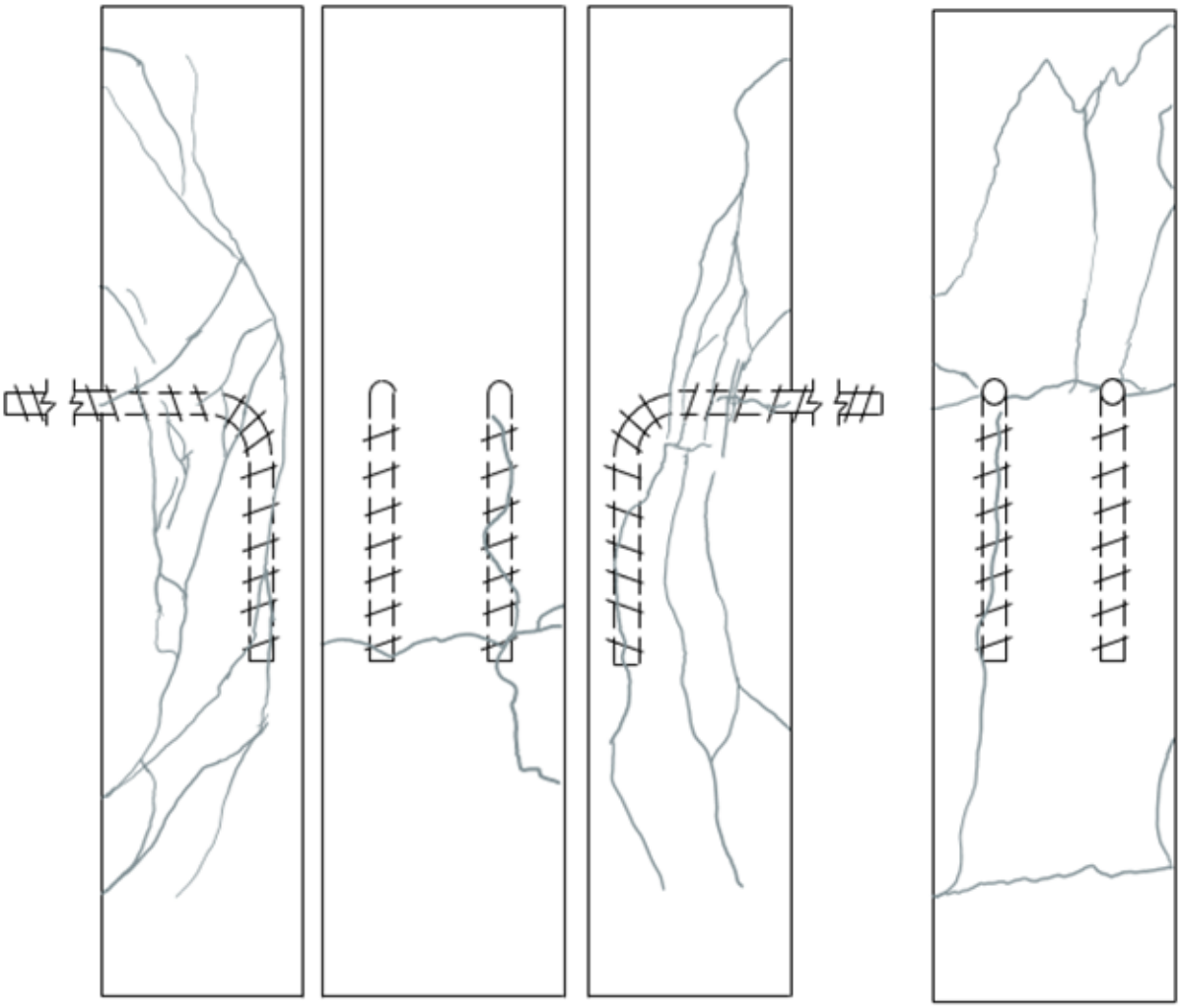

(a) (b) (c) (d)

Figure 4.4: Crack pattern at maximum normalized tensile load for beam-column joint specimen MD4-90: (a) west side face, (b) back face, (c) east side face, and (d) front face

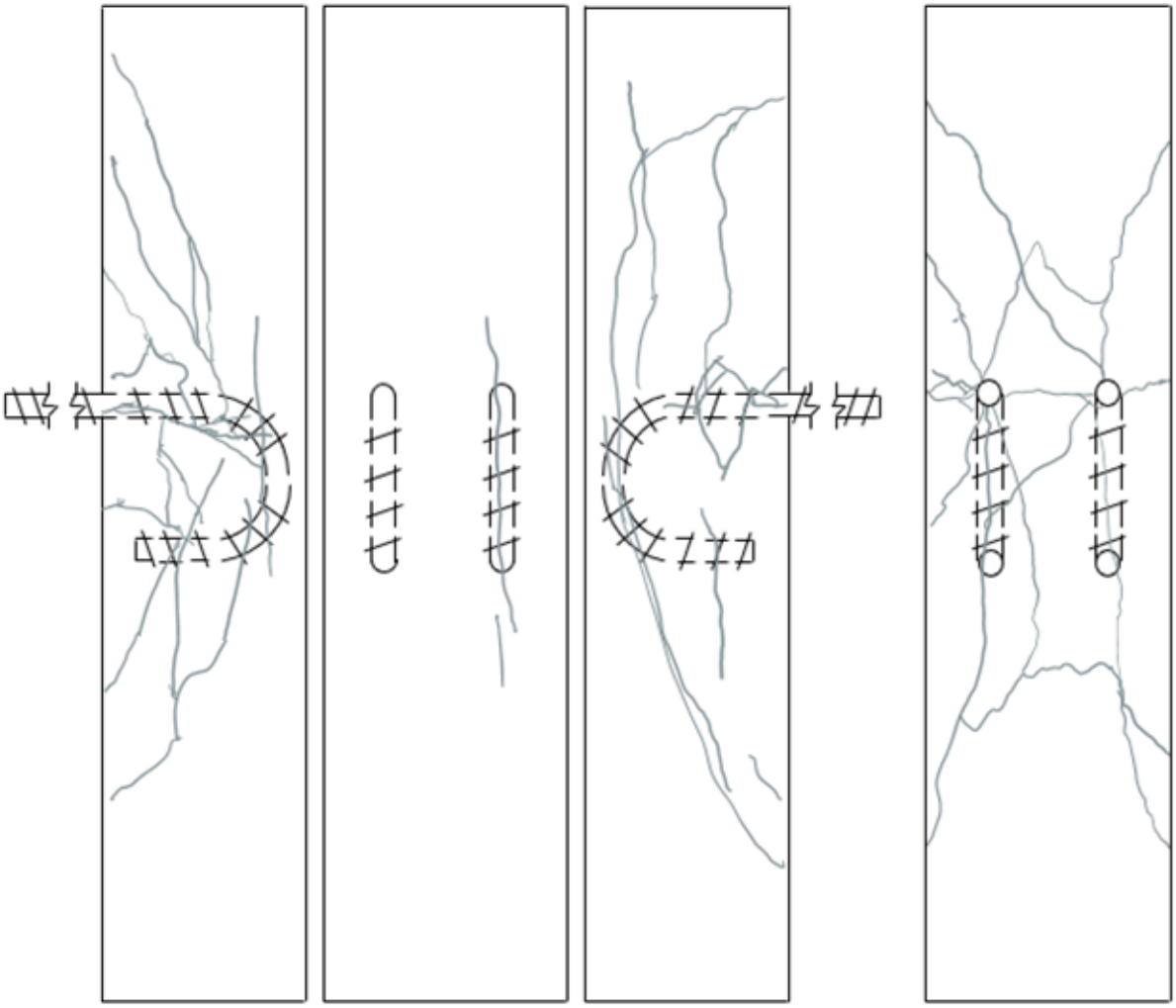

Figure 4.5: Crack pattern at maximum normalized tensile load for beam-column joint specimen MD3-180: (a) west side face, (b) back face, (c) east side face, and (d) front face

4.5.2 Group Effects

The experimental program was designed to prevent group effects, as defined in Section 2.4 and discussed in Section 3.3. The observation of cracks indicating the presence of a delaminated concrete cone (or trapezoid) between the hooked bars is considered potential evidence of group effects. Hooks acting in unison to draw out a large piece of concrete from between them

coinciding with a reduction in strength at maximum load confirms the incidence of group effects (Ajaam et al. 2018).

Specimens P6-90, MD6-90, and MD5-180 exhibited the visual characteristics of group effects in their crack patterns. These specimens were determined not to have exhibited group effects, however, because a reduction in anchorage capacity did not coincide with the observations of cone-like (or trapezoidal-like) failures.

4.5.3 Observed Failure Modes

This section provides details on the crack patterns and other visual observations informing the failure modes of each specimen in this investigation. Failure modes were defined in Section 2.4. Figure 4.6 provides photographs of the two primary failure modes observed, i.e. side blowout (Figure 4.6 (a) showing MD4-90) and front face blowout (Figure 4.6 (b) showing P1-180). Figure 4.6 (c) shows MD1-90 and depicts the secondary failure mode, i.e. tail kickout. Table 4.3 provides the failure mode for each of the 24 beam-column joint specimens.

All beam-column joint specimens in this investigation containing 90° plain or modern deformed hooked bars had a primary failure mode of side blowout, as shown in Figure 4.6 (a). This failure mode is characterized by the release of energy via concrete spalling on a side of the specimen, exposing the adjacent hooked bar. Loss of confinement on the side faces results in an overall loss of anchorage capacity because the concrete remaining on the front face immediately spalls off, exposing reinforcement. Marques and Jirsa (1975) and Sperry et al. (2017) observed the same failure progression of side blowout followed by front spalling for 90° hooks. Tail kickout, shown in Figure 4.6 (c), was documented as a secondary failure mode and was only observed after side blowout had occurred. Half of the specimens (i.e. three of six) containing 90° hooked plain bars and one third of the specimens (i.e. two of six) containing 90° hooked modern deformed bars were observed to experience tail kickout after the initial failure of the specimen. The observed incidence of side blowout in this study is affected by the amount of side concrete

cover and presence of transverse reinforcement in the hook region. Due to the small sample size, it is not possible to draw meaningful conclusions regarding why more plain versus modern deformed 90° hooked bar specimens experienced tail kickout. A higher incidence of tail kickout was observed in specimens containing plain hooked bars and may be attributable to increased overall displacement due to the absence of mechanical interlock (Abrams 1913). The findings regarding beam-column joint specimens containing 90° hooked bars are consistent with Marques and Jirsa 1975 and Sperry et al. 2017b.

All beam-column joint specimens in this investigation containing plain or modern deformed 180° hooked bars failed via front face blowout, as shown in Figure 4.6 (b). Front face blowout is characterized by a trapezoidal failure wherein large amounts of concrete suddenly spalling from the front face upon failure, the bearing capacity of the concrete hypothetically being exceeded, and a large piece of concrete being pulled forward from the front face of the column along with the hooked bars. The side faces of these specimens were observed to spall after front face blowout. The findings regarding beam-column joint specimens with 180° hooked bars are consistent with those of other researchers (Sperry et al. 2017b).

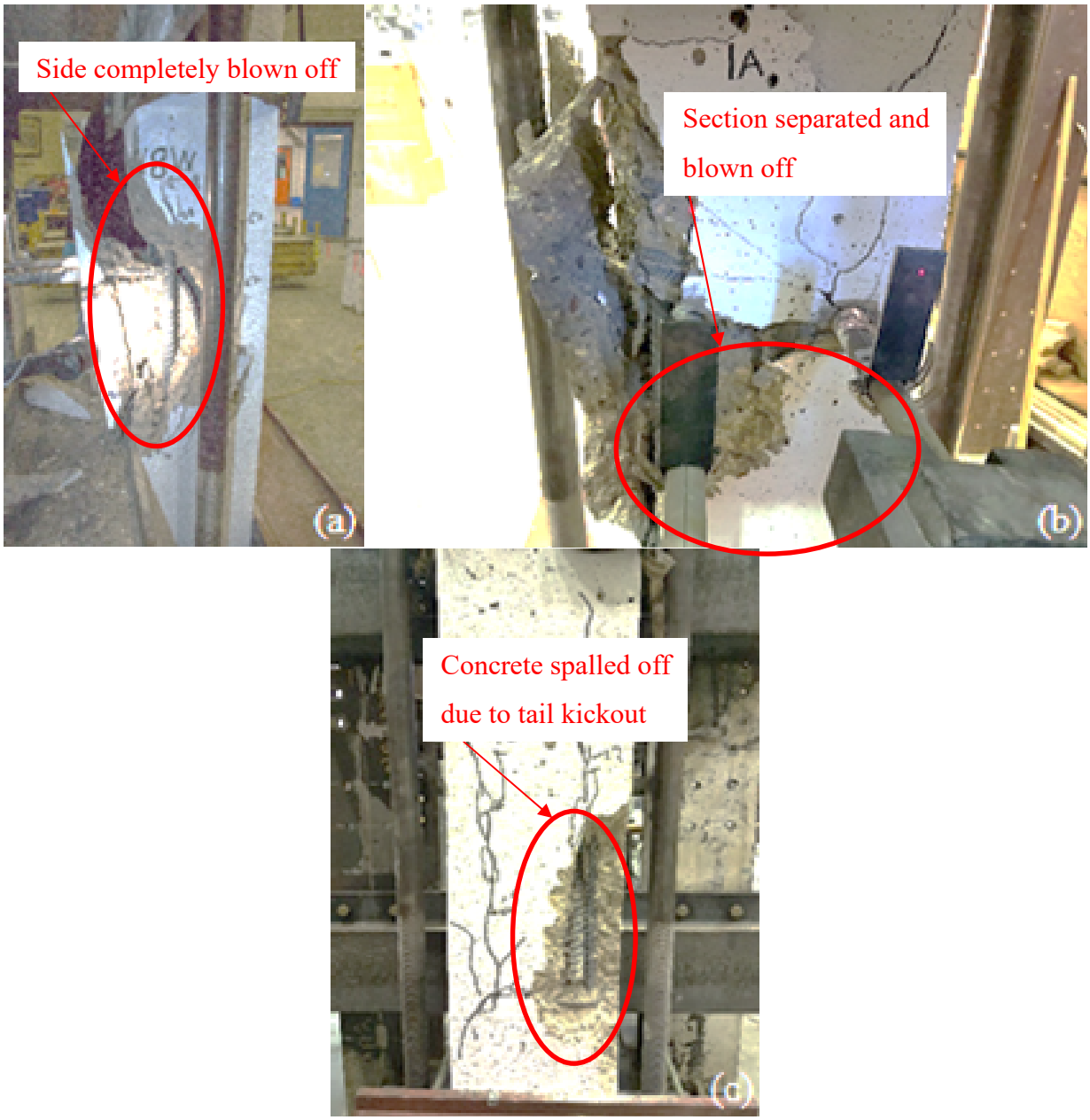

Figure 4.6: Failure modes: (a) side blowout – MD4-90, (b) front face blowout – P1-180, and (c) tail kickout – MD1-90

Table 4.3: Beam-column joint specimen test results

Specimen ID	Phase	Bar position	Maximum normalized tensile load P_{max} (kN/√MPa)	Average maximum normalized tensile load P_{max} (kN/√MPa)	Bar displacement at maximum normalized tensile load (mm)	Average bar displacement at maximum normalized tensile load (mm)	Failure mode
P1-90	1	East	14.8	15.8	8.42	8.31	Side blowout
		West	16.7		8.19		
P2-90	3	East	14.4	14.8	6.94	7.73	Side blowout
		West	15.2		8.53		
P3-90	3	East	16.0	16.3	5.94	7.20	Side blowout
		West	16.6		8.47		
P4-90	3	East	15.5	15.9	8.15	7.59	Side blowout and tail kickout
		West	16.2		7.04		
P5-90	3	East	18.2	18.7	7.62	7.84	Side blowout and tail kickout
		West	19.2		8.06		
P6-90	3	East	18.2	18.4	7.03	7.37	Side blowout and tail kickout
		West	18.6		7.71		
P1-180	1	East	15.9	16.6	-	-	Front face blowout
		West	17.3		-		
P2-180[a]	2	East	21.9[a]	21.9[a]	9.0A	8.30[a]	Front face blowout
		West	22.0[a]		7.56[a]		
P3-180	2	East	19.0	19.3	7.30	8.16	Front face blowout
		West	19.7		9.03		
P4-180[a]	2	East	24.A	19.5[a]	6.42[a]	5.7C	Front face blowout
		West	14.6[a]		5.07[a]		
P5-180	2	East	19.8	19.7	-	-	Front face blowout
		West	19.5		-		
P6-180	2	East	19.2	19.5	9.53	9.17	Front face blowout
		West	19.8		8.82		

[a] Denotes that this specimen was excluded as an outlier, as discussed in Section 4.4.

Table 4.3 Continued: Beam-column Joint Specimen Test Results

Specimen ID	Phase	Bar position	Maximum normalized tensile load P_{max} (kN/√MPa)	Average maximum normalized tensile load P_{max} (kN/√MPa)	Bar displacement at maximum normalized tensile load (mm)	Average bar displacement at maximum normalized tensile load (mm)	Failure mode
MD1-90	1	East	22.4	23.1	12.0	11.2	Side blowout
		West	23.8		10.3		
MD2-90[a]	3	East	21.1[a]	21.C	6.97[a]	7.06[a]	Side blowout
		West	21.7[a]		7.16[a]		
MD3-90	3	East	17.5	17.8	7.74	7.68	Side blowout
		West	18.2		7.62		
MD4-90	3	East	18.8	19.0	7.40	7.61	Side blowout and tail kickout
		West	19.2		7.81		
MD5-90	3	East	22.0	22.2	10.6	9.68	Side blowout
		West	22.4		8.78		
MD6-90	3	East	19.5	20.0	6.76	7.18	Side blowout and tail kickout
		West	20.4		7.60		
MD1-180	1	East	22.1	22.8	8.34	8.51	Front face blowout
		West	23.5		8.67		
MD2-180	2	East	23.2	23.2	7.73	8.14	Front face blowout
		West	23.3		8.54		
MD3-180	2	East	23.9	24.3	11.1	11.9	Front face blowout
		West	24.7		12.6		
MD4-180	2	East	24.0	24.3	8.71	8.70	Front face blowout
		West	24.6		8.69		
MD5-180	2	East	26.0	26.3	11.0	11.4	Front face blowout
		West	26.5		11.8		
MD6-180	2	East	25.0	25.2	12.2	11.2	Front face blowout
		West	25.5		10.1		

[a] Denotes that this specimen was excluded as an outlier, as discussed in Section 4.4.

4.6 Maximum Normalized Tensile Load

The experimental design of this study successfully avoided the yielding of plain hooked bars. Specimen P6-180 achieved the maximum yield strength of all plain specimens tested, which was 69.7% of the yield strength of plain hooked bar. The maximum tensile load data observed for each specimen was normalized by the square root of the compressive strength of the concrete, as discussed in Section 4.2.1. The two load measurements (i.e. one per hook) were then averaged for each specimen because this produced balanced and conservative results. Table 4.3 shows the average maximum normalized tensile load data for all beam-column joint specimens. Two-tailed Student's t-tests were carried out with unequal variances assumed for the statistical analysis of the maximum normalized tensile load data. Sample calculations are provided in Appendix F.

The two-tailed Student's t-test was used to evaluate whether any of the four specimen groups was able to withstand a statistically different average maximum normalized tensile load. The null hypothesis tested was, therefore, that mean load data between specimen groups was equal. Unequal variance of load data was assumed because sample sizes were inconsistent across groups due to the removal of outliers. Table 4.4 presents the results of the statistical analysis including the average; standard deviation; degrees of freedom, v; p-value; and t-statistic of the observed maximum normalized tensile load. Load data was evaluated at the 95% confidence level to ensure statistical significance. The analysis revealed statistically significant differences between the following, given the sample size:

- The resistance of 90° plain versus modern deformed hooked bars;
- The resistance of 180° plain versus modern deformed hooked bars; and
- The resistance of 90° versus 180° modern deformed hooked bars.

No statistically significant difference was noted between the observed maximum normalized tensile load at failure of specimens containing 90° and 180° plain hooked bars.

The finding of a statistically significant difference between the maximum normalized tensile loads of 90° and 180° modern deformed hooked bars contradicts the findings of other researchers, who found no significant difference (Marques and Jirsa 1975, Sperry et al. 2017a,

2017b). This is hypothesized to result from differences in experimental program design, as discussed in Section 2.5.

Table 4.4: Statistical analysis of maximum normalized tensile load

Number of specimens	Comparison	T-statistic	Average (kN/√MPa)	Standard deviation (kN/√MPa)	Degrees of freedom (v)	P-value	Significance level
6	90° plain vs. 90° modern deformed	3.242	16.6	1.56	7	0.0142	98.6
5			20.4	2.20			
4	180° plain vs. 180° modern deformed	6.254	18.8	1.46	6	0.00153	99.8
6			24.4	1.27			
6	90° plain vs. 180° plain	2.271	16.6	1.56	7	0.06436	93.6
4			18.8	1.46			
5	90° modern deformed vs. 180° modern deformed	3.597	20.4	2.20	6	0.0114	98.9
6			24.4	1.27			

4.7 Displacement of Hooked Reinforcing Bars

Displacement refers to the combination of translation and deformation (or 'stretching') of the loaded bar. Deformation cannot be guaranteed to be uniform along the length of the loaded bar and so cannot be removed from displacement data because it cannot be isolated. The displacement measurements include any deflection of the test frame. Displacement was measured from the exposed reinforcement to the test frame, as discussed in Section 3.7. The two displacement measurements (i.e. one per hook) were averaged for each specimen to provide consistency in the manner of reported results, i.e. normalized tensile load data was averaged, as discussed in Section 4.6. Two-tailed Student's t-tests were conducted and unequal variances

were assumed for the statistical analysis of displacement data. The sample calculations provided in Appendix F for maximum normalized tensile load mirror those pertaining to displacement.

Table 4.5 provides the statistical analysis of displacement at the maximum normalized tensile load for each specimen group. The two-tailed Student's t-test analysis revealed no statistically significant differences between the following at the 95% confidence level, given the sample size:

- The displacement at maximum normalized tensile load of 90° plain versus modern deformed hooked bars;
- The displacement at maximum normalized tensile load of 180° plain versus modern deformed hooked bars;
- The displacement at maximum normalized tensile load of 90° versus 180° plain hooked bars; and
- The displacement at maximum normalized tensile load of 90° versus 180° modern deformed hooked bars.

The above results do not validate the results of previous researchers. Marques and Jirsa (1975) found 90° modern deformed hooked bar specimens exhibited less displacement at a given force than did 180° hooked bar specimens. Specimens with hooked modern deformed bars in this study were not found to follow the trend observed by Marques and Jirsa (1975) of a smaller displacement for 90° versus 180° modern deformed hooked bars. This difference in findings could be because Marques and Jirsa (1975) did not evaluate replicates of the different specimen types they tested.

The average displacement of the reinforcement in specimens with plain hooked bars displayed a lower variance than those with modern deformed bars regardless of hook geometry, as shown in Table 4.5. Conclusions cannot be drawn from this finding due to the small sample size. A sample size of 30 or more – less than 30 is considered a small sample in statistics – is recommended to accurately evaluate variance in the behaviour of plain and modern deformed bars containing hooks (Walpole et al. 2007).

Table 4.5: Statistical analysis of hooked bar displacement

Number of specimens	Comparison	T-statistic	Average (mm)	Standard deviation (mm)	Degrees of freedom (v)	P-value	Confidence interval
6	90° plain vs. 90° modern deformed	1.262	7.68	0.390	4	0.276	72.4
5			8.66	1.70			
2	180° plain vs. 180° modern deformed	1.518	8.67	0.710	5	0.204	79.6
6			9.96	1.68			
6	90° plain vs. 180° plain	1.880	7.68	0.390	1	0.311	68.9
2			8.67	0.710			
5	90° modern deformed vs. 180° modern deformed	1.270	8.66	1.70	9	0.240	76.0
6			9.96	1.68			

4.8 Displacement versus Normalized Tensile Load of Hooked Reinforcing Bars

Figure 4.7 shows normalized tensile load data versus displacement with a representative curve for each of the four beam-column joint specimen groups. The curves shown in Figure 4.7 were created by averaging the readings for both east and west bars for each specimen. The representative curves chosen were for P3-90, P6-180, MD6-90, and MD4-180. These particular specimens were chosen as representative of their respective groups, as they best illustrated the average curve shape. Appendix M contains all figures for individual beam-column joint specimens. All four representative curves show a steep, linear positive slope once loading was initiated. The linear sections of the curves represent elastic deformation in the specimens and hooked bars in conjunction with minor, visible displacement. The point at which the hooked bars began to pull out from the specimen after maximum normalized tensile load was achieved corresponds with the point on the graphs at which the rate of displacement increases in conjunction with decreasing normalized tensile load and marked, sudden visible displacement is observed.

As discussed in Section 2.2, mechanical interlock between bar deformations and the surrounding concrete is responsible for a more sudden loss in load carrying capacity at a higher maximum normalized tensile load for specimens containing modern deformed versus plain bars of the same hook geometry. This is evident in Figure 4.7 where the slopes of the curves for the modern deformed hooked bar specimens steeply ascend immediately prior to the attainment of maximum normalized tensile load whereas the slopes for the plain bar specimens begin to gradually decay and plateau. This is hypothesized to occur because the bursting pressure has exceeded the capacity of the concrete. It may also occur because the concrete surrounding and in-between deformations of the reinforcement in specimens containing modern deformed specimens, after adhesion has been overcome, has been crushed or sheared off and cannot contribute any frictional sliding resistance. Frictional sliding resistance continues to contribute to the bond between the concrete and plain bar after adhesion has been overcome and as the bar is pulled from the specimen, flattening the curve for plain hooked bar specimens. The relatively steep negative slopes of the representative curves for modern deformed specimens are also hypothesized to be caused by extensive radial cracking. The crushing and shearing of concrete is hypothesized to be the cause of hooked modern deformed bars of either hook geometry failing more suddenly than plain bars.

Figure 4.7 shows a more sudden loss of anchorage capacity was observed for specimens with 180° modern deformed versus plain hooked bars immediately following the achievement of maximum normalized tensile load. The relatively sudden loss of anchorage capacity of specimen MD4-180 in Figure 4.7 is shown by the approximately 25° steeper slope immediately following the achievement of maximum normalized tensile load when compared to plain hooked bar specimens. Beam-column joint specimen MD6-90 in Figure 4.7 did not exhibit the same sudden loss of load carrying capacity. The sudden loss of anchorage capacity observed in specimens with 180° hooked bars is hypothesized to occur due to the separation of the failure trapezoid from the rest of the specimen, which characterizes front face blowout as discussed in Section 2.5. Specimens with plain reinforcement did not exhibit as pronounced differences in the suddenness

of anchorage capacity loss when compared with modern deformed specimens containing 90° versus 180° hooks.

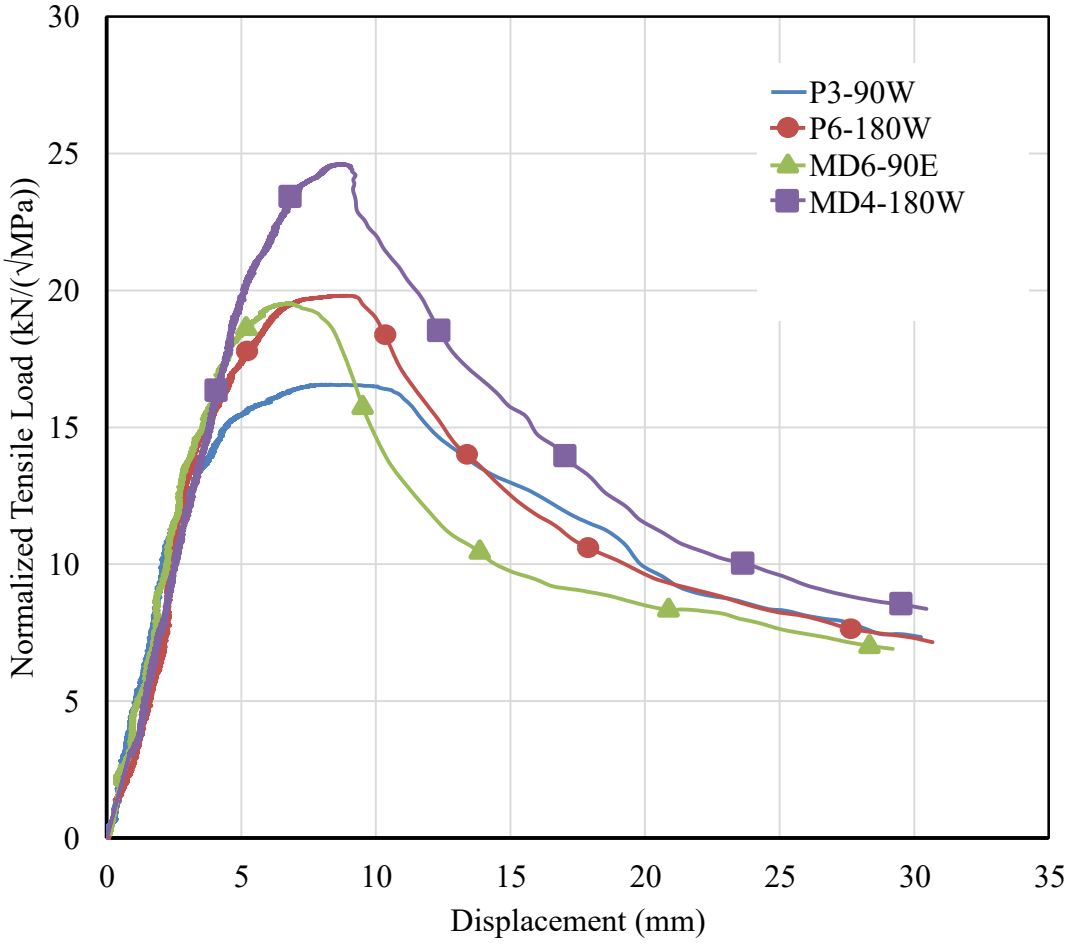

Figure 4.7: Normalized tensile load versus displacement

4.9 Summary

The results of material properties tests, identification of outliers, evaluation of crack patterns and failure modes, and differences in observed suddenness of failure were discussed in this chapter. Evaluations were performed to provide insight into the behaviour of the hooked bars across specimen groups. The statistical analysis of maximum normalized tensile load and displacement at maximum normalized tensile load results was presented. Chapter 5 summarizes this study, presents all conclusions, and provides recommendations for future work.

Chapter 5
Summary, Conclusions, and Recommendations

5.1 Summary

This investigation assessed twenty-four beam-column joint specimens with four different hook configurations, comparing the anchorage capacities of embedded plain and modern deformed bars with 90° and 180° hooks. Six replicates of each configuration were tested under tension to determine whether a statistically significant difference was observable between specimen types. The experimental program was designed to ensure the most accurate possible representation of the anchorage performance of the hooks. The overall specimen dimensions, bar size, concrete cover, lead length, spacing and type of longitudinal and transverse reinforcement, and applied axial load were held constant. Testing of material properties provided assurance that corresponding beam-column joint specimens conformed to CSA and ASTM specifications. A beam-column joint testing mechanism based on the work of Marques and Jirsa (1975) was fabricated in house and tension was applied to the hooked bars until maximum normalized load was achieved. The following sections summarize the results of this investigation and provide recommendations for subsequent work.

5.1.1 Performance of Plain versus Modern Deformed Hooked Bars

The following observations were noted from the testing of beam-column joint specimens with plain versus modern deformed hooks in this investigation. Given the sample size:

- A statistically significant difference at the 95% confidence level was observed between the maximum normalized tensile loads of 90° plain bars, which had a lower load, and the 90° modern deformed hooked bars, which had a higher load.
- A statistically significant difference at the 95% confidence level was observed between the maximum normalized tensile loads of 180° plain bars, which had a lower load, and the 180° modern deformed hooked bars, which had a higher load.

- A statistically significant difference at the 95% confidence level was not observed between the displacements at maximum normalized load for 90° plain and 90° modern deformed hooked bars.
- A statistically significant difference at the 95% confidence level was not observed between the displacements at maximum normalized load for 180° plain and 180° modern deformed hooked bars.
- Plain 90° hooked bars displayed a more extended and gradual decay in slope prior to the achievement of the maximum normalized load than did specimens with 90° modern deformed hooked bars. This is hypothesized to have occurred because bursting pressure exceeded the capacity of the concrete surrounding and between the deformations of the modern deformed bar and ceased to contribute meaningful frictional sliding resistance after the achievement of maximum normalized load; whereas once adhesion was lost, only frictional sliding resistance continued to contribute to bond in specimens containing plain bar, flattening the decay.
- A typical cracking pattern was observed for all beam-column joint specimens containing 90° hooked bars. Cracks originated on the front face of the specimen and radiated outward from the point at which the hooked bars exited the specimen. Transverse cracks projected from the lead length of the embedded bars past the edge of the front face and onto the east and west sides of each specimen. A vertical crack extended along the tail section of the hook on the side faces of the specimen.
- The degree of cracking observed for all beam-column joint specimens containing 90° hooked bars was similar to other studies.
- All beam column joint specimens containing 90° hooks developed cracks on the front face at the same approximate load.
- All specimens containing 90° plain or modern deformed hooked bars had a primary failure mode of side blowout, often accompanied by tail kickout. Three specimens containing 90° plain versus two containing 90° modern deformed bars experienced tail kickout. These findings regarding the incidence of side blowout are subject to influence

by the amount of side concrete cover and presence of transverse reinforcement in the hook region.

- Plain 180° hooked bars displayed a more extended and gradual decay in slope prior to the achievement of the maximum normalized load than did specimens with 180° modern deformed hooked bars. This occurs because concrete surrounding the modern deformed bar ceased to contribute any frictional sliding resistance after the achievement of maximum normalized load whereas once adhesion is lost only frictional sliding resistance continued to contribute to bond in specimens containing plain bar, flattening the decay.
- A typical cracking pattern was observed for all beam-column joint specimens containing 180° hooked bars. Cracks originated on the front face of the specimen and radiated outward from the point at which the hooked bars exited the specimen. Transverse cracks projected from the lead length of the embedded bars past the edge of the front face and onto the east and west sides of each specimen. A vertical crack extended along the tail section of the hook.
- The degree of cracking observed for all beam-column joint specimens containing 180° hooked bars was similar to other studies.
- All beam column joint specimens containing 180° hooks developed cracks on the front face at the same approximate load.
- All specimens containing 180° plain or modern deformed hooked bars had a primary failure mode of front face blowout.
- No specimens showed cracks indicating the presence of a delaminated concrete cone (or trapezoid) between the hooked bars and a reduction in strength at maximum normalized tensile load, indicating no evidence of group effects.

5.1.2 Performance of 90º versus 180º Plain Hooked Bars

The following observations were noted from the testing of beam-column joint specimens with plain hooked bars in this investigation. Given the sample size:

- A statistically significant difference at the 95% confidence level was not observed between the maximum normalized tensile loads of 90° plain bars, which had a lower load, and the 180° plain hooked bars, which had a higher load.
- A statistically significant difference at the 95% confidence level was not observed between the displacements at maximum normalized load of 90° and 180° plain hooked bars.

5.1.3 Performance of 90º versus 180º Modern Deformed Hooked Bars

The following observations were noted from the testing of beam-column joint specimens with modern deformed hooked bars in this investigation. Given the sample size:

- A statistically significant difference at the 95% confidence level was observed between the maximum normalized tensile loads of 90° modern deformed bars, which had a lower load and the 180° modern deformed hooked bars, which had a higher load. This finding differs from conclusions reported by other researchers who did not use replicates. This investigation incorporated replicate specimens in order to determine whether a statistically significant difference was observable between specimen types.
- A statistically significant difference at the 95% confidence level was not observed between the displacements at maximum normalized load for 90° modern deformed and 180° modern deformed hooked bars.

5.2 Impact

This research contributes information to help close the knowledge gap regarding assessments of structures reinforced with plain bar. Engineers-in-training in particular have not been trained in or designed with plain bar. This work provides engineers with knowledge to make more accurate, safe, and cost-effective recommendations in working with these structures.

5.3 Recommendations for Future Work

An extensive replicate-based study of plain hooked bar that investigates the parameters of lead length, bend angle, bend radius of the hooked bars, the presence of confining transverse reinforcement in the hook region, centre-to-centre spacing between the hooked bars, reinforcement diameters, and concrete cover depth is recommended. The value of the recommended future work primarily concerns determination of the sensitivity of performance to variations in the parameters. Investigations of the sensitivity of plain hooked bar to centre-to-centre spacing between the bars will provide additional insight into the incidence of group effects.

Several improvements may be incorporated into future research programs of similar scope. Additional instrumentation such as strain gauges or string pots could be used to quantify hooked bar extension. The use of video cameras recording observations of each specimen face throughout testing would be a recommended improvement to the testing apparatus used in this study. Integrating this video footage with real-time load and displacement data would be essential to meaningfully interpret the footage. Future investigations might use a multi-level modeling approach such as ANOVA to account for autocorrelation of data between the bars in each specimen. This approach would ensure the statistical independence of each data point.

Engineers wishing to develop anchorage capacity with hooked bars beyond what was achieved in this investigation are advised to include transverse reinforcement in the hook region of the column and use increased column depth (Marques and Jirsa 1975).

References

Abrams, D.A. 1913. Tests of Bond between Concrete and Steel. Engineering Experiment Station, University of Illinois, Champaign, IL, USA.

ACI Committee 318. 1963. 318-63: Building Code Requirements for Reinforced Concrete. American Concrete Institute, Farmington Hills, MI, USA.

ACI Committee 318. 1971. 318-71: Building Code Requirements for Reinforced Concrete. American Concrete Institute, Farmington Hills, MI, USA.

ACI Committee 318. 1977. 318-77 Commentary on Building Code Requirements for Reinforced Concrete. American Concrete Institute, Farmington Hills, MI, USA.

ACI Committee 318. 1983. 318-83: Building Code Requirements for Reinforced Concrete. American Concrete Institute, Farmington Hills, MI, USA.

ACI Committee 318. 1986. 1986 Supplement to: 318-83: Building Code Requirements for Reinforced Concrete. American Concrete Institute, Farmington Hills, MI, USA.

ACI Committee 318. 1989. 318-89: Building Code Requirements for Reinforced Concrete and Commentary. American Concrete Institute, Farmington Hills, MI, USA.

ACI Committee 318. 1992. 318-89: Building Code Requirements for Reinforced Concrete and Commentary (Revised 1992). American Concrete Institute, Farmington Hills, MI, USA.

ACI Committee 318. 1995. 318-95: Building Code Requirements for Structural Concrete and Commentary. American Concrete Institute, Farmington Hills, MI, USA.

ACI Committee 318. 1999. 318-99: Building Code Requirements for Reinforced Concrete. American Concrete Institute, Farmington Hills, MI, USA.

ACI Committee 318. 2002. 318-02: Building Code Requirements for Structural Concrete and Commentary. American Concrete Institute, Farmington Hills, MI, USA.

ACI Committee 318. 2005. 318-05: Building Code Requirements for Structural Concrete and Commentary. American Concrete Institute, Farmington Hills, MI, USA.

ACI Committee 318. 2008. 318-08: Building Code Requirements for Structural Concrete and Commentary. American Concrete Institute, Farmington Hills, MI, USA.

ACI Committee 318. 2011. 318-11: Building Code Requirements for Structural Concrete and Commentary. American Concrete Institute, Farmington Hills, MI, USA.

ACI Committee 318. 2014. 318-14: Building Code Requirements for Structural Concrete and Commentary. American Concrete Institute, Farmington Hills, MI, USA.

ACI Committee 318. 2019. 318-19: Building Code Requirements for Structural Concrete and Commentary. American Concrete Institute, Farmington Hills, MI, USA.

ACI Committee 408. 2003. 408R-03: Bond and Development of Straight Reinforcing Bars in Tension. Farmington Hills, MI, USA.

Ajaam, A., O'Reilly, M., Darwin, D., Sperry, J., and Yasso, S. 2018. Anchorage Strength of Closely-Spaced Hooked Bars. ACI Structural Journal, **115**(4): 1143–1152.

ASTM International. 2016. E178-16A: Dealing With Outlying Observations. Annual Book of ASTM Standards. ASTM International, West Conshohocken, PA, USA. p. 11.

ASTM International. 2017a. A354-17: Standard Specification for Quenched and Tempered Alloy Steel Bolts, Studs, and Other Externally Threaded Fasteners. Annual Book of ASTM Standards. ASTM International, West Conshohocken, PA, USA. p. 8.

ASTM International. 2017b. A370-17A: Standard Test Methods and Definitions for Mechanical Testing of Steel Products. Annual Book of ASTM Standards. ASTM International, West Conshohocken, PA, USA. p. 49.

ASTM International. 2018. A615/A615M-18: Standard Specification for Deformed and Plain Carbon-Steel Bars for Concrete. Annual Book of ASTM Standards. ASTM International, West Conshohocken, PA, USA. p. 8.

Beer, F., Johnston, E.R., and DeWolf, J.T. 2005. Mechanics of Materials. 4th edition. McGraw-Hill Education, New York, NY, USA.

Cairns, J., Du, Y., and Law, D. 2006. Residual Bond Strength of Corroded Plain Round Bars. Magazine of Concrete Research, **58**(4): 221–231.

Chun, S., Bae, M.-S., and Lee, B.-S. 2017. Side-Face Blowout Strength of 43 and 57 mm (No. 14 and No. 18) Hooked Bars in Beam-Column Joints. ACI Structural Journal, **114**(5): 1227–1238.

Cleland, D.J., Taylor, S., and Scott, R.H. 2001. Influence of Reinforcement Anchorage on the Bending and Shear Capacity of Bridge Decks. The Structural Engineer, **79**(16): 24–31.

CSA. 1959. CAN/CSA A23.3: Standards for Concrete and Reinforced Concrete. Canadian Standards Association, Ottawa, ON, Canada.

CSA. 1970. CAN/CSA A23.3: Code for Design of Plain and Reinforced Concrete Structures. Canadian Standards Association, Rexdale, Ontario, Canada.

CSA. 1984. CAN/CSA A23.3: Design of Concrete Structures for Buildings. Canadian Standards Association, Toronto, ON, Canada.

CSA. 1994. CAN/CSA A23.3: Design of Concrete Structures. Canadian Standards Association, Ottawa, ON, Canada.

CSA. 2004. CAN/CSA A23.3: Design of Concrete Structures. Canadian Standards Association, Toronto, ON, Canada.

CSA. 2014B. CAN/CSA A23.3: Design of Concrete Structures. Canadian Standards Association, Mississauga, Ontario, Canada.

CSA. 2006. CAN/CSA S6-06: Canadian Highway Bridge Design Code. Canadian Standards Association, Mississauga, Ontario, Canada.

CSA. 2014A. CAN/CSA A23.1-14/A23.2-14: Concrete Materials and Methods of Concrete Construction / Test Methods and Standard Practices for Concrete. Canadian Standards Association, Mississauga, Ontario, Canada.

CSA. 2014C. G30.18-09 (R2014): Carbon Steel Bars for Concrete Reinforcement. Canadian Standards Association, Mississauga, Ontario, Canada.

CSA. 2018. CAN/CSA G40.20-13/G40.21-13 (R2018): General Requirements for Rolled or Welded Structural Quality Steel / Structural Quality Steel. Canadian Standards Association, Mississauga, Ontario, Canada.

Darwin, D., McCabe, S.L., Emmanuel, K., and Schoenekase, S.P. 1992. Development Length Criteria : Bars Not Confined by Transverse Reinforcement. ACI Structural Journal, **89**(6): 709–720.

Ellis, R.M. 1988. Behavior and Design of Reinforced Concrete Ice-Resisting Walls. University of Alberta.

Feldman, L.R., and Bartlett, F.M. 2005. Bond Strength Variability in Pullout Specimens with Plain Reinforcement. ACI Structural Journal, **102**(6): 860–867.

Fenwick, R.C., and Irvine, H.M. 1977. Reinforced Concrete Beam-Column Joints for Seismic Loading. Bulletin of the New Zealand National Society for Erthquake Engineering, **10**(3): 121–128.

Hassan, M.N., and Feldman, L.R. 2012. Behavior of Lap-Spliced Plain Steel Bars. ACI Structural Journal, **109**: 235–244.

Hwang, H.-J., Park, H.-G., and Yi, W.-J. 2017. Development Length of Standard Hooked Bar Based on Non-Uniform Bond Stress Distribution. ACI Structural Journal, **114**(6): 1637–1648.

Interface Inc. 2018. 1200 Standard Load Cell (US & Metric). Interface Inc., Scottsdale, Arizona, USA.

Johnson, L.A., and Jirsa, J.O. 1981. The Influence of Short Embedment and Close Spacing on the Strength of Hooked Bar Anchorages. PMFSEL Report No.81-2. The University of Texas at Austin, Austin, TX, USA.

MacGregor, J.G. 1992. Reinforced Concrete Mechanics & Design. 2nd edition. W.J. Hall. Prentice Hall, Englewood Cliffs.

MacGregor, J.G., and Bartlett, F.M. 2000. Reinforced Concrete Mechanics and Design. 1st edition. Prentice Hall, Scarborough, Ontario, Canada.

MacGregor, J.G., and Wight, J.K. 2012. Reinforced Concrete Mechanics & Design. 6th edition. H. Stark. Pearson, Upper Saddle River, NL, USA.

MacLean, M.S., and Feldman, L.R. 2014. Effects of Casting Position and Bar Shape on Bond of Plain Bars. ACI Structural Journal, **111**(2): 323–330.

Marques, J., and Jirsa, J. 1975. A Study of Hooked Bar Anchorage in Beam-Column Joints. ACI Structural Journal, **18**(72): 198–209.

McCormac, J.C., and Brown, R.H. 2015. Design of Reinforced Concrete. 10th edition. John Wiley & Sons, Inc., Hoboken, NJ ,USA.

McEvily, A., and Kasivitamnuay, J. 2013. Metal Failures: Mechanisms, Analysis, Prevention. 2nd edition. Wiley-Interscience, New York, NY, USA.

Meinheit, D.F., and Felder, A.L. 2014. Vintage Steel Reinforcement in Concrete Structures. 1st edition. Concrete Reinforcing Steel Institute, Schaumburg, IL, USA.

Micro-Epsilon. 2010. OptoNCDT: Laser Displacement Sensors (Triangulation) Manual. MICRO-EPSILON Headquarters, Ortenburg, Germany.

Mindess, S., and Young, F.J. 1981. Concrete. Prentice Hall, Englewood Cliffs, NJ, USA.

Minor, J., and Jirsa, J. 1975. Behavior of Bent Bar Anchorages. ACI Journal Proceedings, **72**(4): 141–149.

Mitutoyo. 2006. SJ-201 Surface Roughness Tester User's Manual Number 99MBB0796A. Mitutoyo Corporation, Kanagawa, Japan.

Mylrea, T.D. 1928. The Carrying Capacity of Semicircular Hooks. ACI Journal Proceedings, **24**(2): 240–263. Farmington Hills, MI, USA.

Nadim Hassoun, M., and Al-Manaseer, A. 2008. Structural Concrete Theory and Design. 4th edition. John Wiley & Sons, Inc., Hoboken, NJ ,USA.

Nawy, E.G. 2003. Reinforced Concrete: A Fundamental Approach. 5th edition. W.J. Hall. Prentice Hall, Upper Saddle River, NL, USA.

Nilson, A.H., Darwin, D., and Dolan, C.W. 2004. Design of Concrete Structures. 13th edition. McGraw-Hill Education, New York, NY, USA.

Omega Engineering Canada. (n.d.). Bolt Load Cells Large I.D. 2.00-3.13 Inch. Available from https://www.omega.ca/en/sensors-and-sensing-equipment/load-and-force/load-cells/p/LC8400 [accessed 4 April 2019].

Orangun, C.O., Jirsa, J.O., and Breen, J.E. 1977. A Reevaulation of Test Data on Development Length and Splices. ACI Journal Proceedings, **74**(3): 114–122.

Park, R., and Paulay, T. 1975. Reinforced Concrete Structures. 1st edition. John Wiley & Sons, Inc., New York, NY, USA.

Peckover, J., and Darwin, D. 2013. Anchorage of High-Strength Reinforcing Bars With Standard Hooks–Initial Tests. Lawrence, KS, USA.

Pinc, R., Watkins, M., and Jirsa, J.O. 1977. The Strength of the Hooked Bar Anchorages in Beam-Column Joints. CESRL Report No. 77-3. The University of Texas at Austin, Austin, TX, USA.

Poudyal, U., and Feldman, L.R. 2018. Evaluating Historical Flexural Members Reinforced with Ransome Bars. ACI Structural Journal, **115**(5): 1443–1451.

Rao, N.R.N., Lohrmann, M., and Tall, L. 1966. Effect of Strain Rate on the Yield Stress of Structural Steels. ASTM Journal of Materials, **1**(1): 1–49.

Soroushian, P., Obaseki, K., Nagi, M., and Rojas, M.C. 1988. Pullout Behavior of Hooked Bars in Exterior Beam-Column Connections. ACI Structural Journal, **85**(3): 269–276.

Sperry, J., Darwin, D., O'Reilly, M., Lepage, A., Lequesne, R.D., Matamoros, A., Feldman, L.R., Yasso, S., Searle, N., DeRubeis, M., and Ajaam, A. 2018. Conventional and High-Strength Hooked Bars: Detailing Effects. ACI Structural Journal, **115**(1): 247–257.

Sperry, J., Yasso, S., Searle, N., DeRubeis, M., Darwin, D., O'Reilly, M., Matamoros, A., Feldman, L.R., Lepage, A., Lequesne, R.D., and Ajaam, A. 2017a. Conventional and High-Strength Hooked Bars-Part 1: Anchorage Tests. ACI Structural Journal, **114**(1): 255–265.

Sperry, J., Yasso, S., Searle, N., DeRubeis, M., Darwin, D., O'Reilly, M., Matamoros, A., Feldman, L.R., Lepage, A., Lequesne, R.D., and Ajaam, A. 2017b. Conventional and High-Strength Hooked Bars-Part 2: Data Analysis. ACI Structural Journal, **114**(1): 255–265.

Tillman, K. (n.d.). All Thread Rod. Available from https://www.allthreadrod.com/grades/ [accessed 1 May 2019].

Walpole, R.E., Myers, R.H., Myers, S.L., and Ye, K. 2007. Probability & Statistics for Engineers & Scientists. 8th edition. Pearson, Upper Saddle River, NL, USA.

Appendix A: Coupler Design

Figure A.1 shows the detailed drawing used to manufacture the couplers used in this experimental program. The couplers were used to transfer applied tensile force from the hydraulic jacks to the reinforcement containing hooks. The couplers held the manufactured wedges and connected to the high strength threaded reinforcement as it was passed through the hydraulic jacks, as discussed in Section 3.7.

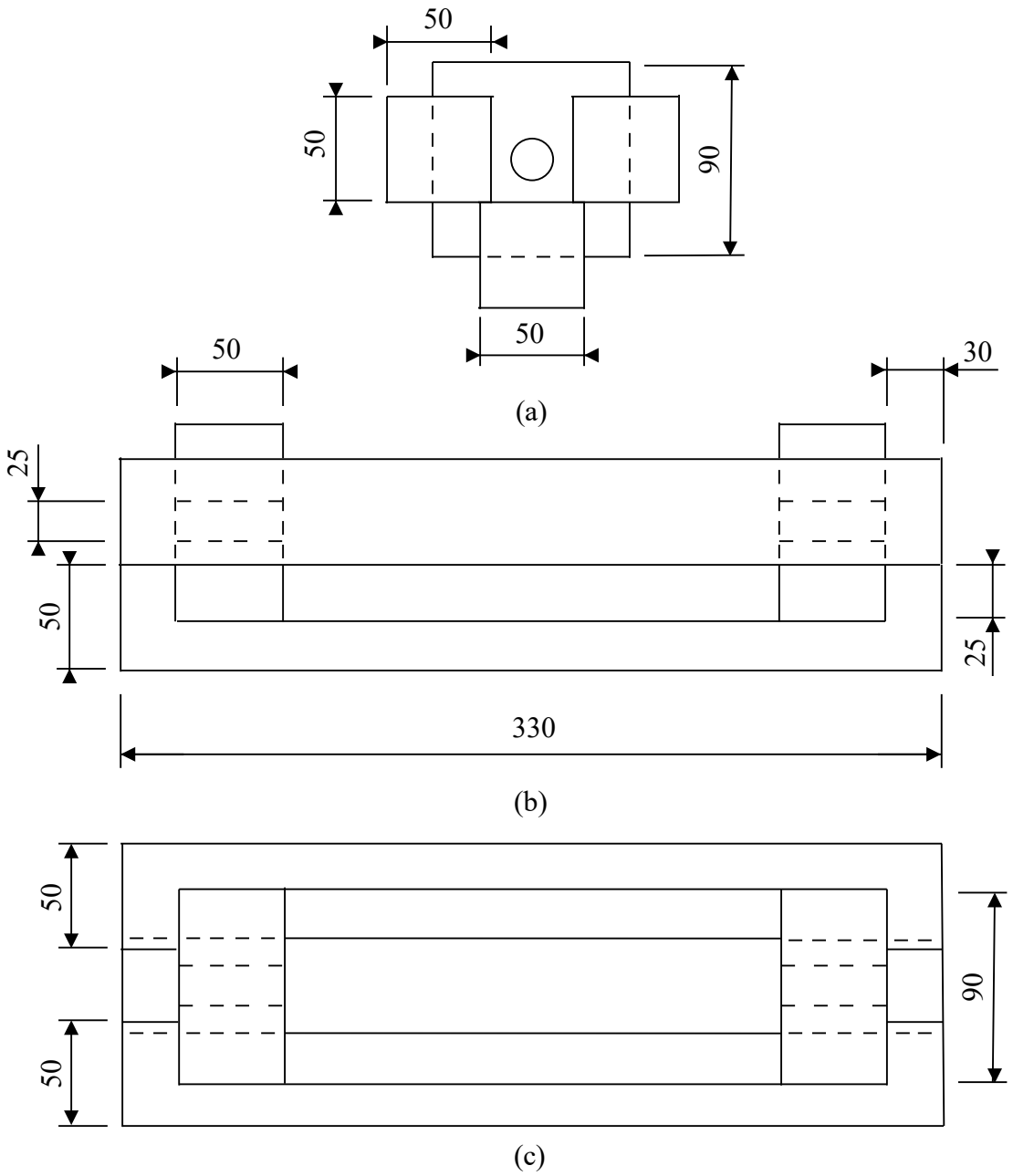

All units in mm

Figure A.1 Coupler design: (a) side view, (b) front view, and (c) elevation view

Appendix B: Plain Reinforcement Test Specimen Design

Three tensile testing coupons were machined from plain reinforcement produced from the same heat batch, as discussed in Section 3.8.3. Figure B.1 shows the detailed drawing for the machined specimens. The coupons were machined to comply with the ASTM Standard A370 and tests were conducted at a load rate of 0.25 MPa/sec to comply with CSA A23.2-14 specifications. The testing process of these specimens is outlined in Section 3.8.3.

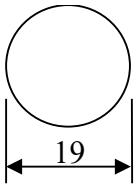

(a)

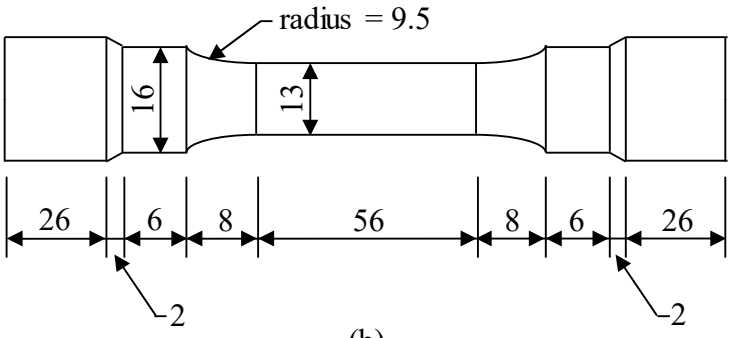

(b)

All units in mm

Figure B.1 Plain reinforcement test specimen design: (a) side view and (b) front view

Appendix C: Companion Cylinder Compressive Stress versus Strain Diagrams at Seven Days

Four concrete companion cylinders were cast alongside each beam-column joint specimen. One companion cylinder was taken from each batch and tested for compressive strength at seven days to ensure proper concrete compressive strength gain. Figures C.1 through C.3 show the stress versus strain behaviours of these individual companion cylinders and present the concrete compressive strength, $f'_{c,7\text{-}day}$, and modulus of elasticity, E_c, for each. The modulus of elasticity was calculated using the average slope in the elastic range of the stress versus strain diagram after the slope had stabilized. Data for cylinder A from phase two is not available because the data did not save after completion of the test.

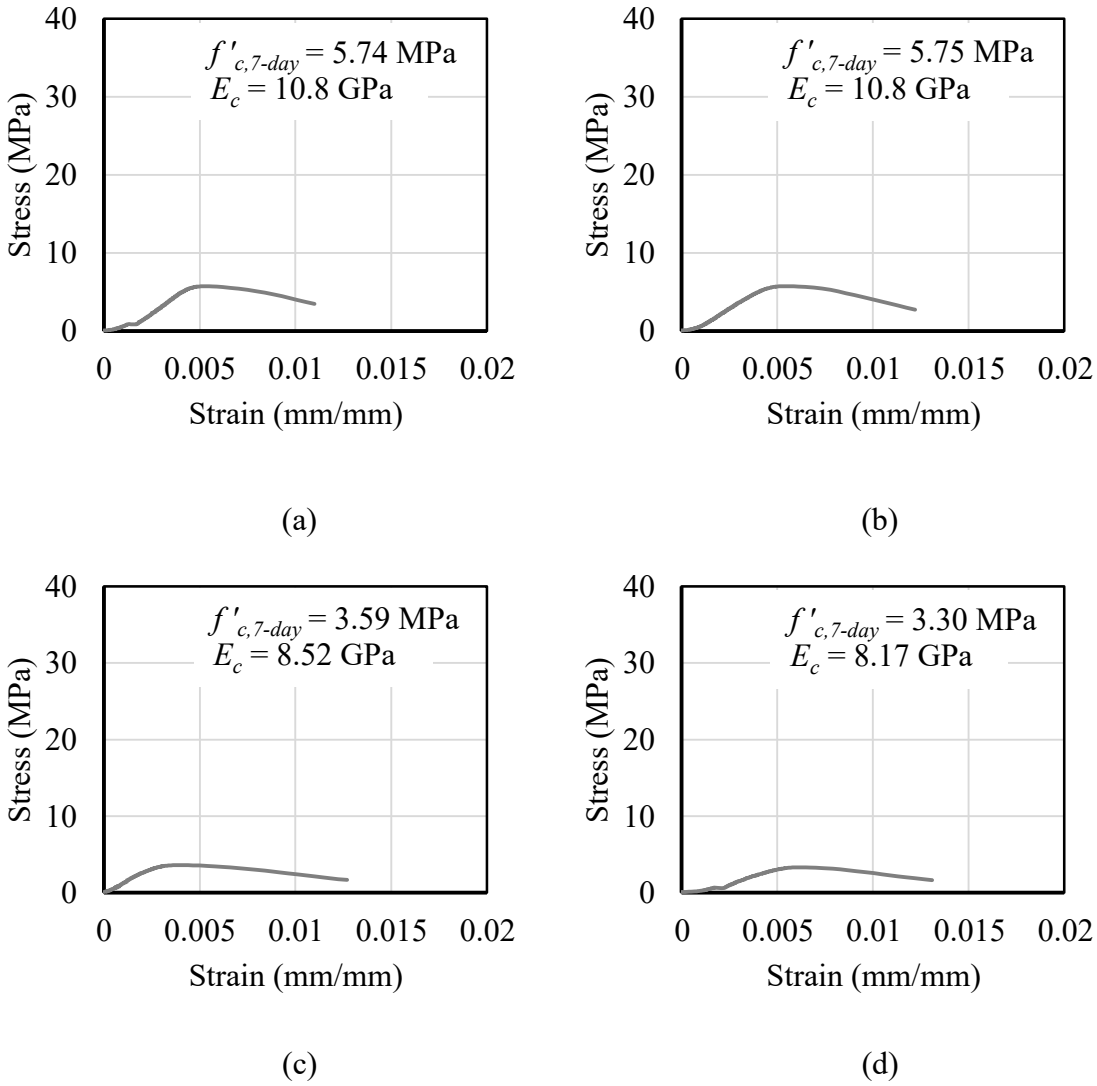

Figure C.1: Concrete compressive companion cylinders at seven days - phase one: (a) cylinder A, (b) cylinder B, (c) cylinder C, and (d) cylinder D

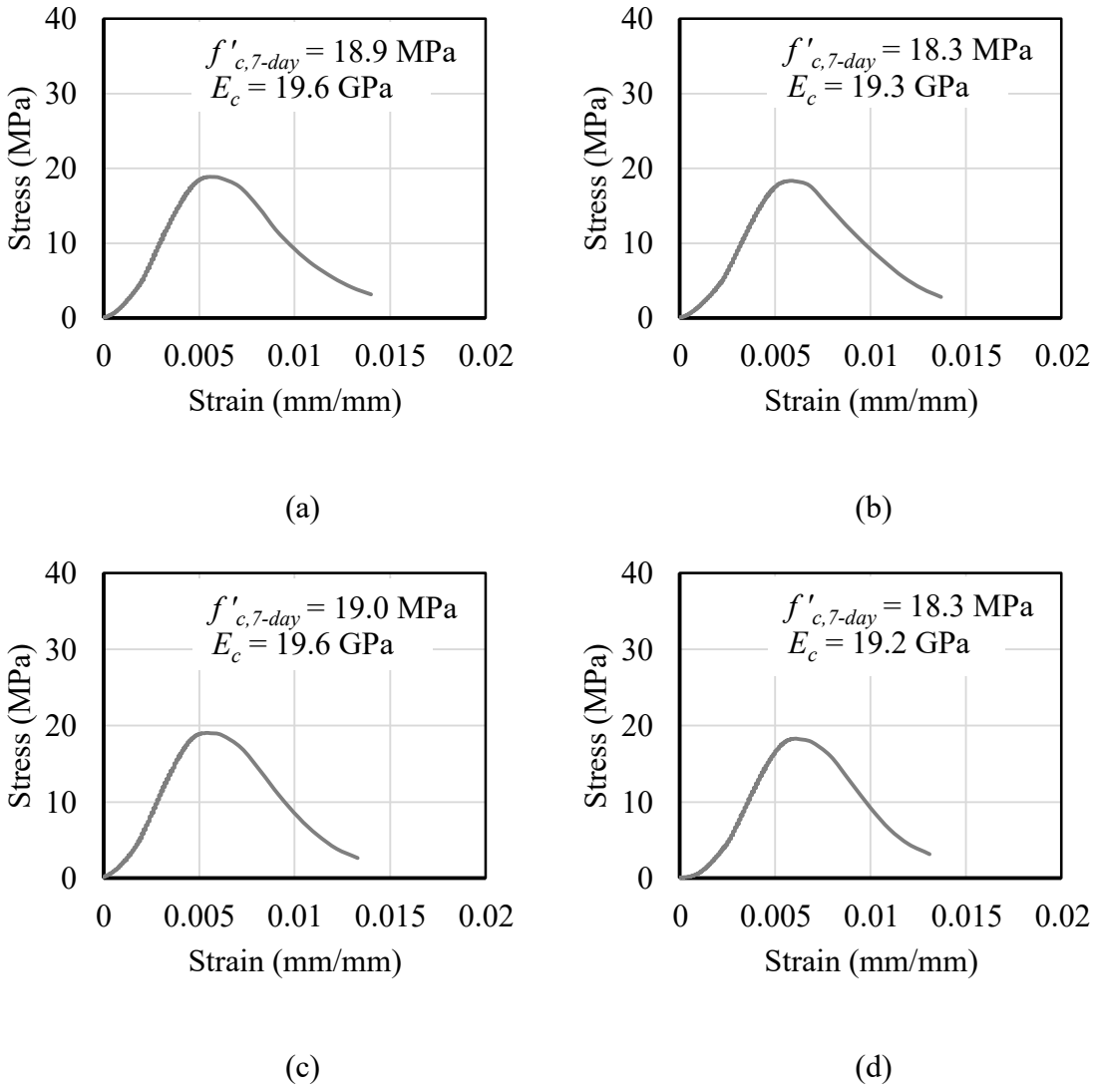

Figure C.2: Concrete compressive companion cylinders at seven days - phase two: (a) cylinder B, (b) cylinder C, (c) cylinder D, and (d) cylinder E

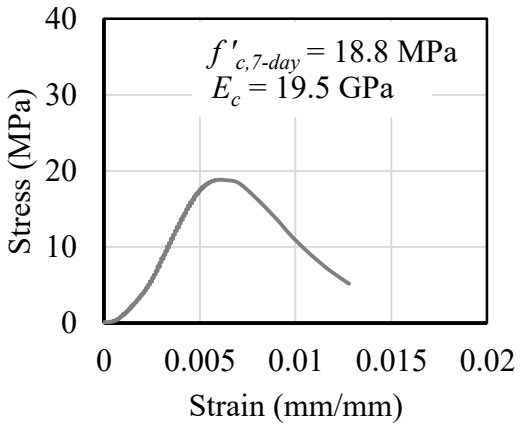

(e)

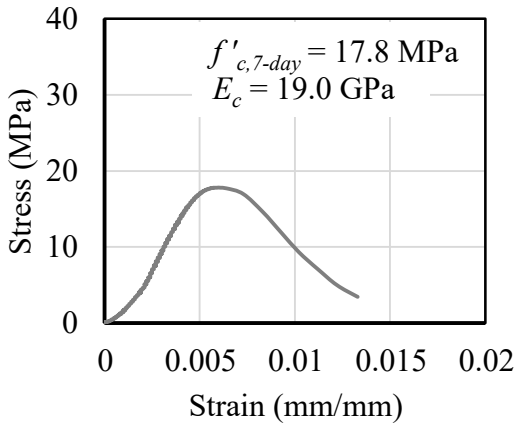

(f)

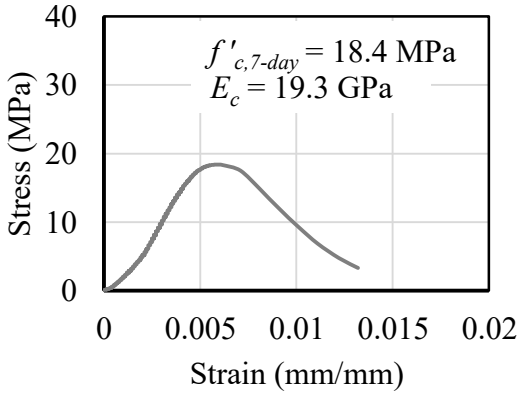

(g)

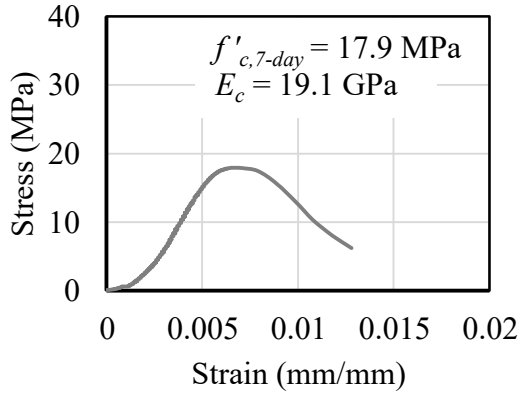

(h)

Figure C.2 continued: Concrete compressive companion cylinders at seven days - phase two: (e) cylinder F, (f) cylinder G, (g) cylinder H, and (h) cylinder I

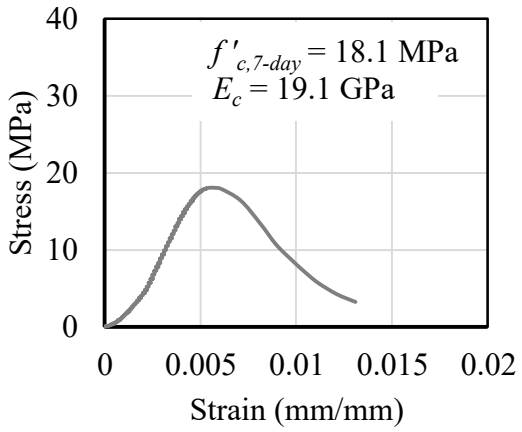

(i)

Figure C.2 continued: Concrete compressive companion cylinder at seven days - phase two: (i) cylinder J

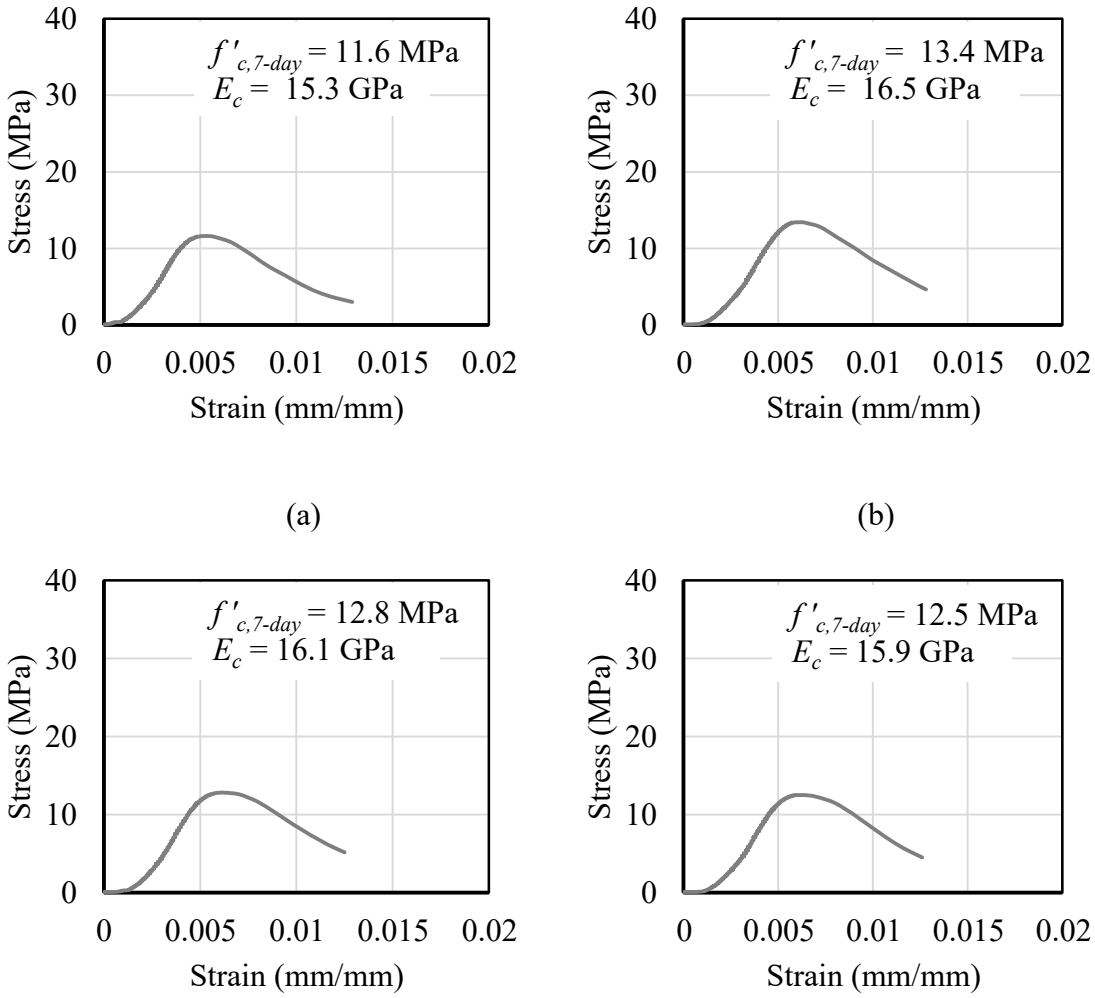

Figure C.3: Concrete compressive companion cylinders at seven days - phase three: (a) cylinder A, (b) cylinder B, (c) cylinder C, and (d) cylinder D

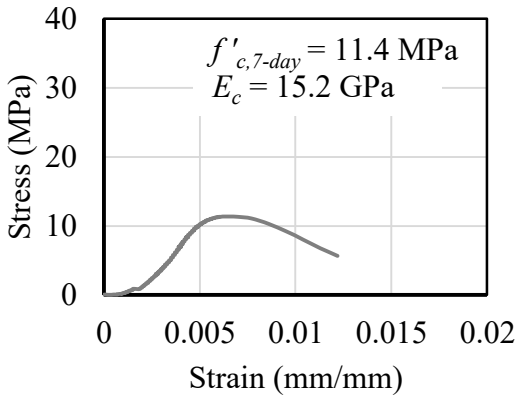

(e)

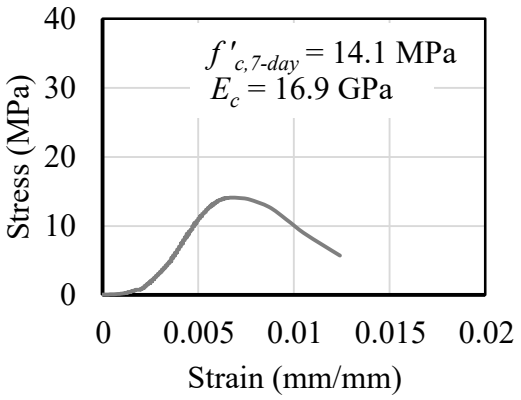

(f)

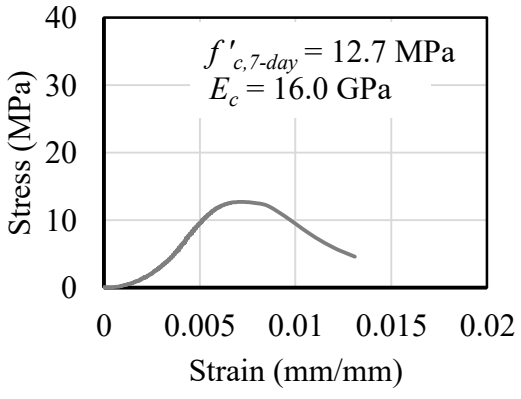

(g)

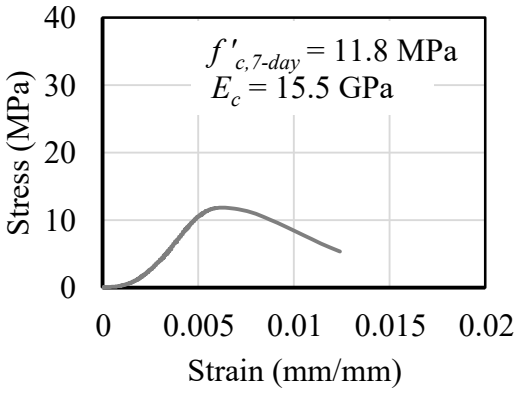

(h)

Figure C.3 continued: Concrete compressive companion cylinders at seven days - phase three: (e) cylinder E, (f) cylinder F, (g) cylinder G, and (h) cylinder H

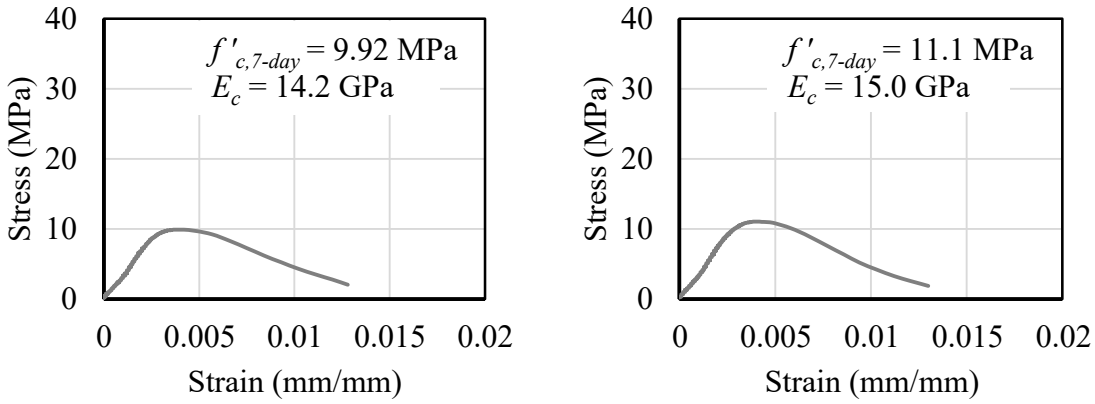

(i) (j)

Figure C.3 continued: Concrete compressive companion cylinders at seven days - phase three: (i) cylinder I and (j) cylinder J

Appendix D: Companion Cylinder Compressive Stress versus Strain Diagrams at the Time of Beam-Column Joint Testing

Each beam-column joint specimen was a minimum of 28 days old at the time of testing. Three concrete companion cylinders were tested for compressive strength alongside each beam-column joint specimen, as outlined in Section 3.8.1 on the day of testing. Figures D.1 to D.24 show the stress versus strain behaviours of individual companion cylinders and present the concrete compressive strength, f'_c, and modulus of elasticity, E_c, for each. The modulus of elasticity was calculated using the average slope in the elastic range of the stress versus strain diagram after the slope had stabilized. Data from one cylinder (B) which is associated with beam-column joint specimen P6-90 failed to save.

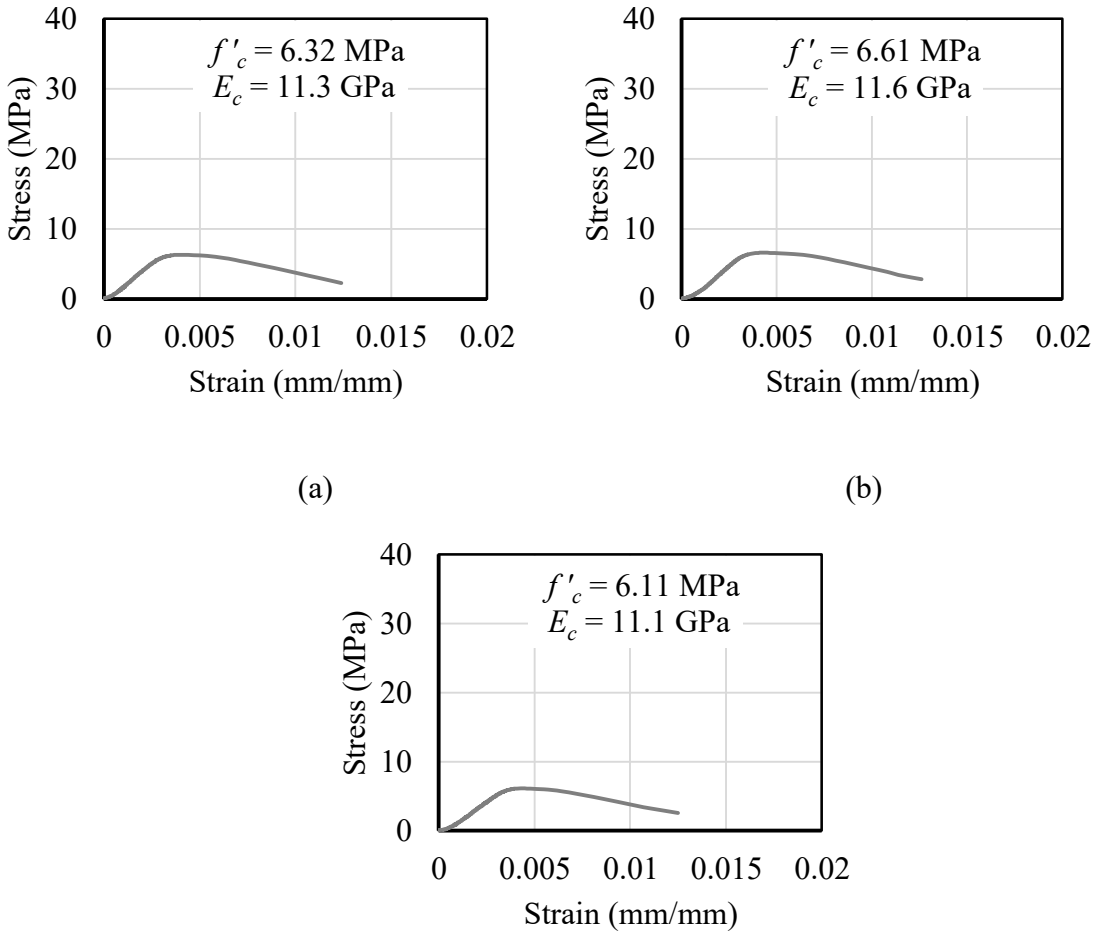

Figure D.1: Concrete compressive companion cylinders for beam-column joint specimen P1-90: (a) cylinder A, (b) cylinder B, and (c) cylinder C

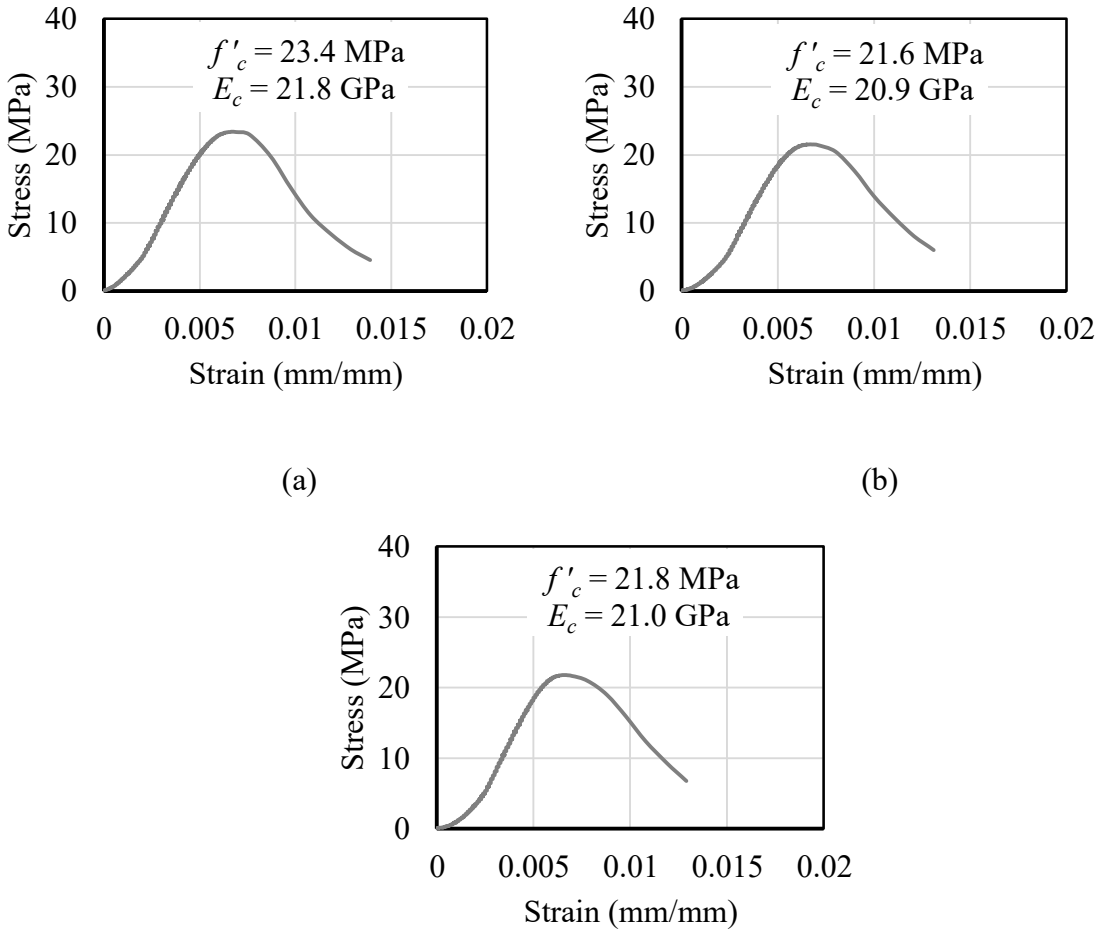

Figure D.2: Concrete compressive companion cylinders for beam-column joint specimen P2-90: (a) cylinder A, (b) cylinder B, and (c) cylinder C

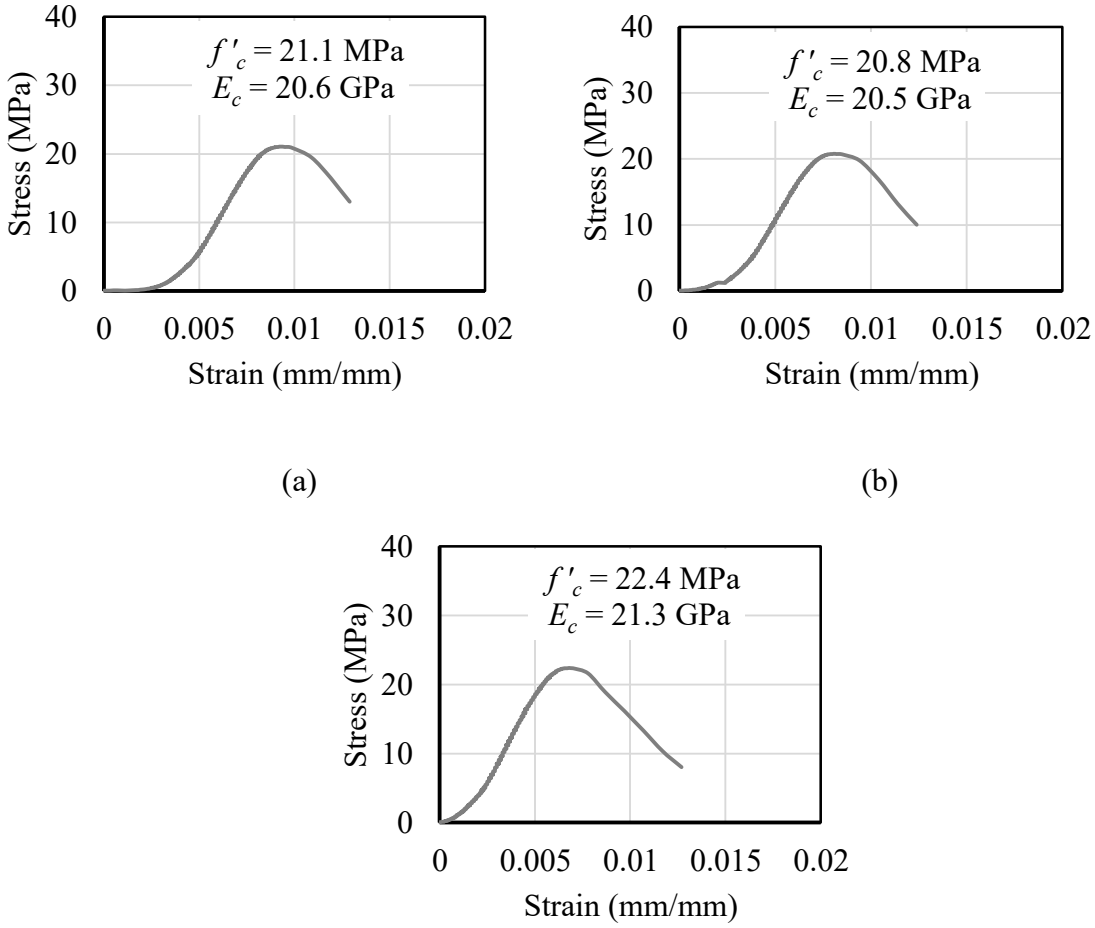

Figure D.3: Concrete compressive companion cylinders for beam-column joint specimen P3-90: (a) cylinder A, (b) cylinder B, and (c) cylinder C

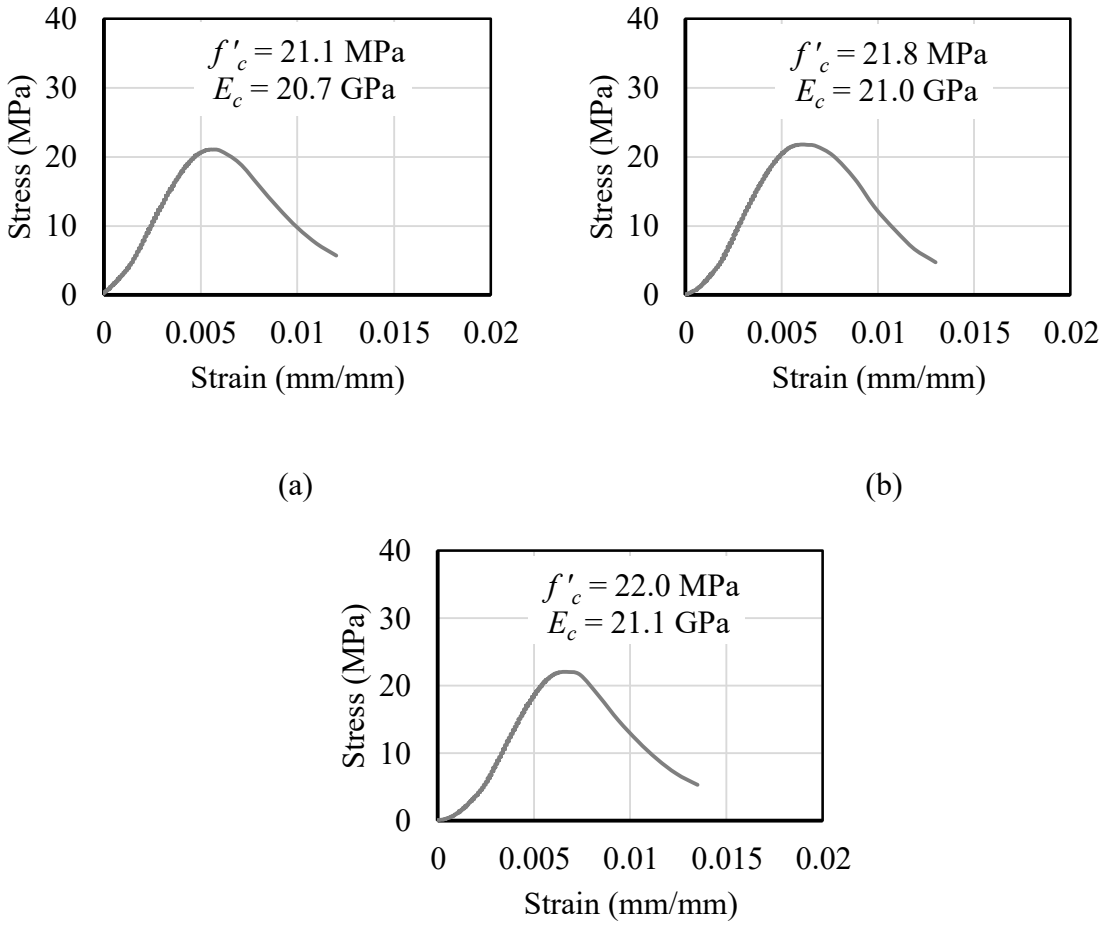

Figure D.4: Concrete compressive companion cylinders for beam-column joint specimen P4-90: (a) cylinder A, (b) cylinder B, and (c) cylinder C

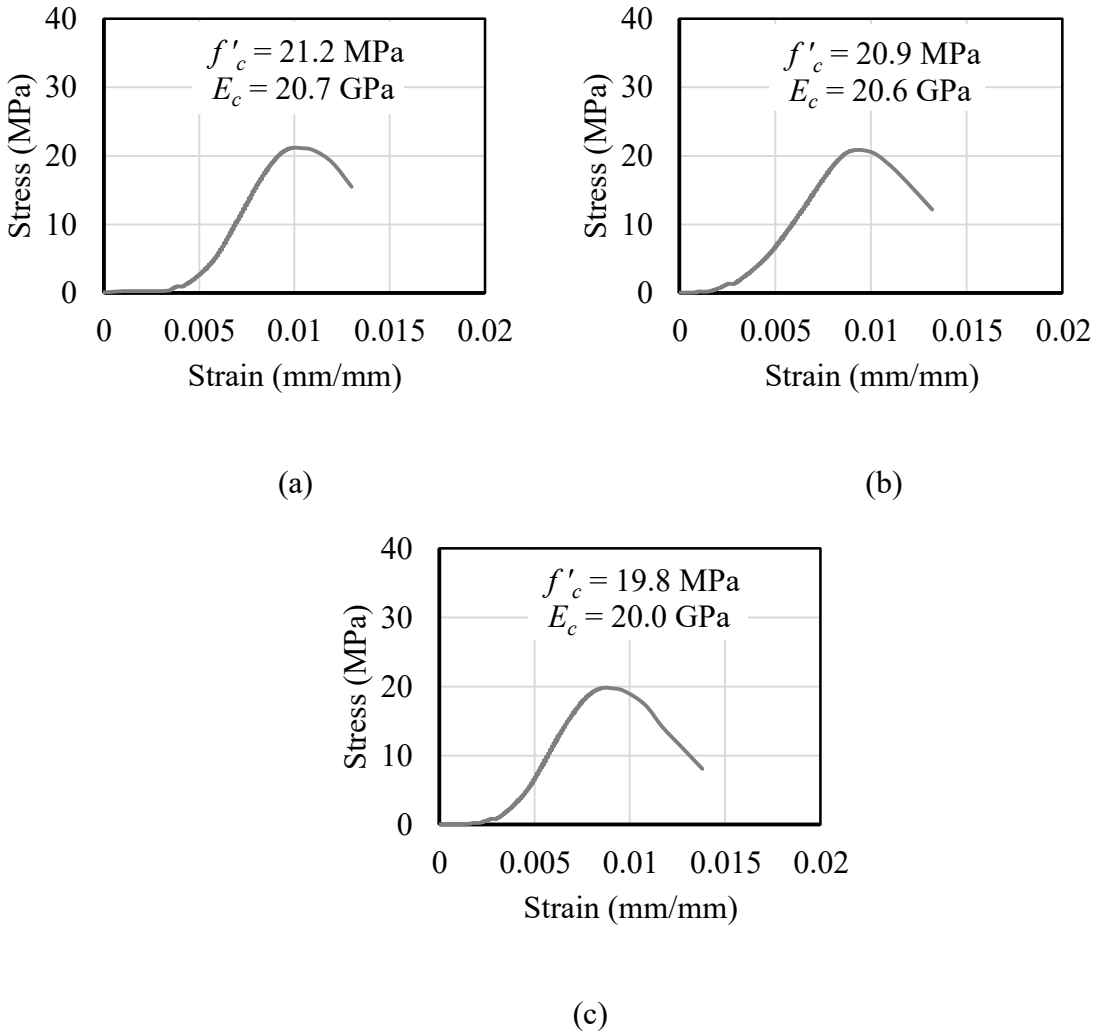

Figure D.5: Concrete compressive companion cylinders for beam-column joint specimen P5-90: (a) cylinder A, (b) cylinder B, and (c) cylinder C

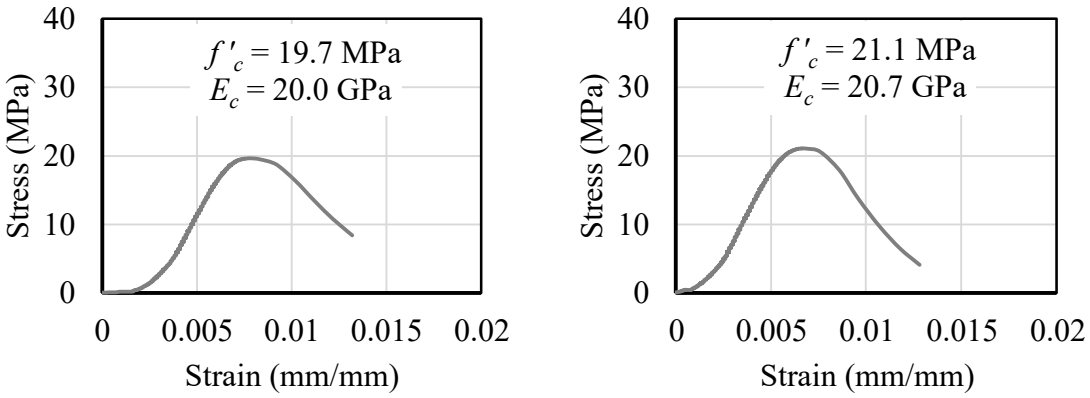

(a) (b)

Figure D.6: Concrete compressive companion cylinders for beam-column joint specimen P6-90: (a) cylinder A, and (b) cylinder C

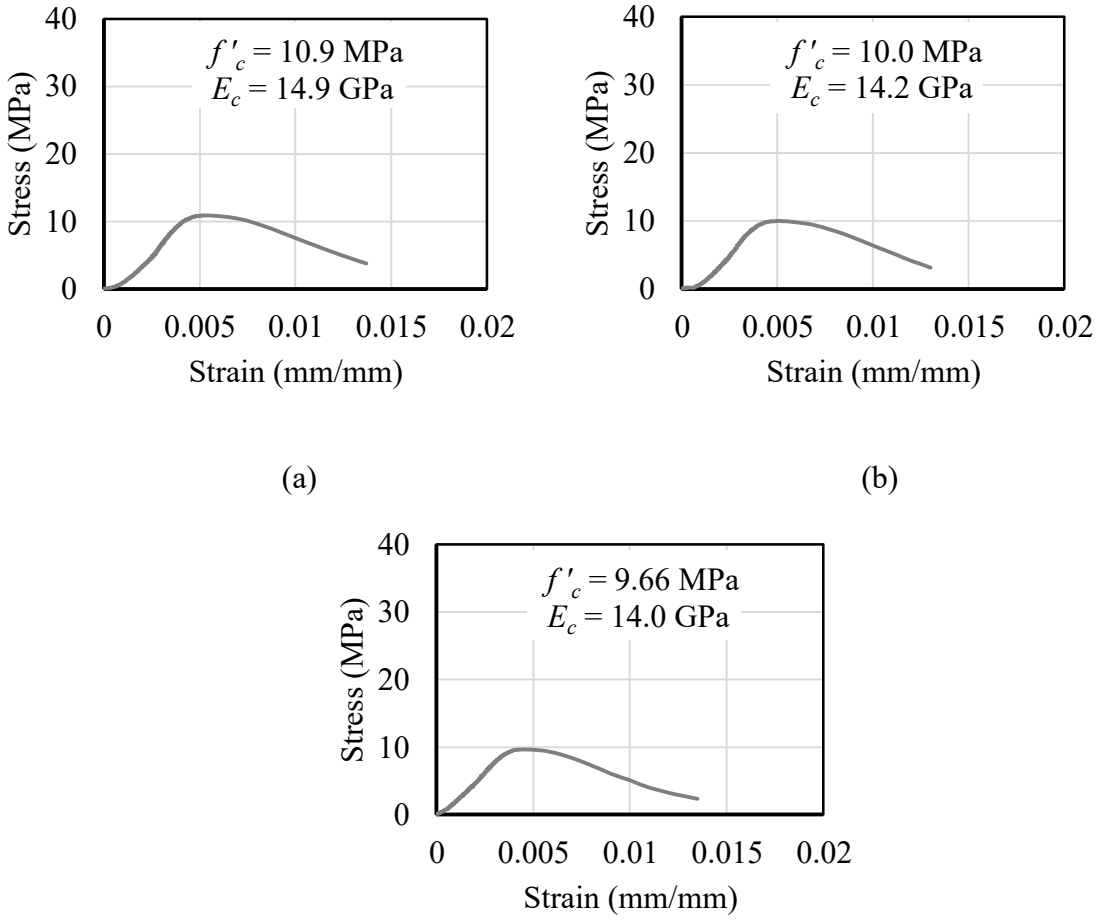

Figure D.7: Concrete compressive companion cylinders for beam-column joint specimen MD1-90: (a) cylinder A, (b) cylinder B, and (c) cylinder C

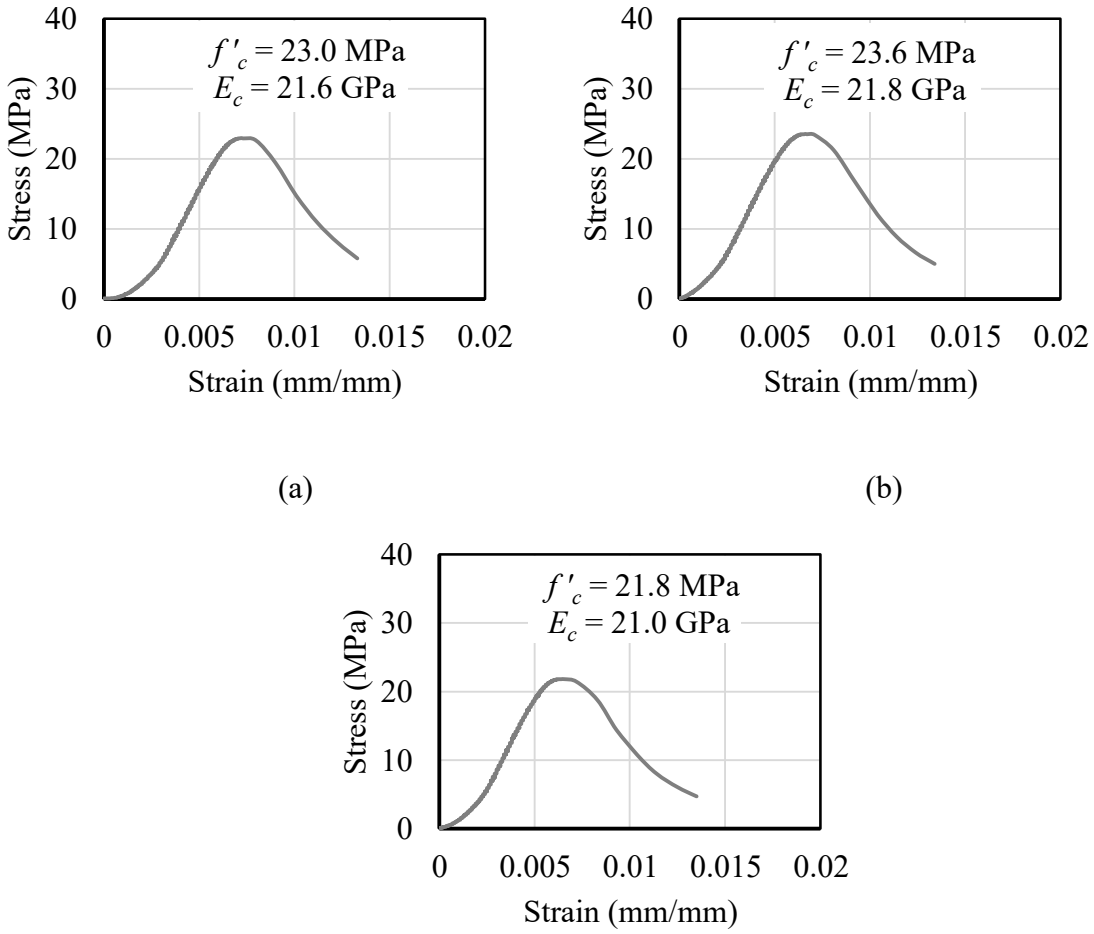

Figure D.8: Concrete compressive companion cylinders for beam-column joint specimen MD2-90: (a) cylinder A, (b) cylinder B, and (c) cylinder C

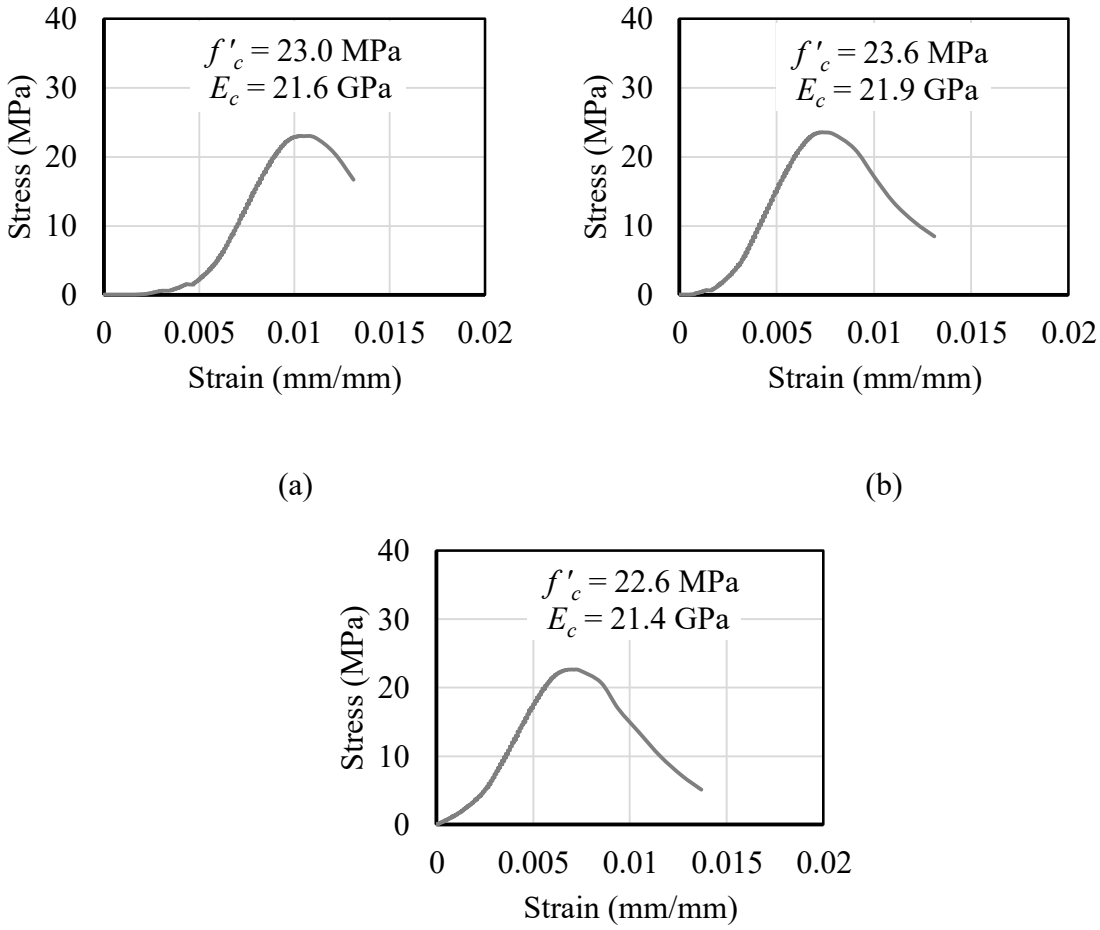

Figure D.9: Concrete compressive companion cylinders for beam-column joint specimen MD3-90: (a) cylinder A, (b) cylinder B, and (c) cylinder C

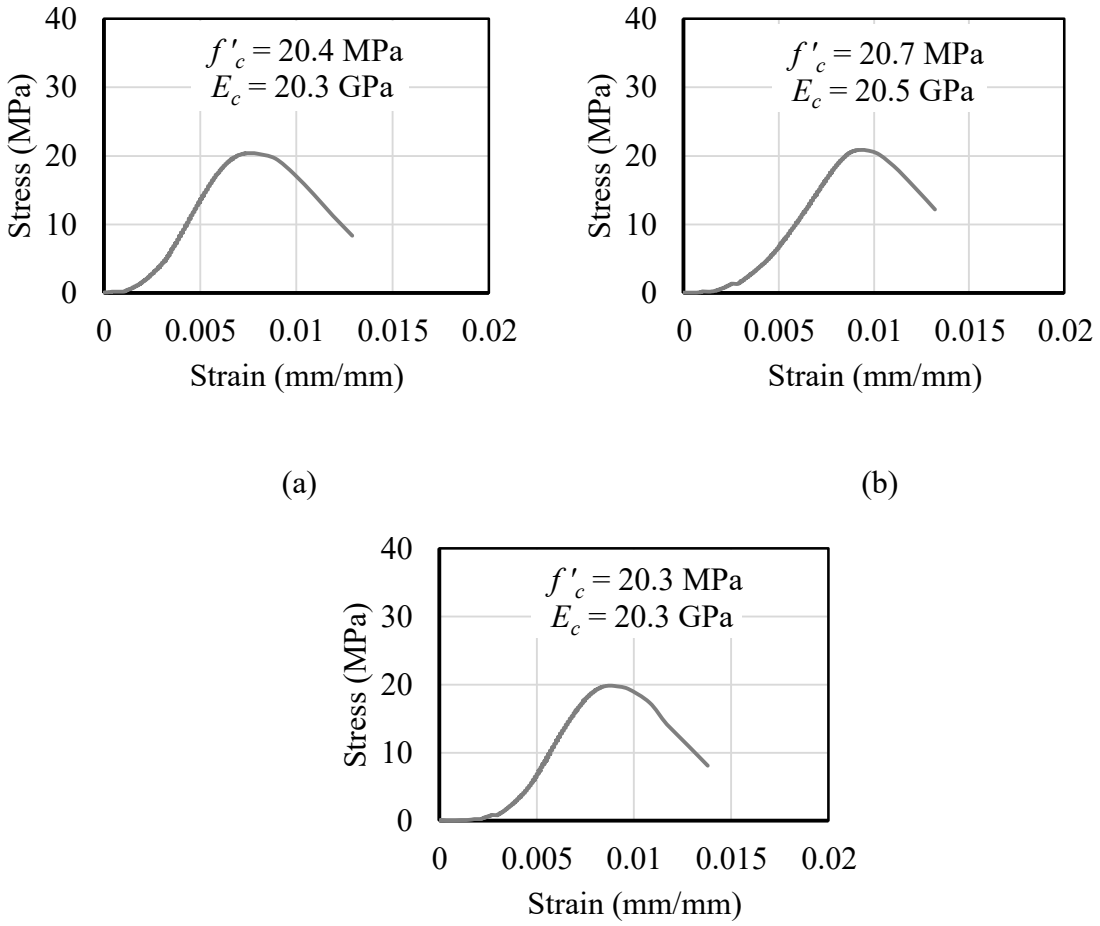

Figure D.10: Concrete compressive companion cylinders for beam-column joint specimen MD4-90: (a) cylinder A, (b) cylinder B, and (c) cylinder C

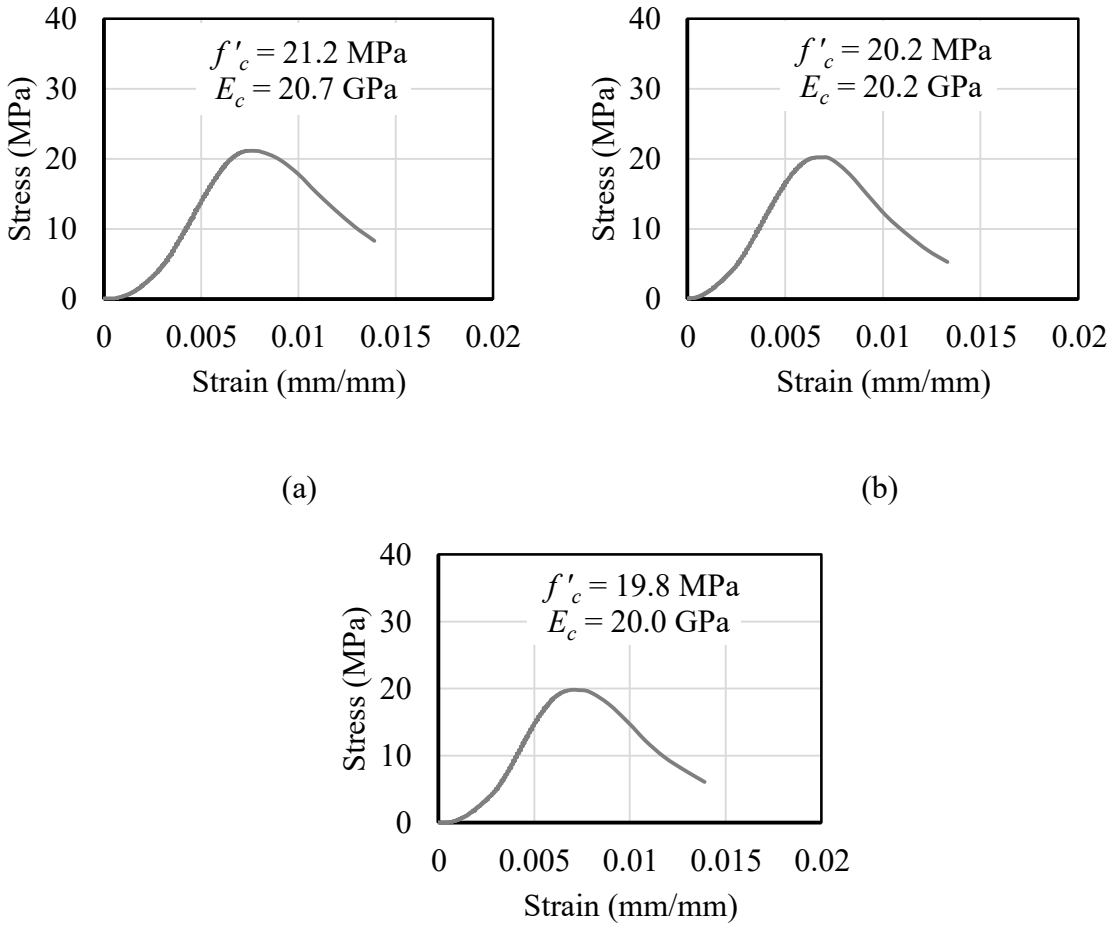

Figure D.11: Concrete compressive companion cylinders for beam-column joint specimen MD5-90: (a) cylinder A, (b) cylinder B, and (c) cylinder C

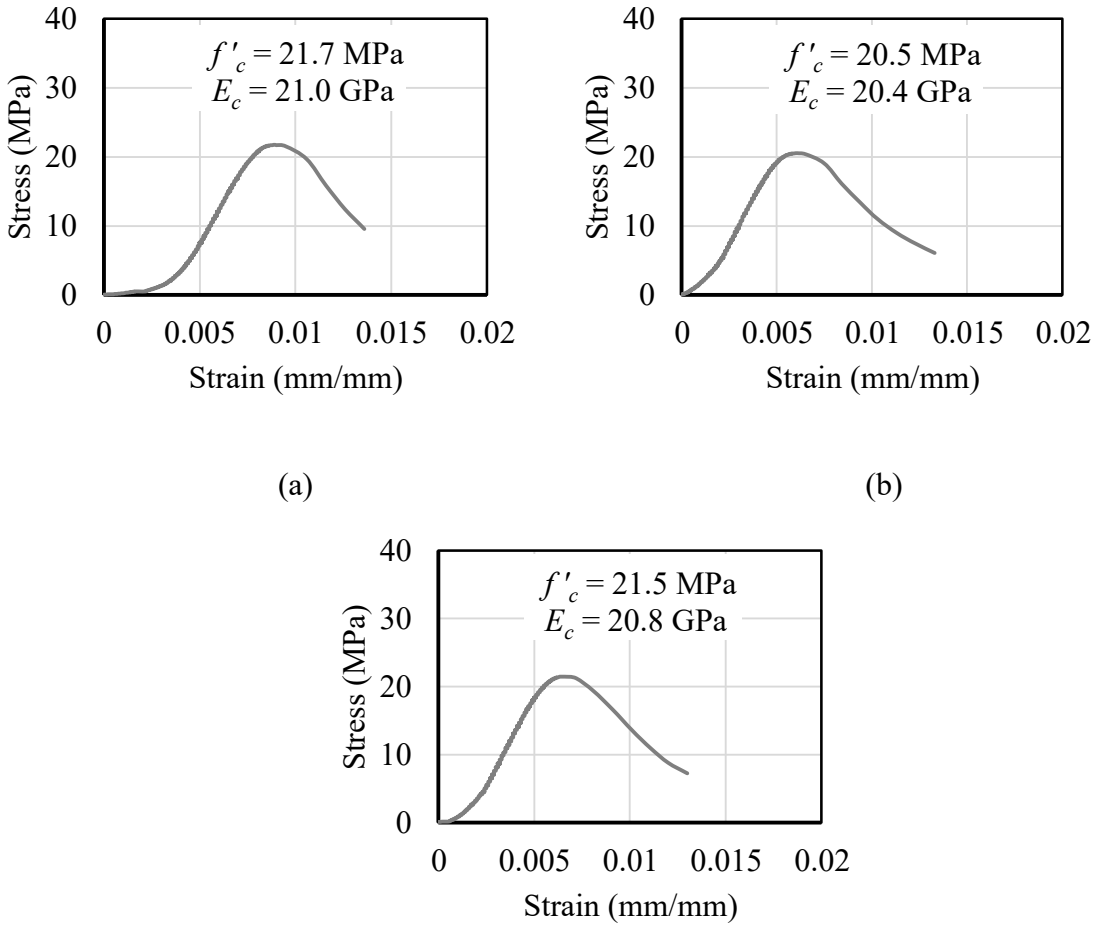

Figure D.12: Concrete compressive companion cylinders for beam-column joint specimen MD6-90: (a) cylinder A, (b) cylinder B, and (c) cylinder C

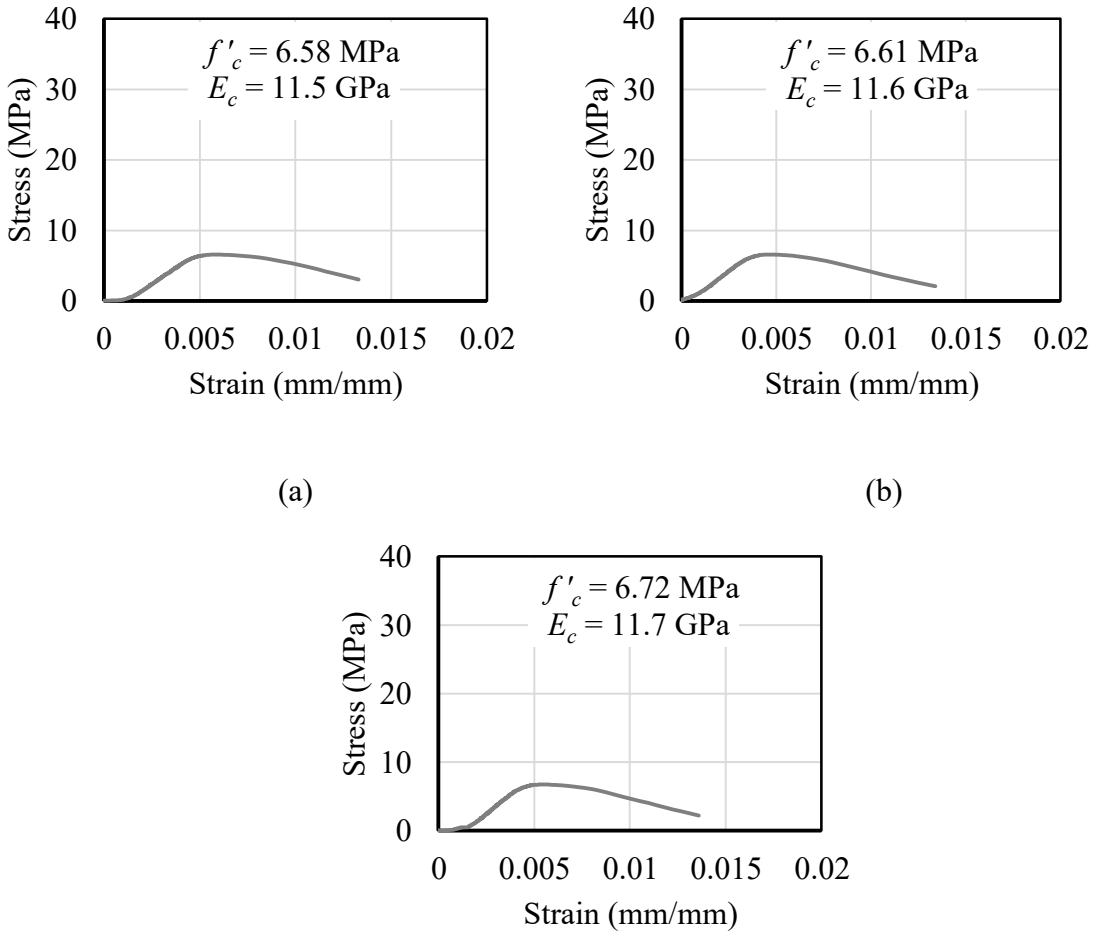

Figure D.13: Concrete compressive companion cylinders for beam-column joint specimen P1-180: (a) cylinder A, (b) cylinder B, and (c) cylinder C

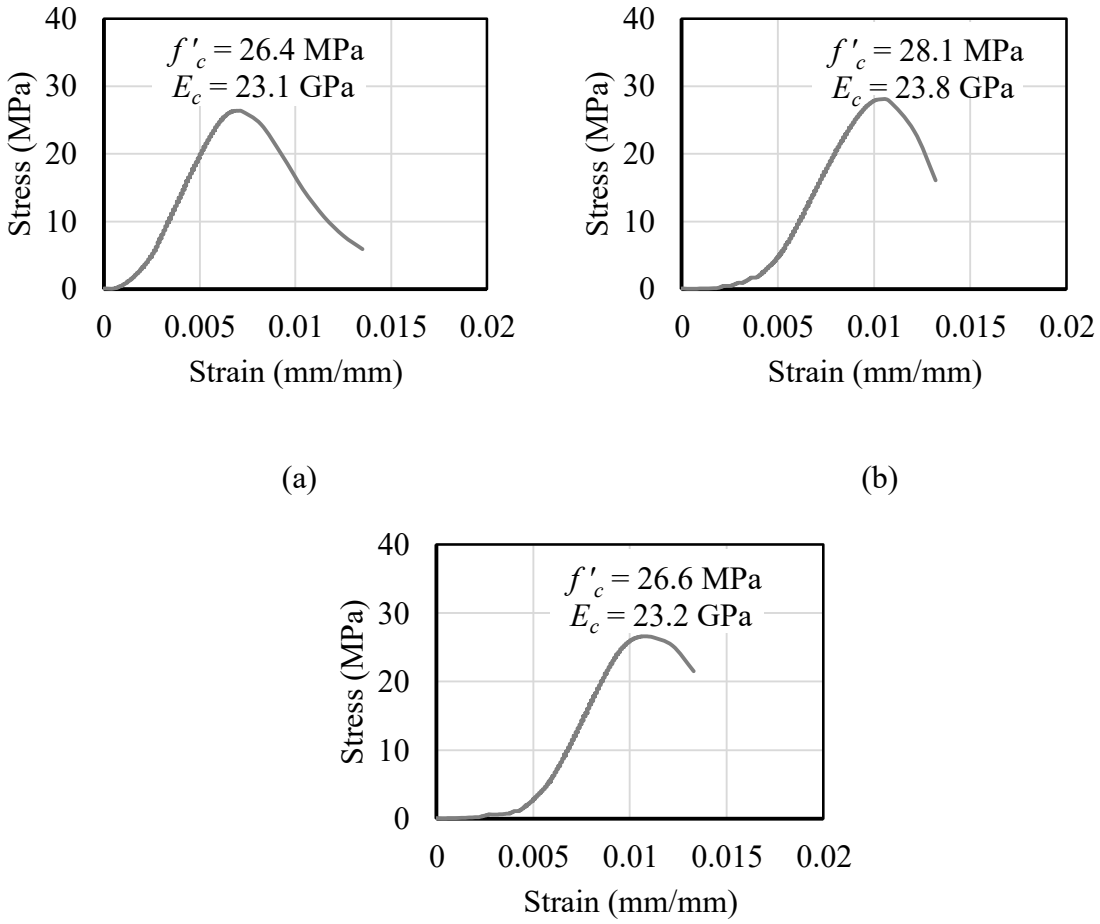

Figure D.14: Concrete compressive companion cylinders for beam-column joint specimen P2-180: (a) cylinder A, (b) cylinder B, and (c) cylinder C

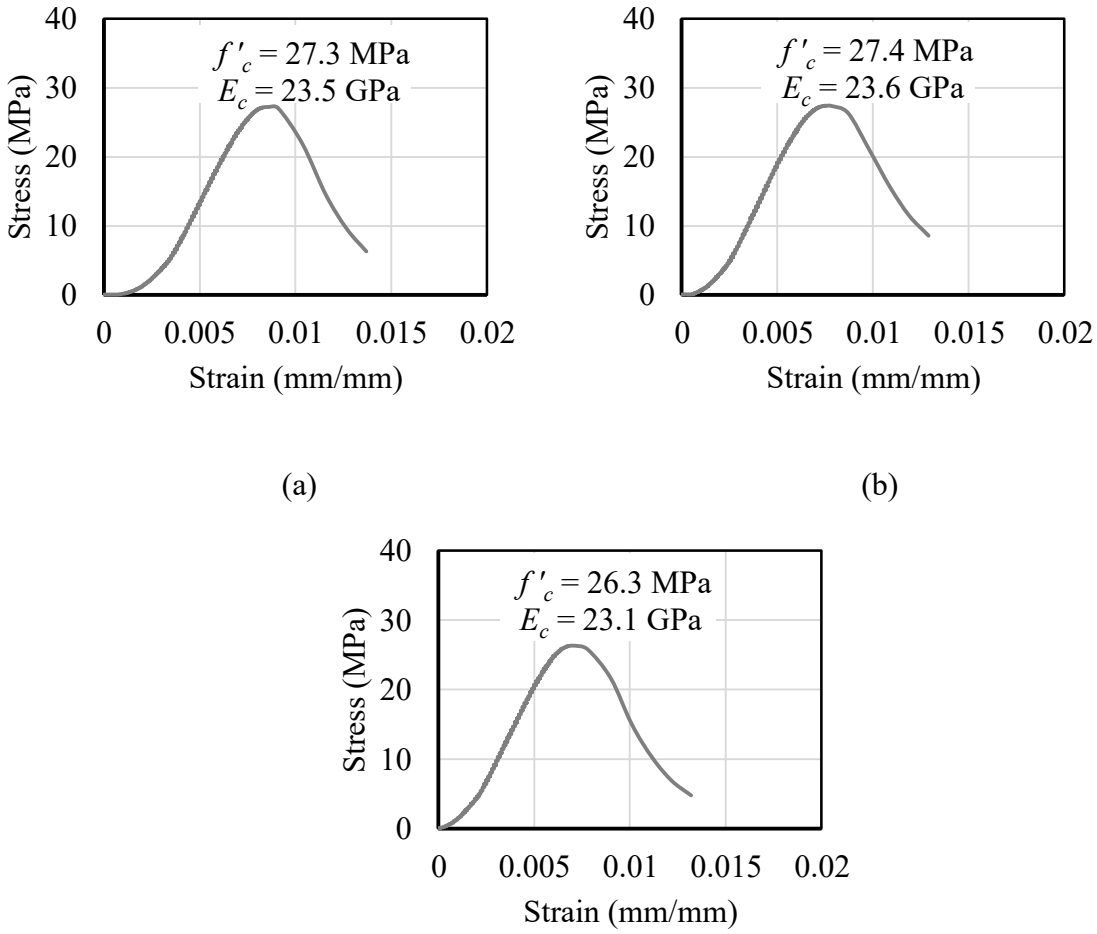

Figure D.15: Concrete compressive companion cylinders for beam-column joint specimen P3-180: (a) cylinder A, (b) cylinder B, and (c) cylinder C

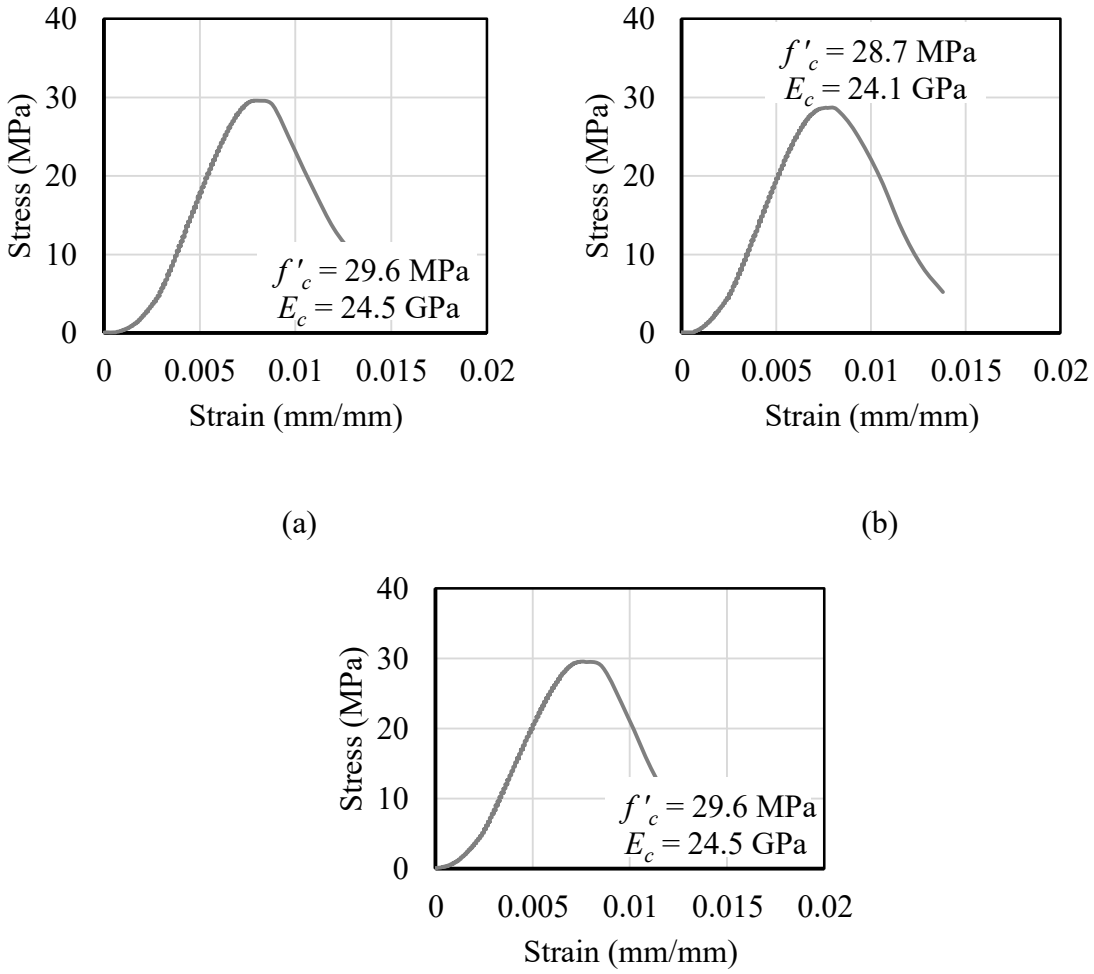

Figure D.16: Concrete compressive companion cylinders for beam-column joint specimen P4-180: (a) cylinder A, (b) cylinder B, and (c) cylinder C

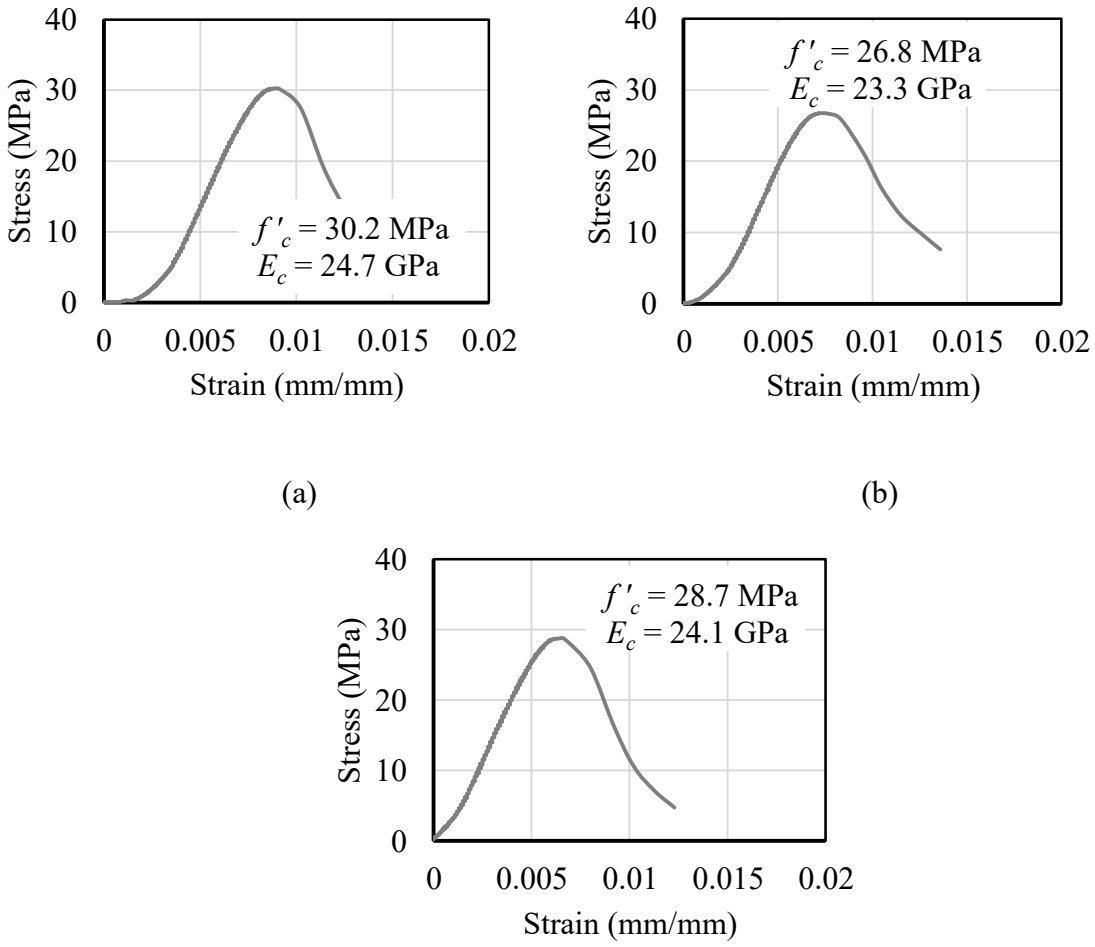

Figure D.17: Concrete compressive companion cylinders for beam-column joint specimen P5-180: (a) cylinder A, (b) cylinder B, and (c) cylinder C

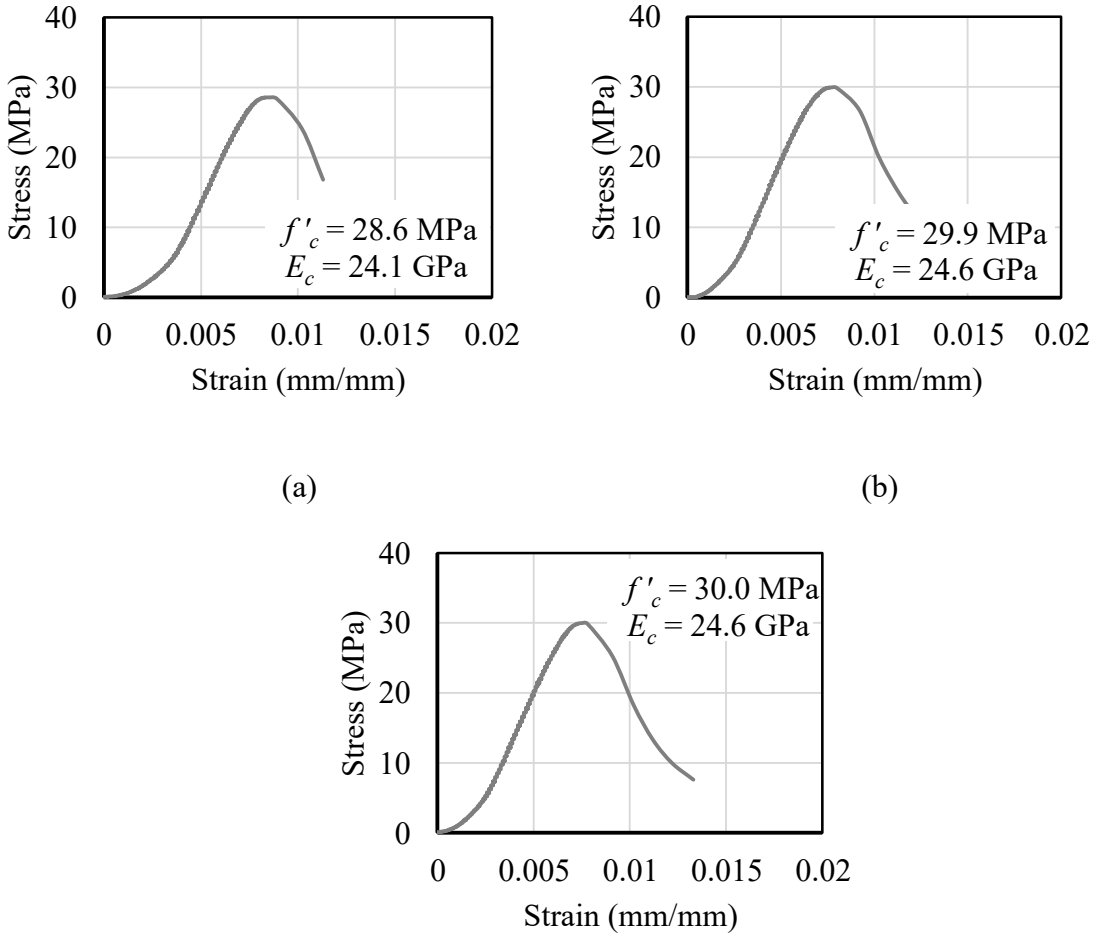

Figure D.18: Concrete compressive companion cylinders for beam-column joint specimen P6-180: (a) cylinder A, (b) cylinder B, and (c) cylinder C

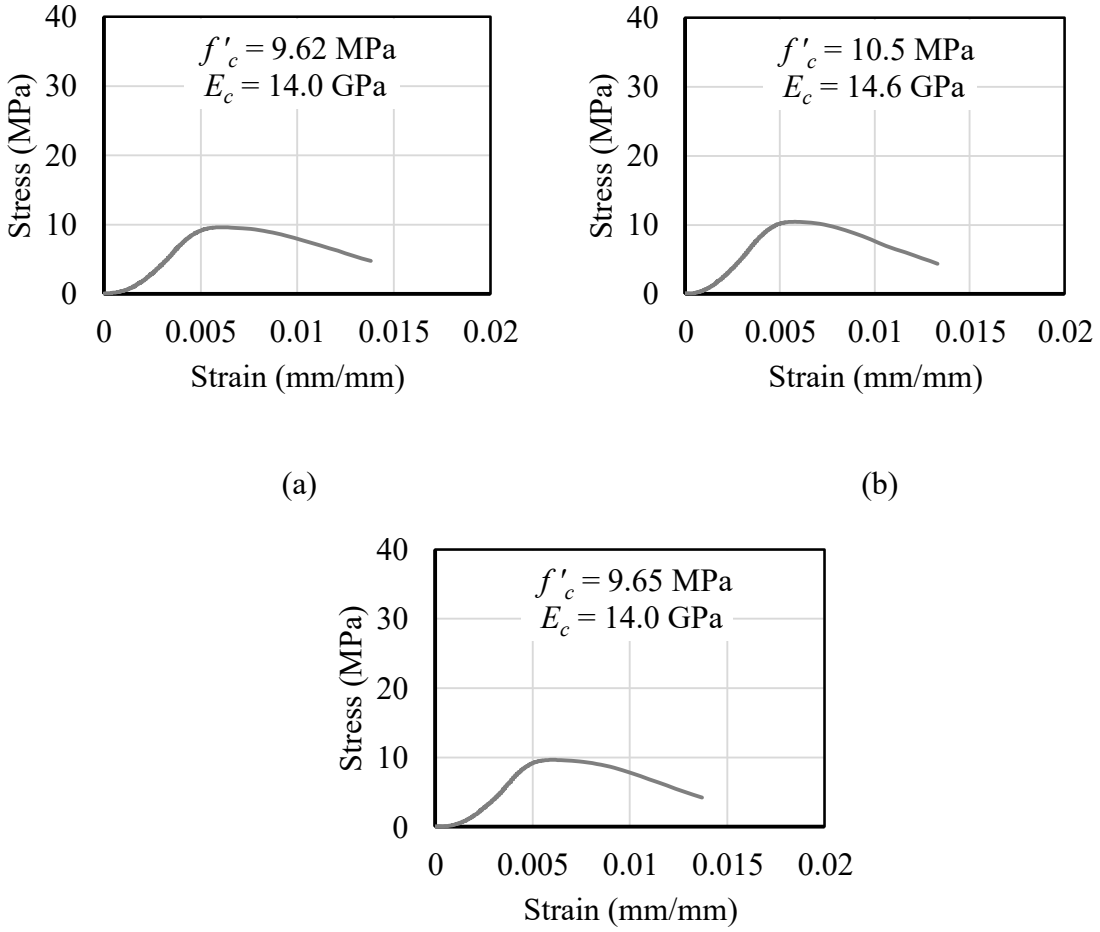

Figure D.19: Concrete compressive companion cylinders for beam-column joint specimen MD1-180: (a) cylinder A, (b) cylinder B, and (c) cylinder C

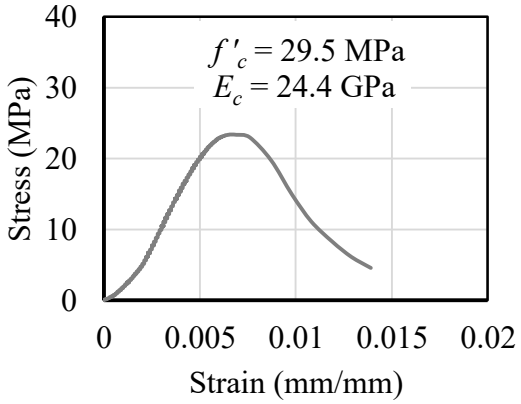

(a)

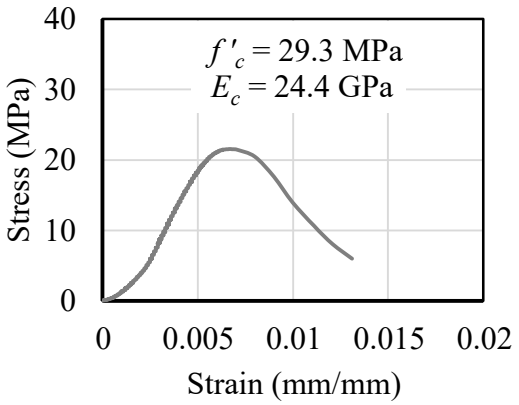

(b)

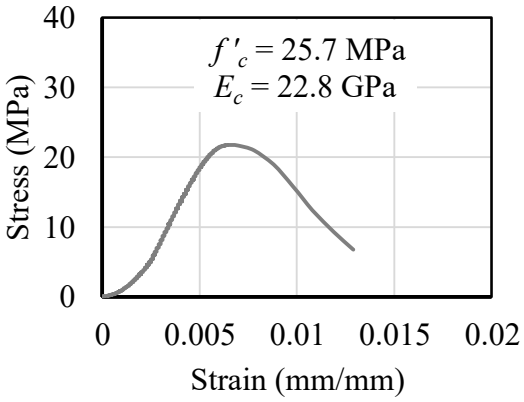

(c)

Figure D.20: Concrete compressive companion cylinders for beam-column joint specimen MD2-180: (a) cylinder A, (b) cylinder B, and (c) cylinder C

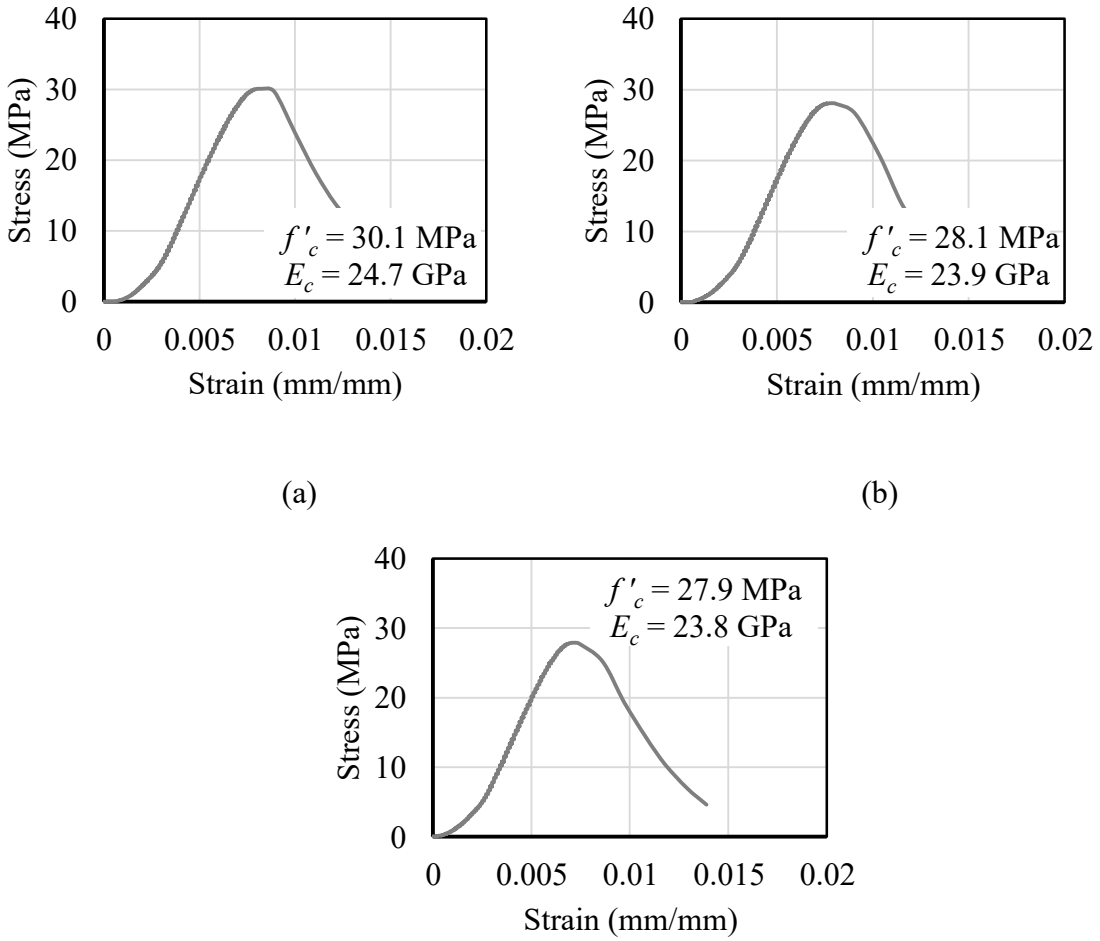

Figure D.21: Concrete compressive companion cylinders for beam-column joint specimen MD3-180: (a) cylinder A, (b) cylinder B, and (c) cylinder C

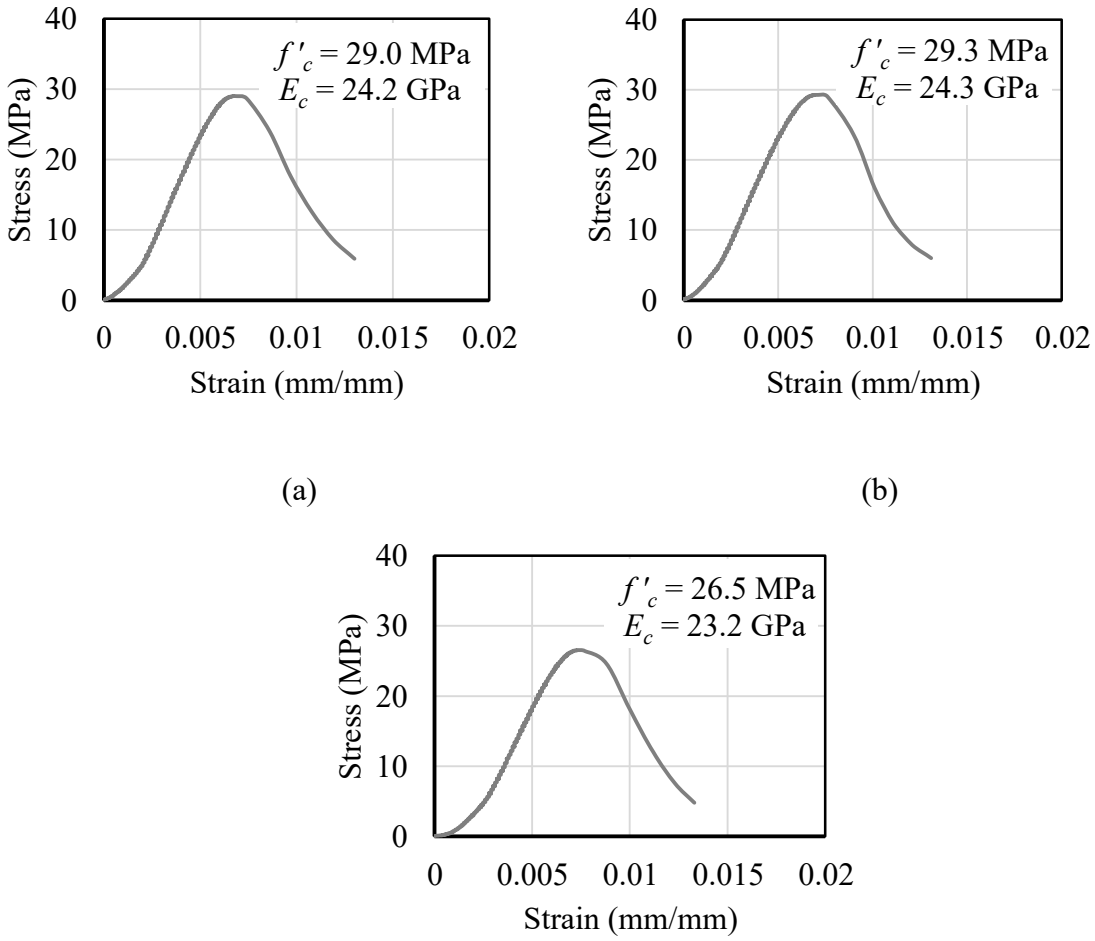

Figure D.22: Concrete compressive companion cylinders for beam-column joint specimen MD4-180: (a) cylinder A, (b) cylinder B, and (c) cylinder C

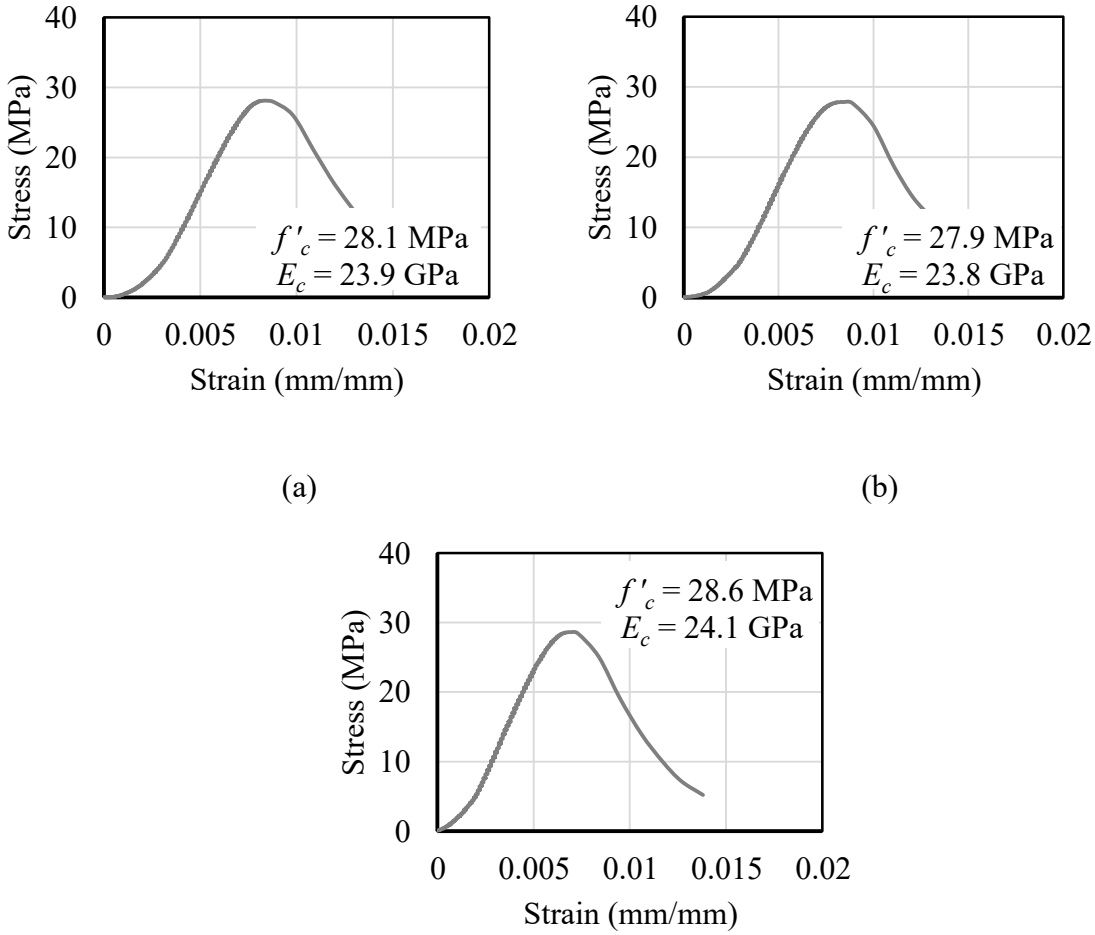

Figure D.23: Concrete compressive companion cylinders for beam-column joint specimen MD5-180: (a) cylinder A, (b) cylinder B, and (c) cylinder C

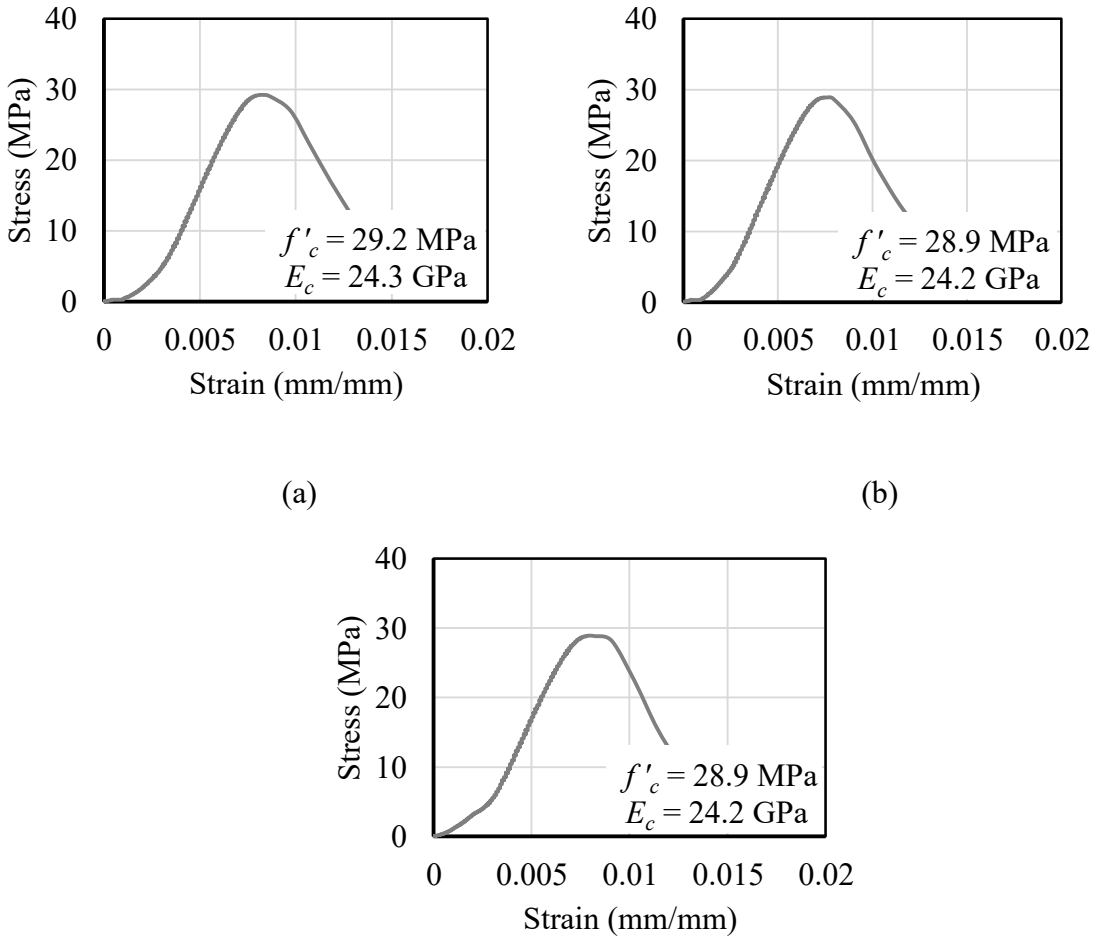

Figure D.24: Concrete compressive companion cylinders for beam-column joint specimen MD6-180: (a) cylinder A, (b) cylinder B, and (c) cylinder C

Appendix E: Companion Cylinder Tensile Stress versus Strain Diagrams at the Time of Beam-Column Joint Testing

Each beam-column joint specimen was a minimum of 28 days old at the time of testing. Three concrete companion cylinders were tested for tensile strength alongside each beam-column joint specimen as outlined in Section 3.8.2. Figures E.1 to E.24 show the stress versus strain behaviours of individual companion cylinders and present the concrete tensile strength, f_r. Data from one cylinder (C) associated with beam-column joint specimen P2-180 is not shown because the data did not save following testing.

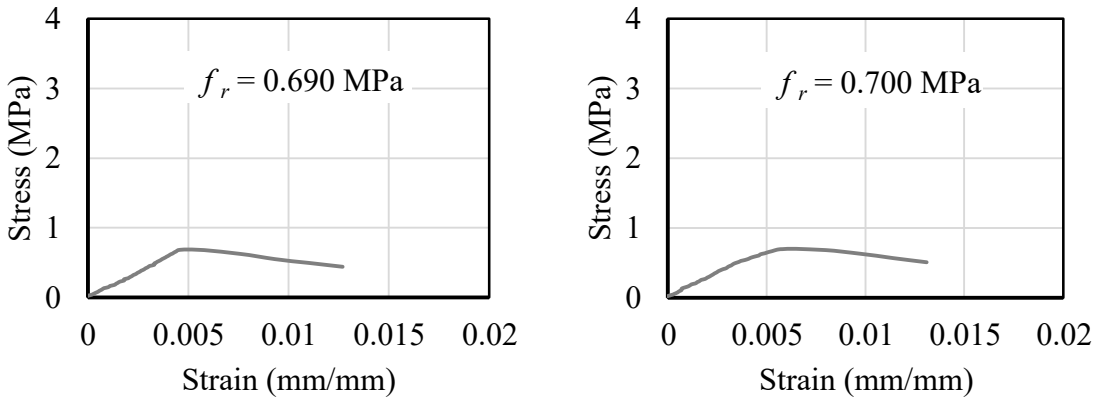

(a)

(b)

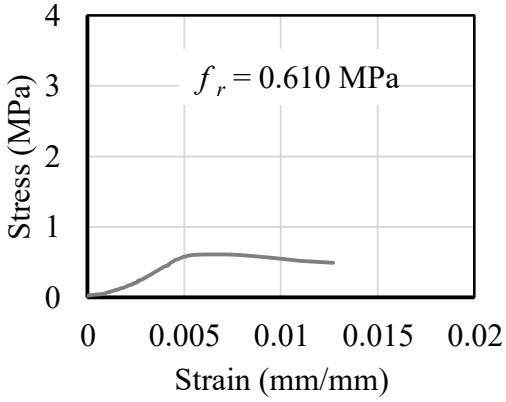

(c)

Figure E.1: Concrete tensile companion cylinders for beam-column joint specimen P1-90: (a) cylinder A, (b) cylinder B, and (c) cylinder C

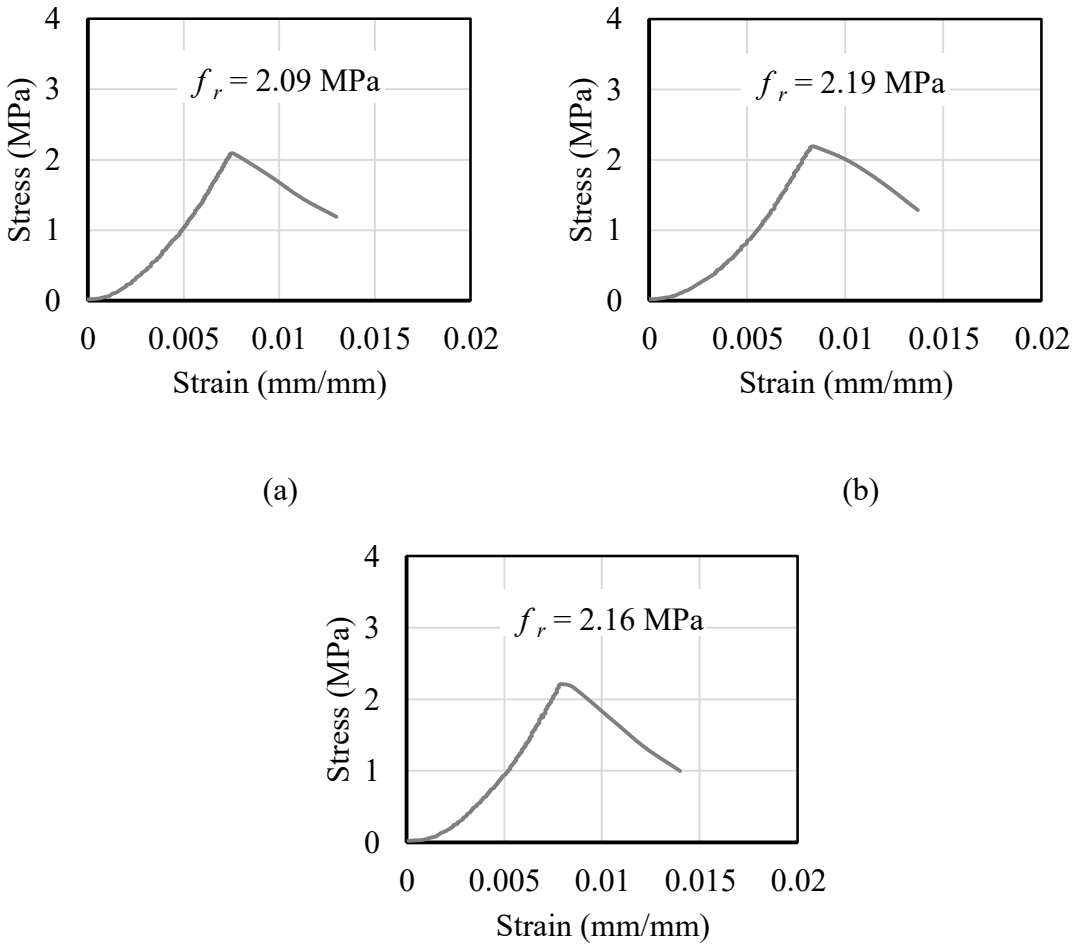

Figure E.2: Concrete tensile companion cylinders for beam-column joint specimen P2-90: (a) cylinder A, (b) cylinder B, and (c) cylinder C

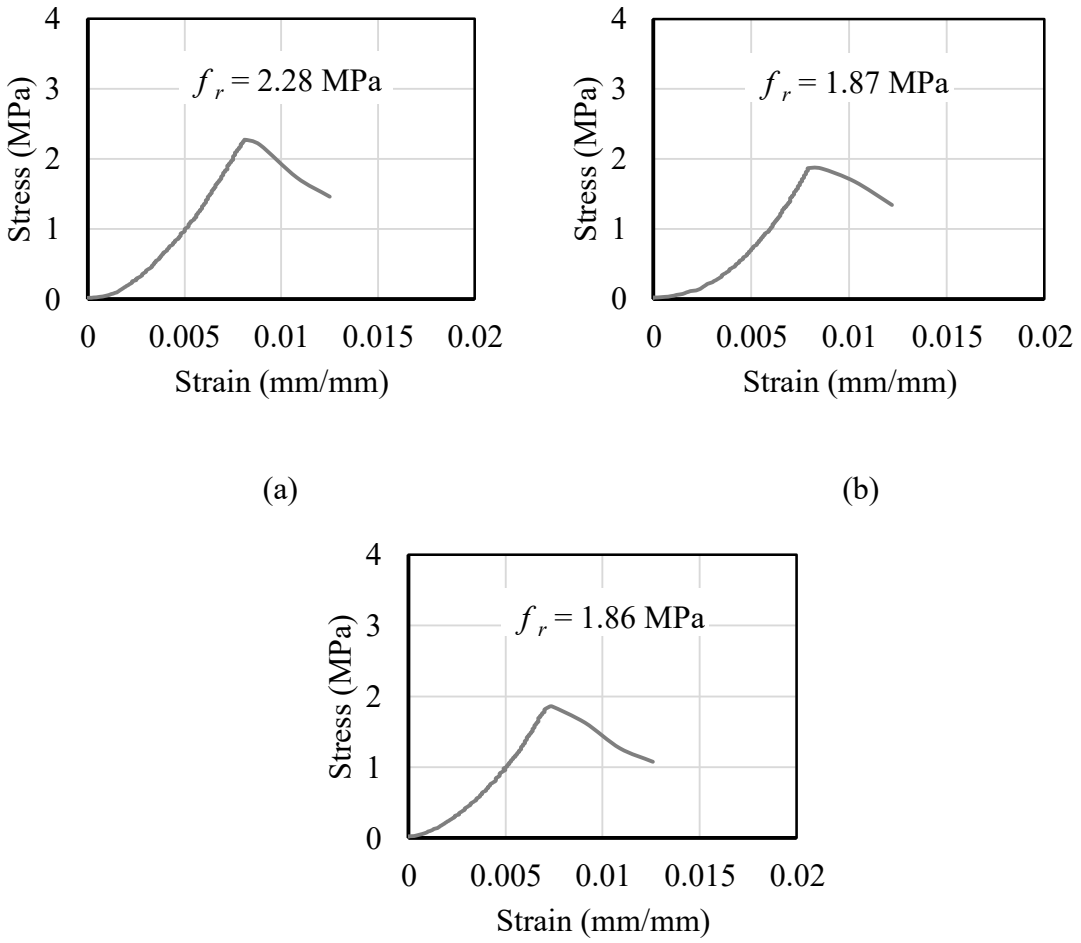

Figure E.3: Concrete tensile companion cylinders for beam-column joint specimen P3-90: (a) cylinder A, (b) cylinder B, and (c) cylinder C

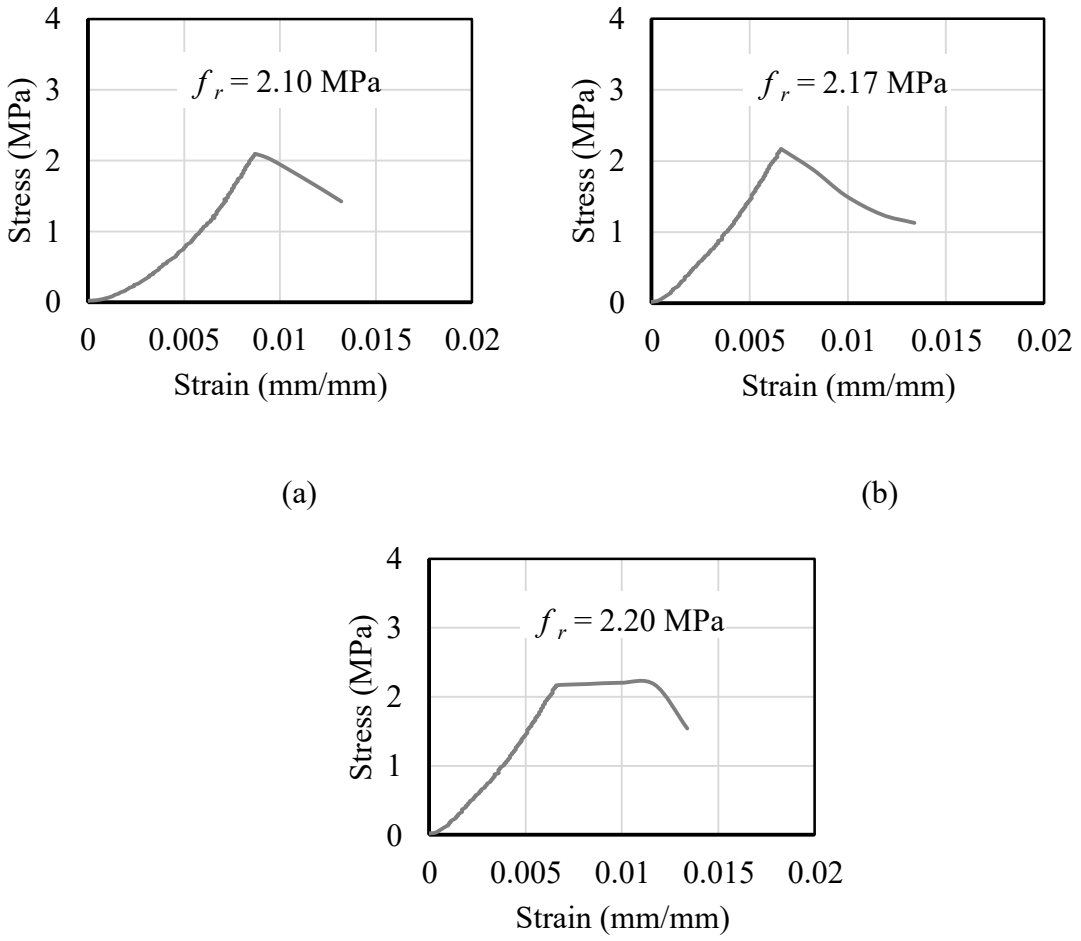

Figure E.4: Concrete tensile companion cylinders for beam-column joint specimen P4-90: (a) cylinder A, (b) cylinder B, and (c) cylinder C

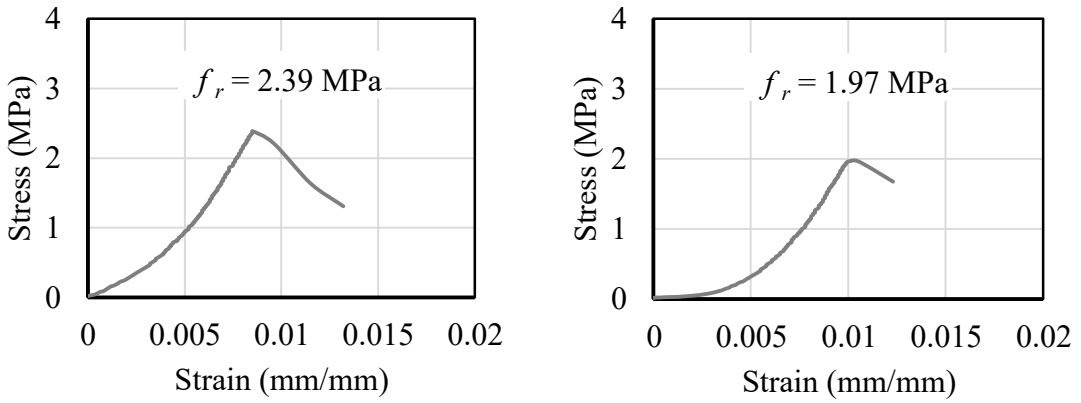

(a)

(b)

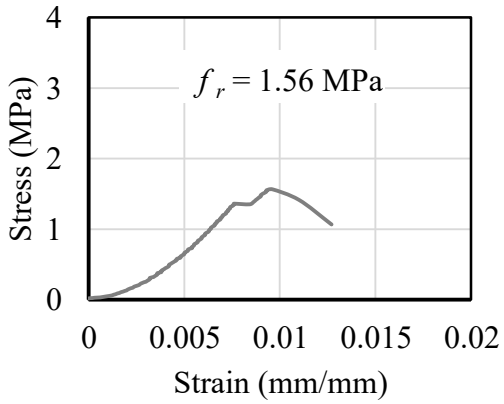

(c)

Figure E.5: Concrete tensile companion cylinders for beam-column joint specimen P5-90: (a) cylinder A, (b) cylinder B, and (c) cylinder C

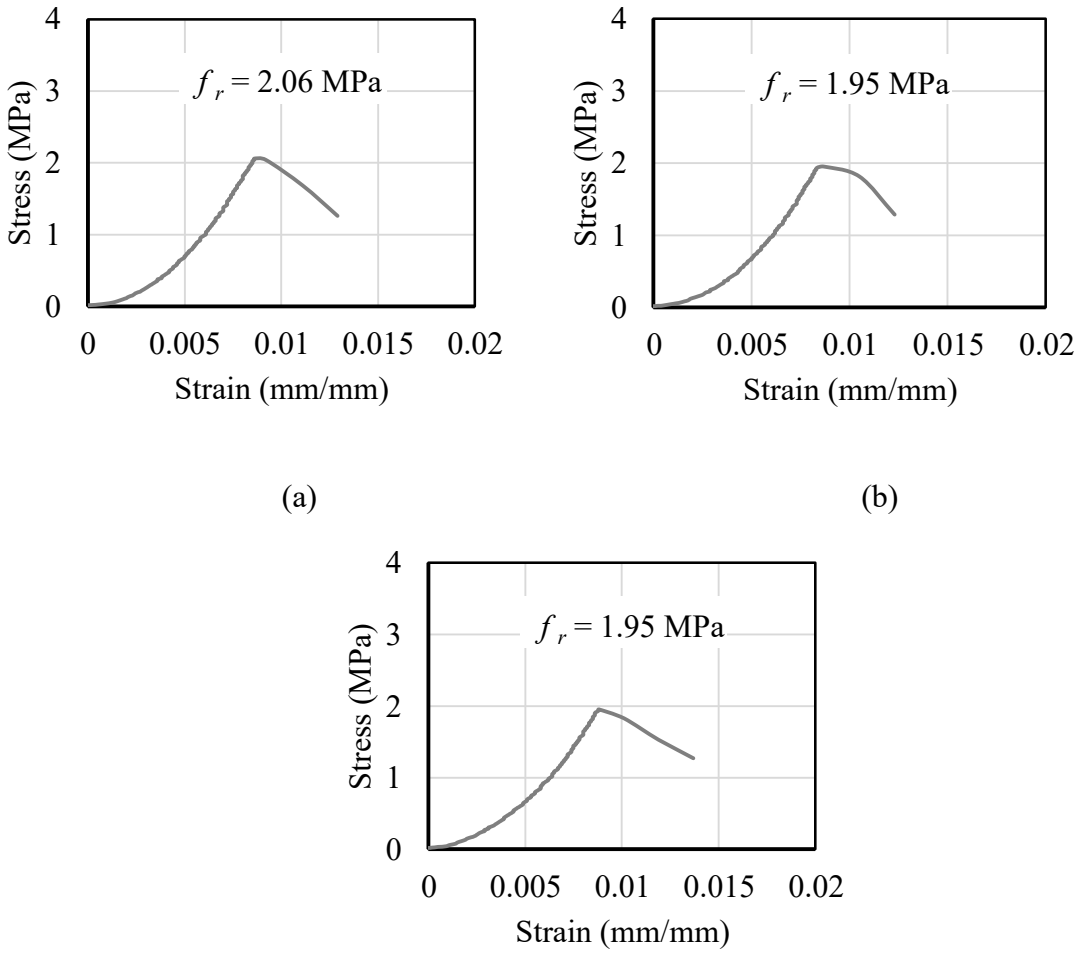

Figure E.6: Concrete tensile companion cylinders for beam-column joint specimen P6-90: (a) cylinder A, (b) cylinder B, and (c) cylinder C

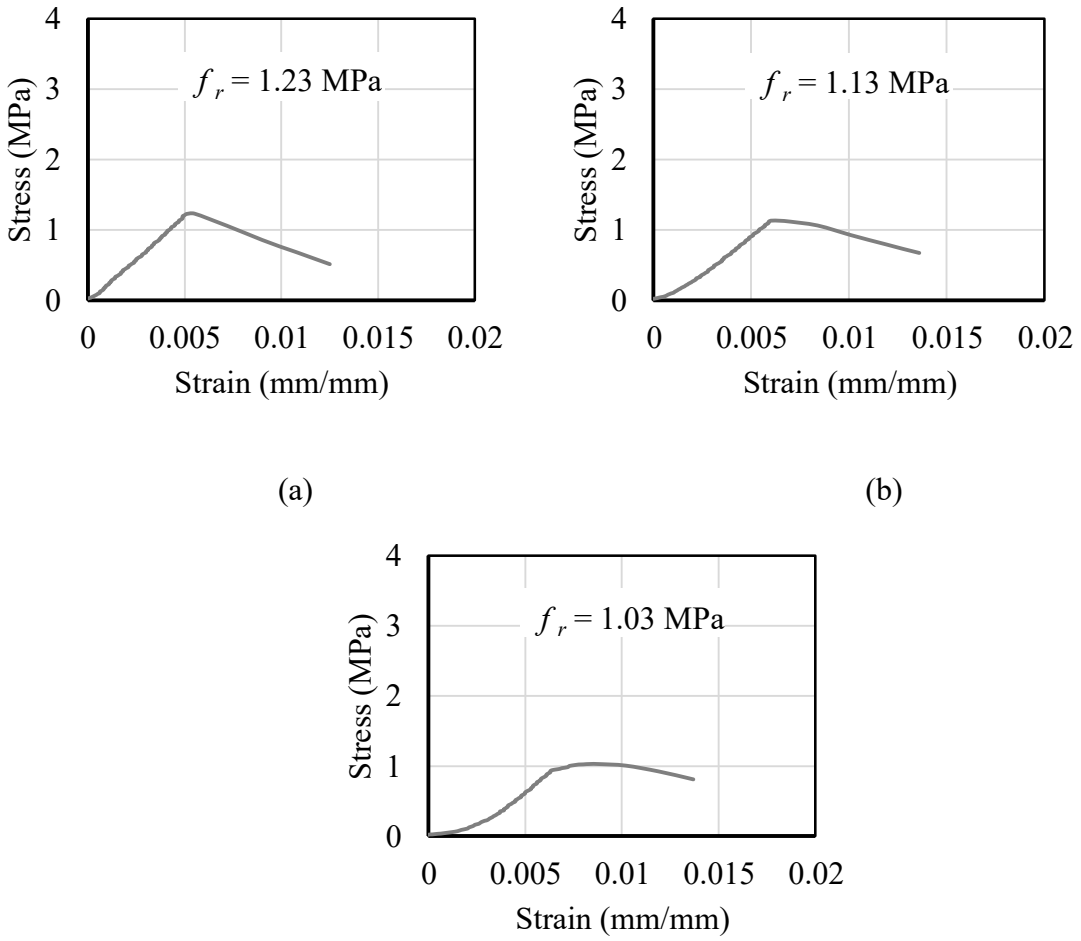

Figure E.7: Concrete tensile companion cylinders for beam-column joint specimen MD1-90: (a) cylinder A, (b) cylinder B, and (c) cylinder C

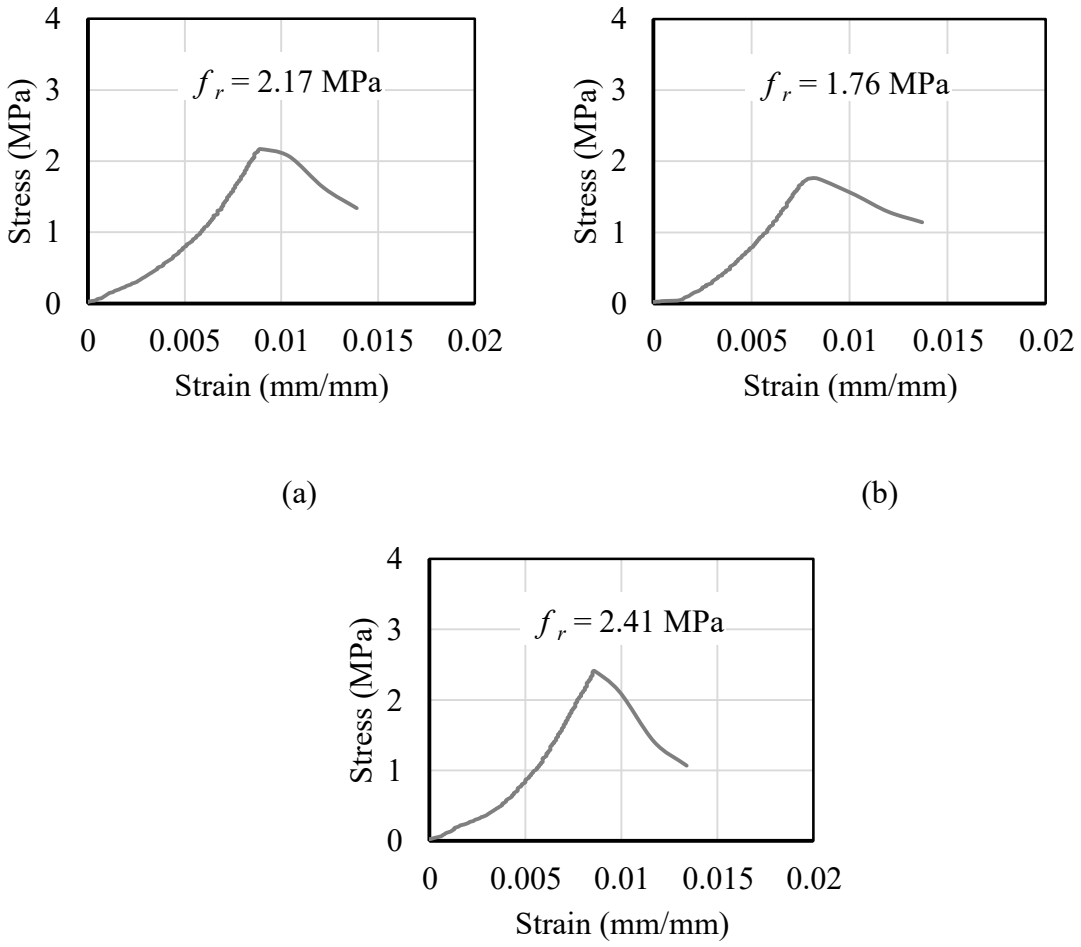

Figure E.8: Concrete tensile companion cylinders for beam-column joint specimen MD2-90: (a) cylinder A, (b) cylinder B, and (c) cylinder C

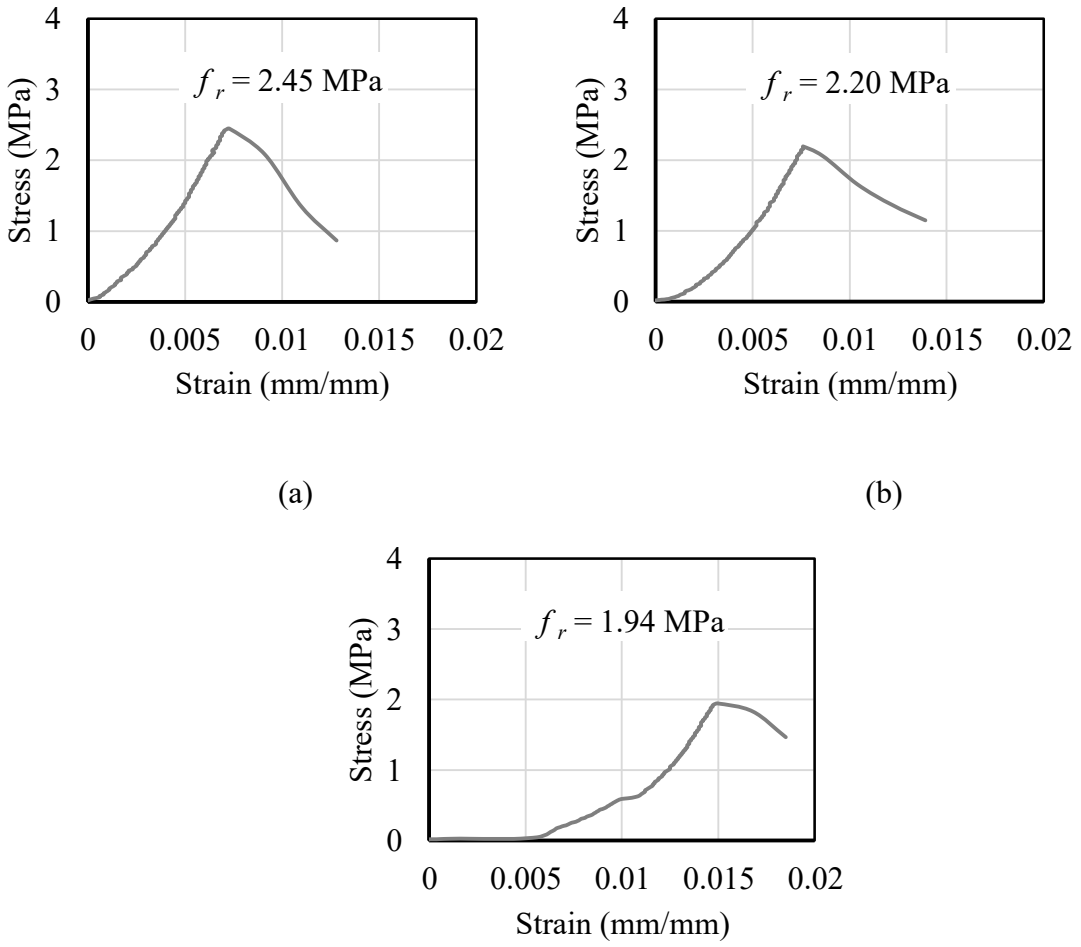

Figure E.9: Concrete tensile companion cylinders for beam-column joint specimen MD3-90: (a) cylinder A, (b) cylinder B, and (c) cylinder C

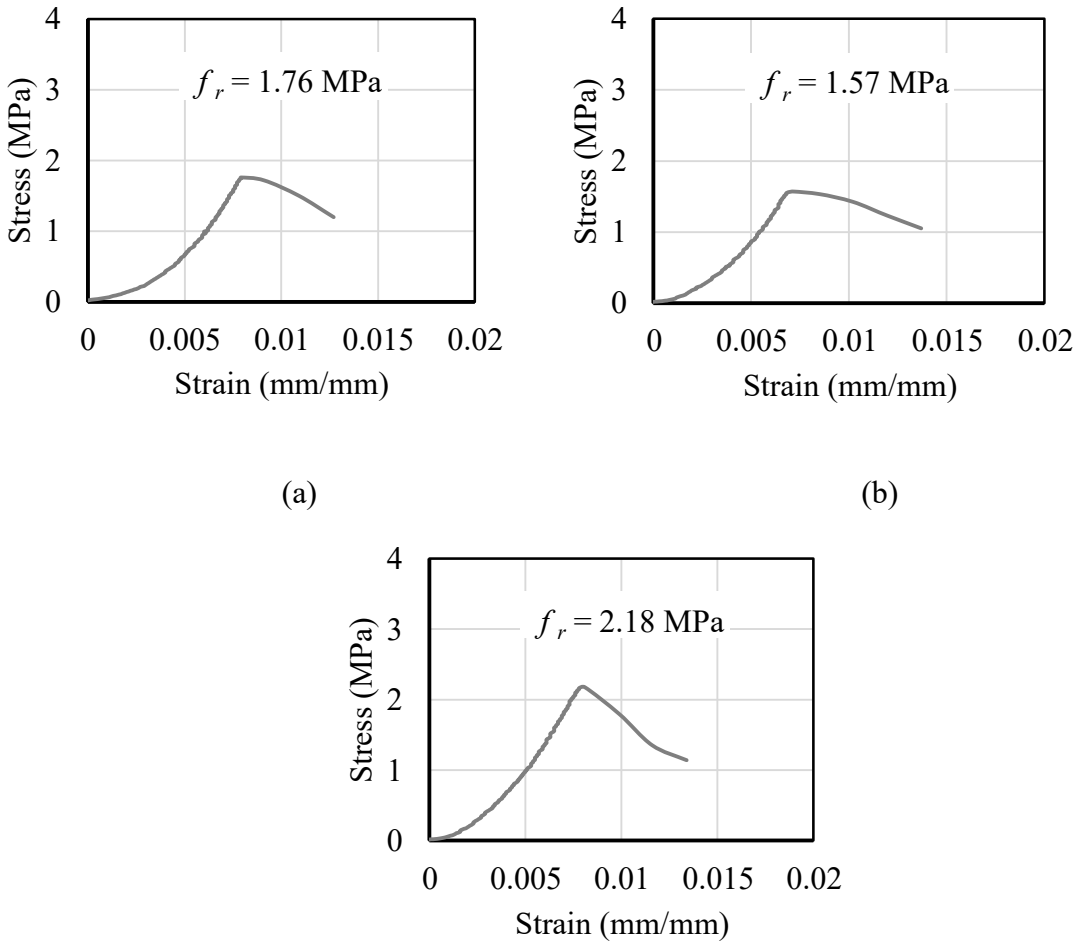

Figure E.10: Concrete tensile companion cylinders for beam-column joint specimen MD4-90: (a) cylinder A, (b) cylinder B, and (c) cylinder C

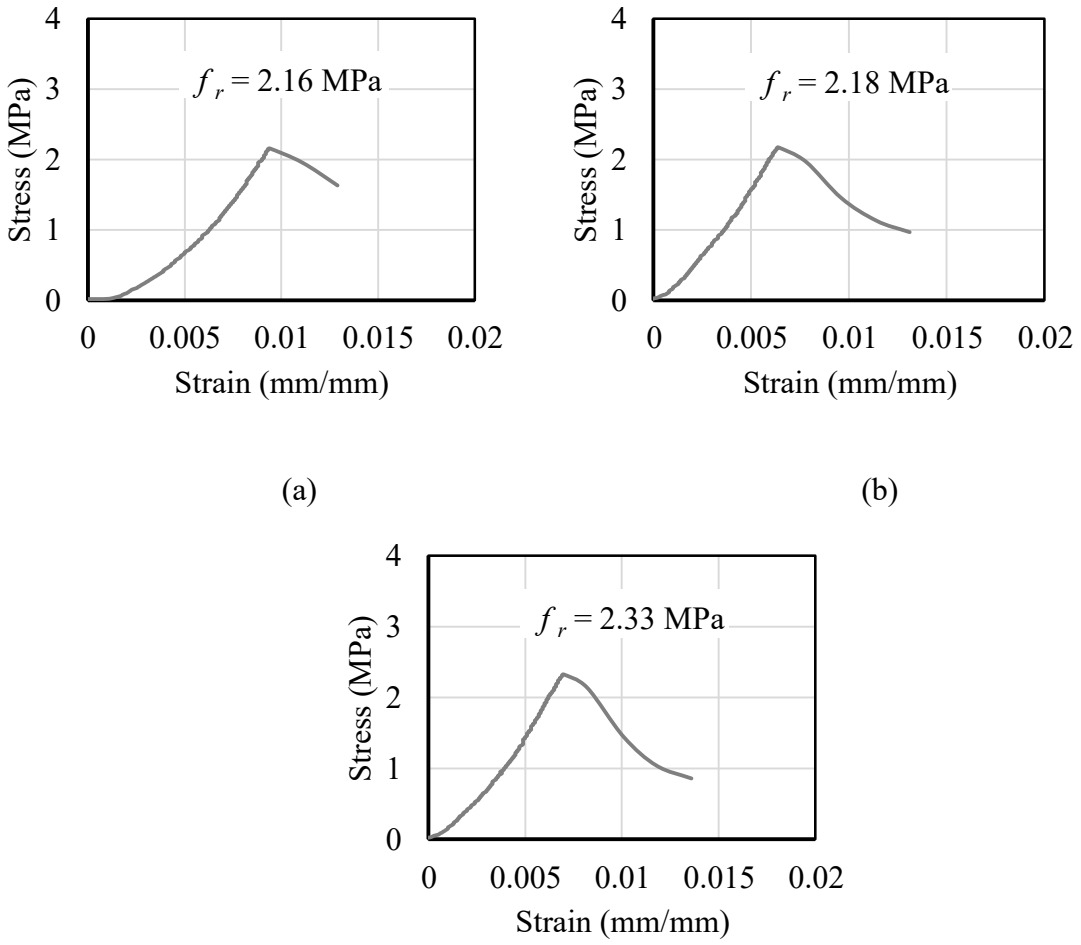

Figure E.11: Concrete tensile companion cylinders for beam-column joint specimen MD5-90: (a) cylinder A, (b) cylinder B, and (c) cylinder C

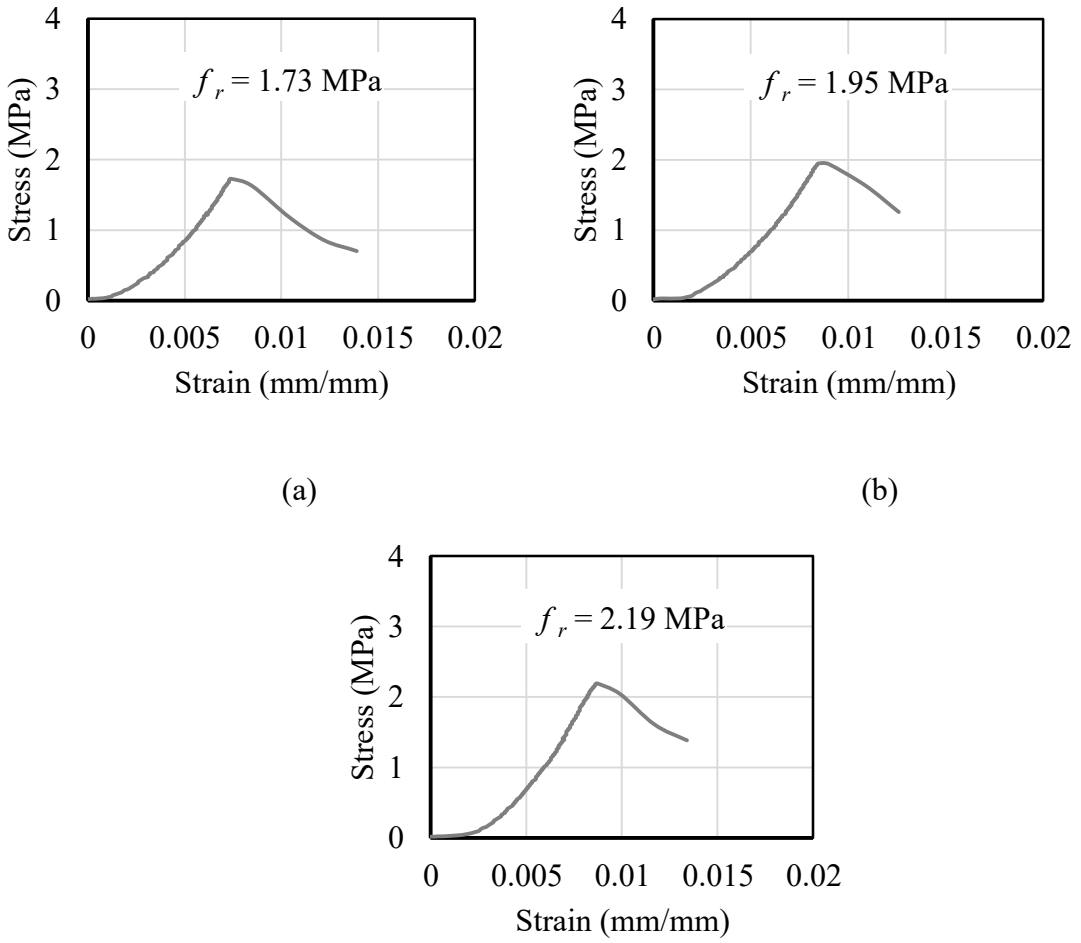

Figure E.12: Concrete tensile companion cylinders for beam-column joint specimen MD6-90: (a) cylinder A, (b) cylinder B, and (c) cylinder C

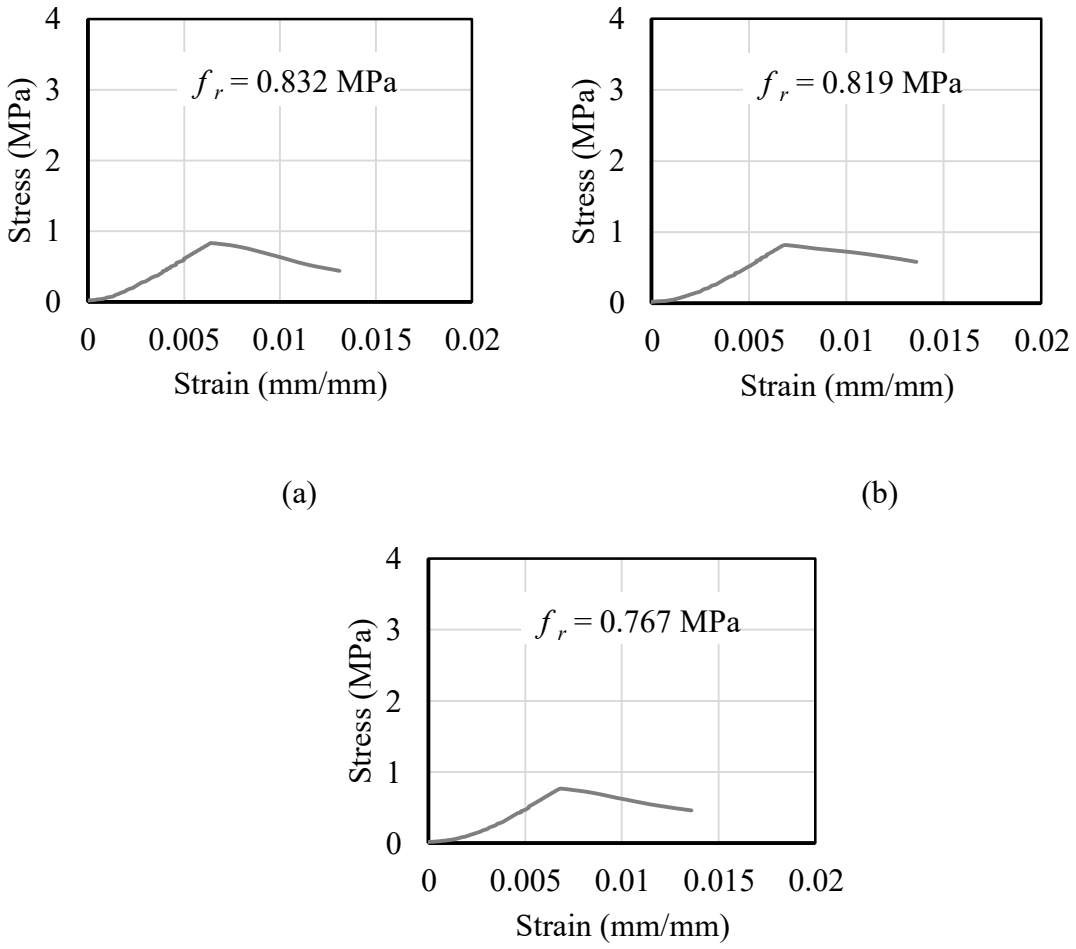

Figure E.13: Concrete tensile companion cylinders for beam-column joint specimen P1-180: (a) cylinder A, (b) cylinder B, and (c) cylinder C

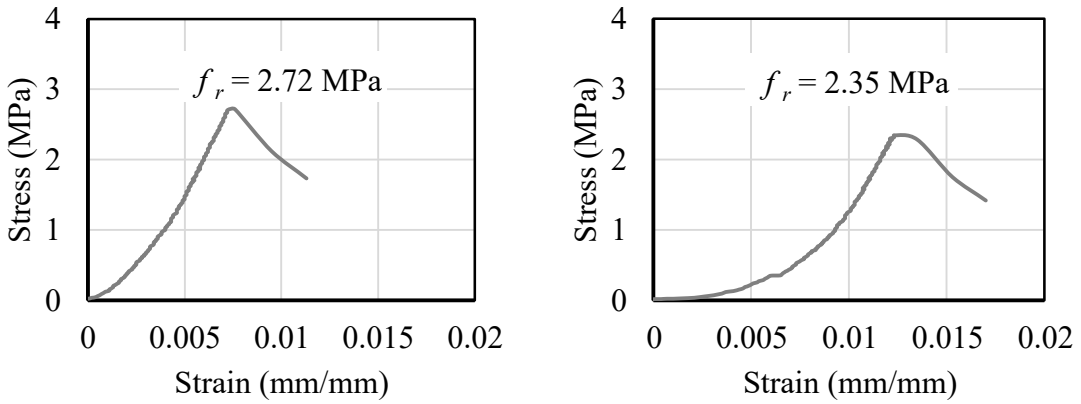

(a) (b)

Figure E.14: Concrete tensile companion cylinders for beam-column joint specimen P2-180: (a) cylinder A, and (b) cylinder B

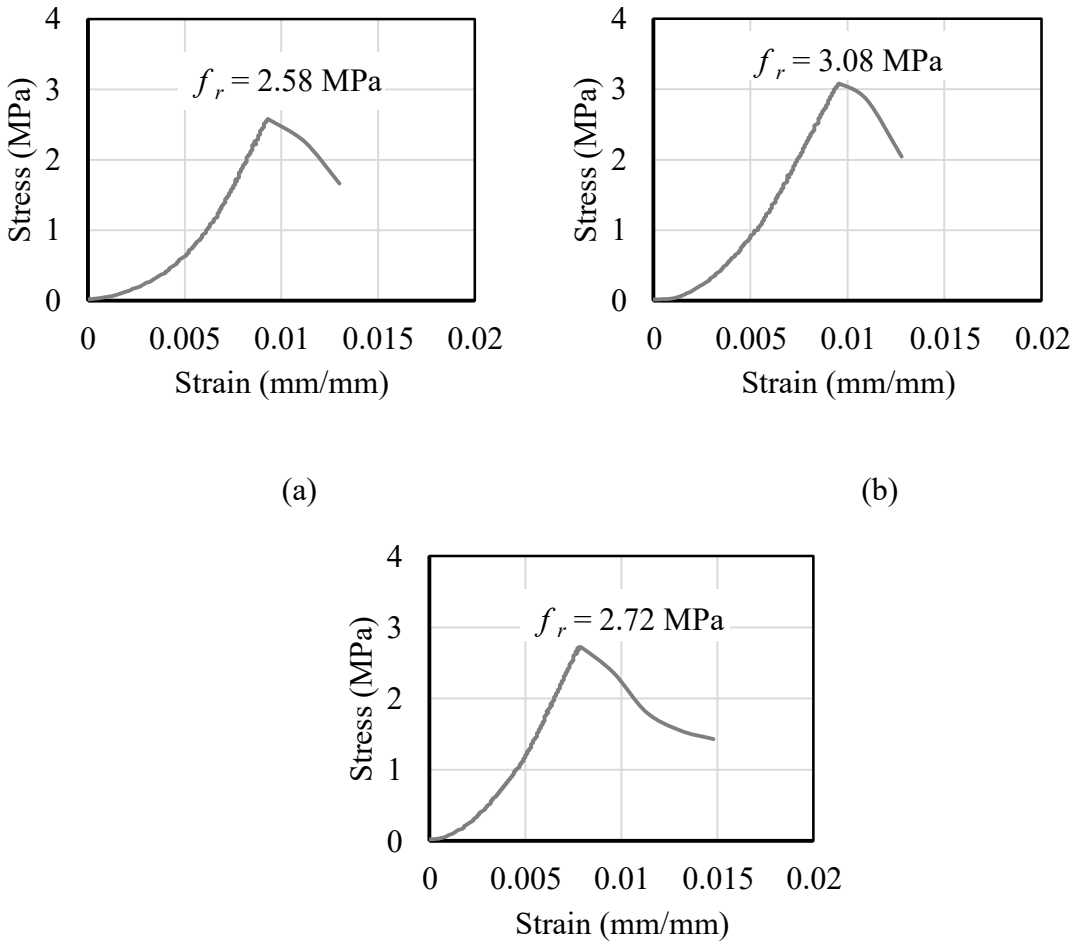

Figure E.15: Concrete tensile companion cylinders for beam-column joint specimen P3-180: (a) cylinder A, (b) cylinder B, and (c) cylinder C

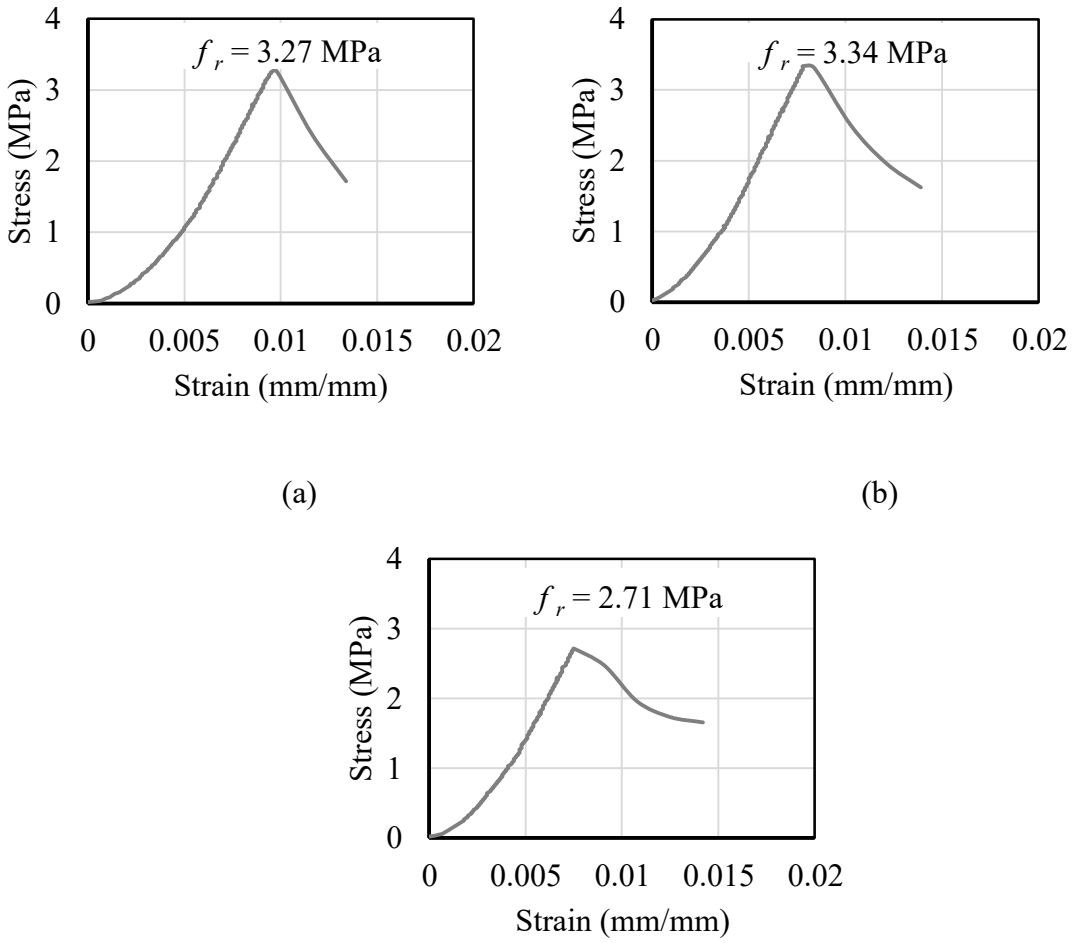

Figure E.16: Concrete tensile companion cylinders for beam-column joint specimen P4-180: (a) cylinder A, (b) cylinder B, and (c) cylinder C

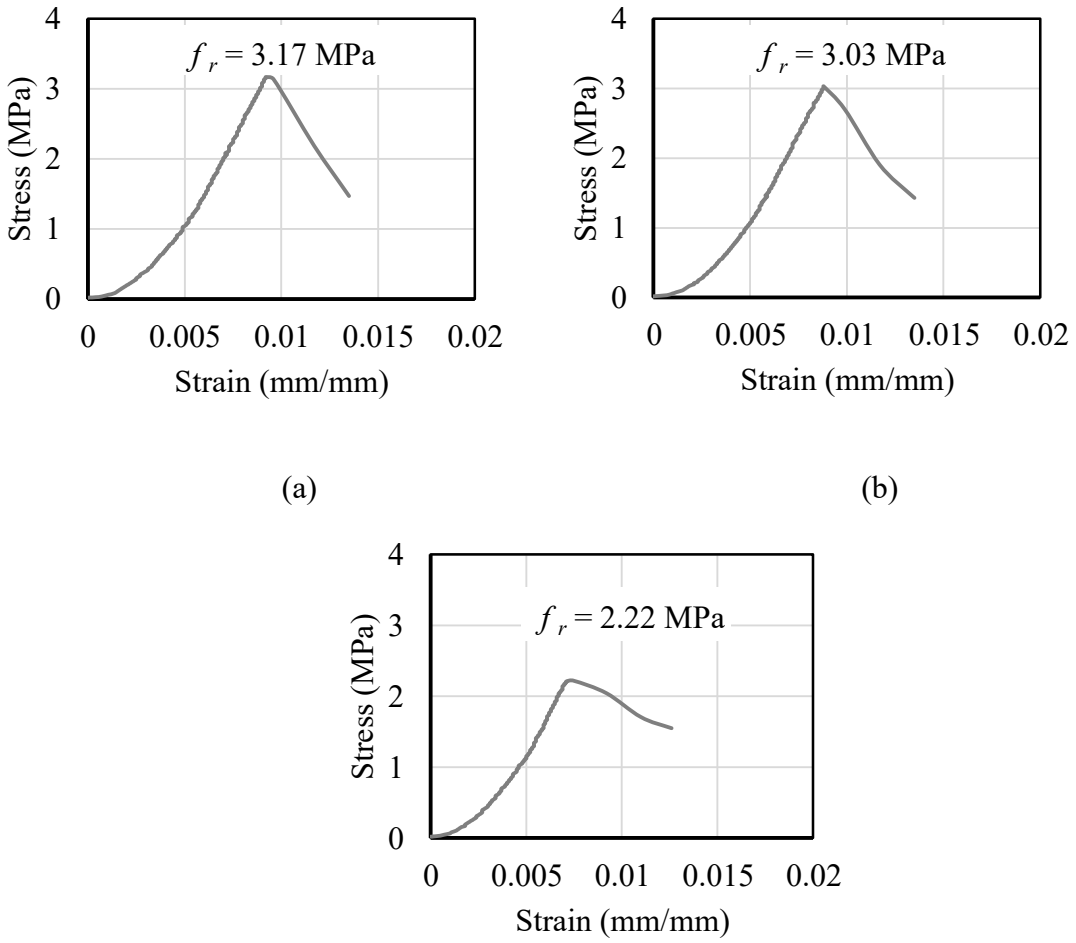

Figure E.17: Concrete tensile companion cylinders for beam-column joint specimen P5-180: (a) cylinder A, (b) cylinder B, and (c) cylinder C

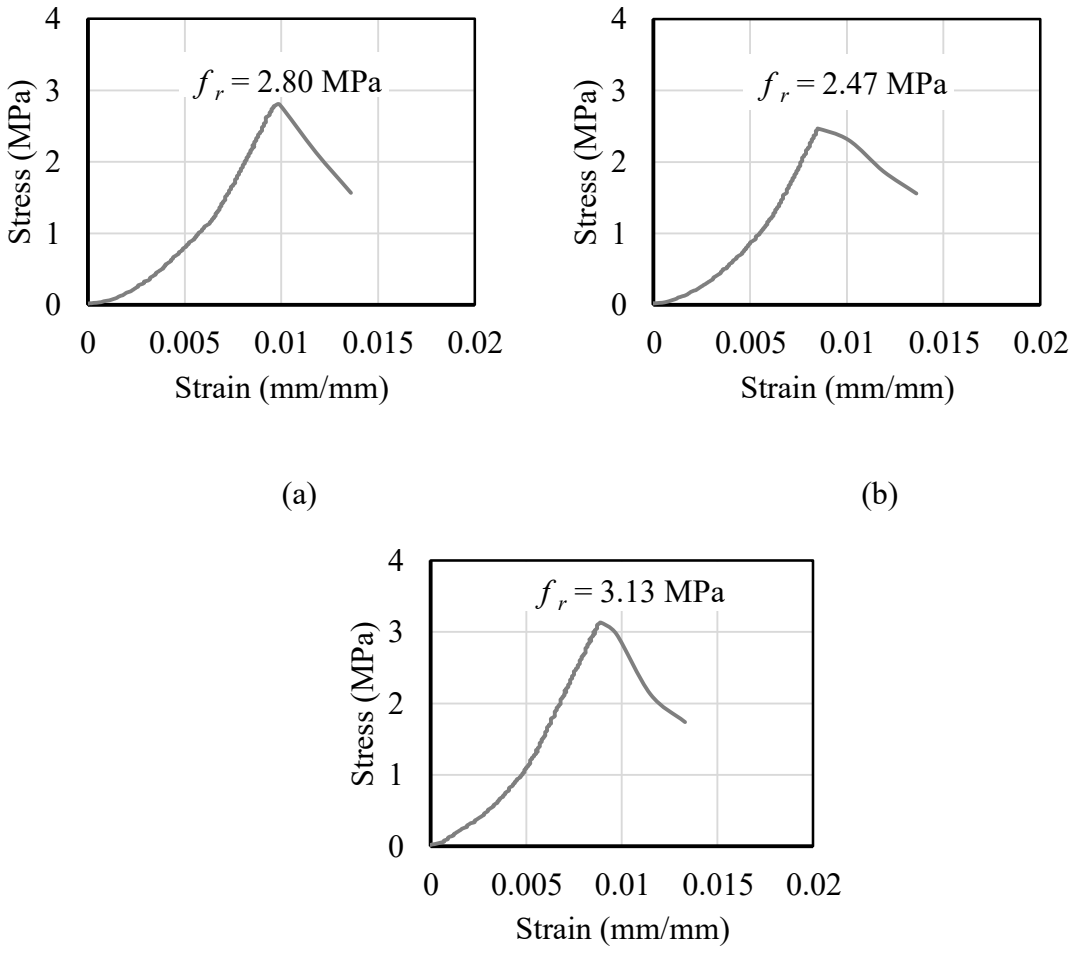

Figure E.18: Concrete tensile companion cylinders for beam-column joint specimen P6-180: (a) cylinder A, (b) cylinder B, and (c) cylinder C

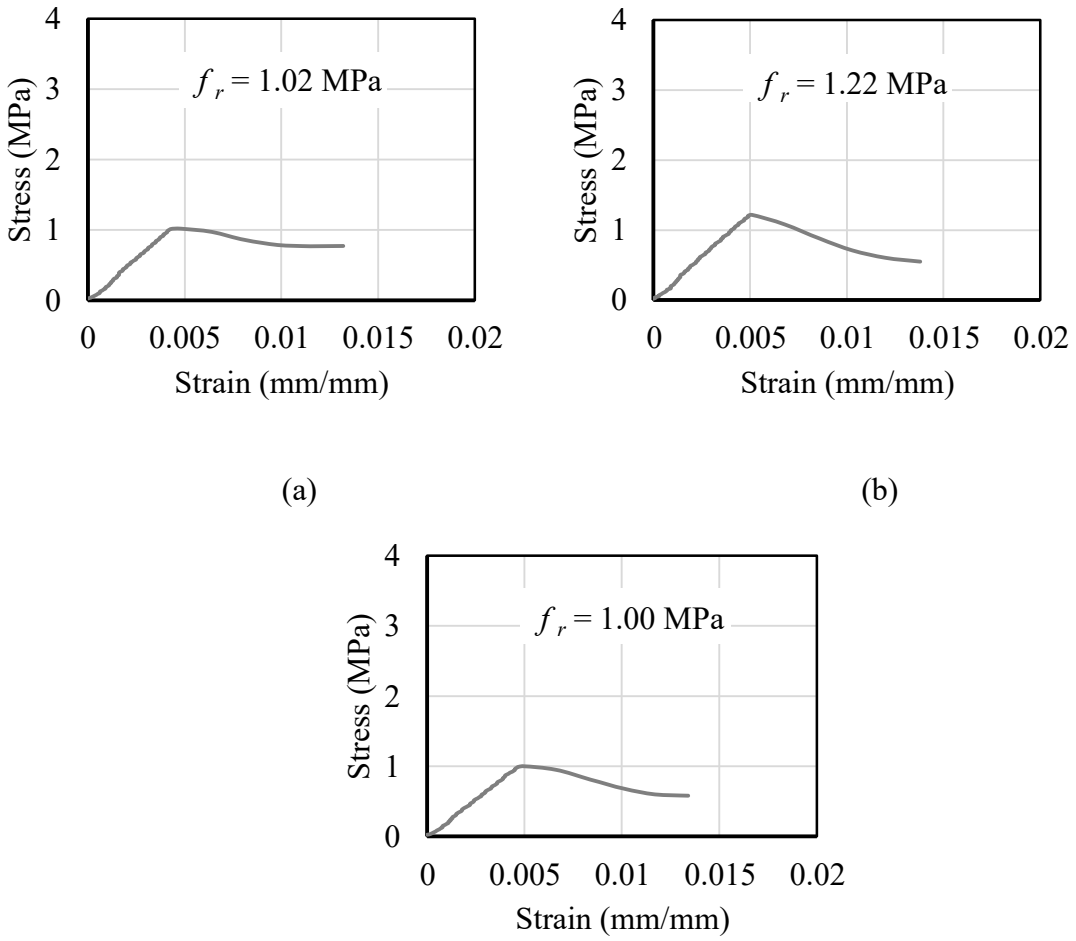

Figure E.19: Concrete tensile companion cylinders for beam-column joint specimen MD1-180: (a) cylinder A, (b) cylinder B, and (c) cylinder C

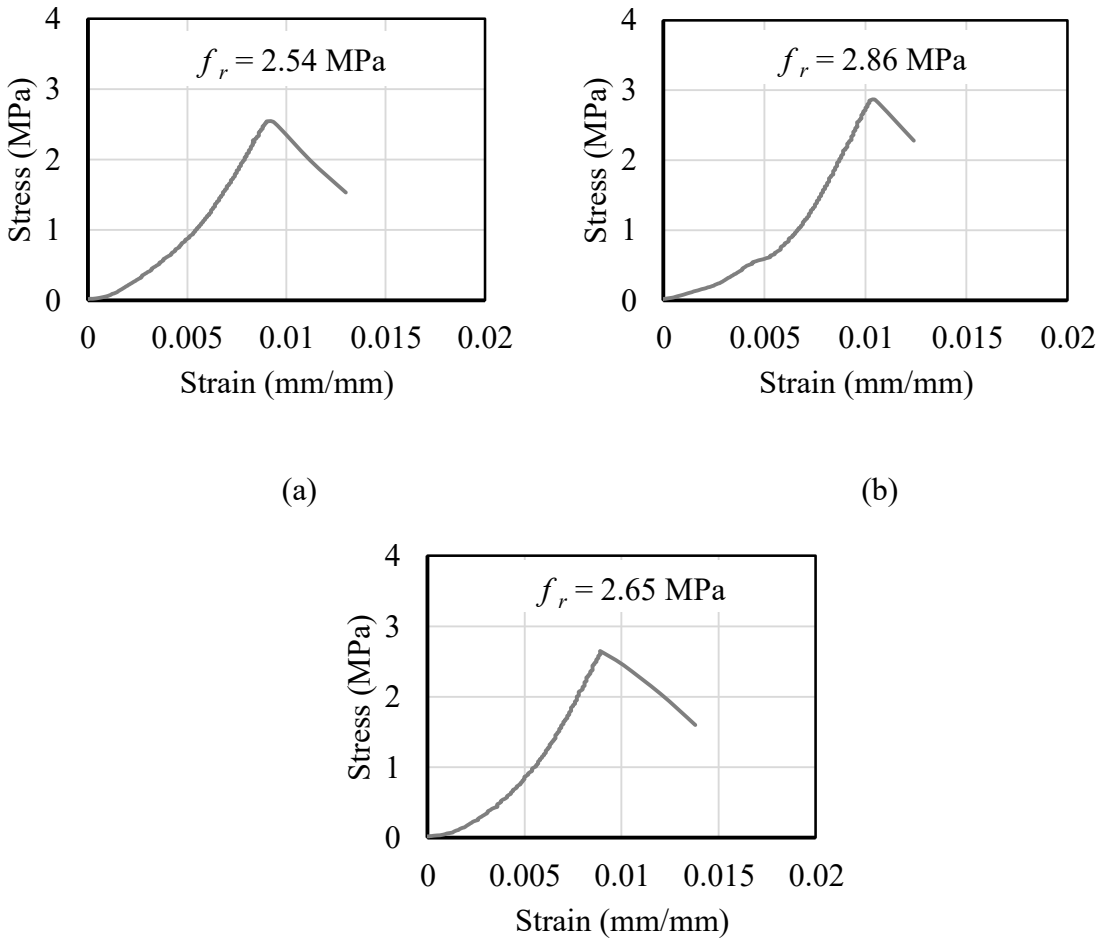

Figure E.20: Concrete tensile companion cylinders for beam-column joint specimen MD2-180: (a) cylinder A, (b) cylinder B, and (c) cylinder C

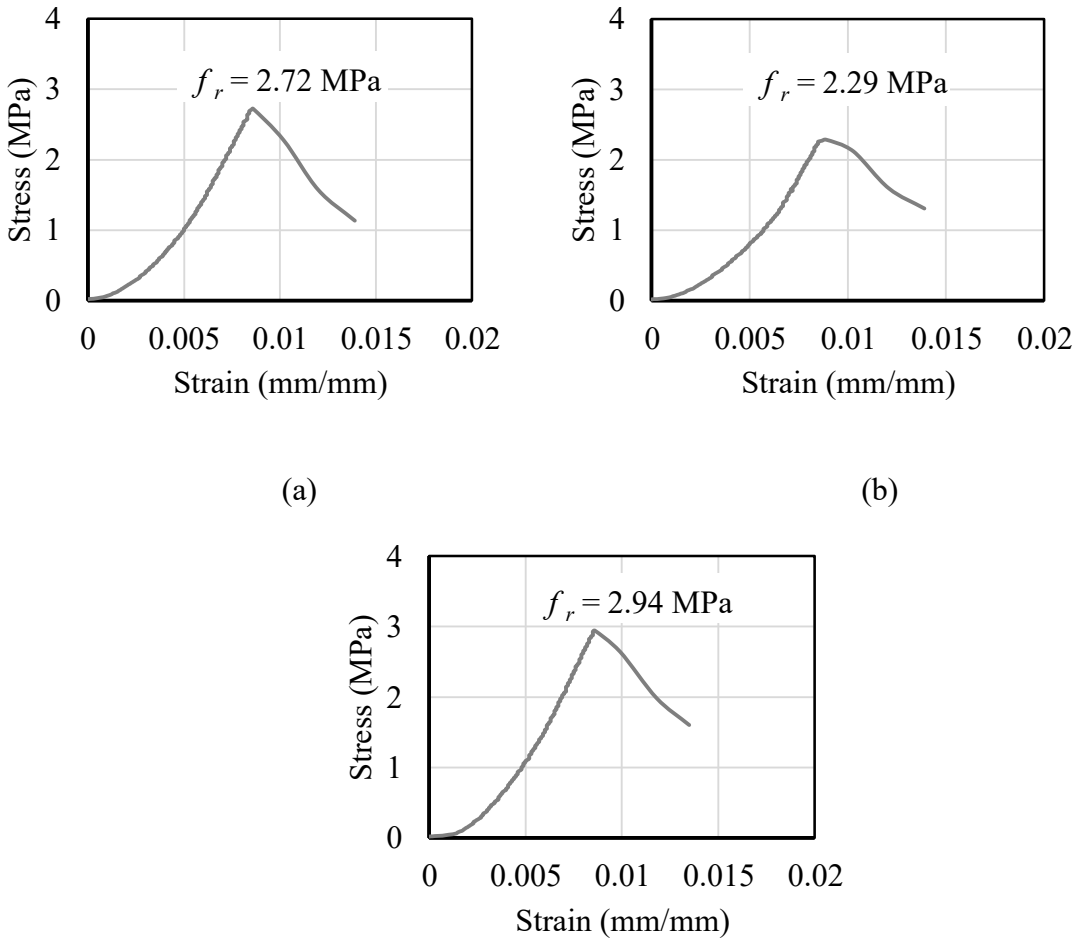

Figure E.21: Concrete tensile companion cylinders for beam-column joint specimen MD3-180: (a) cylinder A, (b) cylinder B, and (c) cylinder C

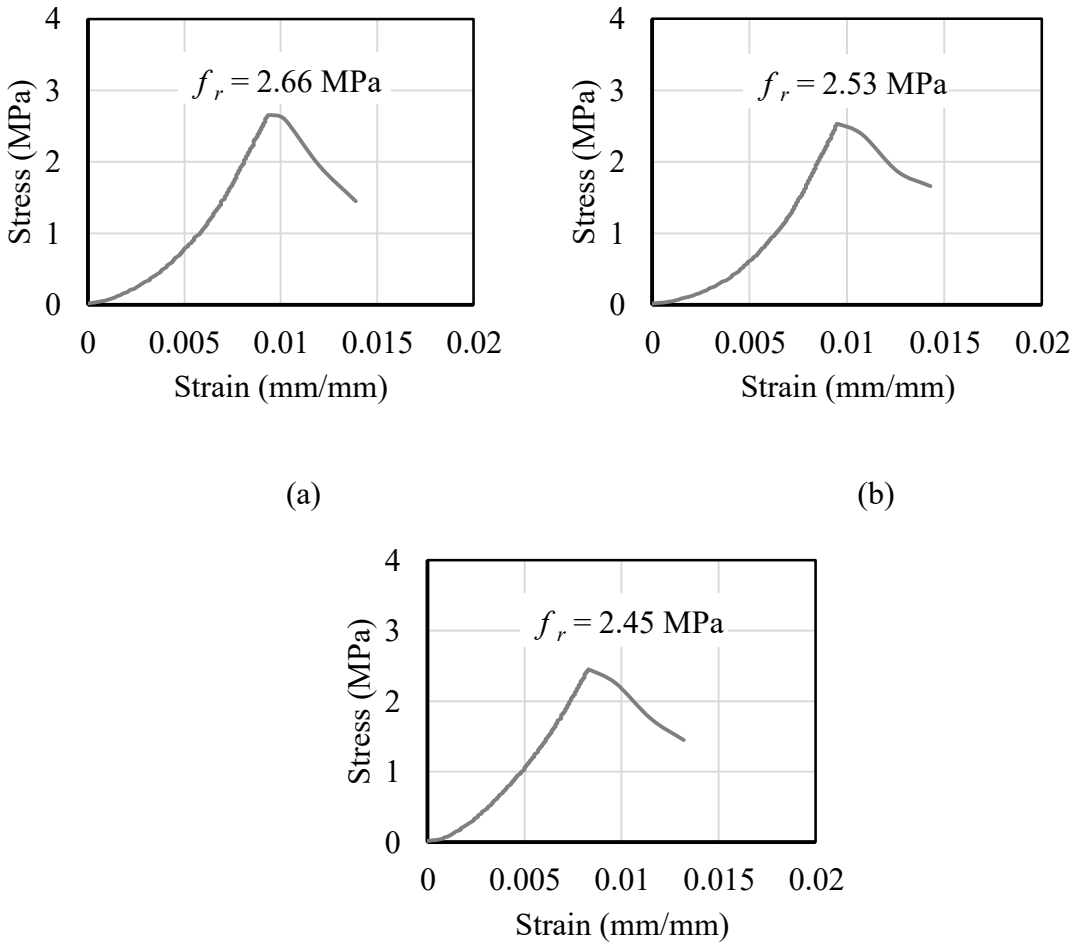

Figure E.22: Concrete tensile companion cylinders for beam-column joint specimen MD4-180: (a) cylinder A, (b) cylinder B, and (c) cylinder C

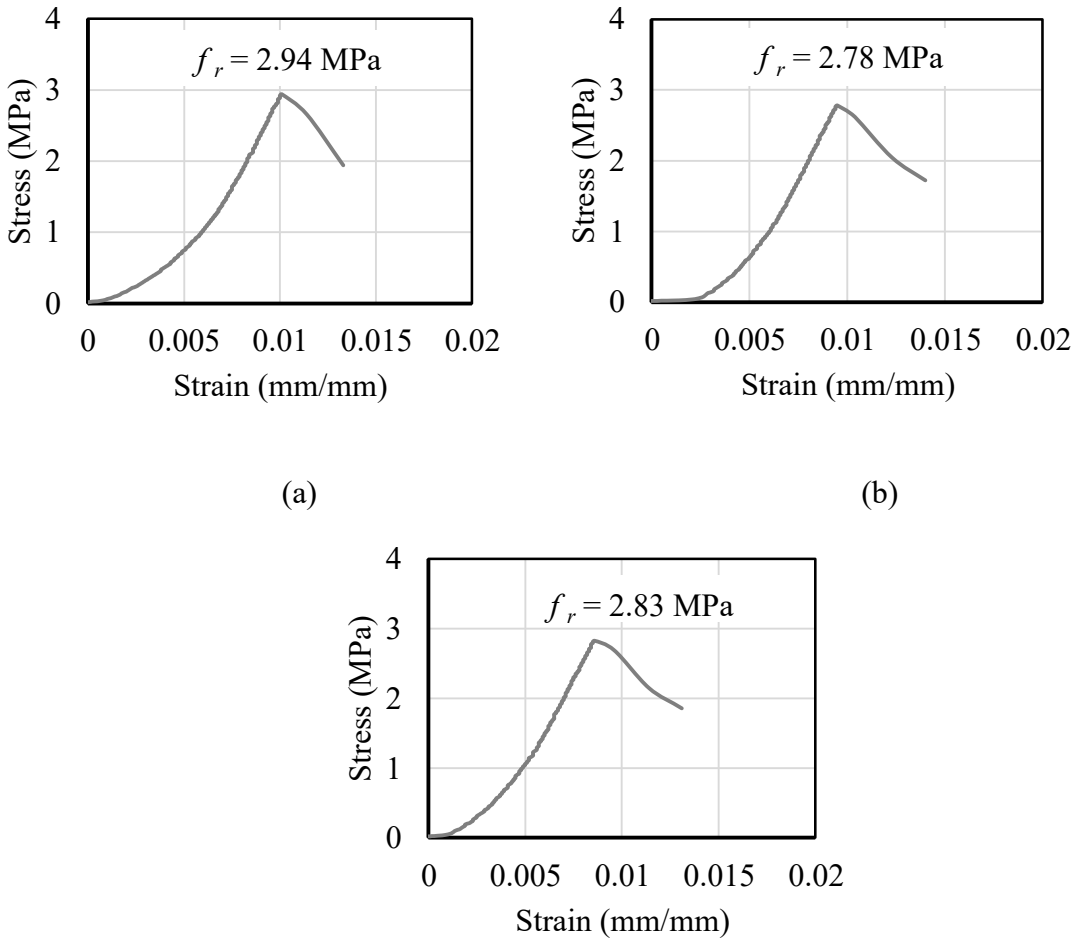

Figure E.23: Concrete tensile companion cylinders for beam-column joint specimen MD5-180: (a) cylinder A, (b) cylinder B, and (c) cylinder C

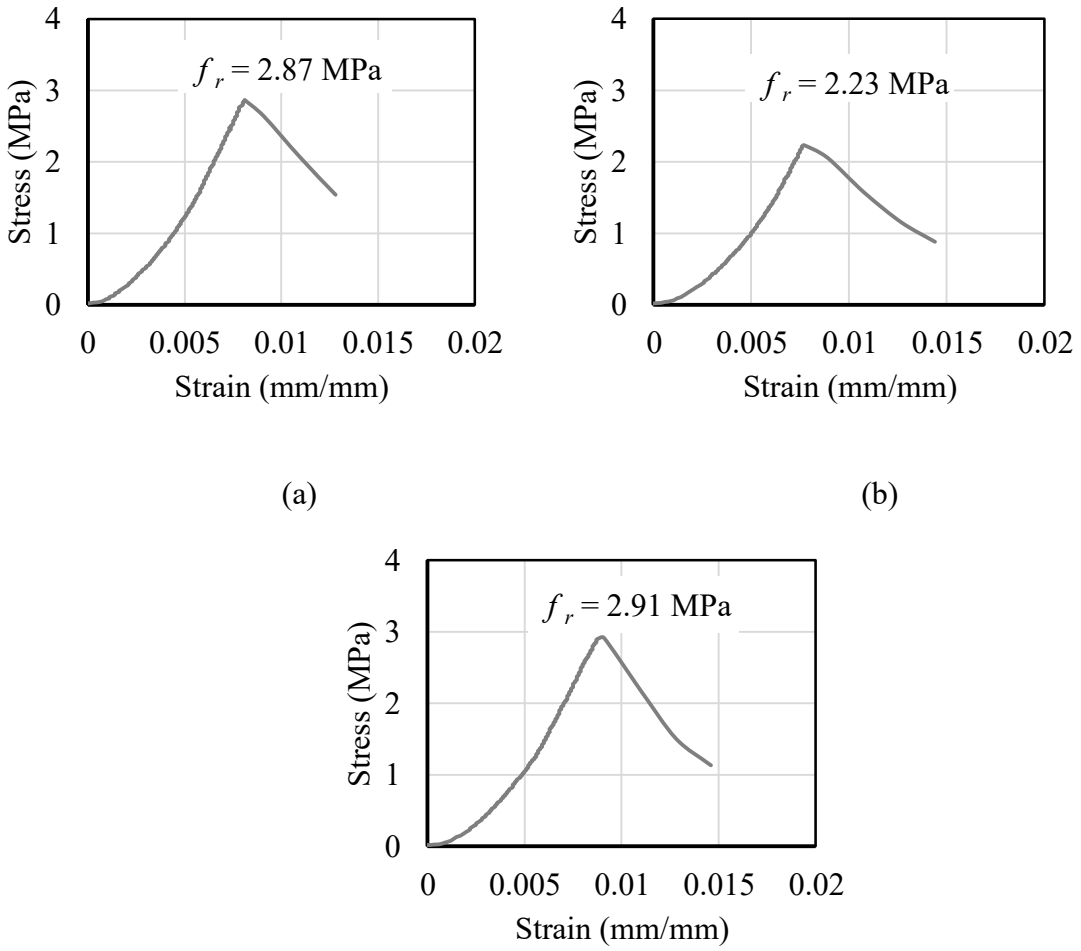

Figure E.24: Concrete tensile companion cylinders for beam-column joint specimen MD6-180: (a) cylinder A, (b) cylinder B, and (c) cylinder C

Appendix F: Sample Calculations for Regression Analysis and Student's T-Test

This appendix provides details of the calculations conducted in the analyses of the experimental results. Unequal variance is assumed. The regression analysis predicting actual tensile strength from observed compressive strength, as discussed in Section 4.2.1, is provided. Details for the Student's t-test, degrees of freedom, and standard deviation calculations are also provided.

Sample Calculation for Regression Analysis

Equation 4.2 calculates the modulus of rupture, f_r, for the concrete companion cylinders tested:

$$f_r = 0.1371\ \lambda\ f'_c{}^{0.891}$$

For a representative f'_c of 20 MPa with normal concrete density (i.e. $\lambda = 1$), the regression analysis would return the following f_r:

$$f_r = 0.1371\ (1)\ (20\text{MPa})^{0.891}$$

$$f_r = 1.98\ \text{MPa}$$

Sample Calculations for the Student's T-Test

For the statistical analysis of maximum normalized tensile load for 90° plain versus 90° modern deformed hooked bars with unequal variance:

Number of specimens containing 90° plain hooked bars, $N_{90P} = 6$

Individual maximum tensile loads for specimens containing 90° plain hooked bars:

($x_{90P1} = 15.8$, $x_{90P2} = 14.8$, $x_{90P3} = 16.3$, $x_{90P4} = 15.9$, $x_{90P5} = 18.7$, $x_{90P6} = 18.4$) kN/√MPa

Average maximum tensile load for specimens containing 90° plain hooked bars, $Y_{90P} = \frac{\sum x_{90Pi}}{N_{90P}}$

$$Y_{90P} = \frac{(15.8+14.8+16.3+15.9+18.7+18.4)\frac{kN}{\sqrt{MPa}}}{6} = 16.6 \text{ kN/}\sqrt{\text{MPa}}$$

Standard deviation for specimens containing 90° plain hooked bars, $S_{90P} = \sqrt{\frac{\sum(x_{90Pi} - Y_{90P})^2}{N_{90P}}}$

$$S_{90P} = \sqrt{\frac{((15.8-16.6)^2+(14.8-16.6)^2+(16.3-16.6)^2+(15.9-16.6)^2+(18.7-16.6)^2+(18.4-16.6)^2)*(\frac{kN}{\sqrt{MPa}})^2}{6}}$$

$S_{90P} = 1.56$ kN/√MPa

Number of specimens containing 90° modern deformed hooked bars, $N_{90MD} = 5$

Individual maximum tensile loads for specimens containing 90° modern deformed hooked bars:

($x_{90PMD} = 23.1$, $x_{90MD2} = 17.8$, $x_{90MD3} = 19.0$, $x_{90MD4} = 22.2$, $x_{90MD5} = 20.0$) kN/√MPa

Average maximum tensile load for specimens containing 90° modern deformed hooked bars, $Y_{90MD} = \frac{\sum x_{90MDi}}{N_{90MD}}$

$$Y_{90MD} = \frac{(23.1+17.8+19.0+22.2+20.0)\frac{kN}{\sqrt{MPa}}}{5} = 20.4 \text{ kN}/\sqrt{\text{MPa}}$$

Standard deviation for specimens containing 90° modern deformed hooked bars,

$$S_{90MD} = \sqrt{\frac{\sum(x_{90MDi} - Y_{90MD})^2}{N_{90MD}}}$$

$$S_{90MD} = \sqrt{\frac{((23.1-20.4)^2 + (17.8-20.4)^2 + (19.0-20.4)^2 + (22.2-20.4)^2 + (20.0-20.4)^2) * (\frac{kN}{\sqrt{MPa}})^2}{5}}$$

$S_{90MD} = 2.20 \text{ kN}/\sqrt{\text{MPa}}$

Test statistic for comparison of specimens containing 90 plain hooked bars versus 90 modern deformed hooked bars, T_{stat}:

$$T_{stat} = \frac{Y_{90MD} - Y_{90P}}{\sqrt{\frac{{S_{90MD}}^2}{N_{90MD}} + \frac{{S_{90P}}^2}{N_{90P}}}} = \frac{20.4\frac{kN}{\sqrt{MPa}} - 16.6\frac{kN}{\sqrt{MPa}}}{\sqrt{\frac{(2.20\frac{kN}{\sqrt{MPa}})^2}{5} + \frac{(1.56\frac{kN}{\sqrt{MPa}})^2}{6}}} = 3.242$$

Degrees of freedom for unequal variance, $v = \frac{(\frac{{S_{90MD}}^2}{N_{90MD}} + \frac{{S_{90P}}^2}{N_{90P}})^2}{\frac{(\frac{{S_{90MD}}^2}{N_{90MD}})^2}{N_{90MD}-1} + \frac{(\frac{{S_{90P}}^2}{N_{90P}})^2}{N_{90P}-1}}$

$$v = \frac{(\frac{(2.20\frac{kN}{\sqrt{MPa}})^2}{5} + \frac{(1.56\frac{kN}{\sqrt{MPa}})^2}{6})^2}{\frac{(\frac{2.20\frac{kN}{\sqrt{MPa}}}{5})^2}{5-1} + \frac{(\frac{1.56\frac{kN}{\sqrt{MPa}}}{6})^2}{6-1}} = 7$$

P-value via Excel[1] = 0.0142

This p-value indicates statistical significance at significance levels of 2% and higher.

[1] Value validated per T-table modified from Walpole et al. 2007

Confidence level = (1 – P value) * 100 = (1 – 0.0142) * 100 = 98.6%

98.6% > 95%, therefore, statistically significant.

Appendix G: Stress versus Strain Diagrams for Coupons Machined from Plain Reinforcing Steel

Three reinforcement companion coupons were machined from excess lengths of the plain reinforcing bars, as outlined in Section 3.8.3. All reinforcement companion coupons were taken from the same heat. Figure G.1 shows the stress versus strain diagrams for the coupons machined for plain reinforcing steel. The dynamic yield stress was taken from the stress-strain diagrams at the point at which slope changed from linear and positive to non-linear. The modulus of elasticity was calculated using the average slope in the elastic range after the slope had stabilized.

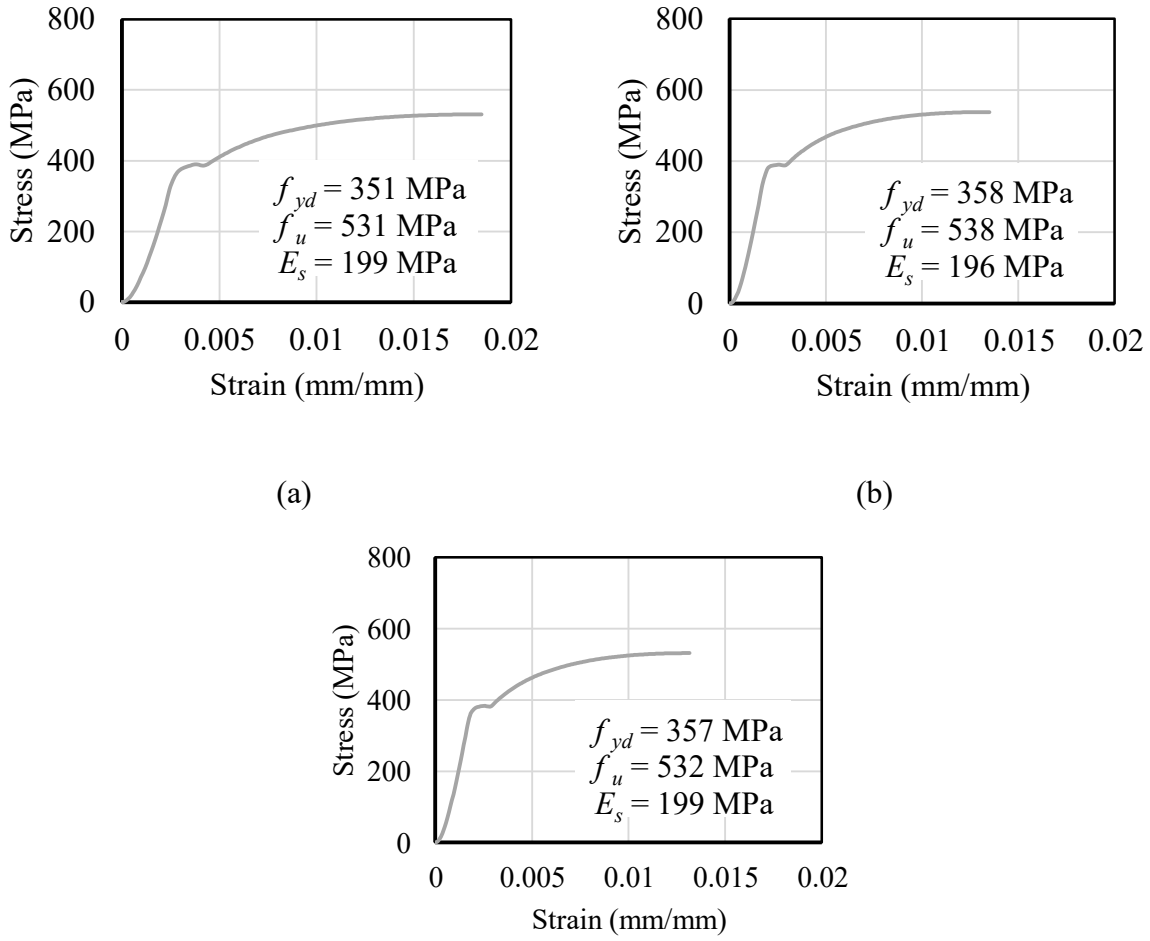

Figure G.1: Stress versus strain diagrams for plain reinforcement: coupon A, (b) coupon B, and (c) coupon C

Appendix H: Stress versus Strain Diagrams for Intact Lengths of Modern Deformed Reinforcing Steel

Three lengths of the modern deformed reinforcement were tested to find the elastic modulus, yield strength and ultimate strength of the reinforcing steel. All lengths were taken from the same heat. Figure H.1 shows the stress versus strain diagrams. Figure H.1 (b) shows the second length (B) failed at approximately 55% of the strain compared to the other two companion coupons. This is hypothesized to have resulted from a stress concentration, random inclusion, or some preexisting damage such as a microcrack in the tested specimen. The dynamic yield stress was taken from the stress-strain diagrams at the point at which slope changed from linear and positive to non-linear. The modulus of elasticity was calculated using the average slope in the elastic range after the slope had stabilized.

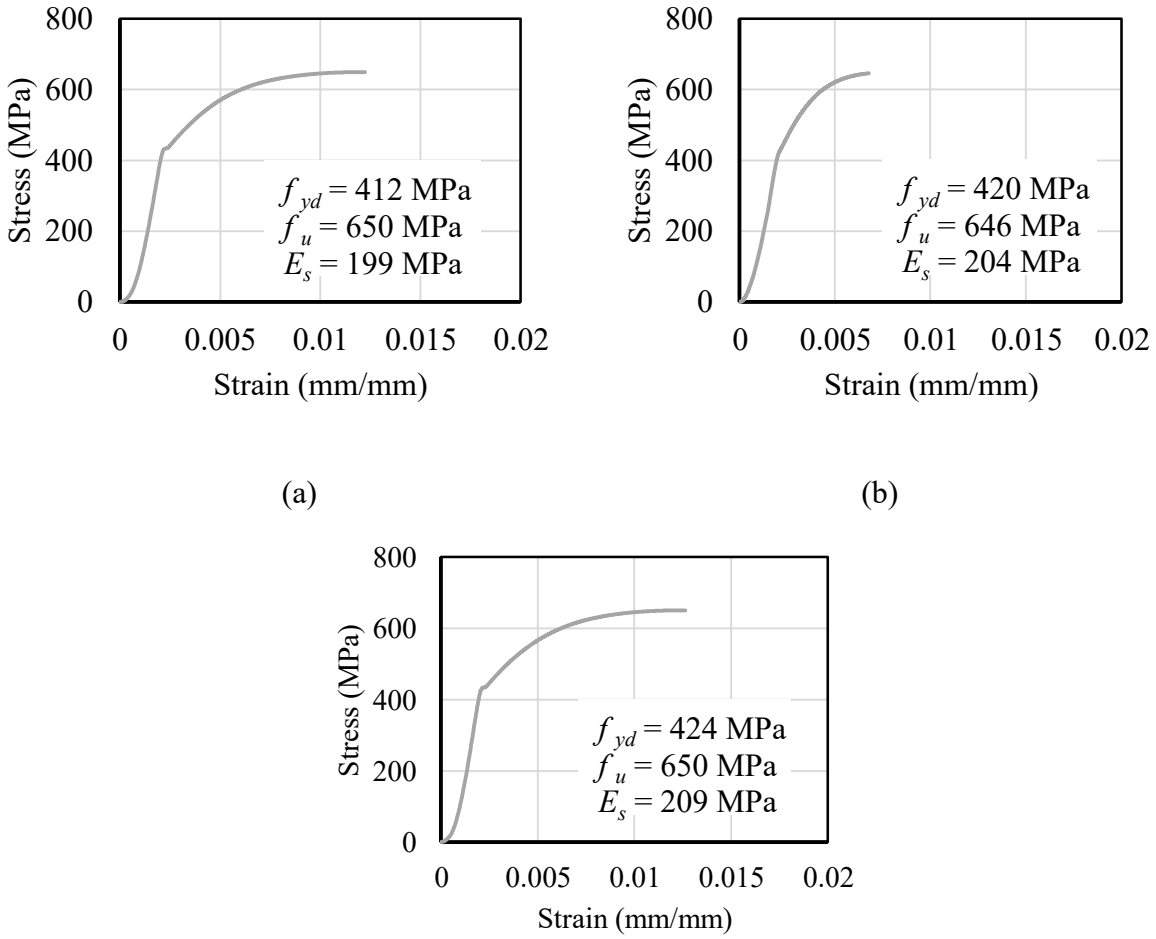

Figure H.1: Stress versus strain diagrams for modern deformed reinforcement: (a) length A, (b) length B, and (c) length C

Appendix I: Axial Load Applied to the Beam-Column Joint Specimens

Applied axial load was held constant throughout testing for each beam-column joint specimen. The axial load was set to the target value of 200kN with a slugging wrench prior to test initiation. Table I.1 provides the average as measured axial load for each beam-column joint specimen test. Section 3.7 describes how the axial load was measured.

Table I.1: Axial load values for each beam column joint specimen

Specimen ID	Average Axial Load P_c (kN)	Standard deviation S_{Pc} (kN)	Specimen ID	Average Axial Load P_c (kN)	Standard deviation S_{Pc} (kN)
P1-90	189	5.07	MD1-90	207	5.70
P2-90	196	3.51	MD2-90	194	0.723
P3-90	196	2.18	MD3-90	201	1.48
P4-90	197	2.42	MD4-90	198	1.29
P5-90	203	1.79	MD5-90	200	0.860
P6-90	209	0.907	MD6-90	197	1.60
P1-180	207	1.92	MD1-180	210	5.26
P2-180	200	4.13	MD2-180	202	1.98
P3-180	208	0.387	MD3-180	212	9.39
P4-180	213	1.55	MD4-180	207	2.66
P5-180	213	4.50	MD5-180	207	0.780
P6-180	211	0.713	MD6-180	201	1.53

Appendix J: Crack Patterns for Beam-Column Joint Specimens

Cracks were marked as testing progressed, as discussed in Section 4.3.1, to accurately assess crack propagation and aid in failure mode determination. Figures J.1 to J.24 show crack patterns at P_{max}. All figures present the west side face, back face, east side face, and front face of each specimen.

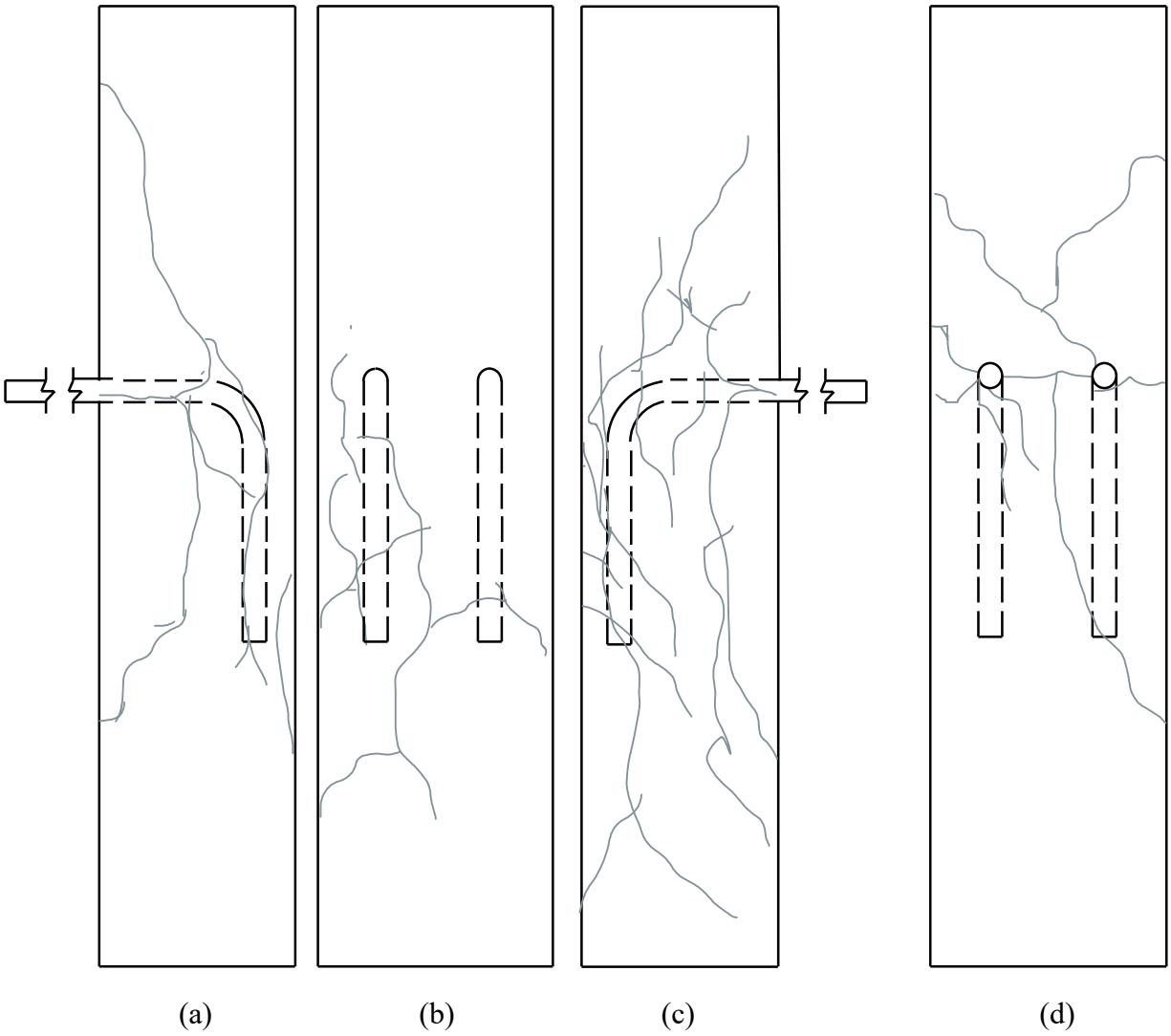

Figure J.1: Crack pattern at maximum normalized tensile load for beam-column joint specimen P1-90: (a) west side face, (b) back face, (c) east side face, and (d) front face

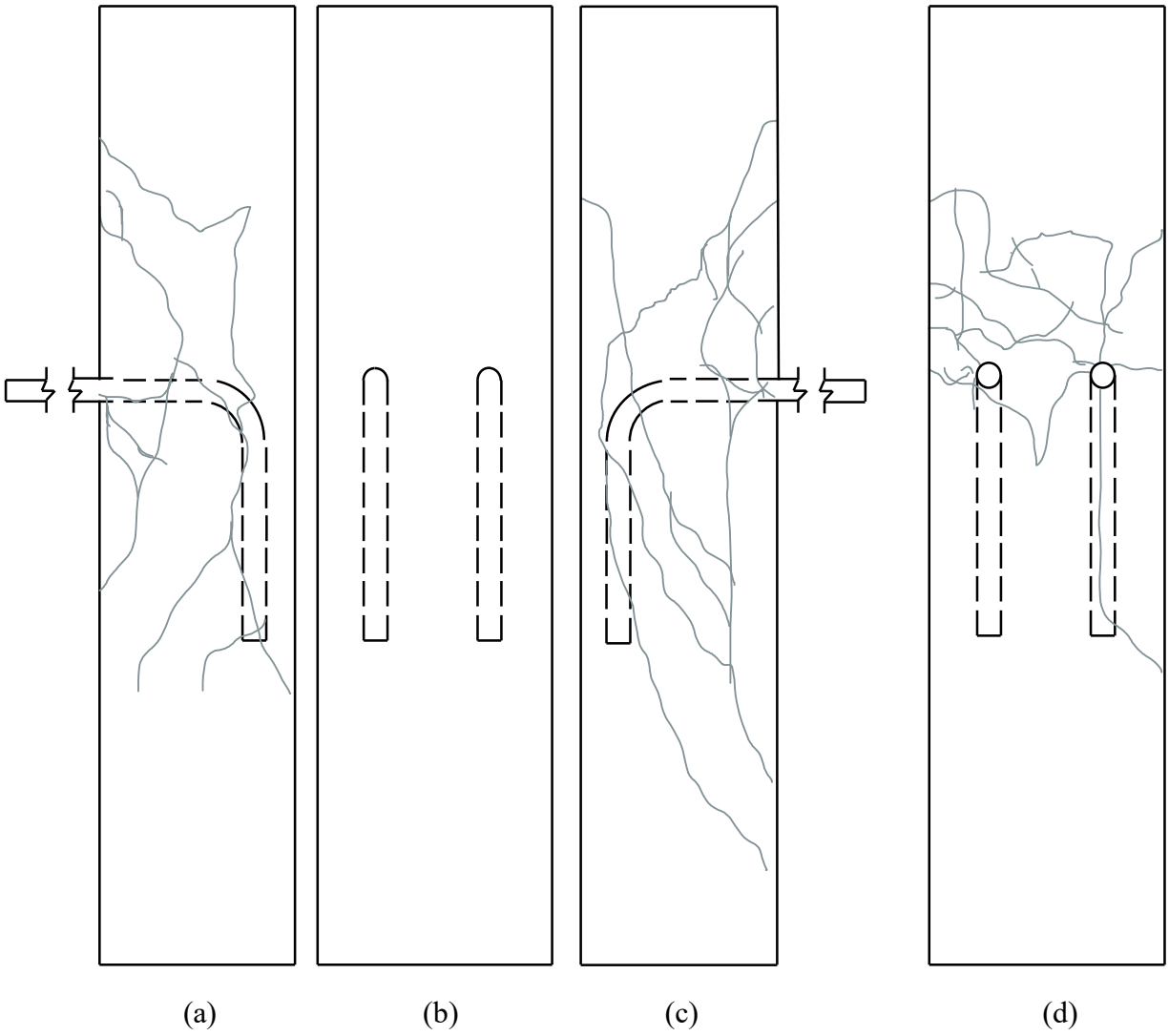

Figure J.2: Crack pattern at maximum normalized tensile load for beam-column joint specimen P2-90: (a) west side face, (b) back face, (c) east side face, and (d) front face

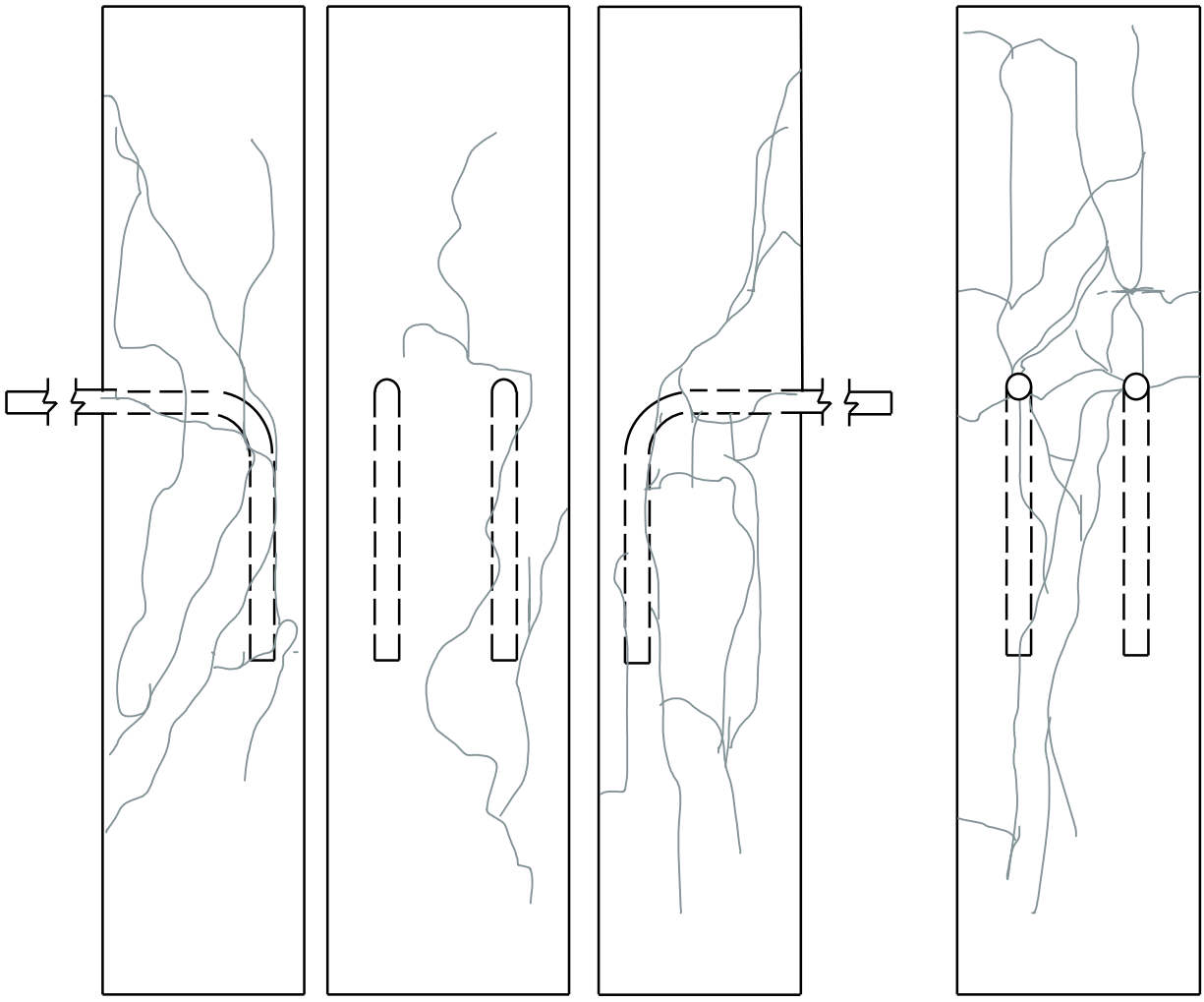

Figure J.3: Crack pattern at maximum normalized tensile load for beam-column joint specimen P3-90: (a) west side face, (b) back face, (c) east side face, and (d) front face

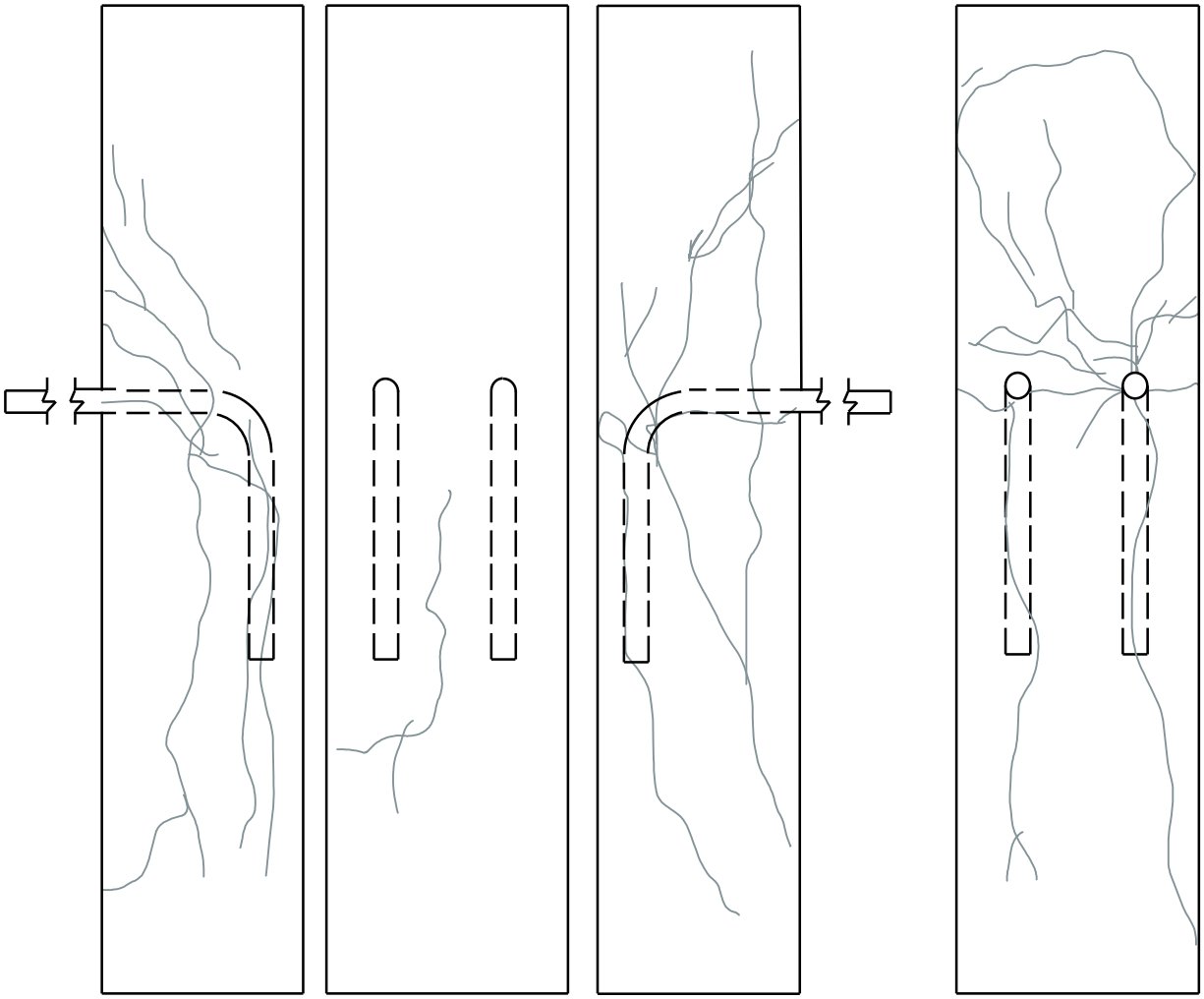

Figure J.4: Crack pattern at maximum normalized tensile load for beam-column joint specimen P4-90: (a) west side face, (b) back face, (c) east side face, and (d) front face

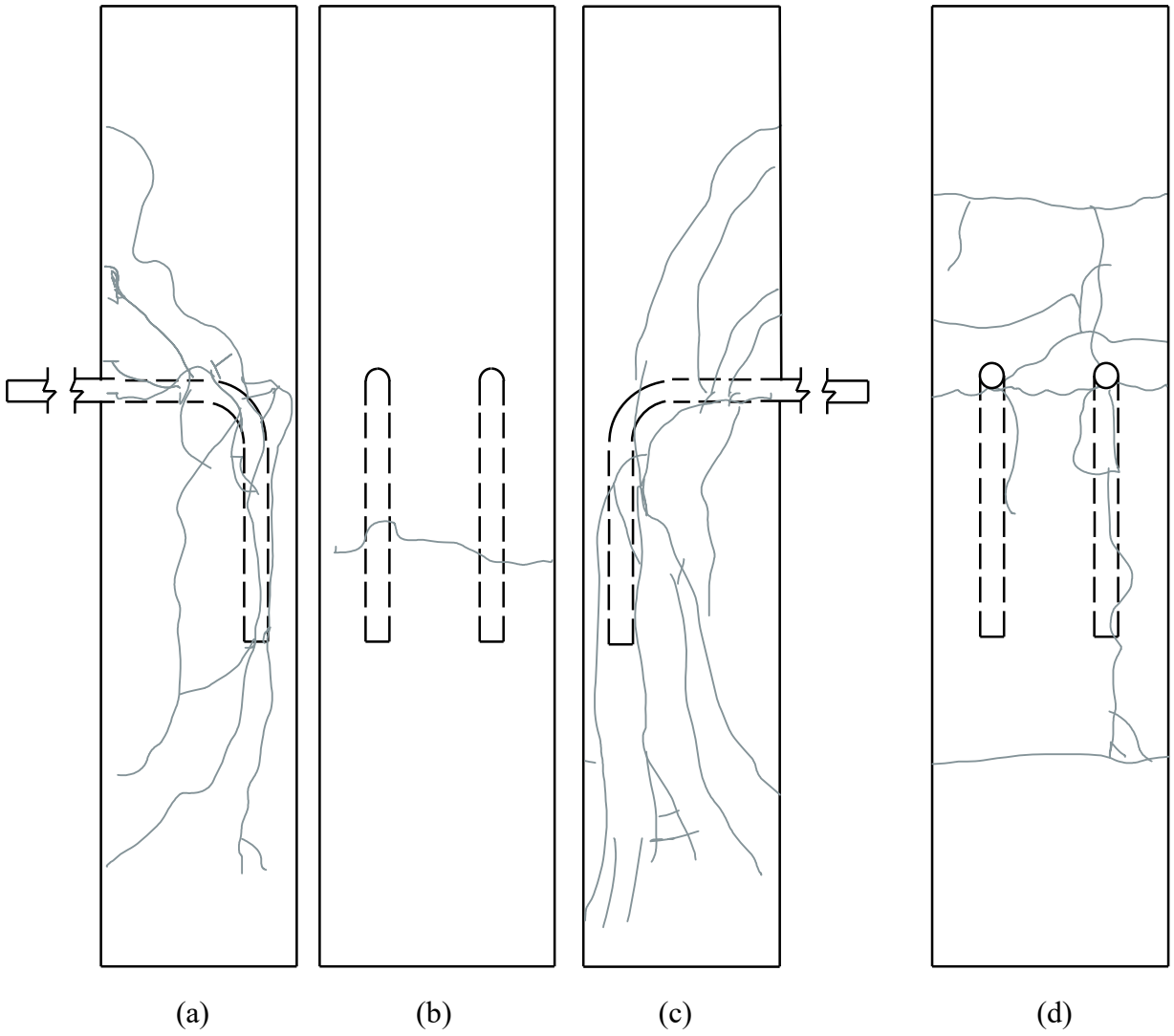

Figure J.5: Crack pattern at maximum normalized tensile load for beam-column joint specimen P5-90: (a) west side face, (b) back face, (c) east side face, and (d) front face

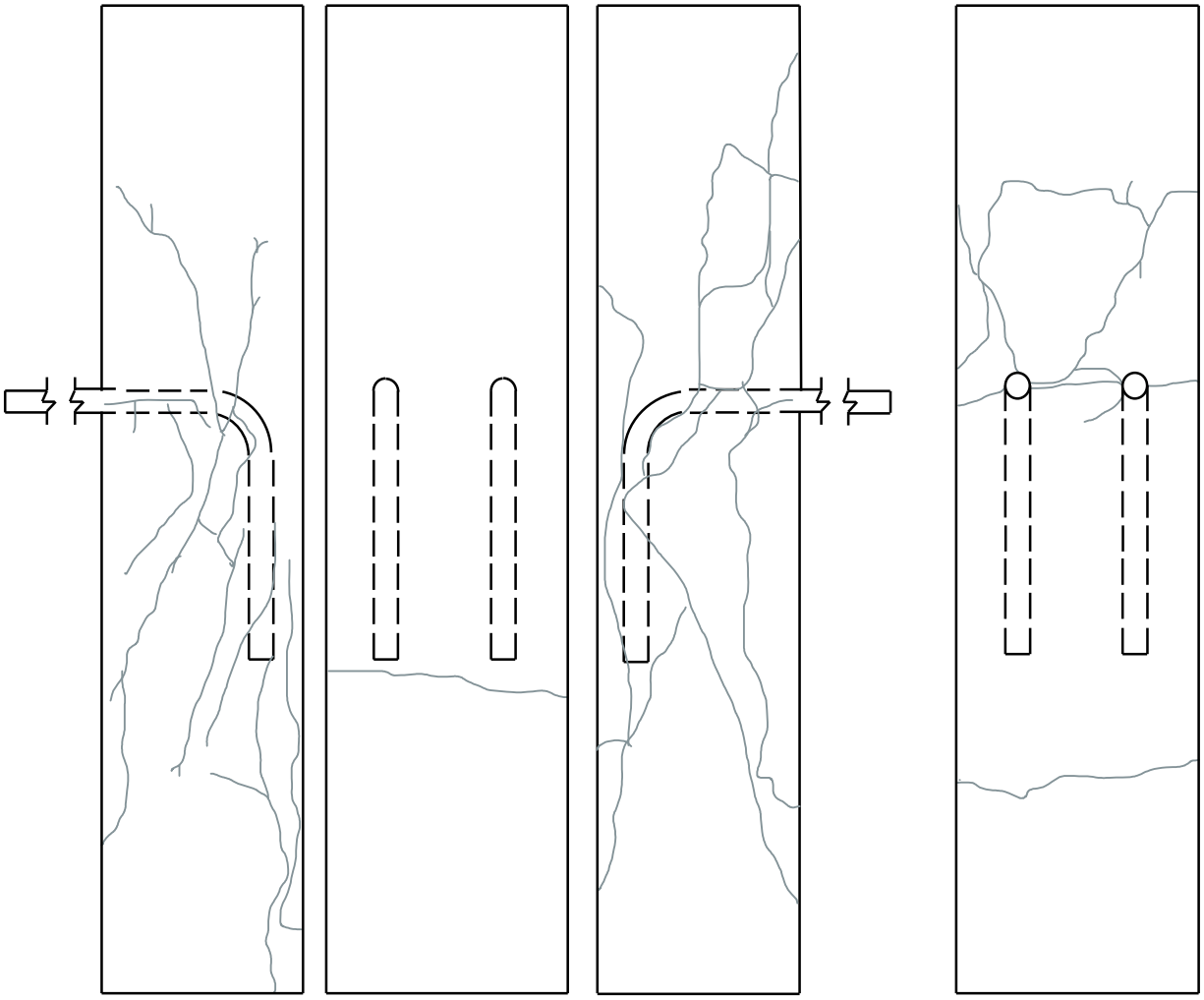

Figure J.6: Crack pattern at maximum normalized tensile load for beam-column joint specimen P6-90: (a) west side face, (b) back face, (c) east side face, and (d) front face

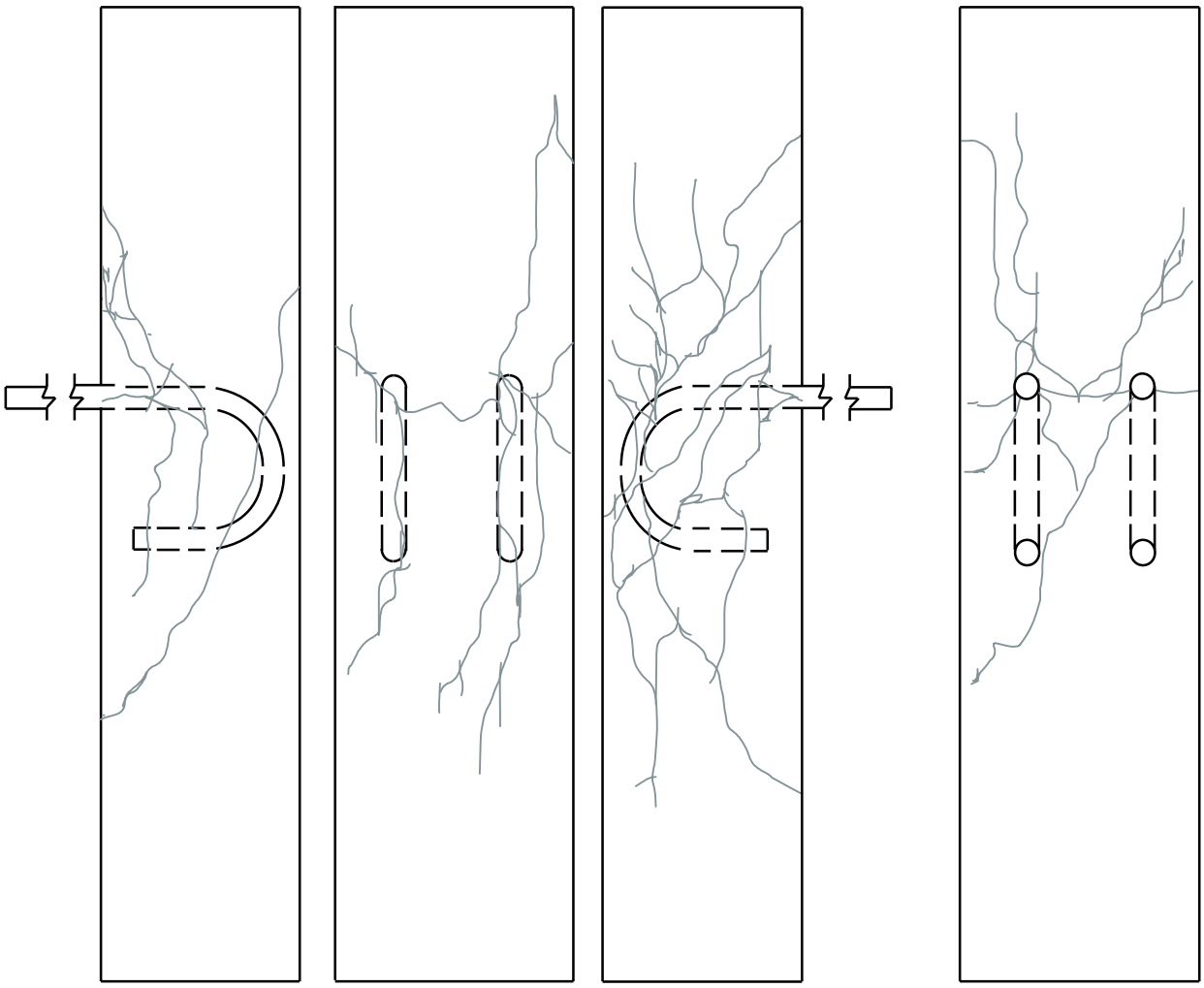

Figure J.7: Crack pattern at maximum normalized tensile load for beam-column joint specimen P1-180: (a) west side face, (b) back face, (c) east side face, and (d) front face

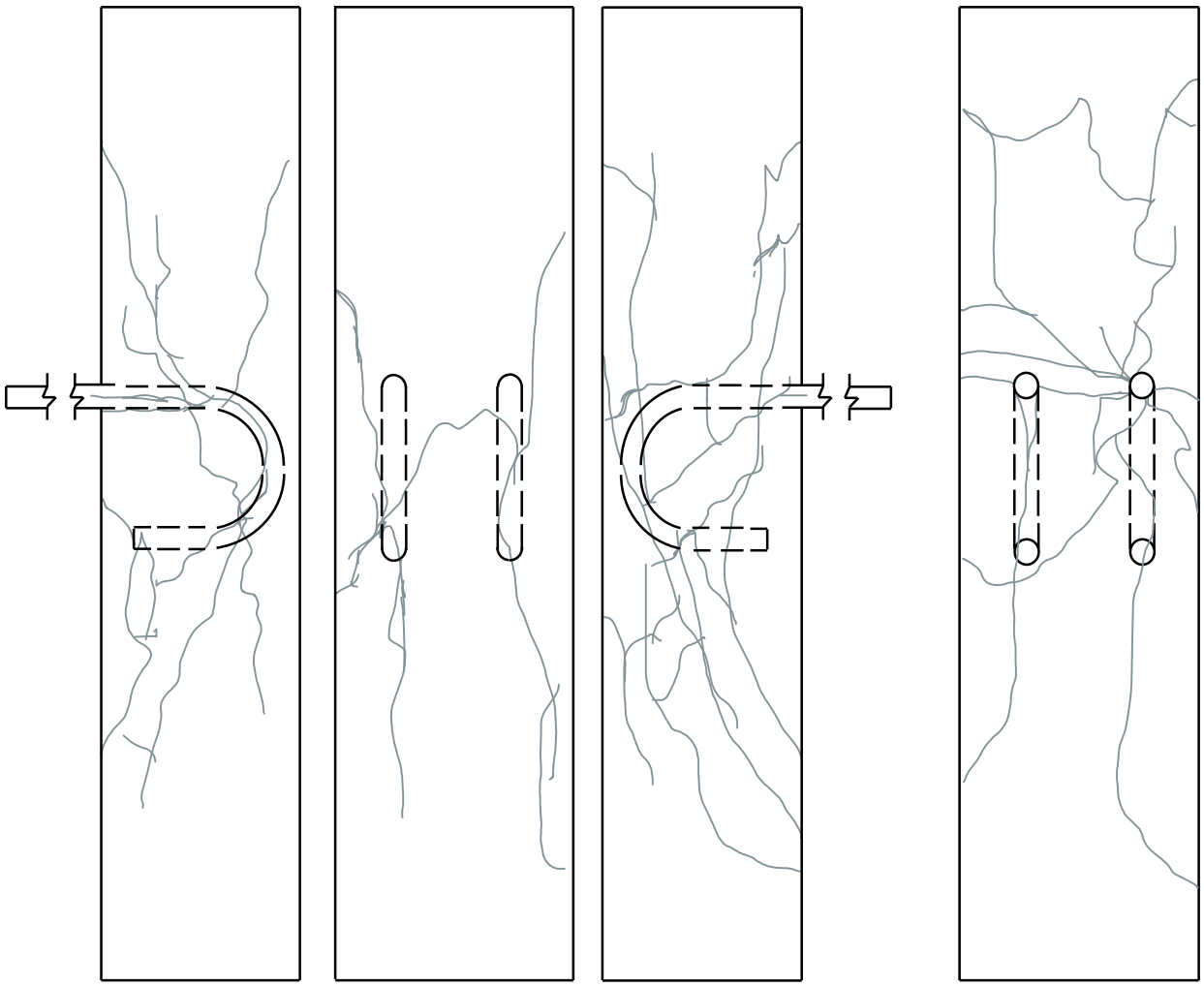

Figure J.8: Crack pattern at maximum normalized tensile load for beam-column joint specimen P2-180, which was deemed an outlier: (a) west side face, (b) back face, (c) east side face, and (d) front face

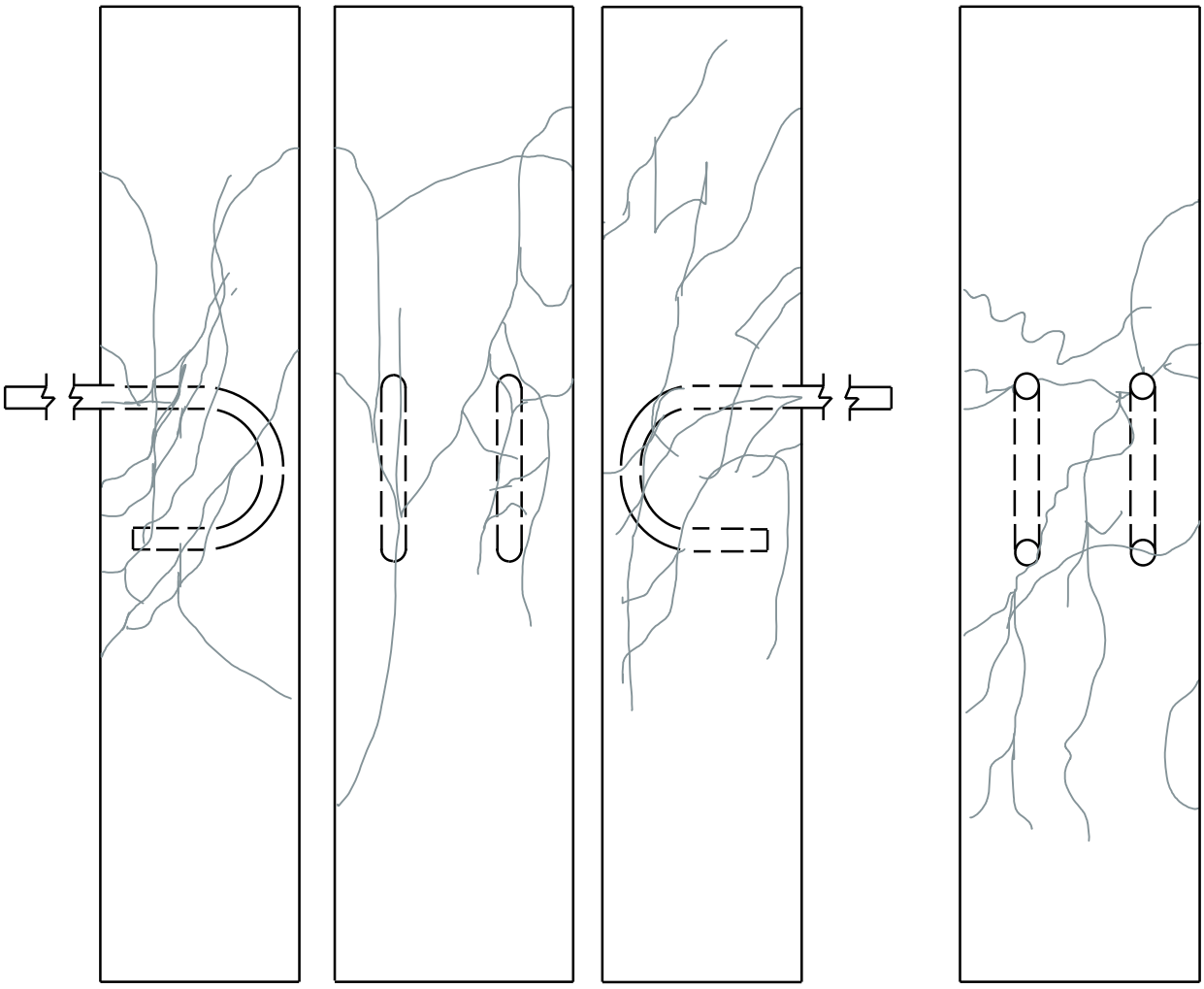

Figure J.9: Crack pattern at maximum normalized tensile load for beam-column joint specimen P3-180: (a) west side face, (b) back face, (c) east side face, and (d) front face

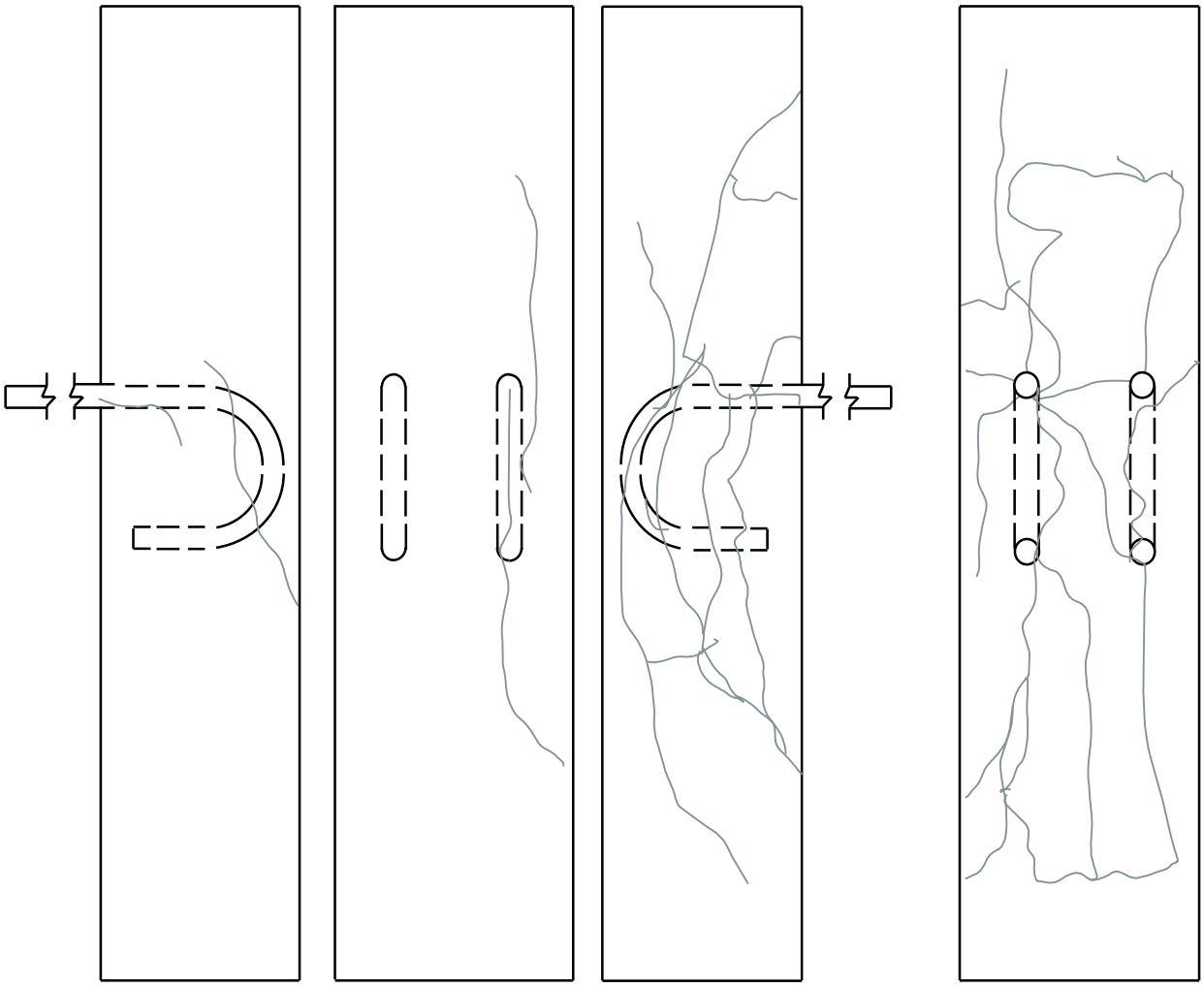

Figure J.10: Crack pattern at maximum normalized tensile load for beam-column joint specimen P4-180 which was deemed an outlier: (a) west side face, (b) back face, (c) east side face, and (d) front face

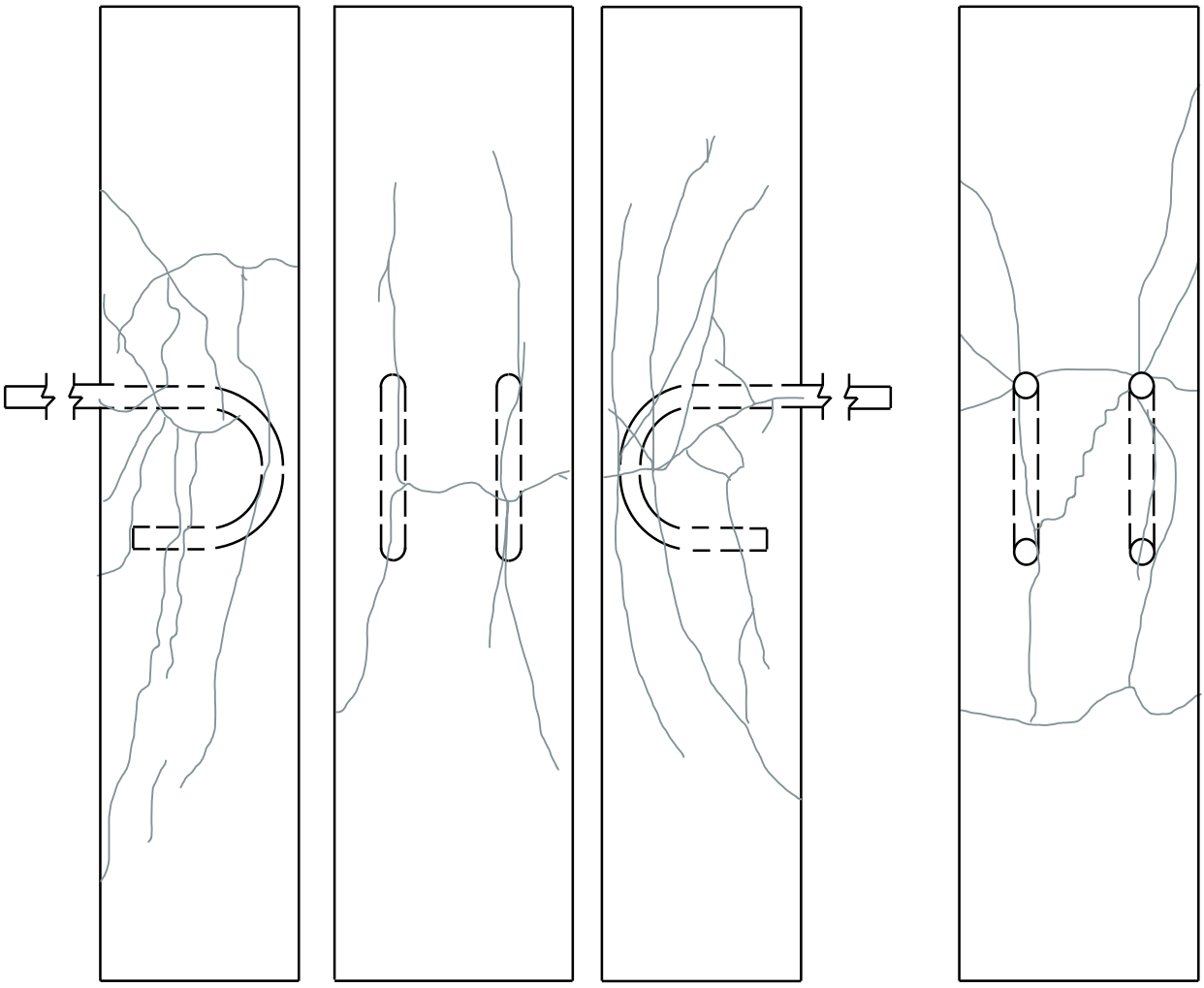

Figure J.11: Crack pattern at maximum normalized tensile load for beam-column joint specimen P5-180: (a) west side face, (b) back face, (c) east side face, and (d) front face

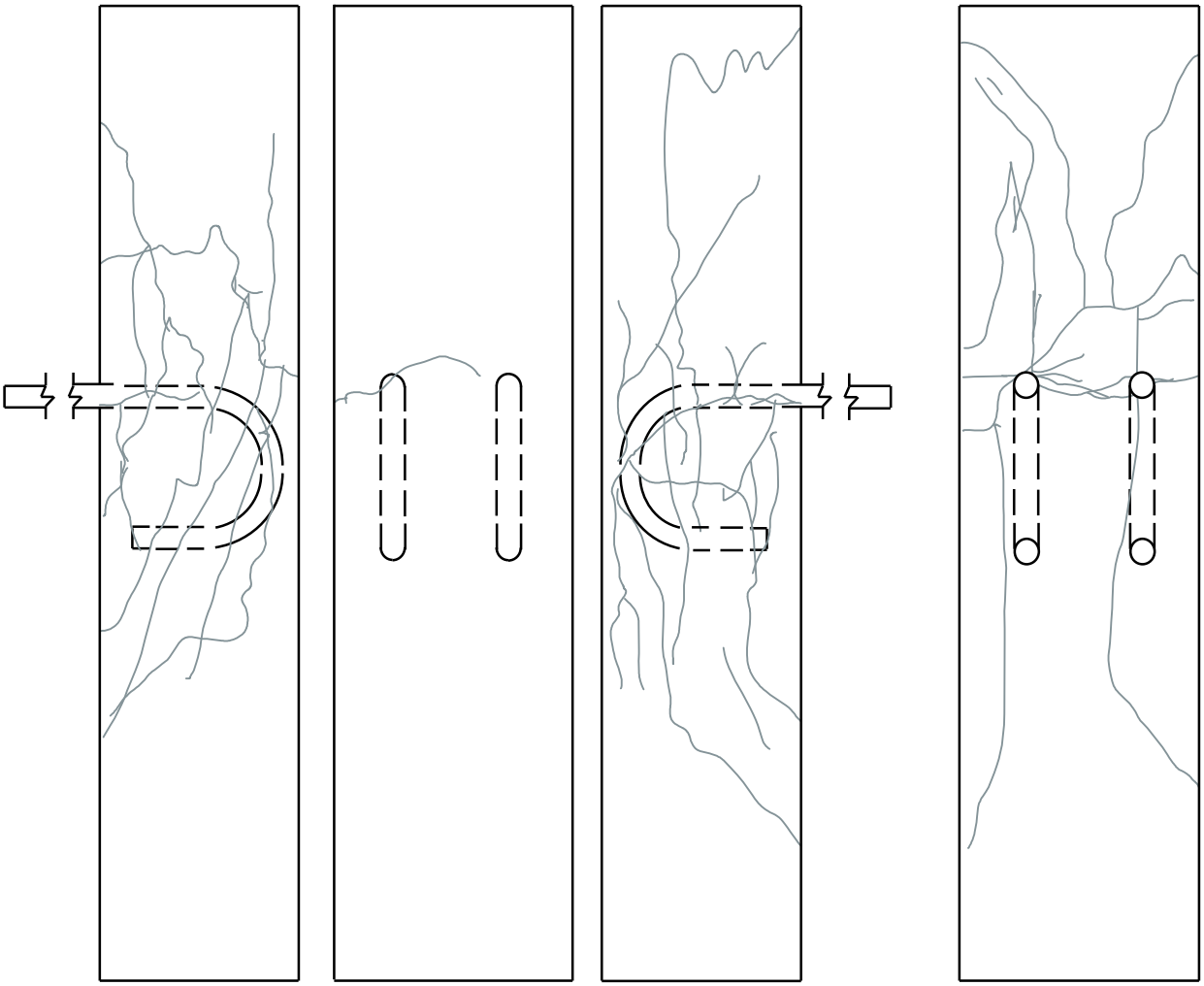

Figure J.12: Crack pattern at maximum normalized tensile load for beam-column joint specimen P6-180: (a) west side face, (b) back face, (c) east side face, and (d) front face

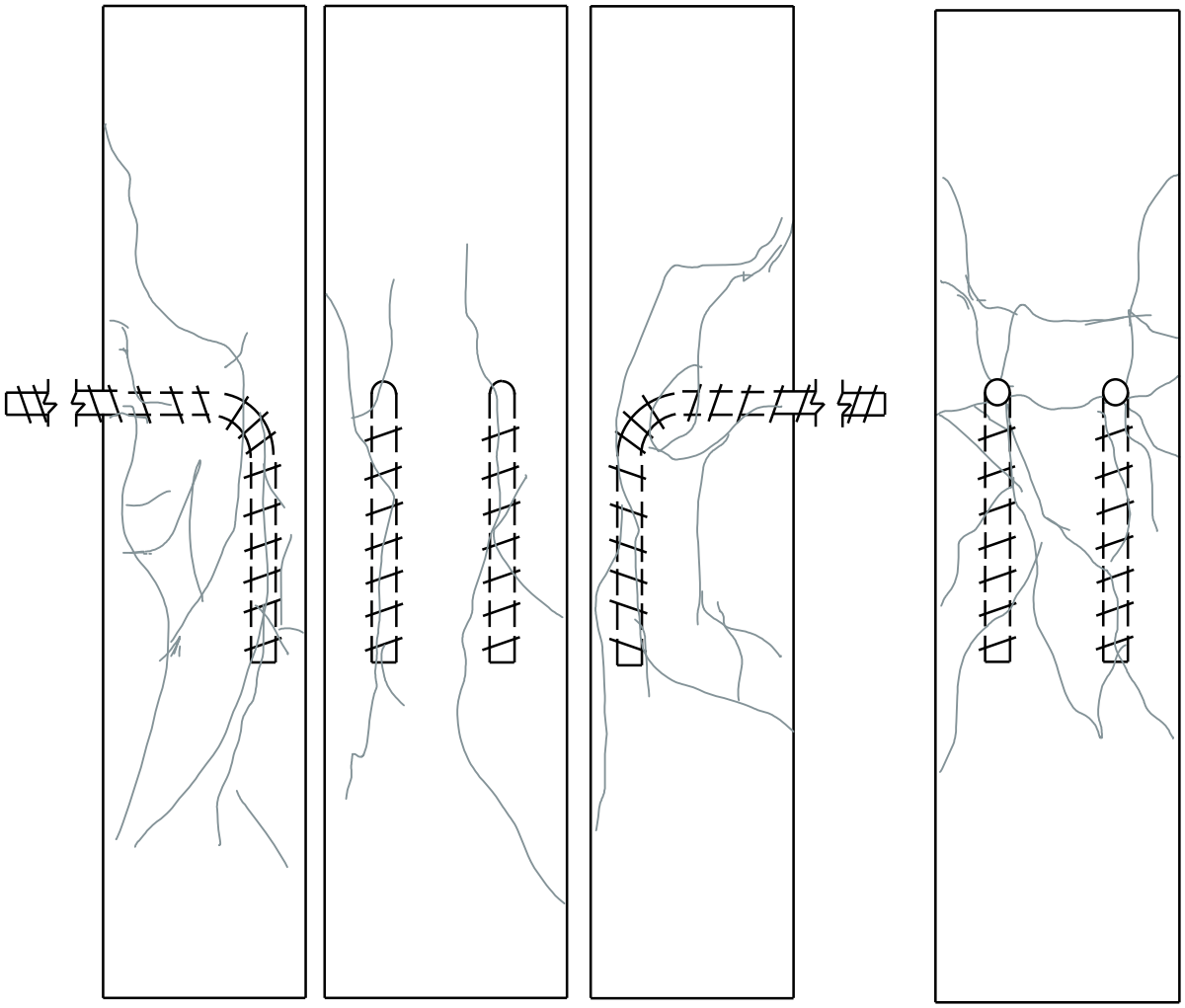

(a) (b) (c) (d)

Figure J.13: Crack pattern at maximum normalized tensile load for beam-column joint specimen MD1-90: (a) west side face, (b) back face, (c) east side face, and (d) front face

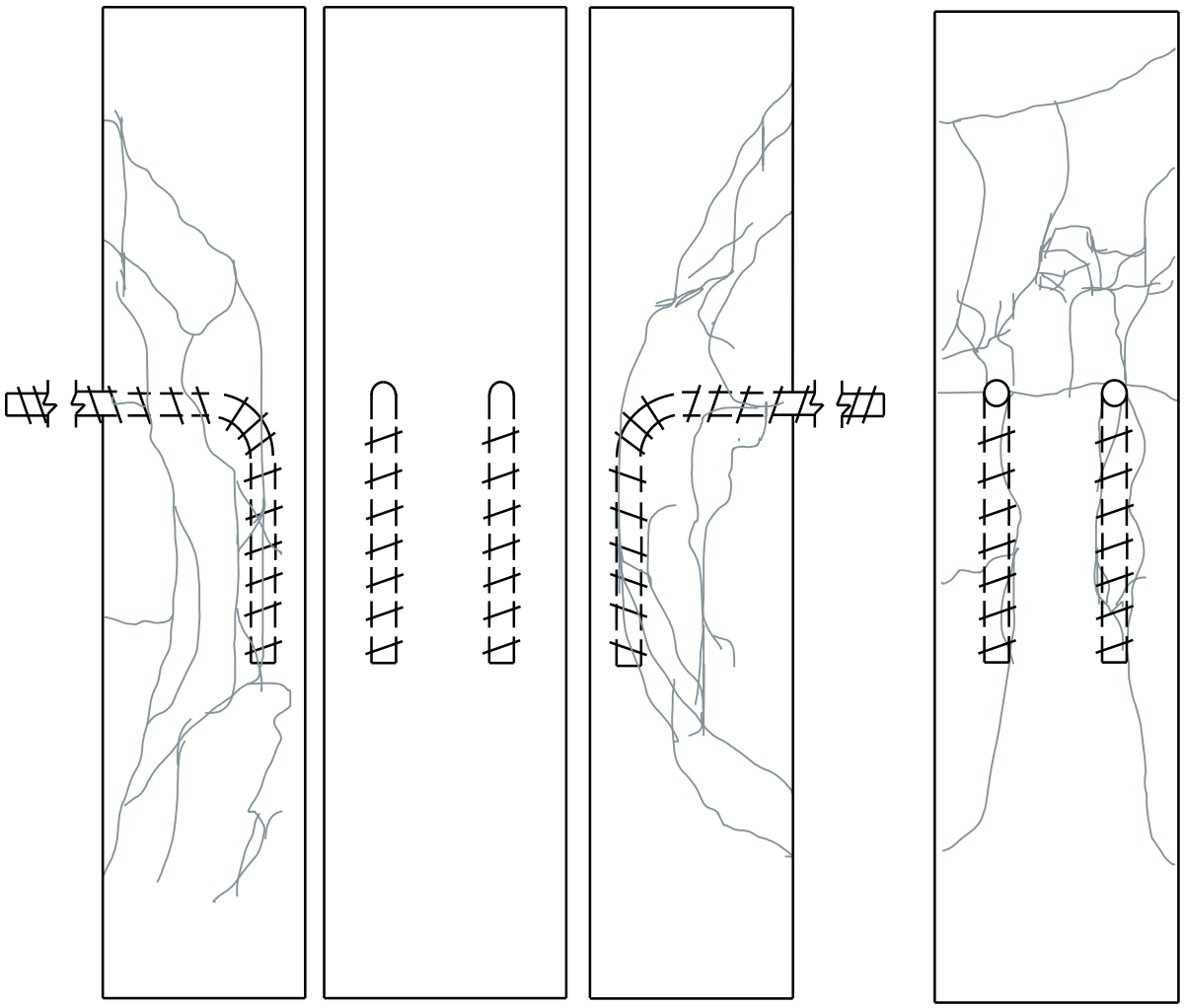

(a) (b) (c) (d)

Figure J.14: Crack pattern at maximum normalized tensile load for beam-column joint specimen MD2-90 which was deemed an outlier: (a) west side face, (b) back face, (c) east side face, and (d) front face

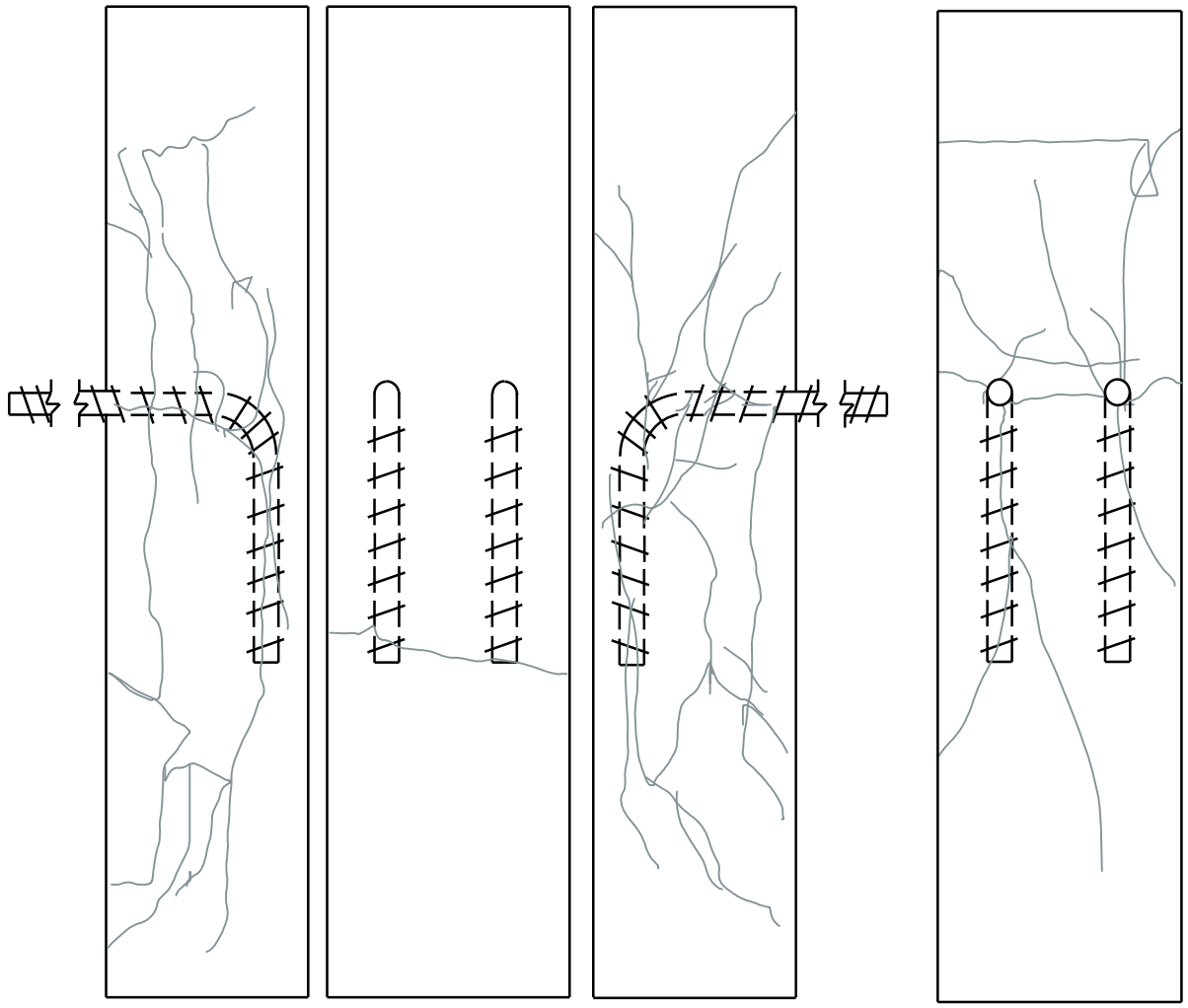

(a) (b) (c) (d)

Figure J.15: Crack pattern at maximum normalized tensile load for beam-column joint specimen MD3-90: (a) west side face, (b) back face, (c) east side face, and (d) front face

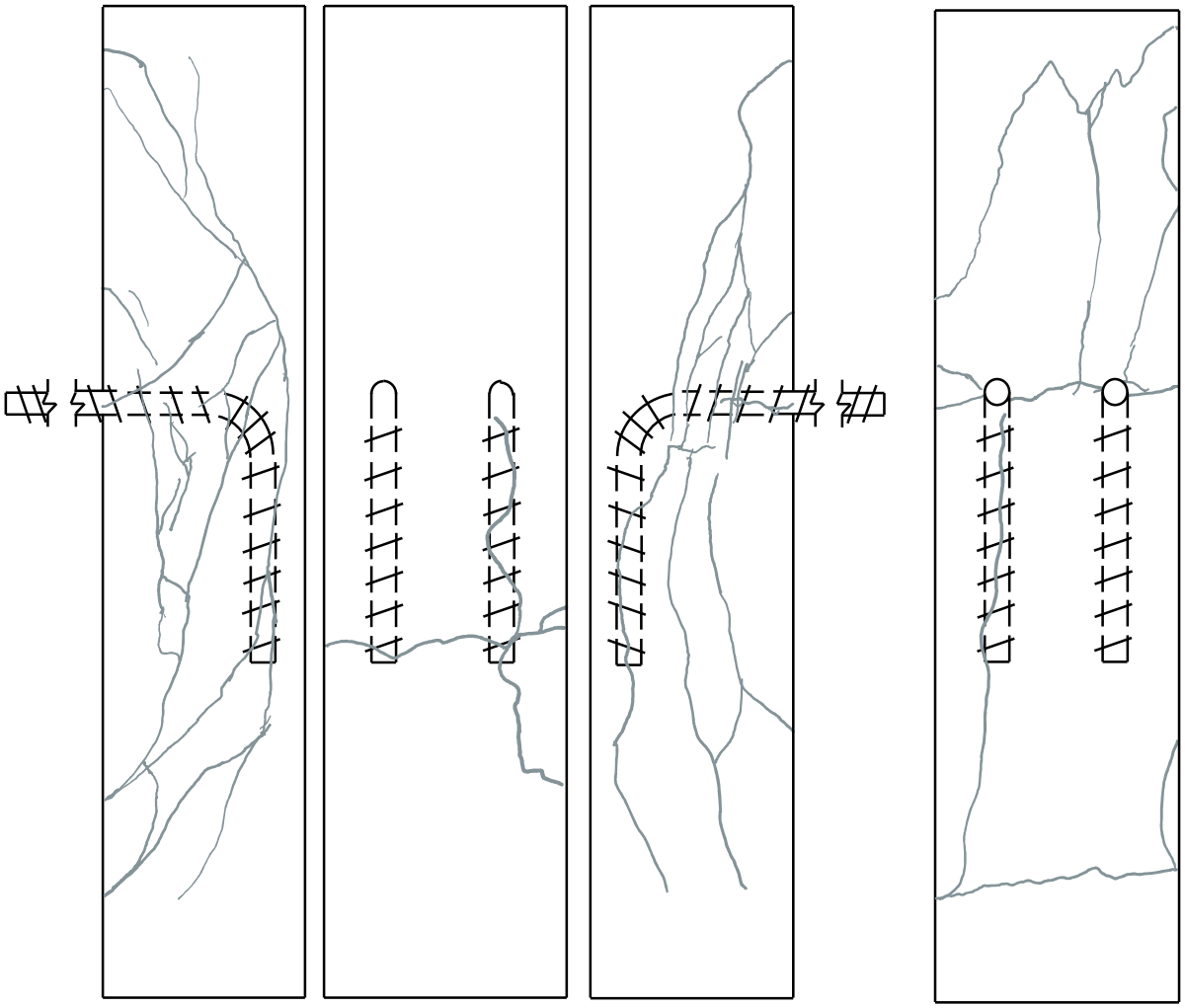

(a) (b) (c) (d)

Figure J.16: Crack pattern at maximum normalized tensile load for beam-column joint specimen MD4-90: (a) west side face, (b) back face, (c) east side face, and (d) front face

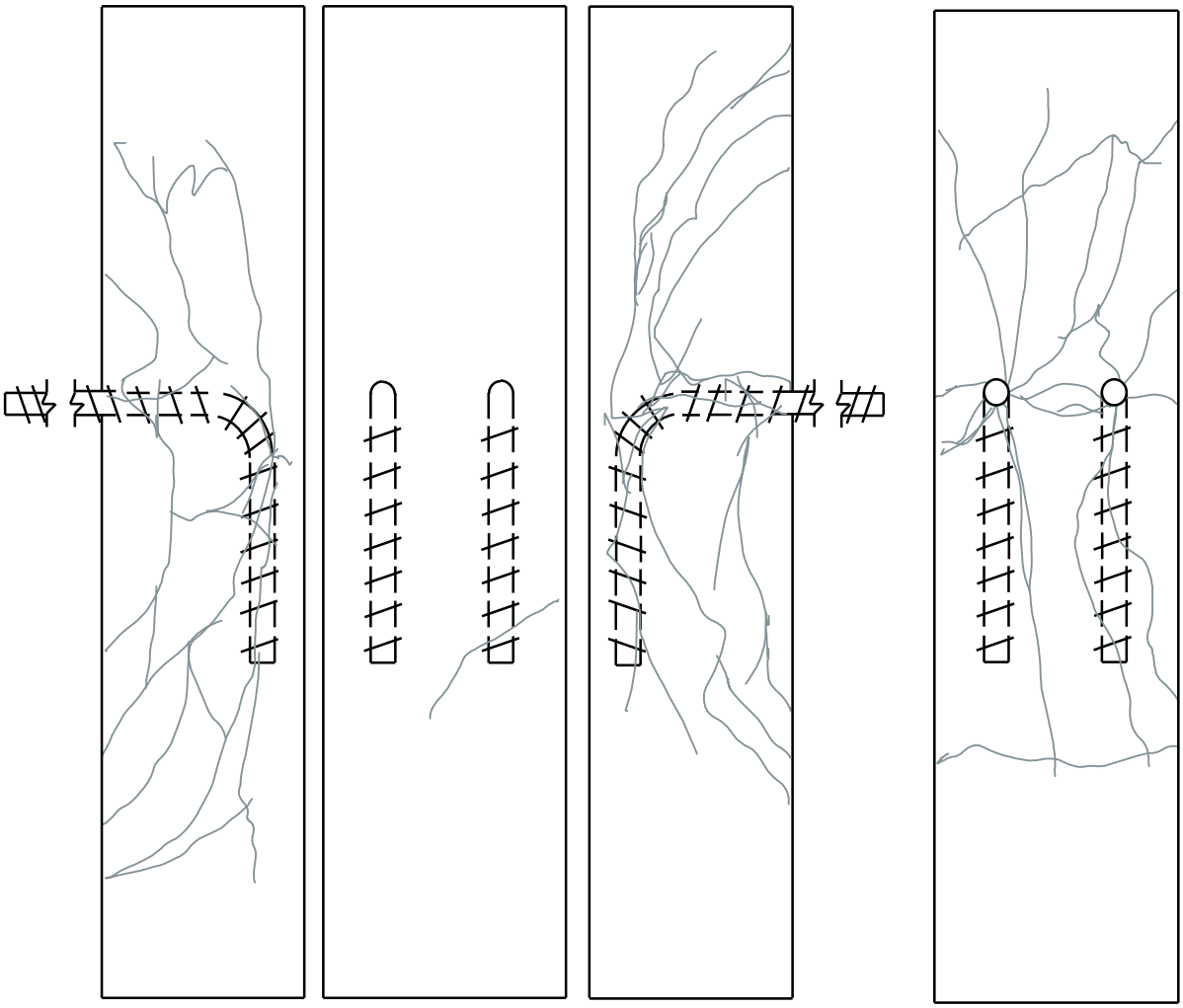

(a) (b) (c) (d)

Figure J.17: Crack pattern at maximum normalized tensile load for beam-column joint specimen MD5-90: (a) west side face, (b) back face, (c) east side face, and (d) front face

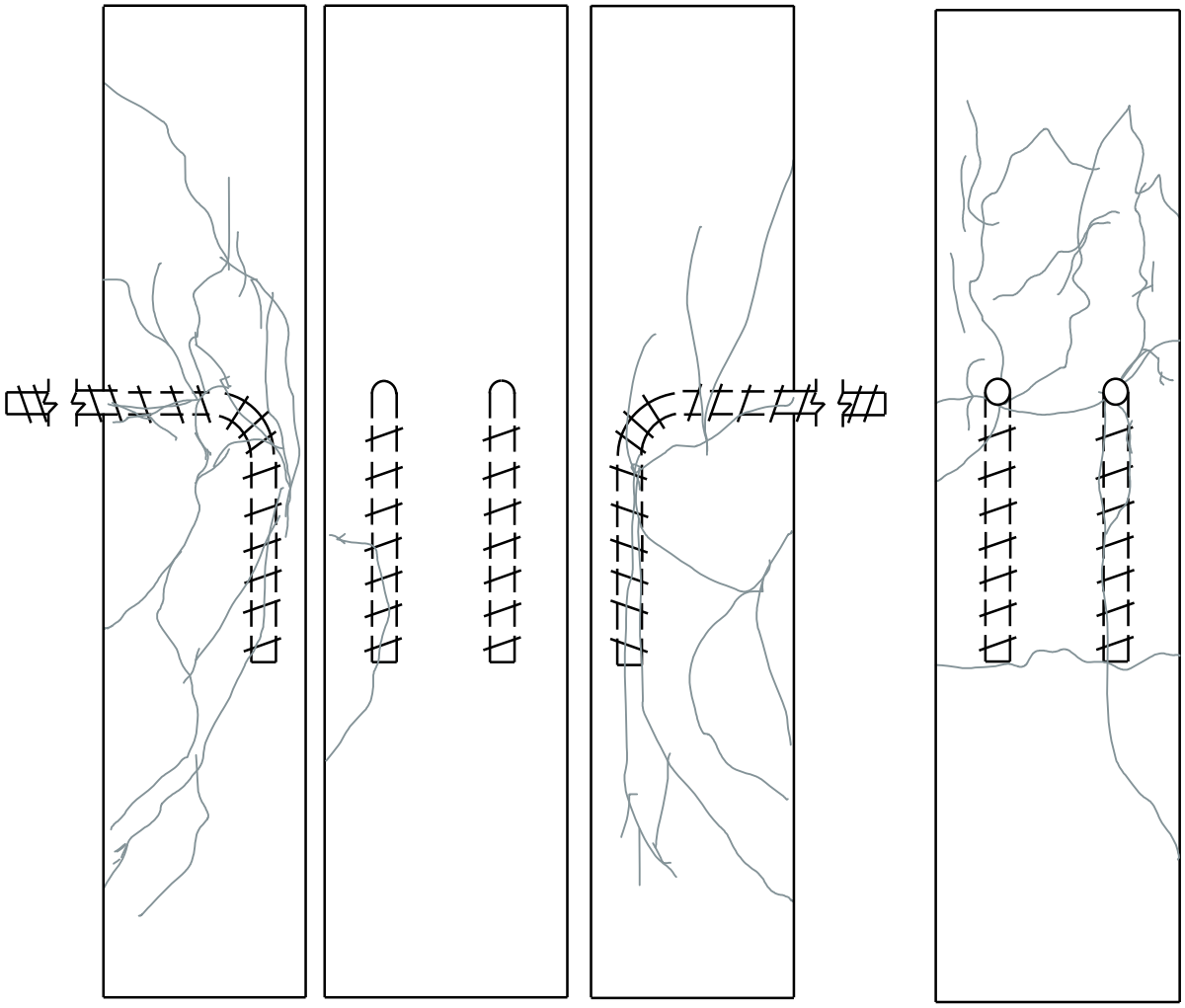

(a) (b) (c) (d)

Figure J.18: Crack pattern at maximum normalized tensile load for beam-column joint specimen MD6-90: (a) west side face, (b) back face, (c) east side face, and (d) front face

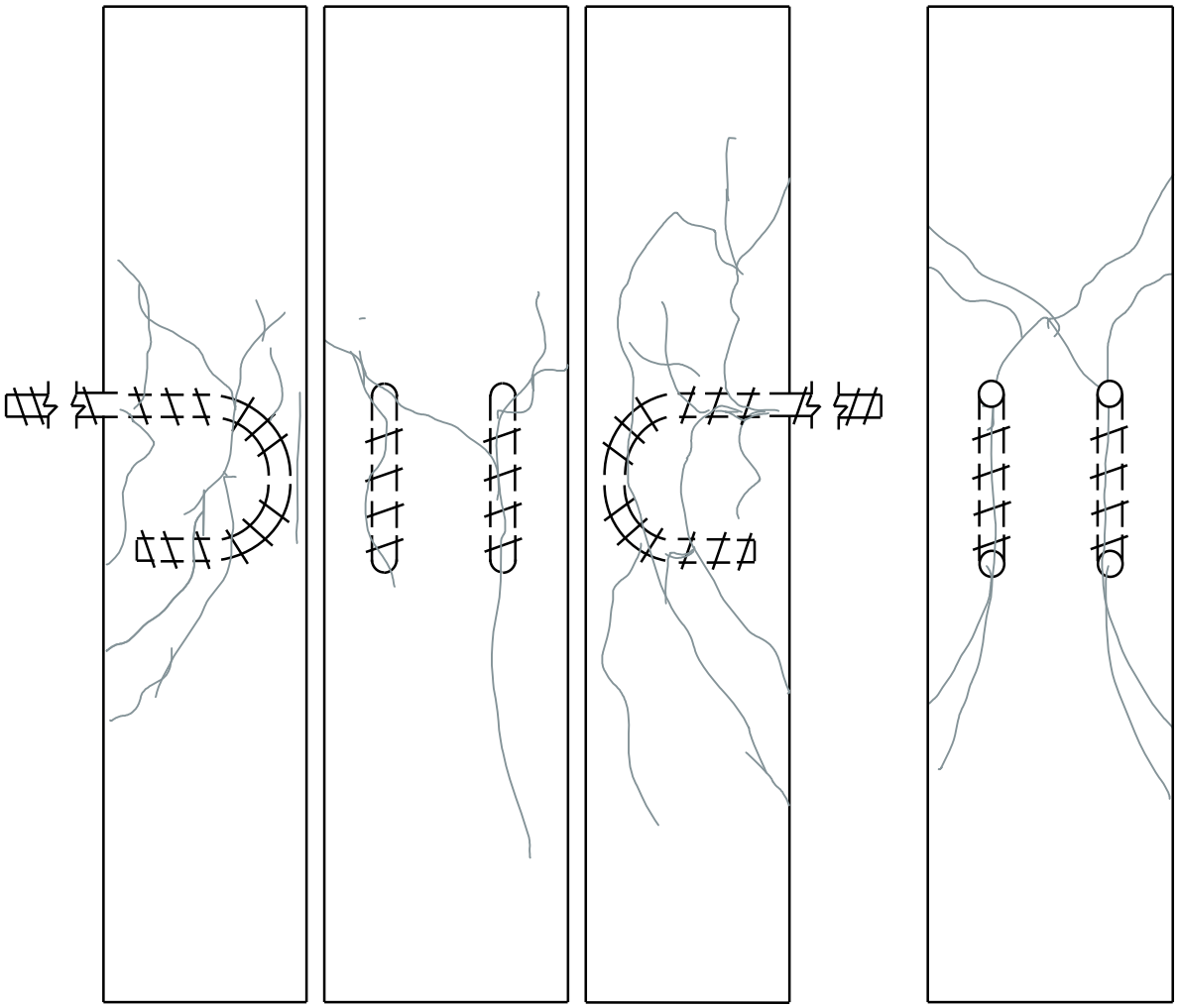

(a) (b) (c) (d)

Figure J.19: Crack pattern at maximum normalized tensile load for beam-column joint specimen MD1-180: (a) west side face, (b) back face, (c) east side face, and (d) front face

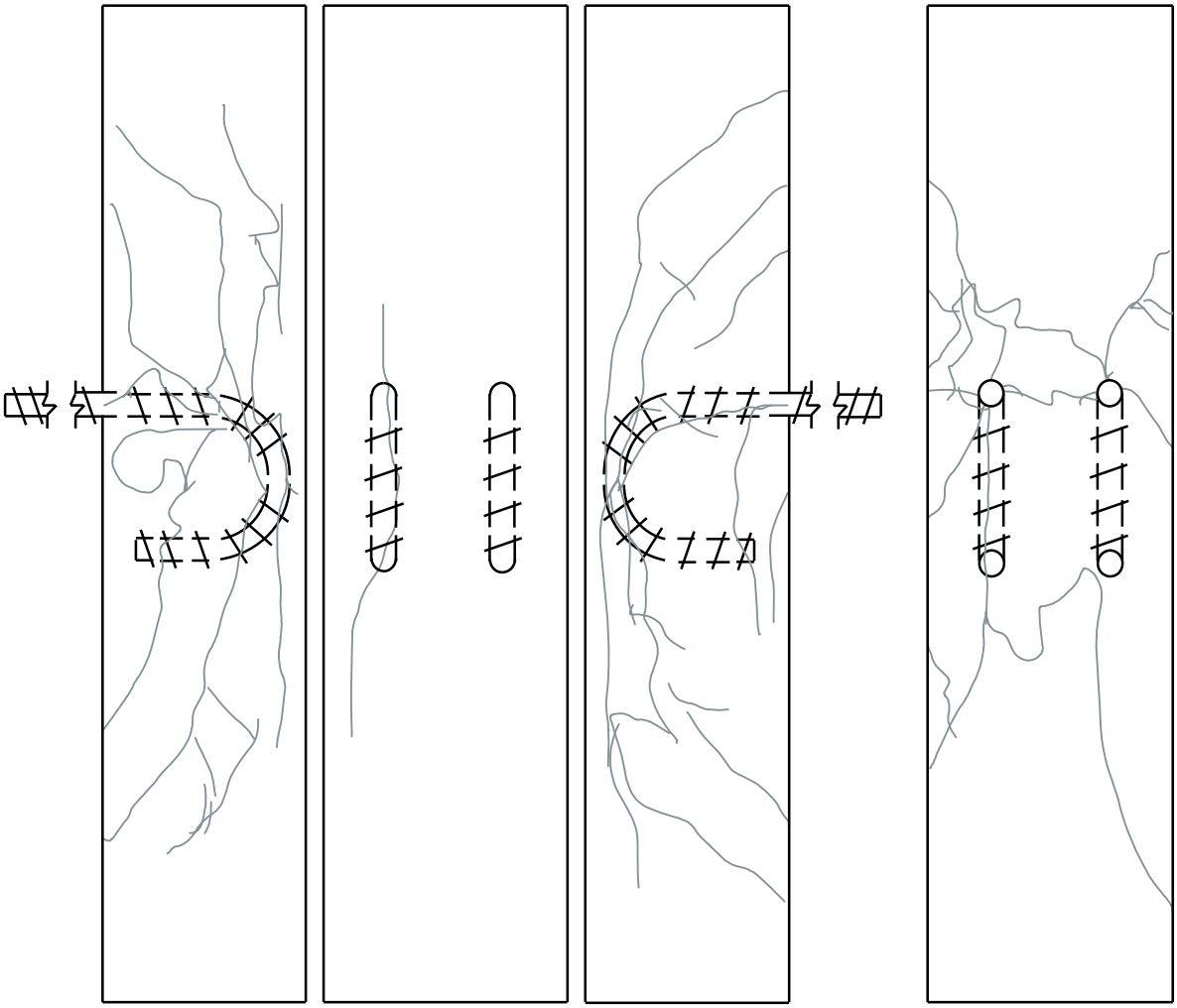

(a) (b) (c) (d)

Figure J.20: Crack pattern at maximum normalized tensile load for beam-column joint specimen MD2-180: (a) west side face, (b) back face, (c) east side face, and (d) front face

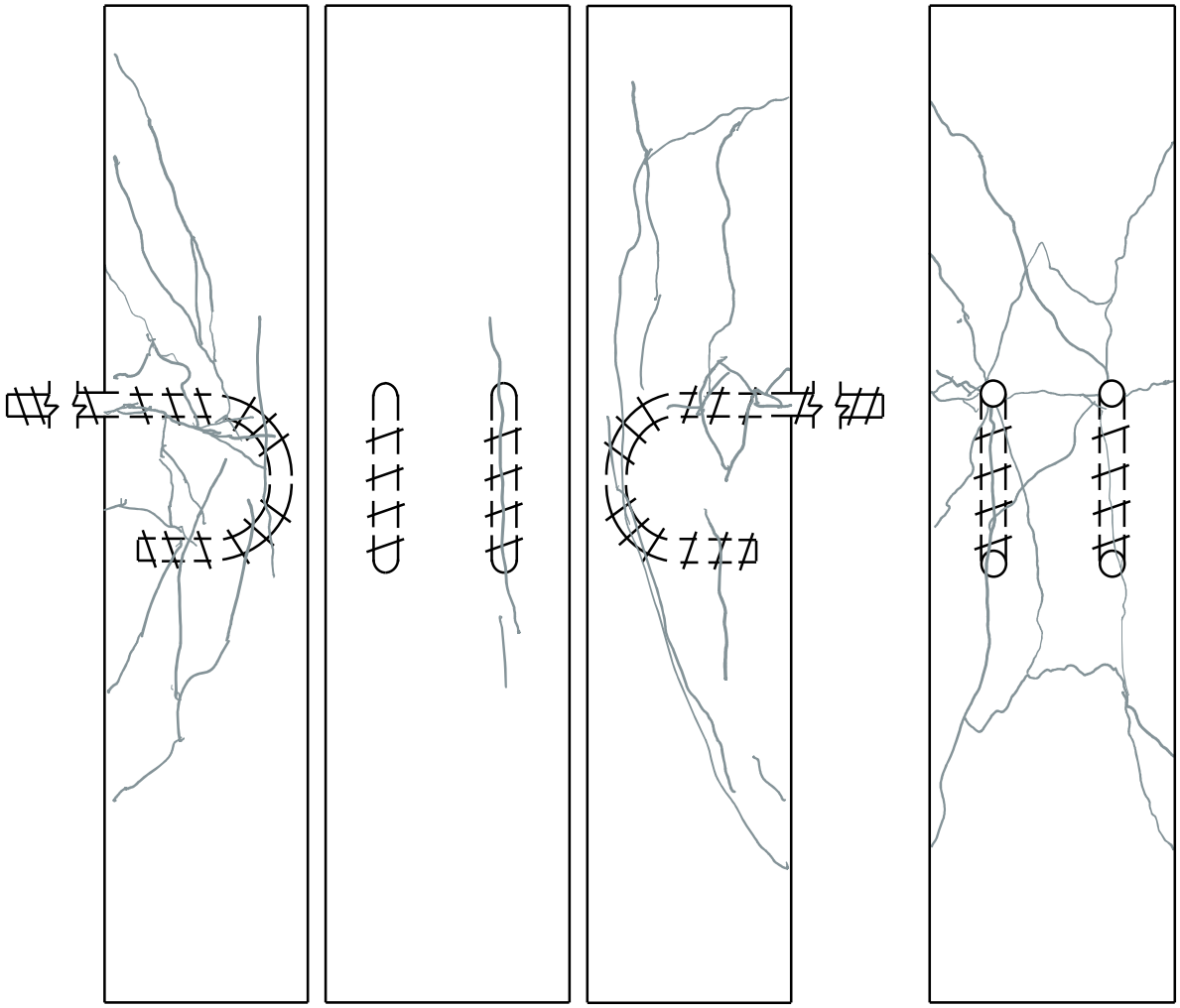

(a) (b) (c) (d)

Figure J.21: Crack pattern at maximum normalized tensile load for beam-column joint specimen MD3-180: (a) west side face, (b) back face, (c) east side face, and (d) front face

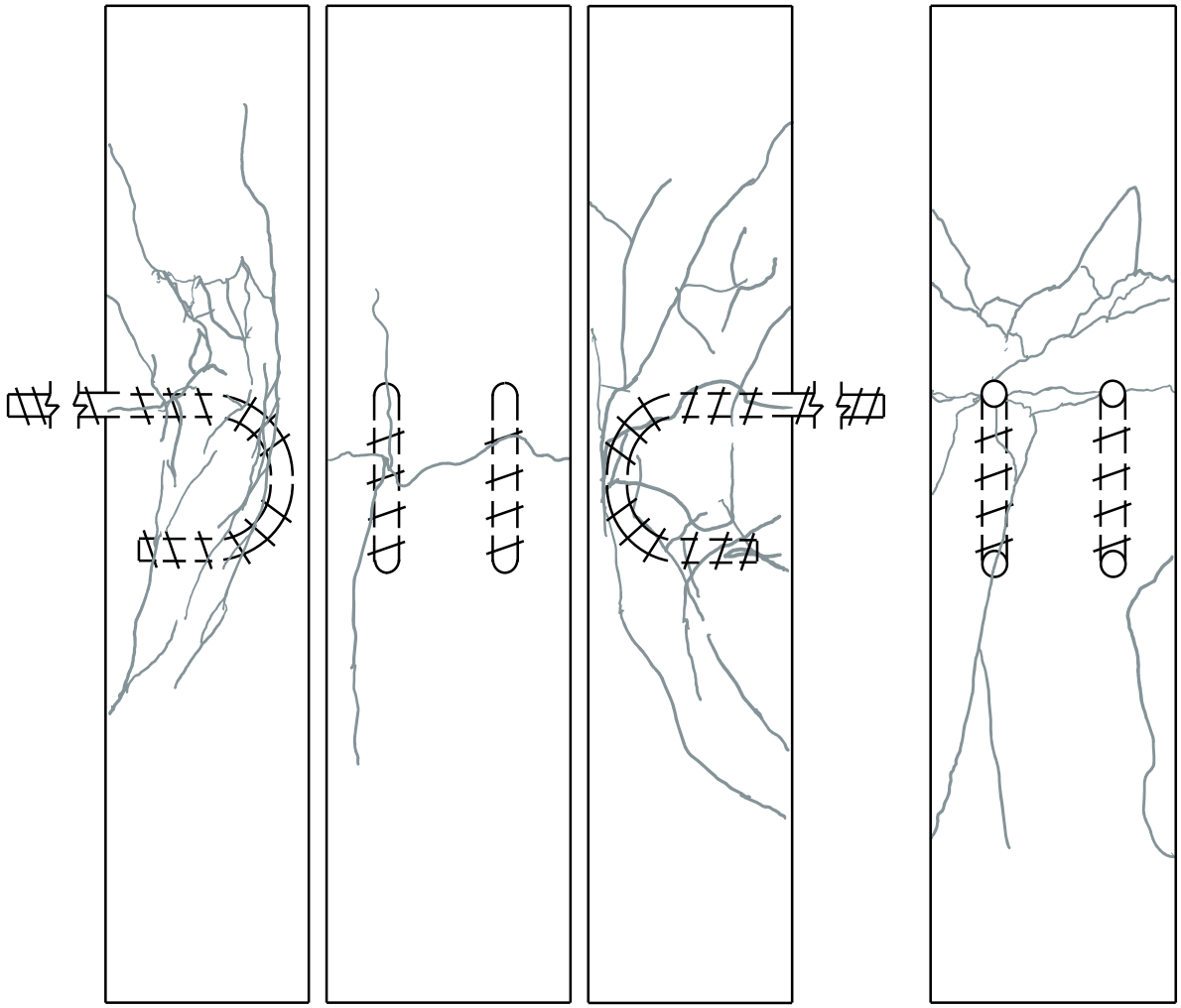

(a) (b) (c) (d)

Figure J.22: Crack pattern at maximum normalized tensile load for beam-column joint specimen MD4-180: (a) west side face, (b) back face, (c) east side face, and (d) front face

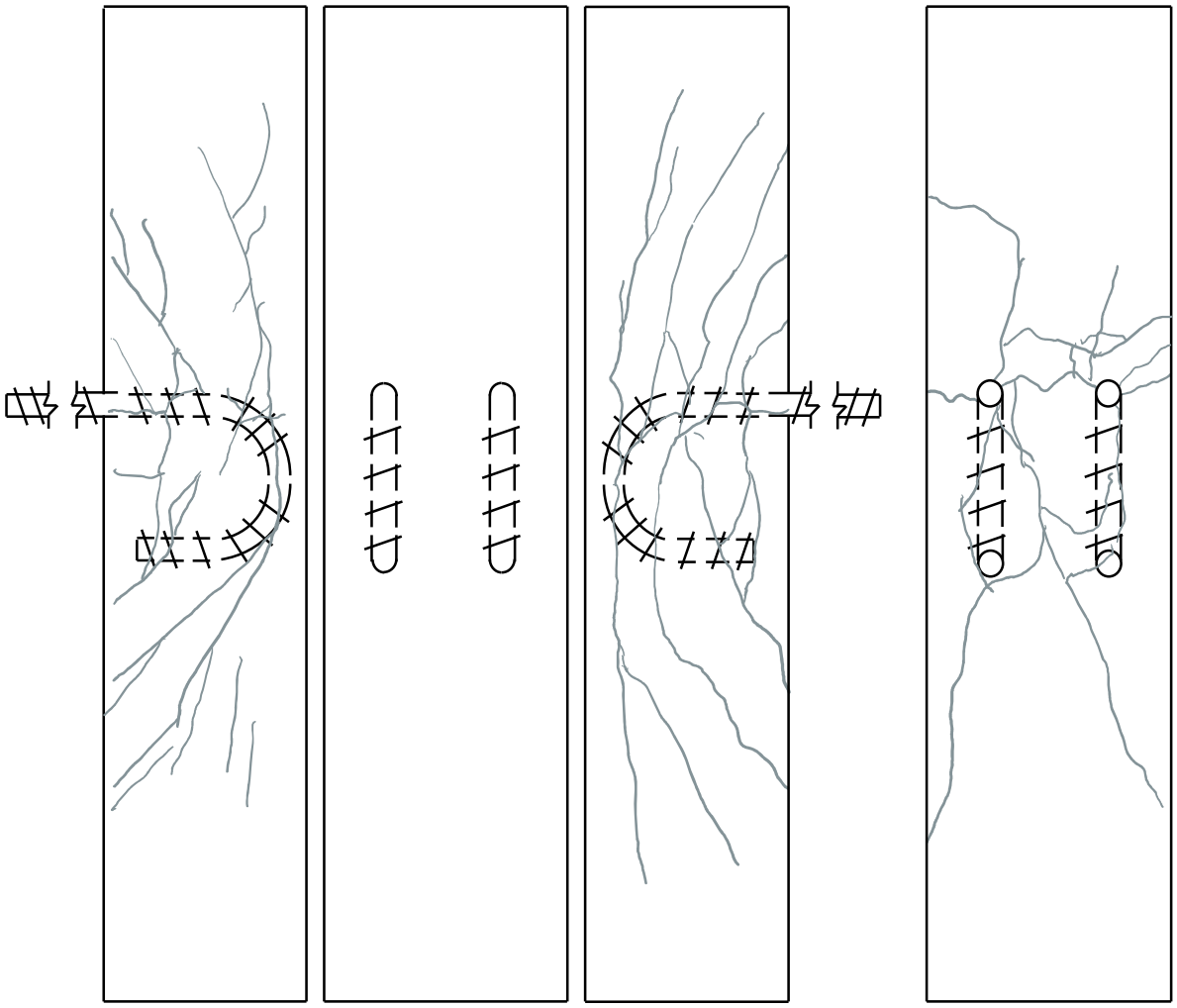

(a) (b) (c) (d)

Figure J.23: Crack pattern at maximum normalized tensile load for beam-column joint specimen MD5-180: (a) west side face, (b) back face, (c) east side face, and (d) front face

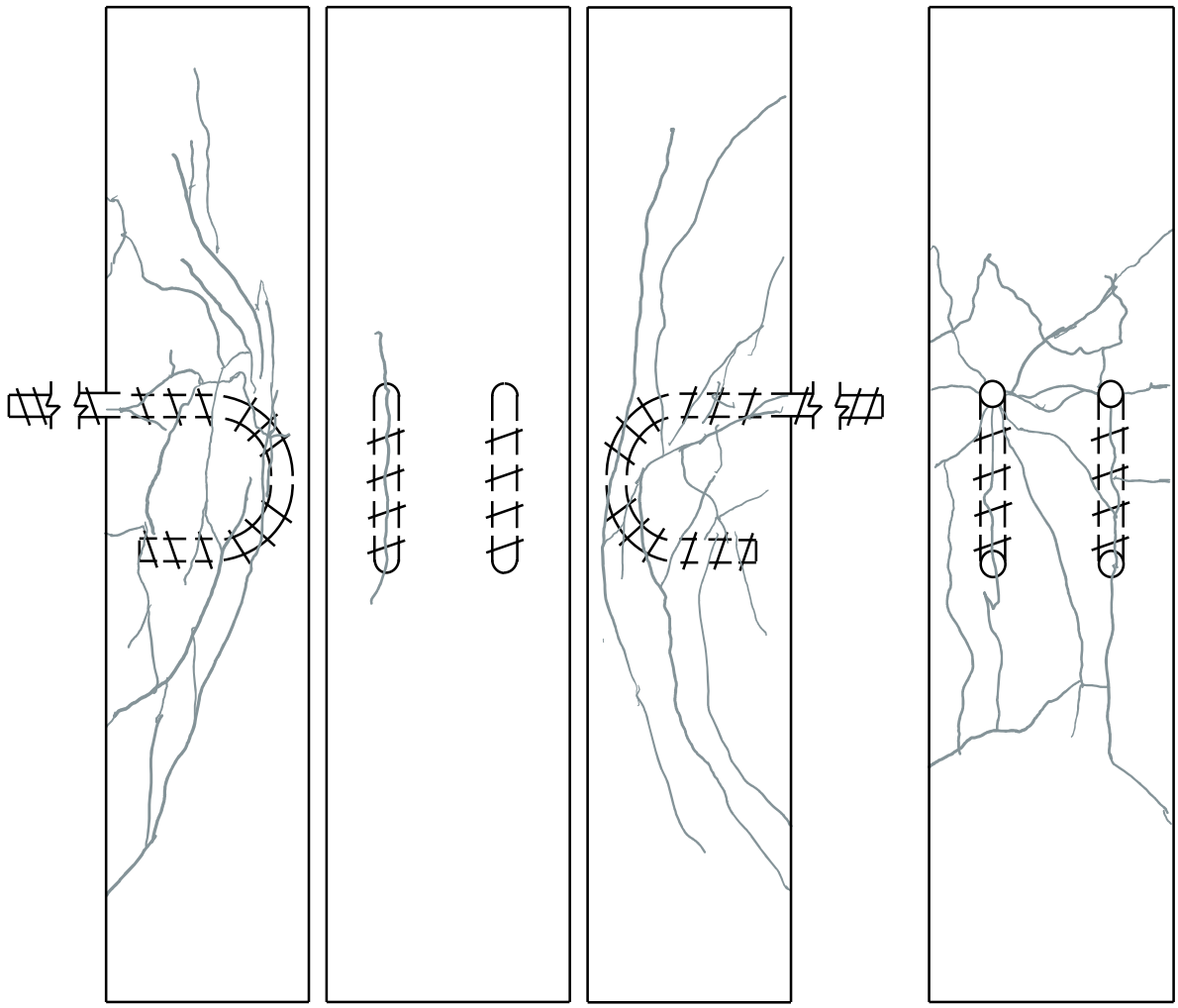

(a) (b) (c) (d)

Figure J.24: Crack pattern at maximum normalized tensile load for beam-column joint specimen MD6-180: (a) west side face, (b) back face, (c) east side face, and (d) front face

Appendix K: Cracking Progression on the Faces of the Beam-Column Joint Specimens

Table K.1 presents the average normalized tensile load at which cracks first appeared on the front and back faces of beam-column joint specimens. The load at which cracks reached the edges of the front and side faces is also presented. Table K.2 presents the standard deviation of the normalized tensile load at which cracks first appeared on the front and back faces of beam-column joint specimens. The standard deviation at which cracks reached the edges of the front and side faces is also reported.

Table K.1: Averages for crack progression for the beam-column joint specimens

Specimen groups	Average normalized tensile load when cracks began on the front face (kN/√MPa)	Average normalized tensile load when cracks reached the edge of the front face (kN/√MPa)	Average normalized tensile load when cracks reached the front edge of the side face (kN/√MPa)	Average normalized tensile load when cracks began on the back face (kN/√MPa)
P90	8.47	8.74	14.9	14.2
MD90	9.46	9.57	18.1	15.9
P180	8.78	9.30	18.2	18.1
MD180	7.63	8.47	22.4	23.7

Table K.2: Standard deviation for crack progression for the beam-column joint specimens

Specimen groups	Standard deviation normalized tensile load when cracks began on the front face (kN/√MPa)	Standard deviation normalized tensile load when cracks reached the edge of the front face (kN/√MPa)	Standard deviation normalized tensile load when cracks reached the front edge of the side face (kN/√MPa)	Standard deviation normalized tensile load when cracks began on the back face (kN/√MPa)
P90	1.71	1.40	1.34	7.06
MD90	1.73	1.68	2.86	9.04
P180	1.38	1.35	3.33	2.09
MD180	0.515	0.501	1.65	1.74

Appendix L: Manual Approximation Method for Average Angle of the Near-Vertical Cracks on the Beam-Column Joint Specimens

Figure L.1 shows the manual approximation of the average angle of the near-vertical cracks for the east face of a representative beam-column joint specimen, P1-90. Manual approximation was necessary due to inherent crack angle variability and in the absence of an automated approach. Table L.1 shows the angles of the near-vertical cracks for individual beam-column joint specimens.

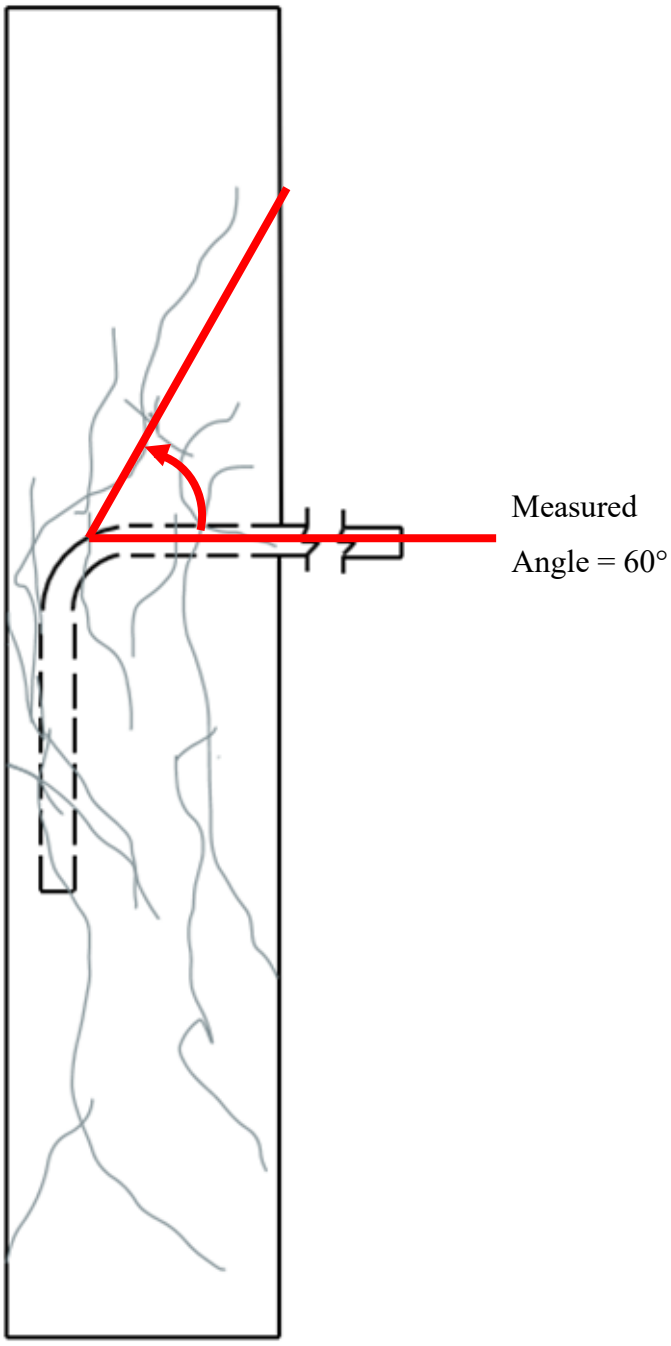

Figure L.1: Crack pattern at maximum normalized tensile load for the east face of the beam-column joint specimen P1-90

Table L.1: Average Angle of the Near-Vertical Cracks on the Beam-Column Joint Specimens

Specimen identification	Vertical angle (°)
P1-90	60
P2-90	55
P3-90	50
P4-90	64
P5-90	50
P6-90	53
P1-180	57
P2-180[a]	58
P3-180	75
P4-180[a]	65
P5-180	70
P6-180	70

Specimen identification	Vertical angle (°)
MD1-90	65
MD2-90[a]	65
MD3-90	65
MD4-90	72
MD5-90	70
MD6-90	70
MD1-180	65
MD2-180	70
MD3-180	72
MD4-180	75
MD5-180	75
MD6-180	75

[a] Denotes that this specimen was excluded as an outlier, as discussed in Section 4.4.

Appendix M: Displacement versus Normalized Tensile Load of Hooked Bars

Figures M.1 to M.4 show the displacement versus normalized tensile load curves for each beam-column joint specimen. Readings for specimens P1-180 and P5-180 both ceased at the time of maximum normalized tensile load due to a malfunction of the laser displacement transducers. This is evident in Figure M.2. Figures M.1 through M.4 show that individual specimen tests terminated across a range of different displacement and applied normalized tensile load values. No conclusions can be drawn from this observation as the variation was caused by the user halting the test upon reaching the maximum normalized tensile load and the speed with which the computer system shut down the hydraulic cylinders. As discussed in Section 3.7, the hooked bars continued to be pulled from the beam-column joint specimen as the test apparatus was shut down.

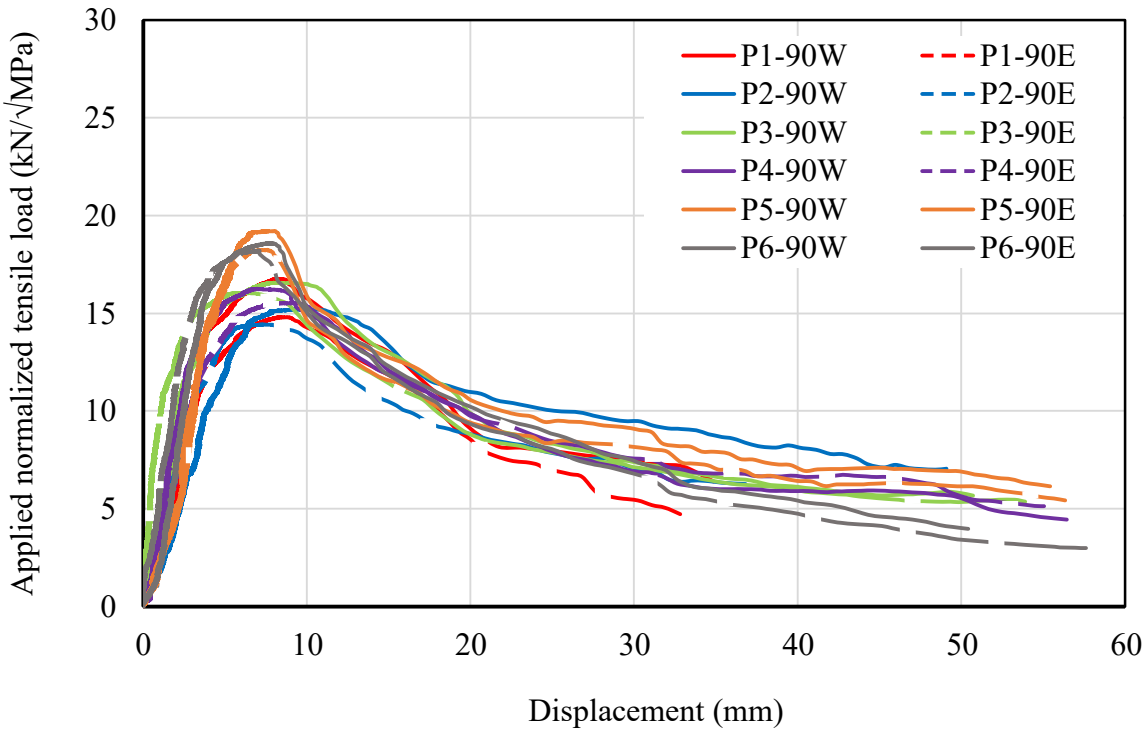

Figure M.1: Displacement versus normalized tensile load graph for plain 90° hooked bars

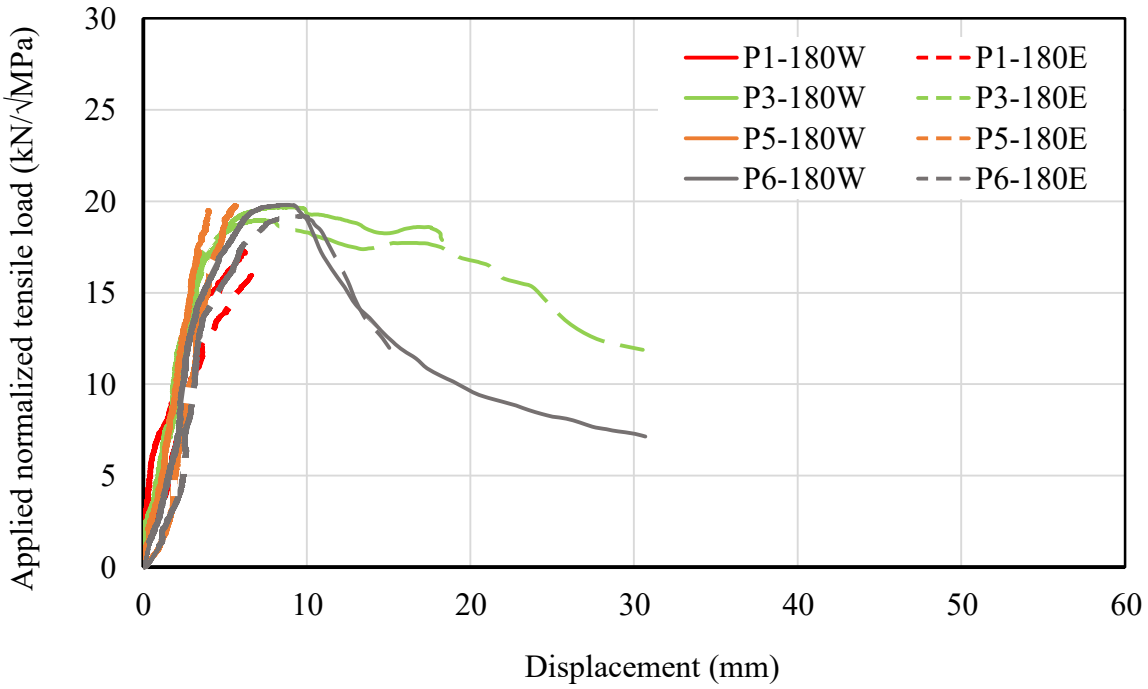

Figure M.2: Displacement versus normalized tensile load graph for plain 180° hooked bars

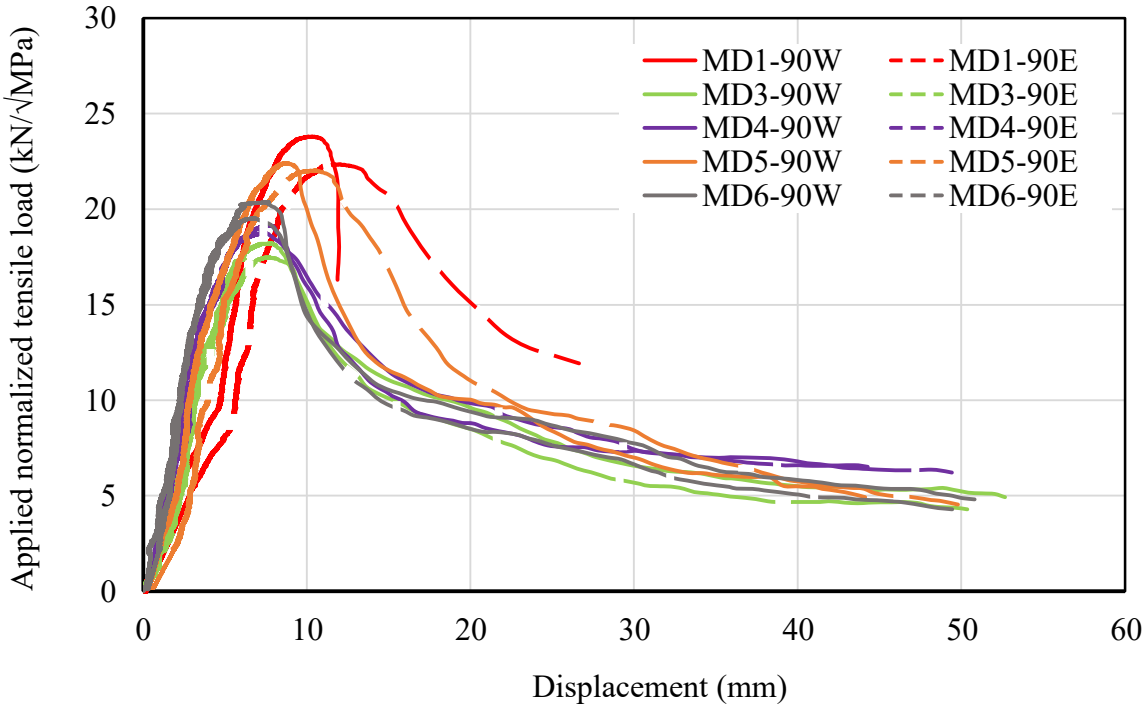

Figure M.3: Displacement versus normalized tensile load graph for modern deformed 90° hooked bars

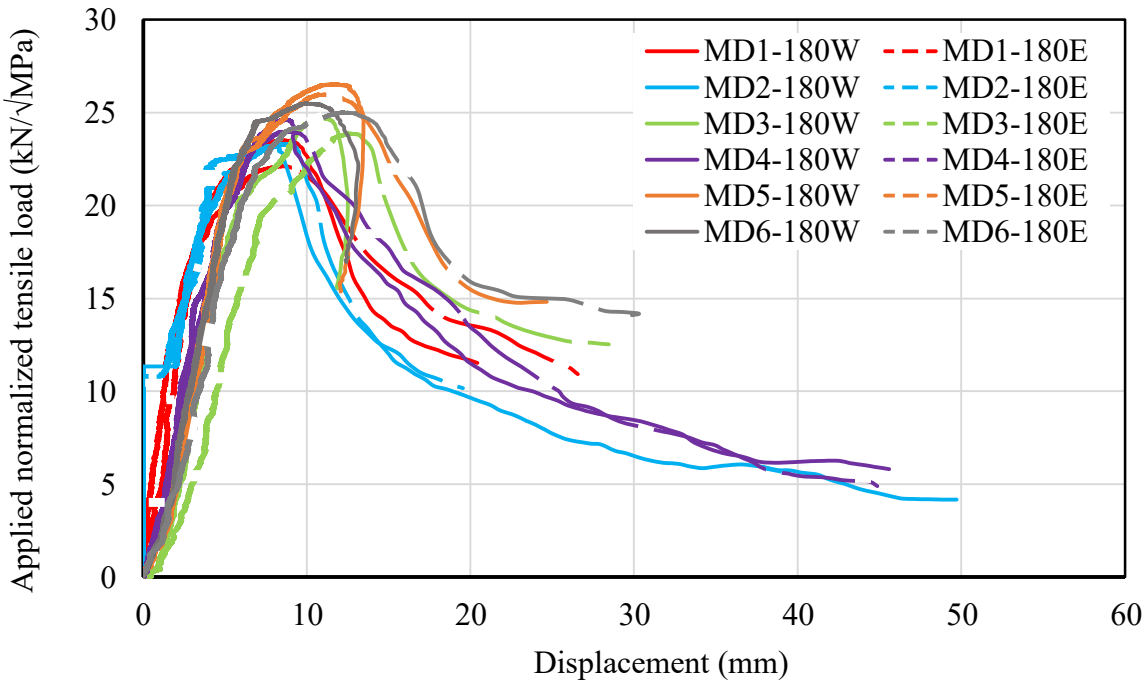

Figure M.4: Displacement versus normalized tensile load graph for modern deformed 180° hooked bars